6-22-2017 12:00 AM

Using Fluid-Mobile Elements to Decipher an Aqueous History Preserved in the Sedimentary Rocks of Gale Crater, Mars

Jeff A. Berger
The University of Western Ontario

Supervisor
Mariek Schmidt
The University of Western Ontario Joint Supervisor
Roberta Flemming
The University of Western Ontario

Graduate Program in Geology
A thesis submitted in partial fulfillment of the requirements for the degree in Doctor of Philosophy

Recommended Citation

Berger, Jeff A., "Using Fluid-Mobile Elements to Decipher an Aqueous History Preserved in the Sedimentary Rocks of Gale Crater, Mars" (2017). *Electronic Thesis and Dissertation Repository*. 4674.
https://ir.lib.uwo.ca/etd/4674

Abstract

Fluid-mobile elements preserve a record of the aqueous history of Mars in the sedimentary rocks of Gale Crater, and they are traceable with the rover *Curiosity's* Alpha Particle X-ray Spectrometer (APXS). This is the fundamental principle behind the scientific questions addressed in the four main chapters of this dissertation. First, we conducted a field study at Hawai'i, an established Mars analogue, to investigate sedimentary processes and alteration in rocks comparable to those in Gale Crater. We conclude that open system, circumneutral weathering is very limited in Gale rocks; acid sulfate alteration and sedimentary mixing of diverse rocks is likely. Second, the Hawaiian samples were analyzed by Particle Induced X-ray Emission spectroscopy (PIXE) to evaluate the technique as an analogue for APXS. Third, we developed a novel, non-standard APXS calibration to determine the composition of a very thin layer of airfall dust on the rover. The global dust is enriched in the fluid-mobile elements sulfur and chlorine, but at a ratio found to be constant around the planet. This enables deconvolution of modern dust from underlying rock in APXS measurements to determine inherent sulfur and chlorine content in ancient rocks. Fourth, we used fortuitous zinc and germanium enrichments in Gale Crater rocks to establish a geochemical tracer pair for fluid processes in Gale. We propose a model in which the two trace elements were enriched together by hydrothermal fluids in the sediment source region, transported into the crater, and then fractionated by low temperature diagenetic fluids. The work presented here constrains fluid events affecting Gale sediments and can aid in unraveling fluid histories as *Curiosity's* traverse continues.

Keywords

Mars, APXS, airfall dust, martian dust, Mauna Kea, Kohala, Hawai'i, Mars analogue, Mars Science Laboratory, germanium, zinc, trace element enrichment, planetary science, Gale Crater, Jake M, geochemistry

Co-Authorship Statement

Chapter 2: A Mars Rover's Perspective of Maunakea and Kohala, Hawai'i: A Gale Crater Analogue for Deconvolving Provenance and Alteration Trends in APXS Geochemistry

Coauthors are Jeff A. Berger, Mariek E. Schmidt, Roberta L. Flemming, and Alicia P. Thomas. Berger planned, coordinated, and conducted fieldwork in Hawai'i and carried out sample preparation and analyses, except for XRF analyses and thin sectioning. Berger interpreted the Hawai'i and MSL data and wrote the manuscript. Schmidt and Flemming are Berger's thesis supervisors, and supervised Berger's work (including fieldwork) by providing feedback and guidance, evaluated and edited the manuscript, and provided financial support. Thomas was a field assistant who provided logistical support and scientific feedback.

This chapter will be submitted to a peer-review journal in 2017.

Chapter 3: Particle Induced X-ray Spectrometry of Hawaiian Materials: An APXS Analogue Study

Coauthors are Jeff A. Berger, Mariek E. Schmidt, John L. Campbell, Erin L. Flannigan, Ralf Gellert, and Roberta L. Flemming. Berger subsampled from the collection of Hawaiian samples from Chapter 2 of this dissertation, as well as from the collections of D. W. Ming and R. V. Morris (Johnson Space Center). Berger prepared all samples for PIXE, conducted data analysis and interpretation, and wrote the manuscript. Schmidt and Flemming are Berger's thesis supervisors, and supervised Berger's work by providing feedback and guidance, evaluated and edited the manuscript, and provided financial support. Campbell and Flannigan conducted PIXE analyses, provided guidance and quality control for data analysis, and assisted with data interpretation. Gellert provided guidance for data analysis and assisted with data interpretation.

Chapter 3 will be submitted to a peer-review journal in 2017.

Chapter 4: A Global Mars Dust Composition Refined by the Alpha Particle X-ray Spectrometer in Gale Crater

Coauthors are Jeff A. Berger, Mariek E. Schmidt, Ralf Gellert, John L. Campbell, Penelope L. King, Roberta L. Flemming, Douglas W. Ming, Benton C. Clark, Irina Pradler, Scott J. V. VanBommel, Michelle E. Minitti, Alberto G. Fairén, Nicholas I. Boyd, Lucy M. Thompson, Glynis M. Perrett, Beverley E. Elliott, and Elstan Desouza. Berger conceived the project and coordinated with rover science planners and engineers to carry out the dust observations by *Curiosity* on Mars. Berger conducted all data analysis, interpreted the data, and wrote the manuscript. Schmidt and Flemming are Berger's thesis supervisors, and supervised Berger's work by providing feedback and guidance, evaluated and edited the manuscript, and provided financial support. Gellert is the Principal Investigator of the APXS and provided guidance and quality control for data analysis, and assisted with data interpretation. Campbell is the Principal Investigator of the X-ray yield software used for the work and provided guidance on data analysis, interpretation, and evaluated and edited the manuscript. King, Ming, Clark, Minitti, and Fairén evaluated the manuscript and provided feedback and edits. Pradler, VanBommel, Boyd, Thompson, Perrett, Elliott, and Desouza supported APXS operations and provided feedback and edits on the manuscript.

This chapter was published in the journal Geophysical Research Letters in December 2015.

Chapter 5: Zinc and Germanium in the Sedimentary Rocks of Gale Crater on Mars Indicate Hydrothermal Enrichment Followed by Diagenetic Fractionation

Coauthors are Jeff A. Berger, Mariek E. Schmidt, Ralf Gellert, Nicholas I. Boyd, Elstan Desouza, Roberta L. Flemming, Matthew R. M. Izawa, Douglas W. Ming, Glynis M. Perrett, Elizabeth B. Rampe, Lucy M. Thompson, Scott J. V. VanBommel, Albert S. Yen. The zinc and germanium results for the MSL mission are a subset of a dataset obtained by the MSL NASA-JPL project, including ~300 APXS measurements over 12 km of *Curiosity's* traverse on Mars. Berger was a member of the APXS Science Team, and was involved in the project primarily by supporting APXS tactical and strategic operations.

Berger also participated in strategic scientific discussions and interpretations relevant to this work. Berger evaluated the Zn and Ge data in the context of the overall MSL dataset. Berger researched the geochemical behavior of the trace elements Zn and Ge, and made novel observations about their distribution in Gale Crater. Based on that, Berger conceived an original model for Zn and Ge as a trace element pair that is relevant to the broad history of Gale Crater. Gellert is the Principal Investigator of the APXS and developed the analytical method for quantifying Ge and Zn. Gellert provided guidance, quality control, data analysis, and assisted with data interpretation. Schmidt and Flemming are Berger's thesis supervisors, and supervised Berger's work by providing feedback and guidance, evaluated and edited the manuscript, and provided financial support. Izawa, Ming, Rampe, Thompson, VanBommel, and Yen evaluated the manuscript and provided feedback and edits. Boyd, Desouza, Thompson, VanBommel, and Perrett provided support to APXS operations and evaluated and provided edits.

This chapter has been reviewed and was accepted for publication in the Journal of Geophysical Research – Planets in July 2017.

Acknowledgements

I am deeply appreciative of the support and guidance of my scientific mentors Dr. Sherry Cady, Dr. Penny King, Dr. Mariek Schmidt, Dr. Roberta Flemming, and Dr. Ralf Gellert.

I thank everyone on the MSL *Curiosity* Science Team and APXS Science Team for respectfully allowing me to live with everyone on Mars for four years. I am indebted to Douglas W. Ming (NASA Johnson Space Center), and Richard V. Morris (NASA Johnson Space Center) for support, invaluable discussions, and access to their sample collections. I am grateful to the Hawai'i Division of Forestry and Wildlife and Scott Rowland (University of Hawai'i) for facilitating access to the Maunakea Forest Reserve. M. E. Schmidt provided support in part from a Canadian Space Agency (CSA) MSL Participating Scientist Grant for which I am thankful. I am also grateful for the support of two Ontario Graduate Scholarship grants 2015-2017, an NSERC CREATE fellowship, and a CSA ASTRO Cluster Program incentive grant.

Table of Contents

List of Tables

Chapter 1

Chapter 2

Chapter 3

Chapter 4

Chapter 5

List of Figures

Chapter 1

Chapter 2

Chapter 3

Chapter 4

Chapter 5

List of Appendices

Chapter 2

Appendix 2-1: A summary of XRF results is attached as an excel file 'Berger_Appendix-2-1.xlsx'.

Appendix 2-2: A summary of literature XRF results for Maunakea [*Morris et al.,* 2000; *Hamilton et al.*, 2008] is attached as an excel file 'Berger_Appendix-2-2.xlsx'.

Appendix 2-3: Summary of site and sample descriptions is attached as an excel file 'Berger_Appendix-2-3.xlsx'.

Appendix 2-4: Detailed maps of Maunakea sample sites are attached as a .pdf file 'Berger_Appendix-2-4.pdf'.

Appendix 2-5: Annotated thin section micrographs are attached as a .pdf file 'Berger_Appendix-2-5.pdf'.

Chapter 3

Appendix 3-1: A sample summary with PIXE results is attached as an excel file 'Berger_ Appendix-3-1.xlsx'. The oxides are corrected by the *ECF* and renormalized on a volatile-free basis.

Chapter 4

Appendix 4-1: The published manuscript "A Global Mars Dust Composition Refined by the Alpha Particle X-ray Spectrometer in Gale Crater" is attached as a .pdf file 'Berger_Appendix-4-1.pdf'.

Chapter 5

Appendix 5-1: APXS results for Zn, Ge, and selected oxides and elements in Gale Crater, sols 0-1360 is attached as a supplemental file named "Berger_Appendix-5-1.xlsx".

List of Abbreviations

Curiosity Spacecraft Instrumentation and Hardware

APXS	Alpha Particle X-ray Spectrometer
ChemCam	Chemical Camera (LIBS)
CheMin	Chemistry and Mineralogy (XRD)
DRT	Dust Removal Tool
Hazcam	Hazard avoidance cameras
MAHLI	Mars Hand Lens Imager
Mastcam	Mast cameras
Navcam	Navigation cameras
O-tray	Titanium Science Observation Tray
SAM	Sample Analysis at Mars

Gale Crater Waypoints, Stratigraphic Units, and Targets

BG	Bradbury Group
BK	Buckskin
CH	Confidence Hills
YKB	Yellowknife Bay

Other Abbreviations

CIA	Chemical Index of Alteration
D_{90}	The depth within a sample from which 90% of the APXS signal is detected
DCF	Dust Correction Factor
ECF	Empirical Correction Factor
FOV	Field of View
IR	Infrared
LIBS	Laser-Induced Breakdown Spectrometry
LOD	Limit of Detection
LOI	Loss on Ignition
MER	Mars Exploration Rover mission
MSL	Mars Science Laboratory rover mission
PIXE	Particle-Induced X-ray Emission spectrometry
Sol	24.6 h; Martian solar day since landing
XRD	X-ray Diffraction
XRF	X-ray Fluorescence
μXRD	Micro-beam X-ray Diffraction

Chapter 1

1. General Introduction

Mars research is rooted in the questions it can answer about the Earth. Fundamental questions in the natural sciences, including the conditions under which life began and persisted, the impact of the biosphere on Earth's planetary evolution, and the initiation of plate tectonics, are informed by the study of Mars. Answers to these fundamental questions are contained within Earth's ancient history, but the story is murky because the first billion years of the rock record have been almost completely erased by plate tectonics. Mars, however, is somewhat frozen in time because its crust has not been recycled, and it preserves very ancient rocks at the surface. Mars is thus a useful place for understanding the early Earth by way of comparison. Following this principle, the consensus research questions driving Mars research include [*Hamilton, ed.*, 2015]: 1) Did Mars ever support life? 2) What is the history of Mars' climate? 3) What was the geologic evolution of Mars?

Fluid-mobile elements are particularly relevant to the questions about Mars' history because they preserve ancient aqueous geochemical conditions in the rocks, and the rover-deployed Alpha Particle X-ray Spectrometer (APXS) is capable of measuring many of these elements in situ. APXS instruments have flown on four missions to Mars: the *Soujourner* rover on *Pathfinder* [*Rieder et al.*, 1997], the Mars Exploration Rovers (MER) *Spirit* and *Opportunity* [*Rieder et al.*, 2003], and the Mars Science Laboratory (MSL) rover *Curiosity* [*Gellert et al.*, 2009]. *Soujourner* measured 11 targets at one landing site; the other three rovers have measured hundreds of targets over traverses summing to ~55 km. The APXS instruments on *Spirit, Opportunity,* and *Curiosity* are arm-mounted and measure ~1.5-2.5 cm spots on rock and soil surfaces. The instrument interrogates sample surfaces with alpha particles and X-rays from radioactive ^{244}Cm sources and measures the characteristic X-rays emitted from the sample. Major, minor, and some trace elements with atomic numbers (Z) greater than 10 (Ne) are analyzed.

The APXS instruments have discovered evidence of varied fluid alteration regimes at three different landing sites located thousands of kilometers apart [e.g., *Ming et al.*, 2008; *Squyres et al.*, 2012; *McLennan et al.*, 2013; *Thompson et al.*, 2016]. Variations in Al/Si and Mg/Si (Figure 1-1) demonstrate diverse alteration conditions, including silica enrichments that are linked to alteration by acidic fluids [*Ming et al.*, 2008; *Schmidt et al.*, 2008; *Yen et al., 2017*], Al enrichments indicative of smectite formation [*Ming et al.*, 2008], and high Al, Na, and K in alkalic rocks in Gale Crater consistent with mantle metasomatism [*Stolper et al.*, 2013; *Schmidt et al.*, 2014; *Treiman et al.*, 2016]. The APXS also quantifies geologically significant trace elements (Ni, Zn, Br, Ge, ± Rb, Sr, Pb, Cu, Se), which have been used to track geochemical processes. For example, Ni and Zn indicate multiple processes (Figure 1-2), including the scavenging of Ni in Mg-sulfates in acidic fluids [*Yen et al.*, 2017], depletion of Ni and Zn by leaching in acidic fluids [*Gellert et al.*, 2015], concentration of Zn by Cl-rich diagenetic fluids in sandstones and veins (see Chapter 5), and Ni enrichment by meteoritic input to the surface [*Yen et al.*, 2006]. By studying these trends in tandem with other rover instrument data (e.g., X-ray diffraction, imaging), the geochemical evidence from APXS data provides constraints for the history of each of the rover sites. In general, the rover missions have revealed that a complex interplay of volcanic, impact, and sedimentary processes on the Martian surface occurred with fluid conditions ranging from hydrothermal [e.g., *Schmidt et al.*, 2008; *Squyres et al.*, 2008, 2012] to low temperature and circumneutral [*McLennan et al.*, 2013] to concentrated acidic brines [e.g., *Morris et al.*, 2006]. The data acquired from the Mars surface by rovers is complementary to detailed studies of meteorites that also point to fluid history on Mars [e.g., *Filiberto et al.*, 2014; *McCubbin et al.*, 2016].

Here, I concentrate on *Curiosity's* APXS dataset to examine geochemical trends and propose constraints for the history of Gale Crater. *Curiosity* landed in Gale Crater to investigate the possibility that ancient conditions were amenable to microbial life [*Grotzinger et al.*, 2012]. Gale Crater was selected as a landing site primarily because orbital remote sensing identified minerals in strata progressing from phyllosilicates to sulfates to anhydrous phases, indicating a "wet to dry" paleoenvironmental transition over time [*Milliken et al.*, 2010]. These strata are kilometers thick, with alluvial and fluvial geomorphologic features indicating fluid flow into the crater with no obvious outlets, suggesting aqueous activity and the possibility of standing water [*Anderson*, 2010]. The habitability of ancient Mars can thus be assessed in Gale Crater by asking these science questions: What was the paleoclimate of Gale Crater? Was liquid water stable for extended periods? What were the geochemical conditions of surface and subsurface liquids (e.g., acidic, neutral)? What is the provenance of the Gale Crater sedimentary rocks? The work presented here seeks to constrain these questions.

The four chapters of the main text of my dissertation reflect the exploratory nature of Mars research because they take advantage of fortuitous discoveries. They also emphasize methods to better understand the rover's dataset. The dissertation contains two main components: 1) an Earth analogue study of Hawai'i and 2) investigations of fluid-mobile elements in *Curiosity's* APXS dataset.

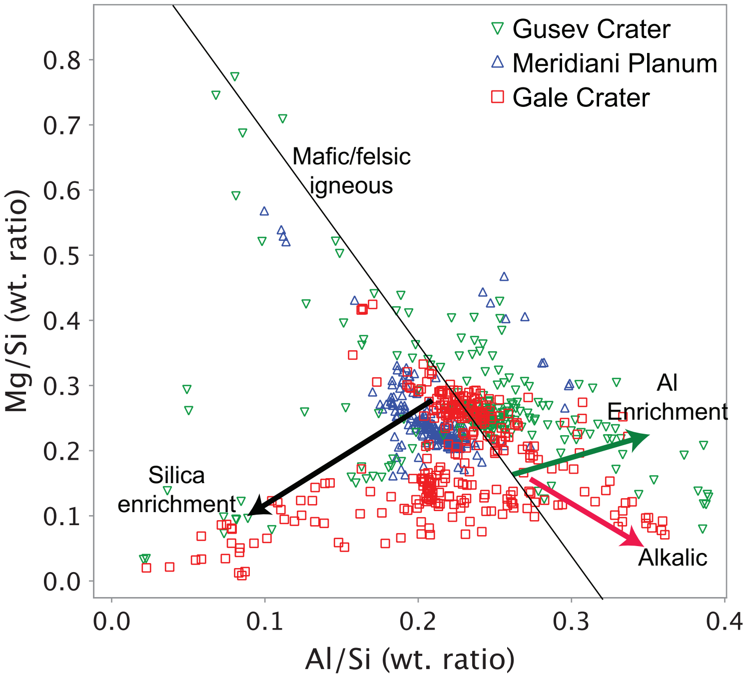

Figure 1-1: Elemental trends in APXS data for Gusev Crater, Meridiani Planum, and Gale Crater. Mg/Si versus Al/Si demonstrates variation due to igneous mafic/felsic fractionation consistent with the Martian meteorites (black line) [*Ming et al.*, 2008; *McSween Jr. et al.*, 2009]. Deviations from this basaltic trend are apparent in enrichments in aluminum (green arrow), silica (black arrow), and in Al and alkali elements at Gale Crater (red arrow). Data are from the Planetary Data System (http://pds-geosciences.wustl.edu).

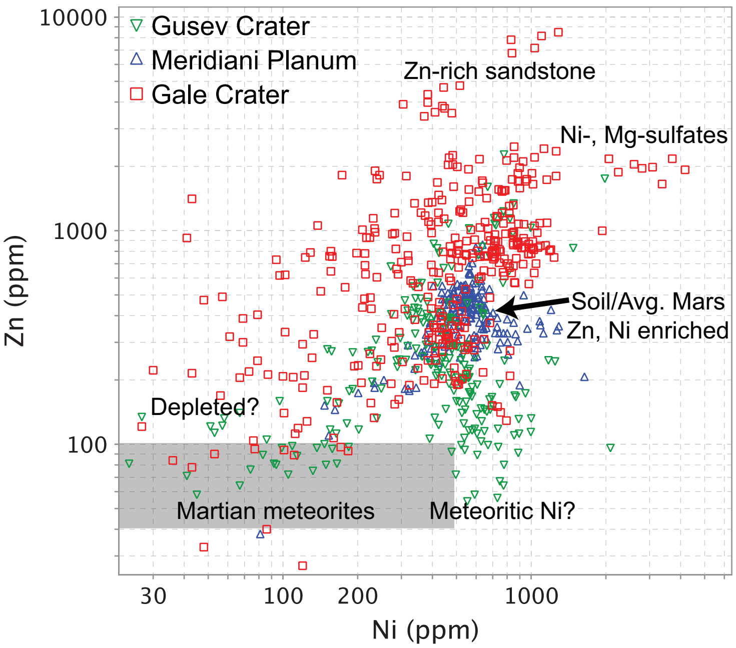

Figure 1-2: APXS results for Zn and Ni on Mars. The average soils (arrow), generally accepted to be representative of the composition of the average Mars crust [e.g., *Yen et al.*, 2005; *Taylor and McLennan*, 2010], are enriched in both Ni and Zn relative to the Martian meteorites (gray box), which have concentrations similar to basalts, picrites, and lherzolites [*Tuff et al.*, 2013].

1.1. Hawai'i Analogue Study

For the analogue component of my dissertation, I conducted a field study of Hawai'i to investigate geochemical and mineralogical trends relevant to Gale Crater. The processes that shaped Mars can be inferred, in part, by observing the processes that shaped Earth. This argument is somewhat cyclical with respect to the statement above that we can learn about Earth by studying Mars, but geologic processes that are well-understood on Earth can be compared with Mars and then in turn be applied to understanding the murkier parts of Earth's history. This is the basic principle motivating Mars analogue studies.

1.1.1. Maunakea and Kohala Geologic Setting

Maunakea and Kohala constitute most of the northern half of the island of Hawai'i and both evolved through similar shield and post-shield volcanic stages. Outcrop on Kohala consists of two volcanic groups dated from ~470 ka to 60 ka: the transitional basalt (tholeiitic to alkalic) of the Pololu Volcanics and the younger hawaiites, mugearites, benmoreites, and trachytes of the Hawi Volcanics [*Lanphere and Frey*, 1987]. Maunakea is capped by two similar groups erupted from ~250 ka to 4 ka: the transitional basalt of the Hamakua Volcanics overlain by the hawaiites and mugearites of the Laupahoehoe Volcanics [*Porter*, 1979; *Wolfe et al.*, 1997]. A compositional gap separates the basaltic Pololu and Hamakua Volcanics from the more felsic, incompatible element-enriched Hawi and Laupahoehoe Volcanics; this gap is wider in the Maunakea lavas because Laupahoehoe rocks have a narrower range of silica and total alkali (Figure 1-3) [*Lanphere and Frey*, 1987; *Wolfe and Morris*, 1996; *Wolfe et al.*, 1997]. A lower degree of melting and crystal fractionation are proposed mechanisms for the evolution of the Kohala and Maunakea magmatic systems [e.g., *Lanphere and Frey*, 1987; *Spengler and Garcia*, 1988; *Wolfe et al.*, 1997].

The Hawaiian climate has varied over the age of the exposed rocks (less than ~500 ka). The dominant weather patterns are thought to have remained constant, with most weather systems approaching from the east-northeast side of the island, causing a rain shadowing effect on the west-southwest sides of Kohala and Maunakea [*Giambelluca et al.*, 2013]. Thus, precipitation and the related weathering rates vary widely on the island. At sites on the northeastern side below the summit of Maunakea, mean annual rainfall is 2300-3100 mm, whereas sites sampled above 2000 m elevation have mean annual rainfall of 210-430 mm [*Giambelluca et al.*, 2013]. This large precipitation gradient enables sampling of the same rock types in different weathering regimes. Climate variation also led to three periods with alpine glaciers on Maunakea evident in till deposits, hayaloclastites, and pillow basalts [*Porter*, 1979; *Wolfe et al.*, 1997].

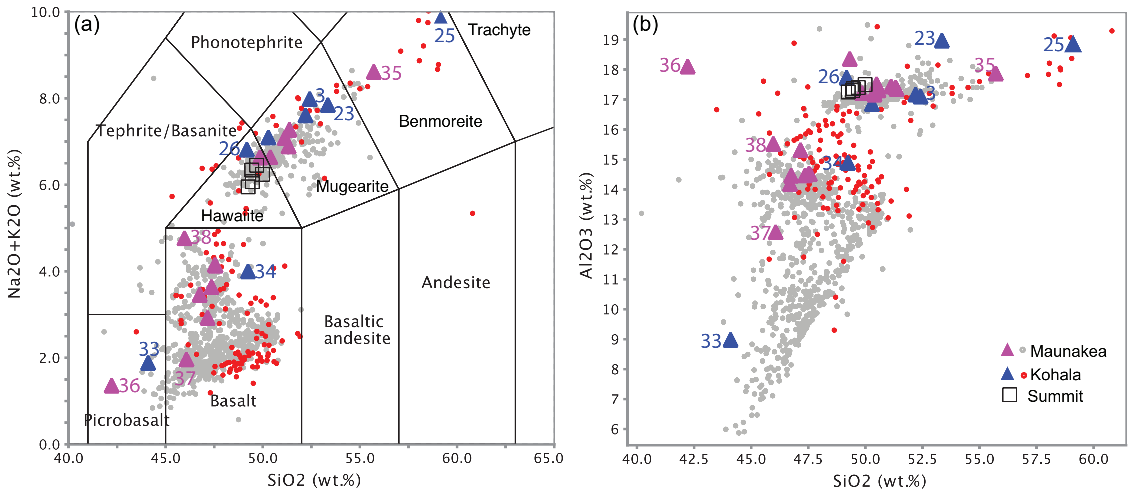

Figure 1-3: (a) Total alkali classification diagram [*Le Maitre et al.*, 1989] and (b) Al_2O_3 versus silica with XRF results for unaltered (or least altered) whole rock volcanics from Maunakea and Kohala (triangles) and the summit of Maunakea (squares). Numbered points denote the weathering profile site numbers discussed in chapter 2 (Table 2-1; MK15 prefix omitted for clarity) and compositions of unaltered (or least altered) rocks in profiles. Gray and red dots are previous whole rock analyses of the post-shield volcanics from Maunakea and Kohala, respectively (data from Georoc database).

1.1.2. Relevance of Hawai'i to Mars

Hawai'i has been studied as a Mars analogue previously because 1) the volcanic units are similar in composition and spectral properties to Mars, 2) some areas have been exposed to a Mars-like arid environment with limited weathering and vegetation, 3) rocks have been exposed to a range of weathering regimes (e.g., acidic, circumneutral), and 4) the island has been isolated from continental input and has a well-constrained geologic history [e.g., *Bell et al.*, 1993; *Golden et al.*, 1993; *Morris et al.*, 1993, 2000, 2001, 2005; *Hamilton et al.*, 2008; *Seelos et al.*, 2010]. The alkali basaltic volcanics of Maunakea are relevant to Mars because they are similar in composition to average Mars as determined by APXS at three distant sites (Figure 1-4). In Gale Crater, a new class of high alkali rocks (mugearitic) named Jake_M was discovered early in the mission. This inspired us to revisit Maunakea and Kohala volcanoes on Hawai'i for a Mars analogue study because the range in compositions overlaps in most major elements with Gale Crater (Figure 1-4). Maunakea also has sedimentary deposits that enabled the study of sediment with a provenance having two well-constrained endmember lithologies (basaltic and mugearitic). This is relevant to *Curiosity's* traverse of sedimentary units in Gale Crater, which contain evidence of a provenance with at least three igneous protolith compositions [*Thompson et al.*, 2016; *Treiman et al.*, 2016].

Our objective was to investigate the geochemical and mineralogical trends associated with igneous, alteration, and physical sedimentary processes, and how they may be distinguished in an APXS-like dataset from Hawai'i. These Hawaiian trends establish a framework that can be applied to Gale Crater to improve interpretations of that APXS dataset. The fieldwork, analyses, and comparison of Hawai'i to Gale Crater comprises Chapter 2 of this dissertation.

The field study of Hawai'i was extended to include an evaluation of Particle-Induced X-ray Emission spectroscopy (PIXE) as a laboratory analogue for APXS. The APXS method is a combination of X-ray fluorescence (XRF) with PIXE, the latter having a greater response for elements lighter than Ti [*Gellert et al.*, 2006]. The PIXE component is not well represented by XRF analyses alone because they have fundamentally different interactions with the sample [e.g., *Campbell and Cookson*, 1984]. Therefore, the XRF analyses used as an APXS analogue in Chapter 2, although accurate, may not best represent APXS analyses. This has been previously demonstrated in systematic deviations in APXS results from XRF results [*Campbell et al.*, 2012]. These deviations were linked to heterogeneities in the sample matrix. This is relevant to APXS because Martian samples are not powdered and fused into glass beads as they are in many XRF analyses [*Johnson et al.*, 1999]. Our objective was to investigate the accuracy of PIXE, evaluate the causes of systematic deviations, and discuss implications for interpreting APXS data. The PIXE study is presented in Chapter 3.

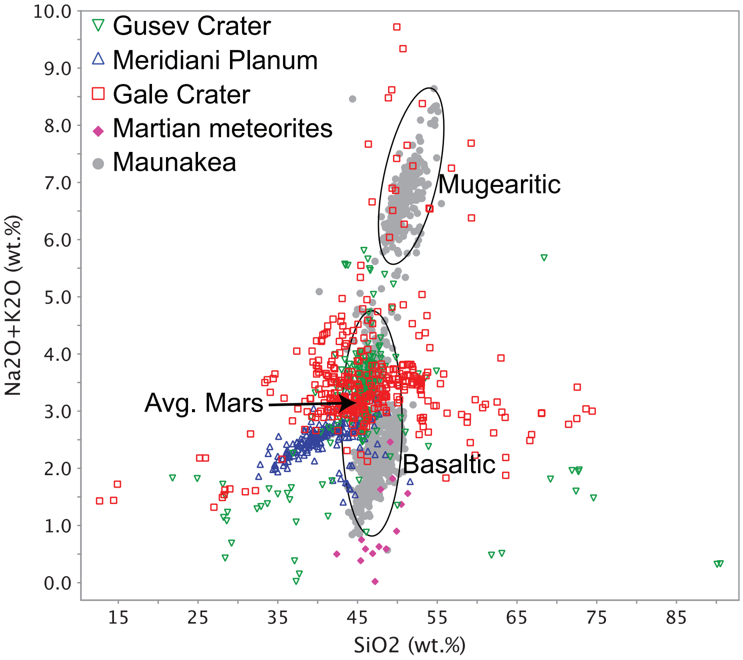

Figure 1-4: APXS results compared to whole rock bulk elemental data for Martian meteorites and relatively unaltered volcanics from Maunakea, Hawai'i. Martian meteorites largely have lower total alkali content than the in situ APXS measurements [*McSween Jr. et al.*, 2009]. Average mars soil has a composition that overlaps with the transitional basalts of Maunakea, but alkalic rocks in Gale Crater have extended the diversity observed in Martian rocks to include mugearitic compositions. Alteration and the addition of oxides and salts account for most of the deviations from the basaltic average Mars. Data from Hawai'i were obtained from the GEOROC database and basaltic and mugearitic compositions are indicated (elipses).

1.2. Exploration of Gale Crater with the APXS

The Gale Crater component of my dissertation evaluates fluid-mobile elements analyzed by APXS in concert with the rover's full dataset in two ways: 1) modern sulfur and chlorine in dust, 2) zinc and germanium enrichments and mobility.

First, a titanium observation tray on the rover that was intended to be a dumping spot for drilled sample ended up being unreliable for its designed purpose, but instead it was an excellent dust collector. Martian dust has a globally uniform composition that likely represents an average composition of the surface [*Yen et al.*, 2005, 2013], but uncertainties remained in its composition because it had previously only been measured on the ground [*Yen et al.*, 2005] and on aluminum spacecraft parts [*Goetz et al.*, 2005]. While *Curiosity's* observation tray collected dust for a couple of years on the Martian surface, I developed a novel method for analyzing thin layers (less than ~100 μm) of material on titanium metal with the APXS. We found an enrichment of fluid-mobile S and Cl in the dust, at the same ratio as soils around the planet, and presented a refined composition of the dust. Chapter 4 covers the dust experiment and interpretations.

Second, a fortuitous Zn and Ge enrichment was discovered in the sedimentary rocks of Gale Crater by the APXS. The two elements are typically enriched together in high temperature fluids [*Bernstein*, 1985]. However, they have differing chemical properties in low temperatures, with Zn being readily mobile in solutions at pH less than 6 [*Drever*, 1997], whereas Ge has low solubility, even at very low pH (< 4) [*Pokrovski and Schott*, 1998]. This contrast can potentially lead to fractionation in low temperature diagenetic fluids. In Chapter 5, we describe the occurrence of Zn and Ge and propose a model in which high temperature fluids enriched the two elements in the Gale Crater sediment source region. They were subsequently transported into the crater, then fractionated in diagenetic fluids. This model provides constraints for fluid conditions in Gale Crater.

To provide context for the discussion of Mars and Gale Crater, below I present an overview of Gale Crater and the APXS method and how the instrument is used in the field remotely by the *Curiosity* Science Team.

1.2.1. Gale Crater Geologic Setting

Curiosity's field site is in Gale Crater, a ~150 km wide impact structure on Mars that was formed ~3.7 - 3.5 Ga during the Late Noachian-Early Hesperian (Figure 1-5) [*Thomson et al.*, 2011; *Le Deit et al.*, 2013]. The crater floor was mantled by sediment sourced from the raised crater wall, crater rim, and central mound through localized valley incision and alluvial fan formation largely before 3.3 - 3.1 Ga [*Grant et al.*, 2014; *Grotzinger et al.*, 2015]. Much of the sediment was removed by aeolian reworking, and *Curiosity's* >1600 sol traverse ('sol' = 24.6 h; Martian solar day since landing) has been through a sequence of eroded sedimentary rocks (Figures 1-5, 1-6). One unit, the Sheepbed mudstone, has been exposed at the surface by erosion for 78 ± 30 Ma [*Farley et al.*, 2014]. The traverse has been within two regions, or stratigraphic groups, named Bradbury and Mt. Sharp [*Grotzinger et al.*, 2015].

Diverse textures and diagenetic features were found in the bedded Gale rocks, which preserve a record of Gale's paleoclimate. Sedimentary rocks include conglomerate, sandstone, and siltstone/mudstone with grain sizes below imager resolution (~16-32 μm per pixel for Mars Hand Lens Imager; MAHLI) [e.g., *Grotzinger et al.*, 2015; *Yingst et al.*, 2015; *Edgett et al.*, 2016]. Igneous outcrop has not been discovered (e.g., lava, tuff, and impact melt), but porphyritic igneous textures have been observed in float and in clasts contained within pebbly sandstone and conglomerate [e.g., *Sautter et al.*, 2015]. Diagenetic fluids are evident in veins, concretions, haloes, and replacement textures [e.g., *Grotzinger et al.*, 2014; *Kah et al.*, 2015; *Yen et al.,* 2017; *Nachon et al.,* 2017]. White Ca-sulfate veins fill fractures that crosscut most units, representing late diagenetic fluids; the timing of other features is less certain but they are hypothesized to be the result of earlier fluids [*Grotzinger et al.*, 2015]. Based on sedimentary and stratigraphic relationships (Figure 1-6), Grotzinger et al. [2014, 2015] presented evidence for the presence of at least one lake in Gale for thousands to millions of years, where bedded sediment was deposited. They proposed that a fluvial deltaic depositional system sourced from the crater rim is preserved in a sequence of coarser sandstone and conglomerate units. This system deposited fine-grained sediment in a lacustrine setting that formed laminated siltstone/mudstone. Recent aeolian erosion in the drier Amazonian climate exposed the current surface.

Morphological, sedimentological, and stratigraphic characteristics differentiate the units of the Bradbury and Mt. Sharp groups of Gale Crater (Figure 1-5) [e.g., *Grotzinger et al.*, 2015], and this is reflected in differences in geochemistry (Figures 1-7, 1-8; Table 1-1). The Bradbury group ranges from basaltic mudstone in the Yellowknife Bay formation (YKB) [*McLennan et al.*, 2013; *Vaniman et al.*, 2014] to hawaiitic and mugearitic sandstone and conglomerate in the overlying Bradbury rise [*Thompson et al.*, 2016]. The Bradbury rise sedimentary rocks are more alkali-rich, with an Al-rich trend (Jake_M), Fe-rich trend (Bathurst Inlet), and a mix of intermediate compositions ("Alkalic other") [*Schmidt et al.*, 2014b, 2014a].

Lower Mt. Sharp has two prominent units: the Murray formation and the unconformably overlying Stimson unit [*Newsom et al.*, 2016]. The Murray formation textures vary, but are primarily finely laminated and fine-grained. The lower section of Murray (including Pahrump Hills) has some distinguishing features from the upper section of Murray (after sol 1157), including ~20% less MgO and ~20% more Al_2O_3, but overall they are relatively uniform in composition (Figures 2b, 3b). An exception is the high silica unit above the Pahrump Hills named for the drill target Buckskin (SiO_2 56-78 wt%) [*Morris et al.*, 2016; *Rampe et al.,* 2017]. The extent of Buckskin is limited to elevations of -4450 to -4445 m, and more or less divides lower and upper Murray which extends from -4460 m in elevation up to Curiosity's location at -4300 m on sol 1636 (at the time of this writing). The cross-stratified pebbly sandstone of the overlying Stimson formation, in contrast, is largely soil-like (SiO_2 ~43 wt%). Both formations, like all Gale units, are cross-cut by Ca-sulfate veins. Unlike the Bradbury group, lower Mt. Sharp units are cross-cut by light toned, high silica haloes associated with fractures (SiO_2 60-75 wt%). Scattered lag deposits of blocky material on top of Murray bedrock have alkalic compositions that are Bradbury-like (Figure 1-7b, 1-8b), but any genetic link to the Bradbury group is not currently clear.

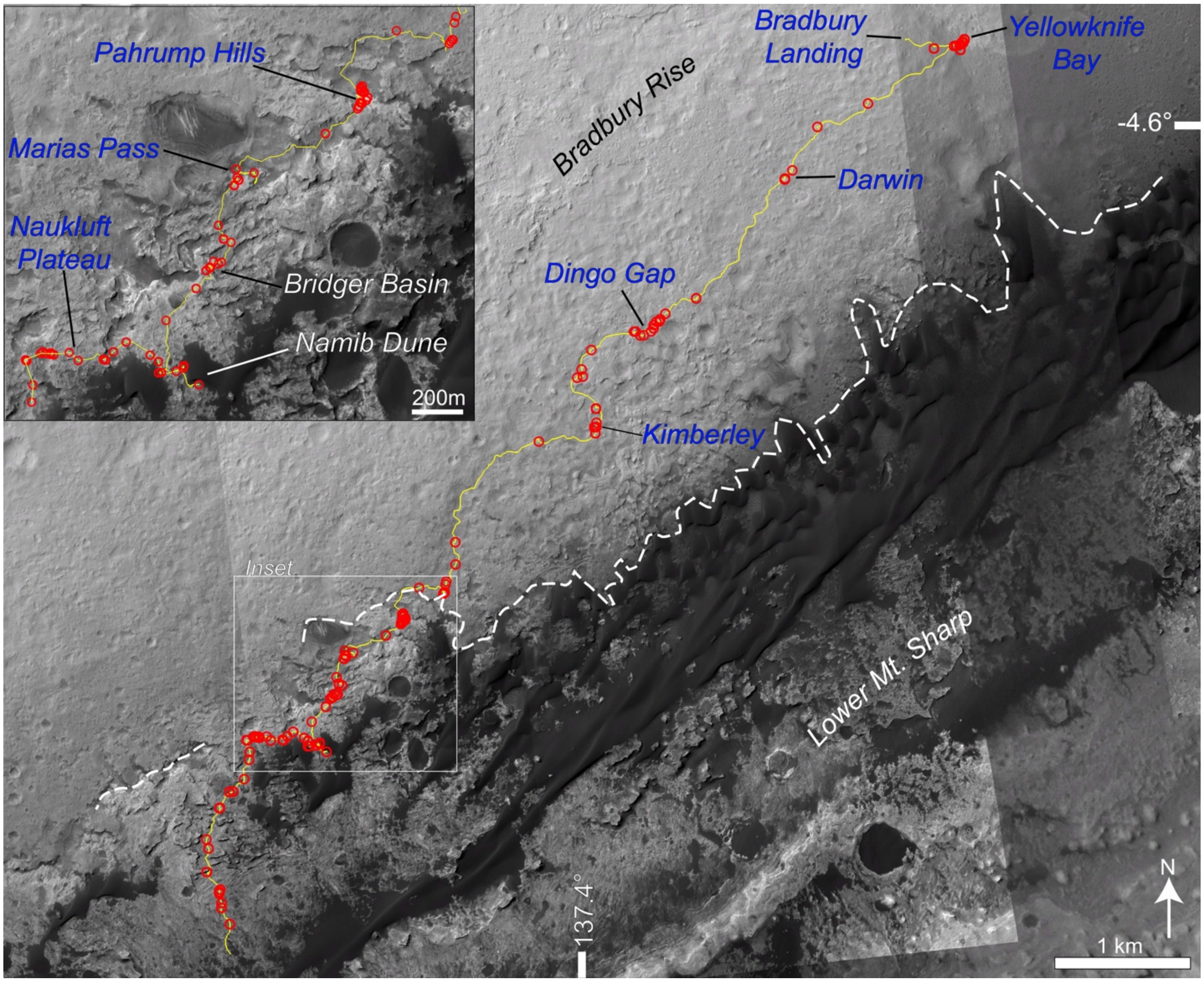

Figure 1-5: Curiosity's traverse in Gale Crater, Mars, over the first 1550 sols. Rover waypoints are indicated, APXS targets are denoted (red circles), and the approximate division between the Bradbury group to the north and the Mt. Sharp group to the south is shown by the white dashed line.

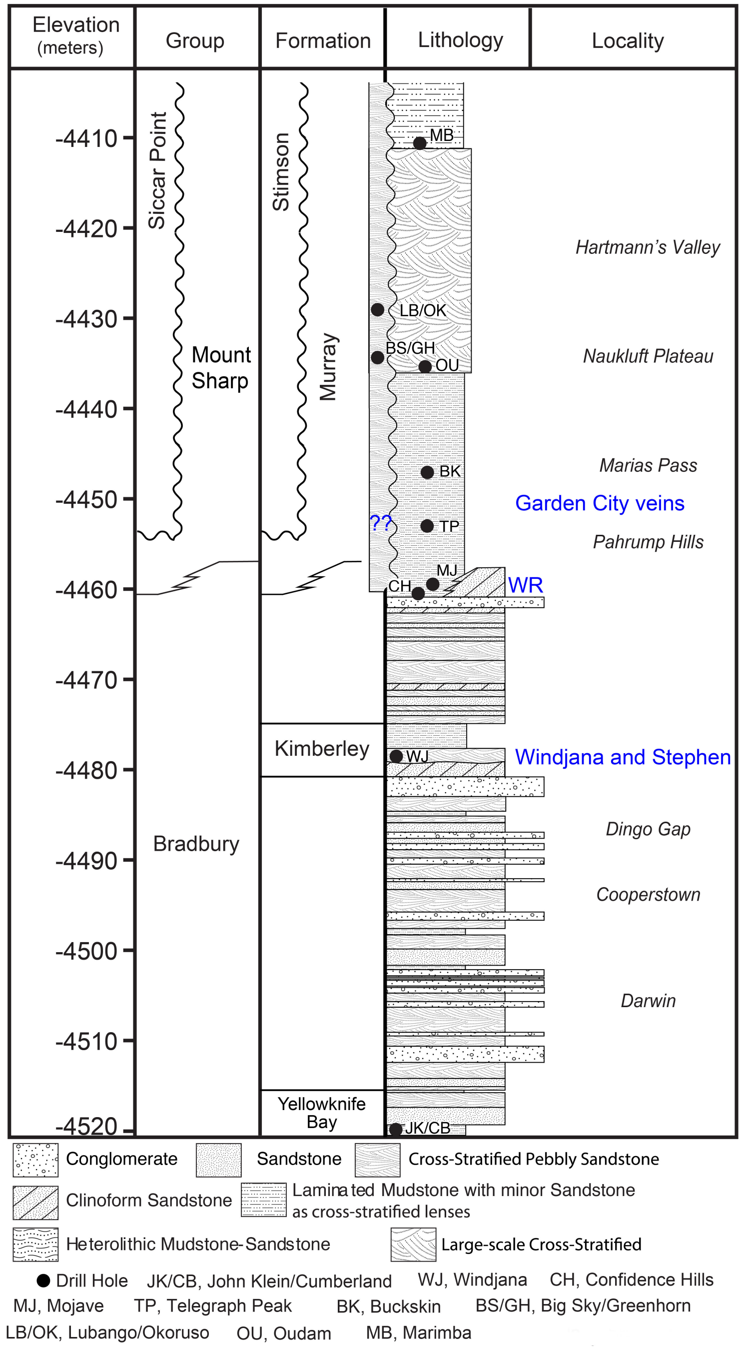

Figure 1-6: Stratigraphic section from Curiosity's traverse in Gale Crater, Mars, over the first 1550 sols. Waypoints are indicated (Figure 1-5) and locations of notable Zn- and Ge-enrichments discussed in chapter 5 are noted in blue. The Whale Rock outcrop is denoted WR. Elevation is used as a proxy for sequencing units because the structure and contacts of units are poorly constrained. The section was adapted from [*Grotzinger et al.*, 2014, 2015; *Treiman et al.*, 2016; *Rampe et al.*, 2017] and the interpretations and graphical section were made by the MSL Sedimentology and Stratigraphy Working Group. Note that these interpretations may change as the mission progresses.

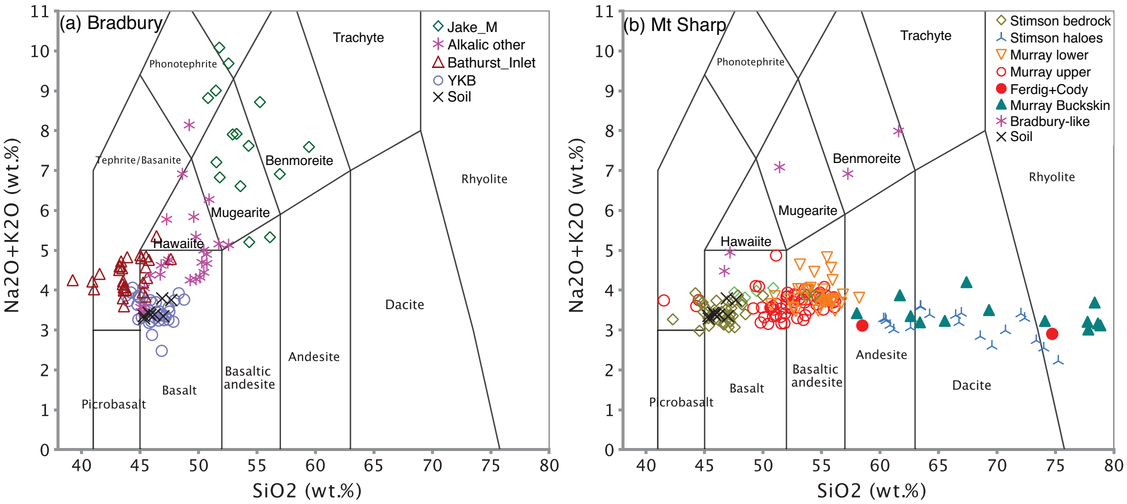

Figure 1-7: Total alkali versus silica classification diagram [*Le Maitre et al.*, 1989], showing Gale Crater APXS results for sols 0-1514 in (a) the Bradbury group and (b) the Mount Sharp group. Concentrations are volatile free and renormalized. Diagenetic features (veins, concretions) are not shown. We note that using volcanic classification is descriptive and conventional for Mars data [e.g., *McSween et al.,* 2009] and does not imply that these are unaltered volcanic rocks.

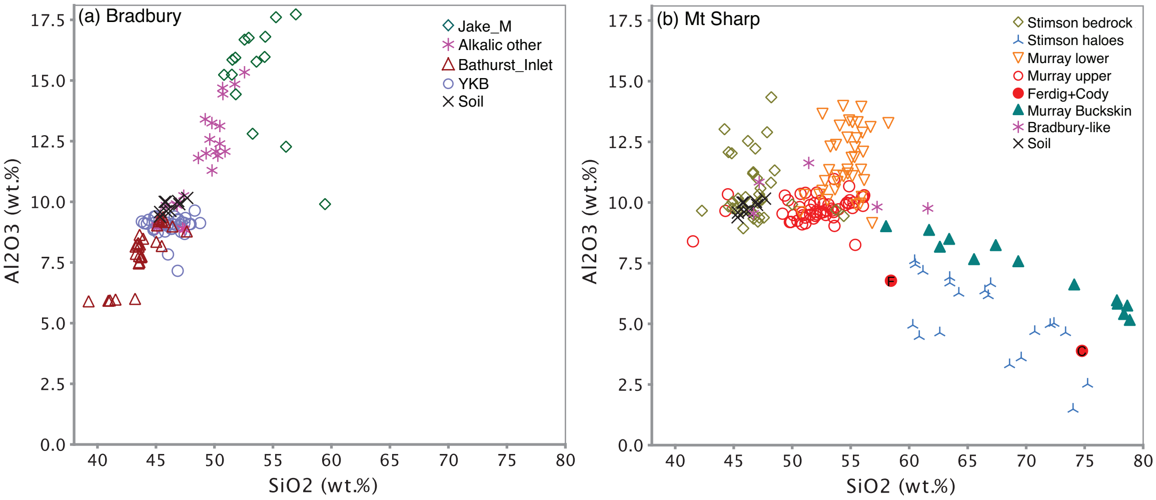

Figure 1-8: Alumina versus silica APXS results for Gale Crater over sols 0-1514 in (a) the Bradbury group and (b) the Mount Sharp group. Concentrations are volatile free and renormalized. Diagenetic features (veins, concretions) are not shown.

Table 1-1: Representative APXS Compositions in Gale Crater[1]

	Average Mars	Bradbury Group			Mt. Sharp Group			
Subgroup	Soil	Jake_M	YKB	Bathurst_Inlet	Murray Bedrock	Murray Buckskin	Stimson Bedrock	Stimson Halo
Target name[2]	Portage	Jake_M	John_Klein	Windjana	Confidence Hills	Buckskin	Okoruso	Lubango
Sol	89	47	230	704	781	1091	1359	1325
SiO_2	45.85 ± 0.54	50.82 ± 0.54	43.99 ± 0.43	39.24 ± 0.43	51.01 ± 0.54	77.76 ± 0.75	45.84 ± 0.54	75.25 ± 0.64
TiO_2	1.27 ± 0.05	0.76 ± 0.03	1.12 ± 0.03	1.12 ± 0.03	1.2 ± 0.05	1.66 ± 0.05	0.95 ± 0.03	1.26 ± 0.03
Al_2O_3	10 ± 0.19	15.23 ± 0.38	9.12 ± 0.19	5.9 ± 0.19	10.31 ± 0.29	5.98 ± 0.19	9.79 ± 0.29	2.51 ± 0.1
FeO*	20.47 ± 0.2	11.38 ± 0.13	22.16 ± 0.26	29.29 ± 0.33	21.01 ± 0.26	5.8 ± 0.07	22.75 ± 0.26	5.1 ± 0.07
MnO	0.45 ± 0.02	0.24 ± 0.01	0.35 ± 0.01	0.58 ± 0.01	0.39 ± 0.01	0.09 ± 0.01	0.4 ± 0.01	0.07 ± 0.04
MgO	9.27 ± 0.25	4.78 ± 0.17	9.61 ± 0.25	12.9 ± 0.25	5.88 ± 0.17	0.87 ± 0.83	9.12 ± 0.25	1.25 ± 0.83
CaO	7.75 ± 0.08	7.05 ± 0.08	8.43 ± 0.08	5.52 ± 0.06	4.85 ± 0.06	3.22 ± 0.04	6.47 ± 0.07	10.15 ± 0.1
Na_2O	2.88 ± 0.14	6.85 ± 0.2	3.14 ± 0.14	1.01 ± 0.07	2.81 ± 0.14	2.2 ± 0.07	3.13 ± 0.14	1.88 ± 0.14
K_2O	0.52 ± 0.02	1.97 ± 0.06	0.59 ± 0.02	3.24 ± 0.1	1.04 ± 0.04	1.01 ± 0.04	0.37 ± 0.01	0.34 ± 0.01
P_2O_5	1.01 ± 0.07	0.88 ± 0.05	0.99 ± 0.07	0.67 ± 0.05	1.08 ± 0.07	1.32 ± 0.07	0.76 ± 0.05	1.77 ± 0.09
Cr_2O_3	0.52 ± 0.03	0.04 ± 0.01	0.5 ± 0.01	0.51 ± 0.01	0.41 ± 0.01	0.11 ± 0.01	0.42 ± 0.02	0.4 ± 0.02
Ni (ppm)	456 ± 30	60 ± 20	710 ± 40	520 ± 30	930 ± 50	130 ± 10	490 ± 30	40 ± 30
Zn (ppm)	327 ± 15	320 ± 20	810 ± 30	1500[2] ± 500	2110 ± 70	330 ± 10	320 ± 10	80 ± 10
SO_3	5.47 ± 0.1	2.81 ± 0.08	5.91 ± 0.08	3.57 ± 0.05	4.86 ± 0.08	4.8 ± 0.08	0.96 ± 0.03	15.07 ± 0.2
Cl	0.69 ± 0.03	0.95 ± 0.03	0.52 ± 0.02	0.57 ± 0.01	0.41 ± 0.02	0.29 ± 0.01	0.5 ± 0.01	0.31 ± 0.02
Br (ppm)	30 ± 10	90 ± 10	30 ± 10	120 ± 10	40 ± 10	60 ± 10	110 ± 10	80 ± 10

[1] Oxides are presented as volatile free and renormalized values in weight percent, except as noted. Error is statistical (1σ) and is considered error in precision.
[2] Compositions are represented by single APXS targets selected as typical for the unit. Most were measurements of fines drilled from ~1-5 cm depth; exceptions are Jake_M (unbrushed surface) and Portage (soil disturbed by the rover's wheel).
[3] This Zn value is the average Bathurst Inlet range (*n* = 29); Windjana was unusually enriched (4775 ± 145).

1.2.2. APXS Deployment and Dataset

The APXS method is a combination of particle-induced X-ray emission (PIXE) and X-ray fluorescence (XRF) techniques for the quantification of major, minor, and many trace elements with atomic number Z ≥ 11 [*Gellert et al.*, 2006, 2009; *Campbell et al.*, 2010, 2011, 2012]. The APXS measures characteristic X-rays excited by α particles and Pu L X-rays emitted from a ^{244}Cm radioisotope source [*Gellert et al.*, 2006, 2009]. APXS data are reduced by a calibration designed for the Mars Exploration Rover (MER) APXS [*Gellert et al.*, 2006], using empirical peak fitting with a nonlinear least squares fit routine [*James and Roos*, 1989] and instrument-specific adjustments, including background contributions, escape peaks, and scatter peaks. Statistical fitting errors presented here (2σ) represent error in precision, which decrease with increasing spectral intensity and resolution and therefore encompass the length of integration, standoff distance, and sensor head temperature. Sixteen elements are reported as major and minor oxides and several trace elements normalized to 100 wt.%. The oxidation state of Fe is not measured; total iron is reported as FeO. Elements with $Z < 11$ are not directly analyzed by the method and so light element components (e.g., water and carbonates) are effectively invisible at abundances below ~10 wt. %. The analytical uncertainty (accuracy) varies for each element and was estimated by *Gellert et al.* [2006] and *Campbell et al.* [2012].

Curiosity's APXS is a field X-ray spectrometer mounted on the rover's robotic arm (Figure 1-9), and the MSL mission strategy for APXS measurements is to assess the habitability and paleoclimate of Mars by determining the in situ chemical composition of rocks and soils [*Grotzinger et al.*, 2012]. To do this, the APXS is deployed at waypoints selected by the MSL Science Team to characterize rock units and test hypotheses (Figure 1-5, 1-6). Some of these waypoints include samples drilled from up to 5 cm in depth (12 samples in the first 1600 sols) [*Anderson et al.*, 2012]. The APXS is also deployed at periodic sites along the rover's traverse to survey the representative bedrock and explore heterogeneity. These observations are coordinated with the full rover science payload [*Grotzinger et al.*, 2012], which can analyze the chemical and mineralogical makeup of Martian samples. The primary geologic instruments include:

(1) APXS, the X-ray spectrometer and focus of this dissertation.

(2) The Chemistry and Mineralogy (CheMin) X-ray diffraction (XRD) instrument in the rover's body [*Blake et al.*, 2012], which can determine the mineralogical composition of drilled and scooped samples.

(3) The Sample Analysis at Mars (SAM) instrument [*Mahaffy et al.*, 2012], comprised of a quadrupole mass spectrometer, tunable laser spectrometer, and gas chromatograph that can analyze a suite of light isotopes, volatiles, and inorganic

and organic compounds. Like CheMin, SAM analyzes drilled and scooped samples.

(4) The ChemCam laser-induced breakdown spectrometer (LIBS) [*Wiens et al.*, 2013], which probes rocks and soils with a ~300-500 µm spot at ~2-7 m from the rover with a laser. The laser generates a plasma that emits ultraviolet, visible, and near infrared energy that is measured with a telescope spectrometer and converted to chemical concentrations.

(5) The Mars Hand Lens Imager (MAHLI) [*Edgett et al.*, 2012], a microscopic imager on the rover's arm.

The data products from ChemCam are often similar to APXS because the instrument team presents major (and some minor) element compositions for rocks and soils. ChemCam, however, cannot quantify S, Cl, Br, Zn, Ge, Ni, Cu, or P accurately at the levels they commonly occur in Gale Crater. In addition, the small spot size of the laser requires many more spots on a rock (~20) than are typically obtained (3-9) in order to statistically represent a bulk rock, although this is highly influenced by grain size [e.g., *Anderson et al.*, 2011]. For the purposes of this dissertation, we focus on the APXS dataset because small variations in the bulk rocks of the elements listed above are key to the hypotheses driving this work.

APXS targets, which are given names picked from geographic places on Earth, are measured either as-is (i.e., unbrushed), after the surface was brushed by the Dust Removal Tool (DRT), or as fines generated by the drill [*Anderson et al.*, 2012]. Every APXS measurement is supported by MAHLI documentation [*Edgett et al.*, 2012], including at least one image of the target from a working distance of ~5 cm resulting in a resolution of ~32 µm/pixel. Drill fines are measured by the APXS as tailings ejected from the 1.6 cm diameter drill hole and as sieved and unsieved sample splits that are also delivered to CheMin and often SAM. The drilled samples are dumped into a small pile on the ground by the rover's subsampling system, and then measured by the APXS. For typical deployments to within 5 mm of the surface of rocks or soils, the APXS field of view (FOV) is ~1.5-2 cm in diameter. Heterogeneity on a scale smaller than the FOV can be examined by measuring multiple (2-5) points, or a raster, over small features (e.g., thin veins) [*VanBommel et al.*, 2016, 2017]. The effective APXS sampling depth ranges from ~5 µm for lighter elements (Na, Mg) to ~100-150 µm for heavier elements (Fe, Zn, Br) [*Rieder et al.*, 2003; *Brückner et al.*, 2008; *Campbell et al.*, 2009; *Berger et al.,* 2014]. The main implication of the sampling depth is that lighter elements tend to reflect the addition of a soil-like airfall dust composition [*Schmidt et al.*, 2014b], but heavier elements are minimally affected in measurements before and after the DRT (see chapter 5). Surface dust can be tracked because airfall dust has a soil-like composition and is enriched in S and Cl at a molar S/Cl ratio of ~3.4 [*Schmidt et al.*, 2014b; *Berger et al.*, 2016a]. Brushing the surface usually lowers S and Cl, and drill fines are free of airfall dust (Figure 1-10). To directly compare APXS results to analogue, volatile-free XRF results for Hawaiian samples with higher accuracy, we report the APXS values herein as SO_3 and Cl free and renormalized to 100 wt.%.

APXS data discussed here (sols 0-1514) have been released to the public and are available through the Planetary Data System (https://pds.nasa.gov).

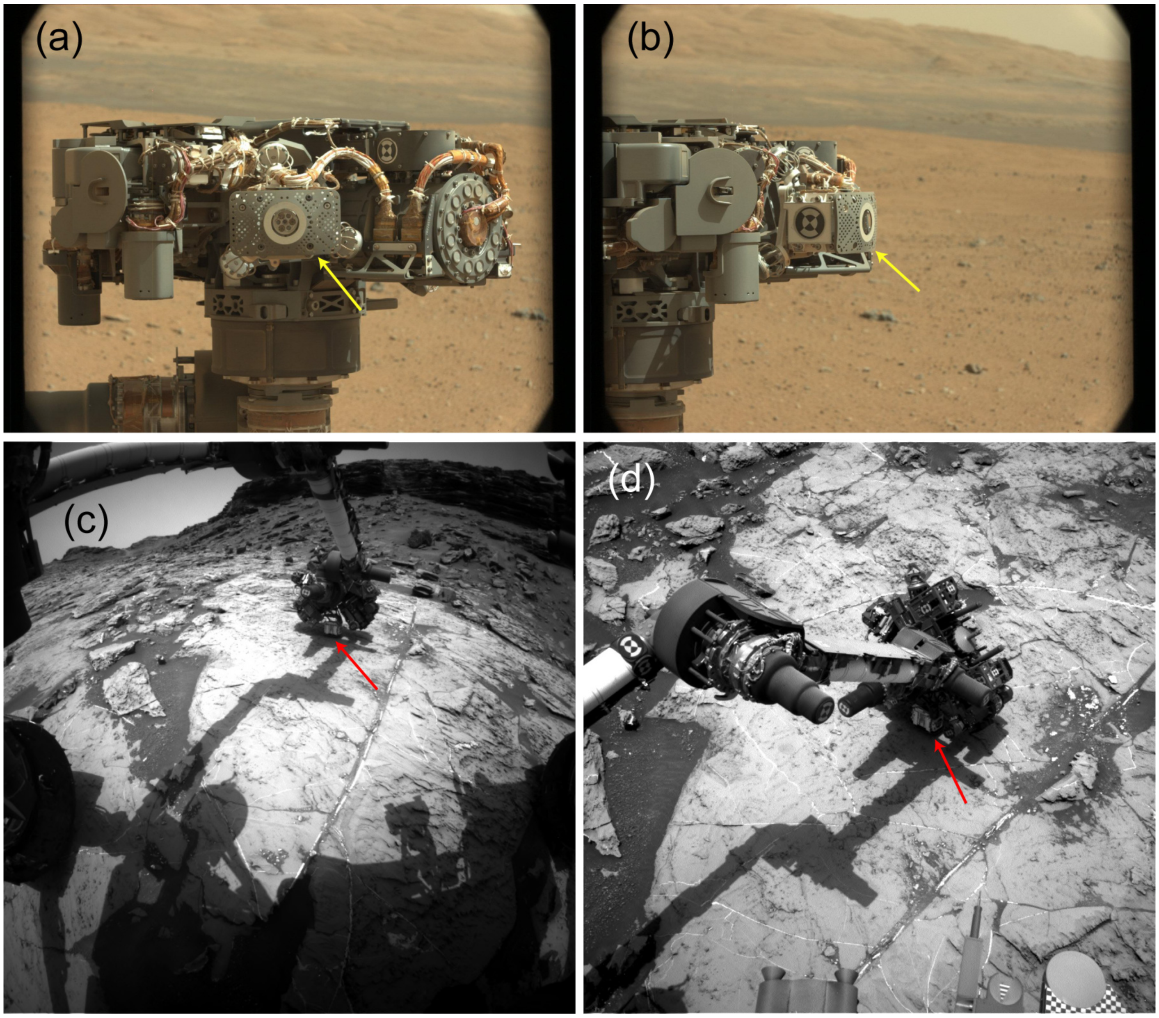

Figure 1-9: Images of the MSL APXS instrument on Mars. The APXS sensor head (indicated by arrows) is a ~7 cm x 7 cm component mounted on the arm containing the ^{244}Cm sources and silicon drift detector, with a faceplate and contact switch. The APXS memory and other electronics are contained in the rover body. (a, b) Mastcam images show the APXS and (c) Hazcam and (d) Navcam images show the APXS deployed to a rock with the faceplate in contact under typical deployment conditions. Mastcam and Navcam are mast-mounted cameras; Hazcam cameras are on the rover body [Maki et al., 2012].

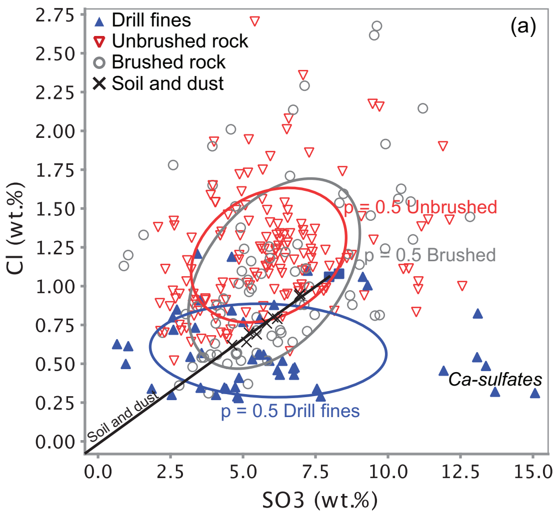

Figure 1-10: Comparison of APXS analyses of the unbrushed (as-is) surface, brushed (DRT) surface, and drill fines. Volatile elements Cl and SO_3 tend to be enriched on surfaces, as seen in APXS analyses of the unbrushed (as-is) surface, brushed (DRT) surface, and in drill fines that sample the subsurface from depths of ~1-5 cm. Mahalanobis elipses show p = 0.5 for the three surface types. After brushing, Cl and SO_3 tend to decrease along the characteristic soil and dust Cl/SO_3 ratio (black line) [*Yen et al.*, 2005; *Berger et al.*, 2016], consistent with the removal of some, but not all, of the dust from the APXS FOV. Drill fines usually have lower Cl, but have a large SO_3 range. SO_3 and Cl values that fall off the dust ratio, or above the effective upper limit measured in airfall dust (~8 wt.% SO_3; ~1 wt.% Cl) indicate an enrichment of the elements that is inherent to the underlying target, not the dust.

1.3. References

Anderson, R. (2010), Geologic mapping and characterization of Gale Crater and implications for its potential as a Mars Science Laboratory landing site, *The Mars Journal*, *5*, 76–128, doi:10.1555/mars.2010.0004.

Anderson, R. B., R. V. Morris, S. M. Clegg, J. F. Bell III, R. C. Wiens, S. D. Humphries, S. A. Mertzman, T. G. Graff, and R. McInroy (2011), The influence of multivariate analysis methods and target grain size on the accuracy of remote quantitative chemical analysis of rocks using laser induced breakdown spectroscopy, *Icarus*, *215*(2), 608–627, doi:10.1016/j.icarus.2011.07.034

Anderson, R. C. et al. (2012), Collecting Samples in Gale Crater, Mars; an Overview of the Mars Science Laboratory Sample Acquisition, Sample Processing and

Handling System, *Space Sci. Rev.*, *170*(1–4), 57–75, doi:10.1007/s11214-012-9898-9.

Bell, J. F., R. V. Morris, and J. B. Adams (1993), Thermally altered palagonitic tephra: A spectral and process analog to the soil and dust of Mars, *Journal of Geophysical Research: Planets*, *98*(E2), 3373–3385, doi:10.1029/92JE02367.

Berger, J. A. et al. (2014), MSL-APXS titanium observation tray measurements: Laboratory experiments and results for the Rocknest fines at the Curiosity field site in Gale Crater, Mars, *J. Geophys. Res. Planets*, 2013JE004519, doi:10.1002/2013JE004519.

Berger, J. A. et al. (2016), A global Mars dust composition refined by the Alpha-Particle X-ray Spectrometer in Gale Crater, *Geophys. Res. Lett.*, 2015GL066675, doi:10.1002/2015GL066675.

Bernstein, L. R. (1985), Germanium geochemistry and mineralogy, *Geochim. Cosmochim. Acta*, *49*(11), 2409–2422, doi:10.1016/0016-7037(85)90241-8.

Blake, D. et al. (2012), Characterization and Calibration of the CheMin Mineralogical Instrument on Mars Science Laboratory, *Space Sci. Rev.*, *170*(1–4), 341–399, doi:10.1007/s11214-012-9905-1.

Brückner, J., G. Dreibus, R. Gellert, S. W. Squyres, H. Wänke, A. Yen, and J. Zipfel (2008), Mars Exploration Rovers: chemical composition by the APXS, in *The Martian Surface*, vol. 1, edited by J. F. Bell III, pp. 58–101, Cambridge University Press, New York.

Campbell, J. L., and J. A. Cookson (1984), PIXE analysis of thick targets, *Nuclear Instruments and Methods in Physics Research Section B: Beam Interactions with Materials and Atoms*, *3*(1–3), 185–197, doi:10.1016/0168-583X(84)90361-6.

Campbell, J. L., M. Lee, B. N. Jones, S. M. Andrushenko, N. G. Holmes, J. A. Maxwell, and S. M. Taylor (2009), A fundamental parameters approach to calibration of the Mars Exploration Rover Alpha Particle X-ray Spectrometer, *J. Geophys. Res.*, *114*(E04006), doi:200910.1029/2008JE003272.

Campbell, J. L., A. M. McDonald, G. M. Perrett, and S. M. Taylor (2011), A GUPIX-based approach to interpreting the PIXE-plus-XRF spectra from the Mars Exploration rovers: II geochemical reference materials, *Nucl. Instrum. Methods Phys. Res. B*, *269*(1), 69–81, doi:10.1016/j.nimb.2010.09.014.

Campbell, J. L., G. M. Perrett, R. Gellert, S. M. Andrushenko, N. I. Boyd, J. A. Maxwell, P. L. King, and C. D. M. Schofield (2012), Calibration of the Mars Science Laboratory Alpha Particle X-ray Spectrometer, *Space. Sci. Rev.*, *170*(1–4), 319–340, doi:10.1007/s11214-012-9873-5.

Drever, J. I. (1997), *The Geochemistry of Natural Waters: Surface and Groundwater Environments*, 3rd ed., Prentice Hall.

Edgett, K. S. et al. (2012), Curiosity's Mars Hand Lens Imager (MAHLI) Investigation, *Space Sci. Rev.*, *170*(1–4), 259–317, doi:10.1007/s11214-012-9910-4

Edgett, K. S. et al. (2016), Recent Observations by Curiosity's Mars Hand Lens Imager (MAHLI) of Rock Strata and Eolian Sediment on the Lower North Slope of Aeolis Mons, Gale Crater, Mars, in *Lunar Planet. Sci. Conf. 47*, p. Abstract 1382.

Farley, K. A. et al. (2014), In Situ Radiometric and Exposure Age Dating of the Martian Surface, *Science*, *343*(6169), 1247166, doi:10.1126/science.1247166.

Filiberto, J., A. H. Treiman, P. A. Giesting, C. A. Goodrich, and J. Gross (2014), High-temperature chlorine-rich fluid in the martian crust: A precursor to habitability, *Earth and Planetary Science Letters*, *401*, 110–115, doi:10.1016/j.epsl.2014.06.003.

Gellert, R. et al. (2006), Alpha Particle X-Ray Spectrometer (APXS): Results from Gusev crater and calibration report, *J. Geophys. Res.*, *111*(E02S05), doi:200610.1029/2005JE002555.

Gellert, R., J. L. Campbell, P. L. King, L. A. Leshin, G. W. Lugmair, J. G. Spray, S. W. Squyres, and A. S. Yen (2009), The Alpha-Particle-X-Ray-Spectrometer (APXS) for the Mars Science Laboratory (MSL) Rover Mission, in *Lunar Planet. Sci., XL*, p. Abstract 2364.

Gellert, R. et al. (2015), Chemical Evidence for an Aqueous History at Pahrump, Gale Crater, Mars, as Seen by the APXS, in *Lunar Planet. Sci., XLVI*, p. Abstract 1855.

Giambelluca, T. W., Q. Chen, A. G. Frazier, J. P. Price, Y.-L. Chen, P.-S. Chu, J. K. Eischeid, and D. M. Delparte (2013), Online Rainfall Atlas of Hawaiʻi, *Bulletin of the American Meteorological Society*, *94*(3), 313–316, doi:10.1175/BAMS-D-11-00228.1.

Goetz, W. et al. (2005), Indication of drier periods on Mars from the chemistry and mineralogy of atmospheric dust, *Nature*, *436*(7047), 62–65, doi:10.1038/nature03807.

Golden, D. C., R. V. Morris, D. W. Ming, H. V. Lauer, and S. R. Yang (1993), Mineralogy of three slightly palagonitized basaltic tephra samples from the summit of Mauna Kea, Hawaii, *Journal of Geophysical Research: Planets*, *98*(E2), 3401–3411, doi:10.1029/92JE02590.

Grant, J. A., S. A. Wilson, N. Mangold, F. Calef, and J. P. Grotzinger (2014), The timing of alluvial activity in Gale crater, Mars, *Geophysical Research Letters*, *41*(4), 1142–1149, doi:10.1002/2013GL058909.

Grotzinger, J. P. et al. (2012), Mars Science Laboratory Mission and Science Investigation, *Space Sci Rev*, *170*(1–4), 5–56, doi:10.1007/s11214-012-9892-2.

Grotzinger, J. P. et al. (2014), A Habitable Fluvio-Lacustrine Environment at Yellowknife Bay, Gale Crater, Mars, *Science*, *343*(6169), 1242777, doi:10.1126/science.1242777.

Grotzinger, J. P. et al. (2015), Deposition, exhumation, and paleoclimate of an ancient lake deposit, Gale crater, Mars, *Science*, *350*(6257), aac7575, doi:10.1126/science.aac7575.

Hamilton, ed., V. E. (2015), *MEPAG (2015), Mars Scientific Goals, Objectives, Investigations, and Priorities: 2015*, white paper, Mars Exploration Program Analysis Group (MEPAG).

Hamilton, V. E., R. V. Morris, J. E. Gruener, and S. A. Mertzman (2008), Visible, near-infrared, and middle infrared spectroscopy of altered basaltic tephras: Spectral signatures of phyllosilicates, sulfates, and other aqueous alteration products with application to the mineralogy of the Columbia Hills of Gusev Crater, Mars, *J. Geophys. Res.*, *113*, 30 PP., doi:200810.1029/2007JE003049.

James, F., and M. Roos (1989), MINUIT functional minimization and error analysis, *D506-Minuit, CERN.*

Johansson, S. A. E., J. L. Campbell, and K. G. Malmqvist (1995), *Particle-Induced X-Ray Emission Spectrometry (PIXE)*, John Wiley & Sons.

Johnson, D. M., P. R. Hooper, R. M. Conrey, and G. Laboratory (1999), XRF analysis of rocks and minerals for major and trace elements on a single low dilution Li-tetraborate fused bead, in *Advances in X-ray Analysis, v, 41, p. 843–867 Le Bas, M.J*, pp. 745–750.

Kah, L. C. et al. (2015), Diagenetic Crystal Clusters and Dendrites, Lower Mount Sharp, Gale Crater, in *Lunar Planet. Sci., XLVI*, vol. 46, p. 1901.

Lanphere, M. A., and F. A. Frey (1987), Geochemical evolution of Kohala volcano, Hawaii, *Contributions to Mineralogy and Petrology*, *95*(1), 100–113.

Le Deit, L. L., E. Hauber, F. Fueten, M. Pondrelli, A. P. Rossi, and R. Jaumann (2013), Sequence of infilling events in Gale Crater, Mars: Results from morphology, stratigraphy, and mineralogy, *J. Geophys. Res. Planets*, *118*(12), 2012JE004322, doi:10.1002/2012JE004322.

Le Maitre, R. W., P. Bateman, A. Dudek, J. Keller, J. Lameyre, M. J. Le Bas, P. A. Sabine, R. Schmid, H. Sorensen, and A. Streckeisen (1989), *A classification of igneous rocks and glossary of terms: Recommendations of the International Union of Geological Sciences Subcommission on the Systematics of Igneous Rocks*, Blackwell Oxford.

Mahaffy, P. et al. (2012), The Sample Analysis at Mars Investigation and Instrument Suite, *Space Sci. Rev.*, *170*(1–4), 401–478, doi:10.1007/s11214-012-9879-z.

Maki, J., D. Thiessen, A. Pourangi, P. Kobzeff, T. Litwin, L. Scherr, S. Elliott, A. Dingizian, and M. Maimone (2012), The Mars Science Laboratory Engineering Cameras, *Space Sci Rev*, *170*(1–4), 77–93, doi:10.1007/s11214-012-9882-4

McCubbin, F. M. et al. (2016), Geologic history of Martian regolith breccia Northwest Africa 7034: Evidence for hydrothermal activity and lithologic diversity in the Martian crust, *Journal of Geophysical Research: Planets*, *121*(10), 2120–2149, doi:10.1002/2016JE005143.

McLennan, S. M. et al. (2013), Elemental Geochemistry of Sedimentary Rocks at Yellowknife Bay, Gale Crater, Mars, *Science*, 1244734, doi:10.1126/science.1244734.

McSween Jr., H. Y., G. J. Taylor, and M. B. Wyatt (2009), Elemental Composition of the Martian Crust, *Science*, *324*(5928), 736–739, doi:10.1126/science.1165871.

Milliken, R. E., J. P. Grotzinger, and B. J. Thomson (2010), Paleoclimate of Mars as captured by the stratigraphic record in Gale Crater, *Geophys. Res. Lett.*, *37*, 6 PP., doi:201010.1029/2009GL041870.

Ming, D. W. et al. (2008), Geochemical properties of rocks and soils in Gusev Crater, Mars: Results of the Alpha Particle X-Ray Spectrometer from Cumberland Ridge to Home Plate, *J. Geophys. Res.*, *113*(E12S39), 28 PP., doi:200810.1029/2008JE003195.

Morris, R. V., D. C. Golden, J. F. Bell III, H. V. Lauer Jr., and J. B. Adams (1993), Pigmenting agents in martian soils: Inferences from spectral, Mössbauer, and magnetic properties of nanophase and other iron oxides in Hawaiian palagonitic soil PN-9, *Geochimica et Cosmochimica Acta*, *57*(19), 4597–4609, doi:10.1016/0016-7037(93)90185-Y.

Morris, R. V. et al. (2000), Mineralogy, composition, and alteration of Mars Pathfinder rocks and soils: Evidence from multispectral, elemental, and magnetic data on terrestrial analogue, SNC meteorite, and Pathfinder samples, *J. Geophys. Res.*, *105*(E1), 1757–1817, doi:10.1029/1999JE001059.

Morris, R. V., D. C. Golden, D. W. Ming, T. D. Shelfer, L. C. Jorgensen, J. F. Bell, T. G. Graff, and S. A. Mertzman (2001), Phyllosilicate-poor palagonitic dust from Mauna Kea Volcano (Hawaii); a mineralogical analogue for magnetic Martian dust?, *Journal of Geophysical Research*, *106*(E3), 5057–5083, doi:http://dx.doi.org.proxy1.lib.uwo.ca/10.1029/2000JE001328.

Morris, R. V. et al. (2005), Hematite spherules in basaltic tephra altered under aqueous, acid-sulfate conditions on Mauna Kea volcano, Hawaii: Possible clues for the occurrence of hematite-rich spherules in the Burns formation at Meridiani

Planum, Mars, *Earth and Planetary Science Letters*, *240*(1), 168–178, doi:10.1016/j.epsl.2005.09.044.

Morris, R. V. et al. (2006), Mössbauer mineralogy of rock, soil, and dust at Meridiani Planum, Mars: Opportunity's journey across sulfate-rich outcrop, basaltic sand and dust, and hematite lag deposits, *J. Geophys. Res.*, *111*(E12S15), doi:10.1029/2006JE002791.

Morris, R. V. et al. (2008), Iron mineralogy and aqueous alteration from Husband Hill through Home Plate at Gusev Crater, Mars: Results from the Mössbauer instrument on the Spirit Mars Exploration Rover, *Journal of Geophysical Research: Planets*, *113*(E12), n/a–n/a, doi:10.1029/2008JE003201.

Morris, R. V. et al. (2015), Update on the Chemical Composition of Crystalline, Smectite, and Amorphous Components for Rocknest Soil and John Klein and Cumberland Mudstone Drill Fines at Gale Crater, Mars, in *Lunar Planet. Sci. Conf. 46*, p. Abstract 2622.

Morris, R. V. et al. (2016), Silicic volcanism on Mars evidenced by tridymite in high-SiO2 sedimentary rock at Gale crater, *PNAS*, *113*(26), 7071–7076, doi:10.1073/pnas.1607098113.

Pokrovski, G. S., and J. Schott (1998), Thermodynamic properties of aqueous Ge(IV) hydroxide complexes from 25 to 350°C: implications for the behavior of germanium and the Ge/Si ratio in hydrothermal fluids, *Geochim. Cosmochim. Acta*, *62*(9), 1631–1642, doi:10.1016/S0016-7037(98)00081-7.

Porter, S. C. (1979), Quaternary Stratigraphy and Chronology of Mauna Kea, Hawaii: A 380,000-yr Record of Mid-Pacific Volcanism and Ice-Cap Glaciation, *Geological Society of America Bulletin*, *90*(7 Part II), 980–1093, doi:10.1130/GSAB-P2-90-980.

Rieder, R., H. Wänke, T. Economou, and A. Turkevich (1997), Determination of the chemical composition of Martian soil and rocks: The alpha proton X ray spectrometer, *Journal of Geophysical Research: Planets*, *102*(E2), 4027–4044.

Rampe, E. B. et al. (2017), Mineralogy of an ancient lacustrine mudstone succession from the Murray formation, Gale crater, Mars, *Earth and Planetary Science Letters*, doi:10.1016/j.epsl.2017.04.021.

Rieder, R., R. Gellert, J. Brückner, G. Klingelhöfer, G. Dreibus, A. Yen, and S. W. Squyres (2003), The new Athena alpha particle X-ray spectrometer for the Mars Exploration Rovers, *J. Geophys. Res.*, *108*(E12), 8066, doi:200310.1029/2003JE002150.

Sautter, V. et al. (2015), In situ evidence for continental crust on early Mars, *Nature Geosci.*, *8*(8), 605–609, doi:10.1038/ngeo2474.

Schmidt, M. E. et al. (2008), Hydrothermal origin of halogens at Home Plate, Gusev Crater, *J. Geophys. Res.*, *113*(E6), E06S12, doi:10.1029/2007JE003027.

Schmidt, M. E., J. A. Berger, D. Blaney, R. Gellert, J. P. Grotzinger, O. Forni, P. L. King, and N. Mangold (2014a), Geochemical Classification of Rocks in Gale Crater with APXS to Sol 360: Sediment Provenance, Mixing, and Diagenetic Processes, in *Lunar Planet. Sci., XLV*, p. Abstract 1504.

Schmidt, M. E. et al. (2014b), Geochemical diversity in first rocks examined by the Curiosity Rover in Gale Crater: Evidence for and significance of an alkali and volatile-rich igneous source, *J. Geophys. Res. Planets*, *119*(1), 64–81, doi:10.1002/2013JE004481.

Seelos, K. D., R. E. Arvidson, B. L. Jolliff, S. M. Chemtob, R. V. Morris, D. W. Ming, and G. A. Swayze (2010), Silica in a Mars analog environment: Ka'u Desert, Kilauea Volcano, Hawaii, *Journal of Geophysical Research: Planets (1991–2012)*, *115*(E4).

Spengler, S. R., and M. O. Garcia (1988), Geochemistry of the Hawi lavas, Kohala volcano, Hawaii, *Contributions to Mineralogy and Petrology*, *99*(1), 90–104.

Squyres, S. W. et al. (2008), Detection of Silica-Rich Deposits on Mars, *Science*, *320*(5879), 1063–1067, doi:10.1126/science.1155429.

Squyres, S. W. et al. (2012), Ancient Impact and Aqueous Processes at Endeavour Crater, Mars, *Science*, *336*(6081), 570–576, doi:10.1126/science.1220476.

Stolper, E. M. et al. (2013), The Petrochemistry of Jake_M: A Martian Mugearite, *Science*, *341*(6153), 1239463, doi:10.1126/science.1239463.

Taylor, S. R., and S. McLennan (2010), *Planetary Crusts: Their Composition, Origin and Evolution*, 1st ed., Cambridge University Press.

Thompson, L. M. et al. (2016), Potassium-rich sandstones within the Gale impact crater, Mars: The APXS perspective, *J. Geophys. Res. Planets*, 2016JE005055, doi:10.1002/2016JE005055.

Thomson, B. J., N. T. Bridges, R. Milliken, A. Baldridge, S. J. Hook, J. K. Crowley, G. M. Marion, C. R. de Souza Filho, A. J. Brown, and C. M. Weitz (2011), Constraints on the origin and evolution of the layered mound in Gale Crater, Mars using Mars Reconnaissance Orbiter data, *Icarus*, *214*(2), 413–432, doi:10.1016/j.icarus.2011.05.002.

Treiman, A. H. et al. (2016), Mineralogy, provenance, and diagenesis of a potassic basaltic sandstone on Mars: CheMin X-ray diffraction of the Windjana sample (Kimberley area, Gale Crater), *J. Geophys. Res. Planets*, *121*(1), 2015JE004932, doi:10.1002/2015JE004932.

Trusdell, F. A. W., and J. EW Morris (2005), Digital database of the geologic map of the Island of Hawaii,

Tuff, J., J. Wade, and B. J. Wood (2013), Volcanism on Mars controlled by early oxidation of the upper mantle, *Nature*, *498*(7454), 342–345, doi:10.1038/nature12225.

VanBommel, S. J., R. Gellert, J. A. Berger, J. L. Campbell, L. M. Thompson, K. S. Edgett, M. J. McBride, M. E. Minitti, I. Pradler, and N. I. Boyd (2016), Deconvolution of distinct lithology chemistry through oversampling with the Mars Science Laboratory Alpha Particle X-Ray Spectrometer, *X-Ray Spectrom.*, doi:10.1002/xrs.2681.

VanBommel, S. J., R. Gellert, J. A. Berger, L. M. Thompson, K. S. Edgett, M. J. McBride, M. E. Minitti, N. I. Boyd, and J. L. Campbell (2017), Modeling and mitigation of sample relief effects applied to chemistry measurements by the Mars Science Laboratory Alpha Particle X-ray Spectrometer, *X-Ray Spectrom.*, doi:10.1002/xrs.2755.

Vaniman, D. T. et al. (2014), Mineralogy of a Mudstone at Yellowknife Bay, Gale Crater, Mars, *Science*, *343*(6169), 1243480, doi:10.1126/science.1243480.

Wiens, R. C. et al. (2013), Pre-flight calibration and initial data processing for the ChemCam laser-induced breakdown spectroscopy instrument on the Mars Science Laboratory rover, *Spectrochimica Acta Part B: Atomic Spectroscopy*, *82*, 1–27.

Wolfe, E. W., and J. Morris (1996), *Geologic map of the Island of Hawaii*, IMAP, USGS Numbered Series.

Wolfe, E. W., W. S. Wise, and G. B. Dalrymple (1997), The Geology and Petrology of Mauna Kea Volcano, Hawaii: A Study of Postshield Volcanism, *US Geological Survey professional paper*, (1557), 1–129.

Yen, A. S. et al. (2005), An integrated view of the chemistry and mineralogy of martian soils, *Nature*, *436*(7047), 49–54, doi:10.1038/nature03637.

Yen, A. S. et al. (2006), Nickel on Mars: Constraints on meteoritic material at the surface, *J. Geophys. Res.*, *111*(E12), E12S11, doi:10.1029/2006JE002797.

Yen, A. S. et al. (2013), Evidence for a global martian soil composition extends to Gale crater, in *Lunar Planet. Sci., XLIV*, p. Abstract 2495.

Yen, A. S. et al. (2017), Multiple stages of aqueous alteration along fractures in mudstone and sandstone strata in Gale Crater, Mars, *Earth and Planetary Science Letters*, doi:10.1016/j.epsl.2017.04.033.

Yen, A. S. et al. (2017), Acidic Fluids Across Mars: Detections of Magnesium-Nickel Sulfates, vol. 48, p. 2553.

Yingst, R. A., K. S. Edgett, M. McBride, M. E. Minitti, K. Stack, and W. Goetz (2015), Sedimentary Early Mars Revealed at the Microscale: The Gale Crater Example, in *Lunar Planet. Sci. Conf. 46*, p. Abstract 1378.

Chapter 2

2. A Mars Rover’s Perspective of Maunakea and Kohala, Hawai’i: A Gale Crater Analogue for Deconvolving Provenance and Alteration Trends in APXS Geochemistry

2.1. Chapter summary and key points

Basaltic and alkalic sedimentary rocks in Gale Crater on Mars have mixed provenance and have been affected by a range of alteration and weathering processes. To better understand how these processes are captured in geochemical data by the rover *Curiosity’s* Alpha Particle X-ray Spectrometer (APXS), we conducted a field investigation of the analogous post-shield volcanics capping Maunakea and Kohala volcanoes on Hawai’i. The post-shield volcanics have two igneous lithologies with discrete compositions and a compositional gap (basaltic and hawaiitic/mugearitic). Hydrolytic alteration is widespread, and is characterized by silica and alkali leaching with passive enrichment of Fe, Al, and Ti in oxdes/oxyhydroxides, indicating open system, circumneutral alteration. Localized acid sulfate alteration is distinct, characterized by silica retention and Mg depletion, with variable alkali retention and Al and Fe depletion. Sedimentary deposits on Maunakea have compositions that reflect the physical mixing of the two parent igneous lithologies, falling on a spectrum between the two, spanning igneous compositional gaps. In Gale Crater, the rocks of the Bradbury group are similar to Maunakea in that they are physical mixtures of igneous endmembers. Unlike Maunakea, the Bradbury group has three parent components: basaltic, potassic basalt, and mugearitic. Open system hydrolytic alteration did not occur extensively in Gale Crater sediment; alteration was apparently isochemical and limited in the Bradbury group and Stimson formation. Silica enrichment with Mg, Fe, and Mn depletion in the Murray formation and in fracture haloes of the Mt. Sharp group is consistent with the acid sulfate alteration observed at Hawai’i, and supports the interpretation that acidic fluids altered these units. Maunakea and Kohala are valuable Gale Crater analogues where higher-resolution analyses and geologic context can aid our interpretations of Gale Crater geochemical observations.

2.2. Introduction

Sedimentary rocks in Gale Crater on Mars have mixed provenance and have been affected by a range of alteration and weathering processes [e.g., *Schmidt et al.*, 2014b; *Thompson et al.*, 2016; *Treiman et al.*, 2016; *Rampe et al.,* 2017; *Yen et al.,* 2017]. The compositional diversity arising from these processes is reflected in geochemical trends identified in basaltic and alkalic sedimentary rocks by the Alpha Particle X-ray Spectrometer (APXS) instrument on the Mars rover *Curiosity* [*Gellert et al.*, 2009]. Uncertainties about parent sediment sources, as well as constraints provided by *Curiosity's* instruments, present challenges for the assessment of the relative importance of these processes. We therefore look to Mars analogues on Earth where higher-resolution analyses and geologic context can aid our interpretations of Gale Crater geochemical observations.

Alkalic post-shield volcanics (mugearites) were identified as a new Martian analogue composition upon discovery of the high-alkali rock class named Jake_M [*Stolper et al.*, 2013; *Schmidt et al.*, 2014b]. Hawaiites and mugearites cap Maunakea[1] and Kohala volcanoes on Hawai'i, which has previously been studied as a Mars analogue [e.g., *Bell et al.*, 1993; *Morris et al.*, 2000b, 2001; *Hamilton et al.*, 2008]. We therefore selected Hawai'i for an analogue study because tholeitic basalt, transitional basalt, and alkalic volcanics with compositions similar to Gale Crater have been exposed to a range of weathering, alteration, and sedimentary processes. Our aim was to characterize Hawaiian geochemical trends (direction and magnitude) associated with sediment transport, weathering, and alteration of rocks with these relevant compositions.

The igneous, weathering, alteration, and physical sedimentary processes that operate on Hawai'i have been studied extensively on the island chain [e.g., *Nakamura et al.*, 1965;

---

[1] Here, we use the name "Maunakea", rather than "Mauna Kea", per the recommendation of Hawaiian language experts at the University of Hawai'i at Hilo College of Hawaiian Language.

Porter, 1979; *Farr and Adams*, 1984; *Lanphere and Frey*, 1987; *Spengler and Garcia*, 1988; *Porter*, 1997; *Wolfe et al.*, 1997; *Capo et al.*, 2000; *Kurtz et al.*, 2002; *Schiffman et al.*, 2002] as well as at other basaltic sites with Mars analogue potential [e.g., *Colman*, 1982; *Eggleton et al.*, 1987; *Smith et al.*, 1987; *Nesbitt and Wilson*, 1992; *Gislason et al.*, 1996; *Pokrovsky et al.*, 2005; *Óskarsson et al.*, 2012]. Previous works have also approached these processes from the Mars analogue perspective, as we do here. These include geochemical and mineralogical investigations of the aqueous alteration of high alkali basalt [*Hadnott et al.*, 2017], Icelandic basalt and palagonitic tuff [*Bishop et al.*, 2002; *Ehlmann et al.*, 2012], and other basalt, basaltic glass, and basaltic minerals under various temperature, pH, and Eh conditions [*Hausrath et al.*, 2008; *Hausrath and Brantley*, 2010; *Hausrath et al.*, 2013; *Hausrath and Tschauner*, 2013]. Others have focused on the formation of alteration rinds and coatings under acidic [*Morris et al.*, 2000a; *Schiffman et al.*, 2006; *Minitti et al.*, 2007; *Seelos et al.*, 2010] and cold, arid conditions [*Salvatore et al.*, 2013]. Maunakea has been investigated previously by workers who recognized palagonitic and acid-sulfate altered Hawaiian tephra has characteristics similar to altered Martian rock, soil, and dust [e.g., *Bell et al.*, 1993; *Morris et al.*, 2000b, 2001; *Hamilton et al.*, 2008].

The most common alteration regimes reported for Hawai'i include pedogenic, palagonitic, and acid sulfate, and a key objective of this work is to characterize these regimes from a Mars rover perspective. The differences between pedogenic and palagonitic alteration are discussed in more detail below, but hydrolysis is the primary process by which alteration progresses in the two regimes [*Morris et al.*, 2000a]. Broadly speaking, hydrolysis, or hydrolytic alteration, involves the replacement of ions in primary minerals and glass with H^+ or OH^-. Acid sulfate alteration similarly disrupts bonds in minerals and glass and adds SO_4^{2-} [e.g., *Morris et al.*, 2000a]. Hydrolytic and acid sulfate alteration, therefore, can mobilize ions and lead to depletions via leaching, enrichments via passive accumulation in residue, or enrichments via transport, concentration, and reprecipitation. Key considerations for differentiating alteration regimes in a rover analogue dataset include:

(1) Water is not detected by the APXS, and the addition of H^+ or OH^- by hydrolysis is not apparent in the Martian dataset.

(2) Mineralogy is often poorly constrained, and secondary indicator minerals (e.g., phyllosilicates, hydroxides, oxides) can retain much of the bulk chemical characteristics of the parent lithology in a closed, isochemical system. Thus, closed system alteration may be indistinguishable from unaltered material in APXS data.

(3) The APXS is well-suited for characterizing sulfates because high precision enables the determination of sulfate cations (Ca^{2+}, Mg^{2+}, K^+) by rastering targets [e.g., *VanBommel et al.,* 2016]. However, sulfur analyses are affected by the presence of S-rich dust (see Chapter 4) on target surfaces, so the presence of S alone in an APXS analysis is not evidence of acid sulfate alteration (Figure 1-10).

Our approach to Hawai'i as a Mars analogue is novel because we seek to integrate multiple geological processes to try to understand the complex history evident in Gale Crater. An underlying question in our hypotheses is "what can *Curiosity* detect with its payload?" That is, what hypotheses may or may not be unambiguously testable with *Curiosity*? Many geological questions that may have glaringly apparent answers in a thin section could very well be an unsolvable mystery inside *Curiosity's* dataset. Here, we compare Hawai'i and Gale Crater observations and propose interpretations for Gale Crater processes based on similarities and differences between the two sites.

2.3. Methods

2.3.1. Maunakea and Kohala Samples

Site selection and sampling was designed to survey the broadest accessible range of volcanic material and related weathering and alteration products as well as sedimentary deposits. The four major volcanic rock types of Kohala and Maunakea (Hawi, Pololu, Hamakua, Laupahoehoe) were sampled from multiple flows and tephra deposits (Figure 2-1). Fresh, unaltered and weathered samples were extracted from the same outcrop of individual flows to obtain weathering profiles (Table 2-1). Public highway roadcuts exposed the best weathering profiles because the unaltered (or least altered) interior of individual flows could be sampled along with a progression of moderately to highly weathered rocks at the subaerial margin. Additional samples of fresh and weathered rocks were collected, with most sites located in the Maunakea Forest Reserve. Sediment was sampled at Maunakea between 2000 and 3500 m in elevation, and included outwash sand and pebbles, diamict, and layered slope deposits exposed in gulches. Soils were not sampled. Site locations and samples are described in Appendix 2-3 and mapped in Appendix 2-4.

Access to Maunakea above ~3500 m and at cinder cones was not permitted for this field study, so additional samples from the summit were provided from the collections of D. W. Ming and R. V. Morris at NASA-JSC. Most of these are split samples of < 1 mm grain size fractions of tephra with previously published chemical and mineralogical data [*Morris et al.*, 2000b; *Hamilton et al.*, 2008]. The samples were grouped into three categories based on sulfur content, LOI, and K_2O/MgO: 1) fresh, unaltered tephra, 2) tephra with hydrolytic alteration, and 3) tephra with acid sulfate alteration. Most of the altered tephra had elevated LOI (>2 wt%) compared to unaltered tephra. Hydrolytic alteration is distinguished from acid sulfate alteration by lower SO_3 content (< 0.5 wt%) and lower K_2O/MgO (< 0.5) [Figure 5 in *Morris et al.*, 2000b]. We refer to this expanded sample set, that is, samples from the Ming/Morris collections analyzed and described previously, as “Maunakea summit” samples to distinguish them from the original fieldwork and analytical work conducted for this study. We also refer to tephra that has undergone hydrolytic alteration as “hydrolytic tephra” and acid sulfate altered tephra as “acid sulfate tephra”. We include in our discussion a previous analysis of an acid sulfate altered tholeiitic basalt from the Sulfur Banks at Kilauea [*Morris et al.*, 2000a]. This rock had six 1 cm slabs sampled from within the least altered interior of the rock (9 cm depth) and then at intervals of decreasing depth to obtain a profile of the increasing alteration toward the surface.

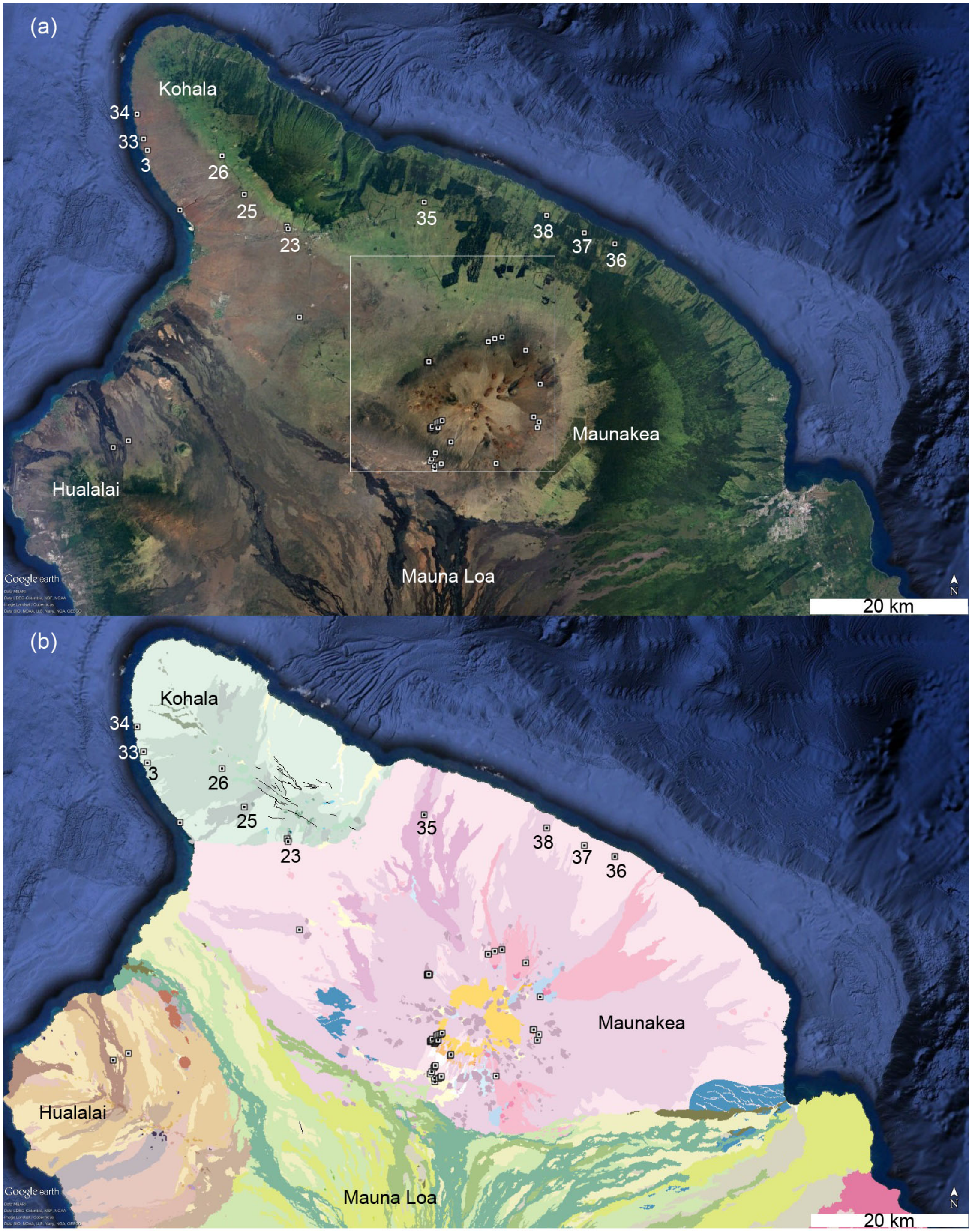

Figure 2-1: Regional map of Kohala and Maunakea on Hawai'i showing (a) satellite images (Landsat; compiled by Google) and (b) geology [*Wolfe and Morris*, 1996; *Trusdell and EW Morris*, 2005]. Sampling sites from this study are indicated by small squares and numbered sites correspond to weathering profiles (Table 2-1; MK15 prefix omitted for clarity). Detailed maps of the sites contained within the outlined box in (a) are presented in Appendix 2-4.

Table 2-1: Summary of weathering profiles.

Volcano	Site ID[1]	Volcanic group	TAS classification[2]
Kohala			
	MK15-3	Hawi	Mugearite
	MK15-23	Hawi	Mugearite
	MK15-25	Hawi	Benmoreite
	MK15-26	Hawi	Hawaiite
	MK15-33	Pololu	Basalt
	MK15-34	Pololu	High alkali basalt
Maunakea			
	MK15-35	Laupahoehoe	Benmoreite
	MK15-36	Hamakua	Basalt
	MK15-37	Hamakua	Basalt
	MK15-38	Laupahoehoe	High alkali basalt

[1] See Figure 2-1 for site locations and Appendix 2-3 for detailed descriptions.

[2] Total alkali (Na_2O + K_2O) versus silica classification [*Le Maitre et al.*, 1989].

2.3.2. Analytical Techniques

The strategy for sample analysis was to emulate the APXS and CheMin instrument datasets. During Mars surface operations, both instruments *approximate* a bulk, whole rock analysis of a small "hand sample" roughly the volume of a full drill hole (~10 cm^3). In detail, the instruments detect variation on a much smaller scale, but we find it to be a reasonable assumption to apply to an Earth analogue study. Thus, our approach was to characterize the samples with bulk X-ray fluorescence spectrometry (XRF) and XRD. Chapter 3 demonstrates that using XRF as an APXS analogue is not ideal because the Martian targets cannot be prepared such that matrix effects are minimized (i.e., by fusing samples). Nevertheless, XRF is more accurate than APXS [*Johnson et al.,* 1999; *Gellert et al.,* 2006] and we find it to be appropriate for the objectives of this work. Samples were prepared to qualitatively represent field characteristics, such that secondary alteration phases were preserved 'as-is' and roughly in the same volumetric proportions found in a ~10-25 cm^3 hand sample. Fresh samples were also prepared to represent the unaltered parent igneous composition. In these samples, secondary alteration phases were removed from surfaces and fractures before sample preparation.

The chemical composition of ~10-50 g split samples (after crushing in an Al_2O_3 crusher to approximately < 1 cm pieces) was determined with XRF at the Peter Hooper Geoanalytical Lab at Washington State University using the method of *Johnson et al.* [1999]. The samples were split qualitatively such that relative proportions of different phases (altered, unaltered) in the rock were preserved. Fused beads are made with a 2:1 Li-tetraborate:sample dilution and analyzed with a constant voltage on a Rh target. Volatiles and Fe oxidation state are disregarded and the major elements are normalized to 100 wt. % with Fe as total FeO. A suite of trace elements were analyzed, but we limit our discussion largely to include only Ni and Zn, which are reported in the APXS dataset (LOD ~30 ppm) and are commonly enriched on the Martian surface.

Bulk mineralogy was determined for select samples (also split after crushing in an Al_2O_3 crusher to approximately < 1 cm pieces) representing a range of unaltered to highly altered samples by powder XRD. The samples were split qualitatively such that relative proportions of different phases (altered, unaltered) in the rock were preserved. Standard powder XRD methods were employed [e.g., *Poppe et al.*, 2000] with a Rigaku SmartLab XRD system at Brock University. Ten to twenty grams of sample was powdered by milling for 20 min in an Al ball mill. Back-packed powders were analyzed with Cu Kα X-rays at 40 kV and 44 mA at a continuous rate of 1 degree/minute over a 2-90° 2θ range. Patterns were evaluated and phases were identified with Bruker EVA and QualX software, using standard powder diffraction files from the International Centre for Diffraction Data (ICDD) database and Open Crystallography Database, respectively.

Additional textural and mineralogical information was obtained from standard optical petrography and μXRD analysis. Sub-mm scale, in situ mineralogy of thin sections and hand samples was evaluated with a Bruker D8 Discover μXRD at the University of Western Ontario (Earth Sciences Department), employing a 60 mm Co gobel mirror, 300 μm snout, and a Vantec 500 two-dimensional detector. Analyses consisted of two frames covering ~2-90° 2θ at 30 minutes per frame. Individual phases in thin sections were targeted with a spot size of ~300 μm. Coatings and rinds on hand samples were also targeted. Single crystal (i.e., spotty 2D patterns rather than rings) and roughness effects were reduced, but not entirely removed, by scanning through omega and by targeting flat, smooth hand sample surfaces. Note that the diffractometers used for this work have different anodes, so Cu and Co 2θ values are noted.

2.4. Maunakea and Kohala Results and Interpretation

Below we summarize the results and geologic interpretations for weathering profiles, hydrolytic and acid sulfate Maunakea summit tephra, and sedimentary materials. Results for XRF from this study are presented in Appendix 2-1 and a summary of XRF results from previous Maunakea summit work is presented in Appendix 2-2. Four XRF duplicate runs for the new analyses (i.e., duplicate beads made from the same powder) demonstrate results consistent with established precision for the method [*Johnson et al.*, 1999]. XRD results are summarized in Appendix 2-6 and representative XRD scans are shown in Figure 2-2. Petrographic descriptions are summarized in Appendix 2-5 and Appendix 2-7.

2.4.1. Weathering Profiles

The weathering profiles share broadly similar outcrop characteristics (Figure 2-3). The most extensively weathered profiles were found at low elevations in the north/northeast region (Figure 2-1; sites MK15-36-38). Other profiles at higher elevations and in the more arid western regions of Maunakea and Kohala are less developed and are commonly only preserved in thin rinds (< 1 mm) above 2500 m elevations. For this reason, the most comprehensive profiles we could access were Hamakua basalts and alkali basalts that are exposed on the lower flanks of Maunakea; a well-developed mugearitic profile was not found. Flow interiors, exposed by roadcut construction, were fairly well-preserved, although rinds had formed on surfaces and in fractures and vesicles, and some phenocrysts had red/brown rims indicating oxidation. At the semi-tropical sites, voids, vesicles, and fractures in the flow interior were commonly altered and filled with fine-grained loose material or, less frequently, with botryoidal white coatings and white, prismatic crystals. The latter two phases did not effervesce with HCl and are interpreted to be amorphous silica and zeolite, respectively. Toward the margin of the profiles, flow surface breccia is mixed with sediment. Sediment with varying degrees of soil development mantles most Maunakea and Kohala flows below ~2800 m elevation.

Weathering and breakdown of parent rock is concentrated within this regolith near the brecciated flow surfaces. Blocks (10s cm) at this margin have rinds and are fractured and are more likely to be friable due to chemical weathering/alteration.

Most of the differences between the outcrops are attributable to the extent of weathering. The different igneous lithologies (basalts, mugearites, etc) do display systematic weathering characteristics, however, that appear to result from their starting chemical compositions and phenocryst assemblages. Basalts weather progressively from the dark gray of the parent to a yellow/red and then to a dark, brick red. Mugearites change from the feldspar-rich light gray of the parent to a yellow/red and light brown. One Kohala benmoreite outcrop (MK15-25) was unique because it had indications of weathering in red/brown rims on pyroxene phenocrysts, thudded with a hammer strike, and hand samples were very friable and fell apart into a fine-grained powder. Despite these characteristics, the apparently weathered outcrop had the same gray color as the parent lava. The differences in yellow and red in the weathering product is most likely due to ferric Fe phases [e.g., *Cornell and Schwertmann*, 2006]. These qualitative color variations may indicate different ferric phases (e.g., yellow Fe oxy-hydroxide vs. red hematite), more or less total ferric content, or different oxidation pathways for Fe (e.g., olivine versus titano-magnetite), the latter of which hosts relatively more of the Fe in mugearites and weathers more slowly than olivine [e.g., *Nesbitt and Wilson*, 1992].

The eight weathering profiles span nearly the full range of parent volcanic rock compositions at Maunakea and Kohala (Table 2-1; Figure 1-3), but all share similar weathering trends in bulk chemical composition. Incipient weathering is characterized by loss of K_2O and Na_2O (Figure 2-4). In the alkalic profiles, K_2O drops by a larger percentage than Na_2O in incipiently weathered samples (Figure 2-4 a, b); the removal of Na_2O is greater than K_2O in the basaltic profiles (Figure 2-4 c-e). The decrease in alkali elements continues regularly with further weathering. Silica and divalent cations Ca^{2+} and Mg^{2+} also display mobility and depletion. In the basalt profiles, more Ca is lost than Mg, indicating different solubilities and/or compatibilities with secondary phases. Elevated MgO is observed in some moderately altered profiles (MK15-37, MK15-38), but it is depleted in all highly-weathered samples (Figure 2-5). This variation in MgO does not correlate qualitatively with olivine content or olivine texture (e.g., ± olivine phenocrysts). Silica is consistently depleted in all weathered samples (Figure 2-4b). Incipient weathering is characterized by a modest decrease in silica, K_2O, and Na_2O. We note that this depletion, which is apparent in the least altered samples at sites MK15-33 and MK15-36, indicates that they are not completely unaltered lava and thus we use them at the 'least altered' sample against which to compare more altered samples. Among all rock types, major element enrichments uniformly include Ti, Al, and Fe (Figure 2-4). Other conserved minor and trace elements are Mn, P, Ni, and Zn.

Bulk powder XRD and optical petrography for unaltered samples are consistent with typical mineral assemblages for basaltic and alkalic rocks (Figure 2-2) [e.g., *Lanphere and Frey*, 1987; *Wolfe et al.*, 1997]. Basalts are primarily plagioclase, pyroxene, and olivine, as are the transitional Hamakua basalts. Alkali basalts (4.0 wt% Na_2O+K_2O) are similar and contain olivine phenocrysts (34A), but olivine decreases in abundance in thin sections and is not detectable with confidence in XRD of high alkali basalts (5.0 wt% Na_2O+K_2O; MK15-38A). Hawaiites and mugearites are primarily plagioclase feldspar with a trachytic texture and uniformly distributed "salt and pepper" oxide opaques. Sodian anorthite is generally the best feldspar fit for most patterns with a fit probability of ~0.70-0.75. Anorthoclase is detectable in mugearites (p ~0.70). The overall trend from basalt to increasing alkali and alkalic volcanics is a progressive decrease in olivine and pyroxene and increased prevalence of feldspar peaks (Figure 2-2). Oxides are abundant in mugearite sections (~10-15% by volume); Fe-Ti spinel peak overlap with feldspar results in decreased certainty for XRD identification (p ~0.5-0.6). Apatite is detected in mugearites, also with low certainty (p ~0.5), but it is apparent as acicular inclusions in plagioclase and olivine in some flows (sites MK15-3, MK15-61).

In bulk powder XRD, incipient to moderate weathering is dominated by primary igneous mineral peaks (Figure 2-2). Samples with incipient weathering and with small amounts of alteration phases in fractures, vesicles, and thin rinds (< 1 mm thick) reflect primarily the parent mineralogy with narrow feldspar peaks and no definitive crystalline alteration phases except for hematite at a moderate probability (p = 0.60). Moderately to highly weathered samples maintain feldspar and pyroxene reflections but with decreasing intensity and peak resolution. Definitive, low angle reflections indicative of phyllosilicates were not detected in any samples, nor were carbonates, sulfates, or other major mineral groups. In general, samples with minimal alteration that is texturally evident (e.g., red staining, isotropic plagioclase) did not have confident detections of common basalt alteration products (clay minerals, oxides and oxy-hydroxides) in bulk powder XRD. The secondary phases are thus below the XRD detection limit, and/or obscured by peak overlap, or are X-ray amorphous (e.g., nanophase Fe-oxide/oxyhydroxides).

Petrographic textures and μXRD reveal more details about progressive alteration and the diversity of secondary phases (Figures 2-S1, 2-S2). The process of incipient surface weathering is represented by thin rinds less than 1 mm thick. Rinds range from pale yellow brown to brown with patchy brick red. White material is common (no effervescence with HCl) with two morphologies that frequently occur together 1) smooth, pearly luster, layered, and sometimes botryoidal and 2) granular and friable. The first has a morphology common to amorphous silica (MK15-3c) [*Farr and Adams*, 1984] and is thus likely a coating rather than a rind. Both morphologies have similar XRD characteristics, with a high background below 20° 2θ (Co K) indicative of allophane [e.g., *Pokrovsky et al.*, 2005; *Yesavage et al.*, 2015], and broad hump between 20-35° 2θ (Co K) consistent with amorphous silica [e.g., *Herdianita et al.*, 2000]. These amorphous characteristics are apparent in the rinds investigated, with the inclusion of primary minerals and secondary oxides with varying peak intensity that is usually very low and therefore low in relative abundance. The amorphous silica hump varies, but is in all rind XRD scans. We interpret this to be because mobile silica is available to precipitate on rock surfaces and the ‘rind’ is probably a mixture of in-situ altered primary phases and associated secondary phases with silica ‘coating’. A cross section of a thin yellow/brown rind on a mugearite (MK15-61b; Figure 2-S3), starting from the interior rock and moving to the rind, has narrow feldspar and Fe-Ti spinel peaks, with varying relative intensities, then a full change to the amorphous-dominated rind. This indicates that the transition from unaltered rock to the rind is on a scale smaller than the 300 μm diameter X-ray beam size.

The progression of more advanced weathering in the bulk rock was examined in polished thin sections with μXRD. Evidence of weathering begins with red rims around olivine grains (Figure 2-S1). Thin (~2 μm) beaded threads of red fine-grained secondary phases penetrate into the grains along the ordered olivine structure, as has been described for iddingsite [*Gay and LeMaitre*, 1961; *Smith et al.*, 1987]. This proceeds until the olivine is converted mostly to an opaque oxide pseudomorph. XRD 2D patterns for the highly oxidized olivine phenocrysts (MK15-37d), which are 1-2 mm and fill the μXRD FOV, display spots (rather than rings) due to single crystal preferred orientation. Peak positions indicate an Fe-spinel, and minimal or no olivine. That the secondary oxides do not diffract X-rays as a fine-grained randomly oriented cluster of crystallites (i.e., as rings in 2D patterns) suggests that the secondary alteration oxide is either a single crystal or crystallites have highly preferred orientation. While clay minerals are a component of typical iddingsite in intermediate stages of alteration [*Smith et al.*, 1987], no diagnostic low 2θ peaks are in the patterns.

Other major components weather along different pathways. The groundmass degrades soon after olivine develops red rims, becoming more transmissive and fine-grained with a 'clay-like' texture in thin section. Weathering of plagioclase is first evident in degradation of euhedral crystal faces and a disruption of birefringence such that most are isotropic (Figure 2-S1). With moderate to moderately extensive weathering, plagioclase laths and igneous textures are generally well-preserved as isotropic pseudomorphs. The pseudomorphs have μXRD peaks indicative of gibbsite, including a broad peak at a d-spacing of 7.4 angstroms [*Nakamura et al.*, 1965], but they do maintain feldspar diffraction peaks. Gibbsite is pervasive in highly weathered samples including in pseudomorphs after plagioclase and as translocated gibbsite filling vesicles and fractures. Oxides show red-stained haloes that extends into the surrounding matrix, but persist as opaque phases in moderately to highly weathered samples.

A notable sample (MK15-37e) from the basalt profile MK15-37 has some exceptions to the overall profile trends (Figure 2-4e). It was identified in the field as highly weathered (fine-grained, friable, dominated by ferric oxides and having minimal crystalline basaltic material), but has a K_2O enrichment (1.2 wt%) of 4X over its parent composition (0.3

wt%). In all other major and minor oxides (Appendix 2-1), the rock has characteristics consistent with highly weathered basalts (Na and silica leaching with passive Fe, Al, and Ti enrichment). The XRD pattern has a smaller number of broad peaks with positions corresponding with Fe-Ti spinel, chromite, and hematite; no K-bearing secondary phase was identified and no evidence of clay minerals was present. This sample also contains narrow quartz peaks, which is the only detection of quartz in this sample set. Trace elements suggest that the K_2O enrichment is a secondary accumulation of K precipitated from a leachate. In all samples, Rb and K_2O have a strong correlation ($r = 0.97$). In the sample, Rb is 55 ppm, and Rb/K_2O (46) falls significantly off the Rb/K_2O value of nearly every other Hawaiian sample (~20). We interpret this to be due to K_2O and Rb fractionation caused by mobilization in solution.

To summarize, the weathering profiles are consistent with circumneutral, oxidizing, open system, incongruent alteration [e.g., *Nesbitt and Wilson*, 1992]. Desilication, leaching of alkali and alkaline earth elements, and passive enrichment of Fe, Al, and Ti in oxides/oxyhydroxides characterizes this low temperature pedogenic alteration regime. Passive enrichment of MgO is observed in incipient to moderate hydrolytic alteration likely due to slow dissolution kinetics, but with moderate and extensive weathering MgO is released and leached [*Morris et al.*, 2000b]. This fits with most of the profiles, and since MgO is more readily leached in acid sulfate solutions, the small differences in MgO may be an indicator for the difference between minimal acidic and hydrolytic alteration. The samples do not have clay minerals, and the formation of gibbsite indicates an elevated Al/Si gradient in fluids that interacted with the rock [*Nakamura et al.*, 1965]. Incipient weathering is characterized by depletion in silica and K_2O and Na_2O. Extensive weathering is characterized by high FeO, Al_2O_3, TiO_2, and low silica. An index that is sensitive to this type of alteration is the chemical index of alteration (CIA) determined by *Nesbitt and Young* [*Nesbitt and Young*, 1982] and calculated as

$$\mathrm{CIA} = [Al_2O_3 / Al_2O_3 + CaO + Na_2O + K_2O] \times 100$$

using molecular proportions (Figure 2-6a). Because Al and Ti are immobile, they can be used in ratios to trace mobility of other elements when parent compositions are not well constrained. Another indicator for pedogenic weathering is the ratio (Na + K)/Ti, which decreases with increasing weathering. This indicator readily shows alkali leaching in incipient cases that the CIA is not sensitive to (e.g., site MK15-35; Figure 2-6b).

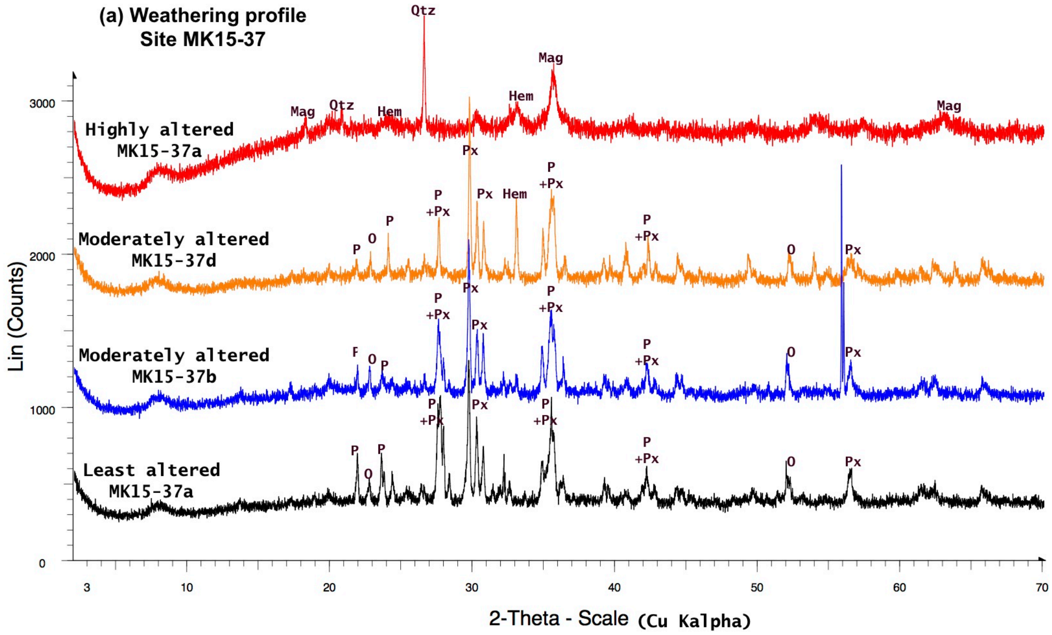

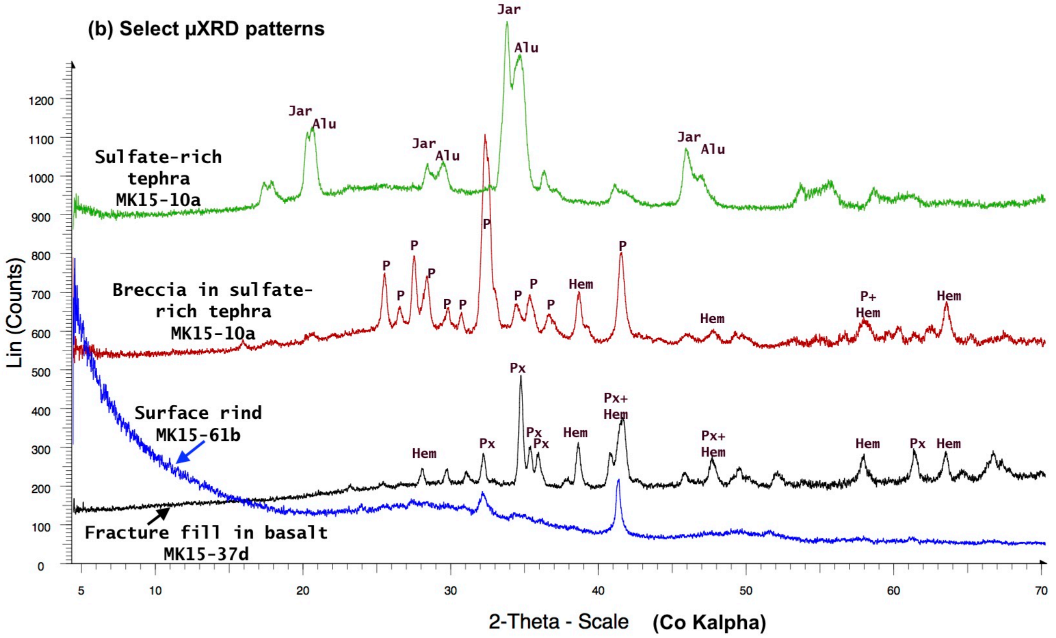

Figure 2-2: (a) Bulk powder raw XRD patterns of samples from a basalt weathering profile (site MK15-37). (b) Select µXRD patterns of altered samples. Select peaks are indicated (P = plagioclase; Px = pyroxene; O= olivine; Hem = hematite; Mag = magnetite; Qtz = quartz; Jar = jarosite; Alu = alunite) and the broad hump at ~20-40° 2θ is due to amorphous material. The broad peak at ~8° 2θ in (a) is due to the Al metal sample holder.

Figure 2-3: Representative weathering profile of Kohala pololu basalt from site MK15-33. (a) The interior of the flow preserves unweathered dark gray basalt. Many surfaces have a thin (< 1 mm) pale yellow to light red rind. The top of the flow is mantled by sediment. (b) Moderately weathered basalt at the margin of the flow. The rock is brown and friable and has common white coatings. (c) Extensively altered basalt in the foreground, and at the top ~20 cm of the flow.

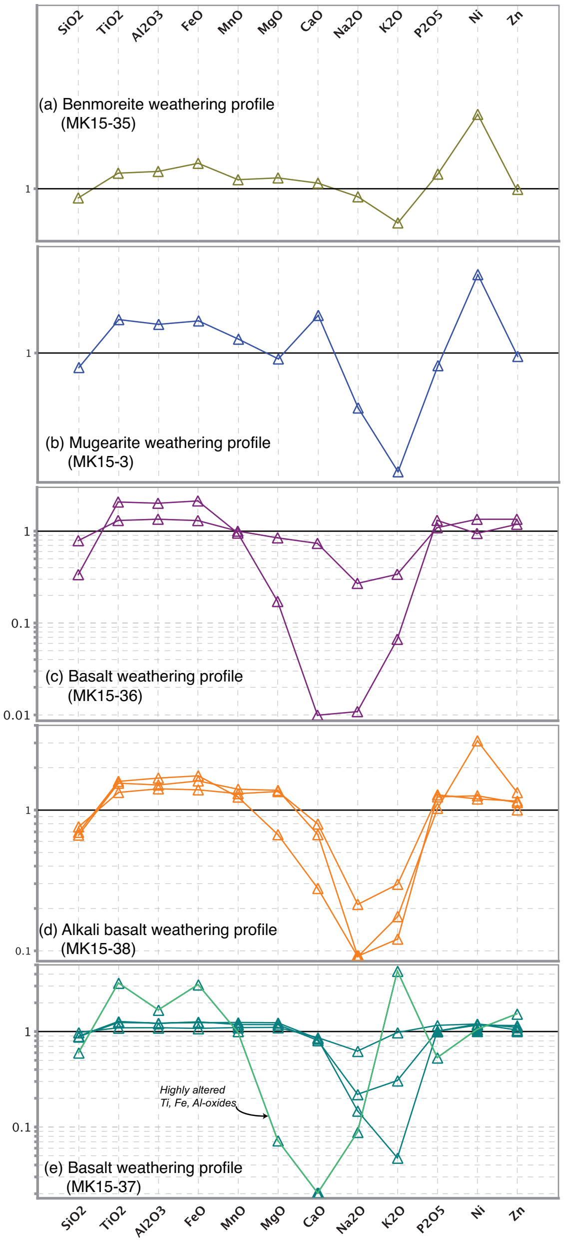

Figure 2-4: Oxide and trace elements of representative weathering profiles, normalized to the least altered parent composition. (a, b) Incipient weathering of benmoreite and mugearite indicates K_2O is readily mobilized and leached. (c-e) Extensive basalt weathering results in the progressive loss of K, Na, Ca, and Si, while Ti, Al, Fe, Mn, P, Ni, Zn, and ± Mg are retained, eventually forming an Fe-, Al-, Ti-rich composition.

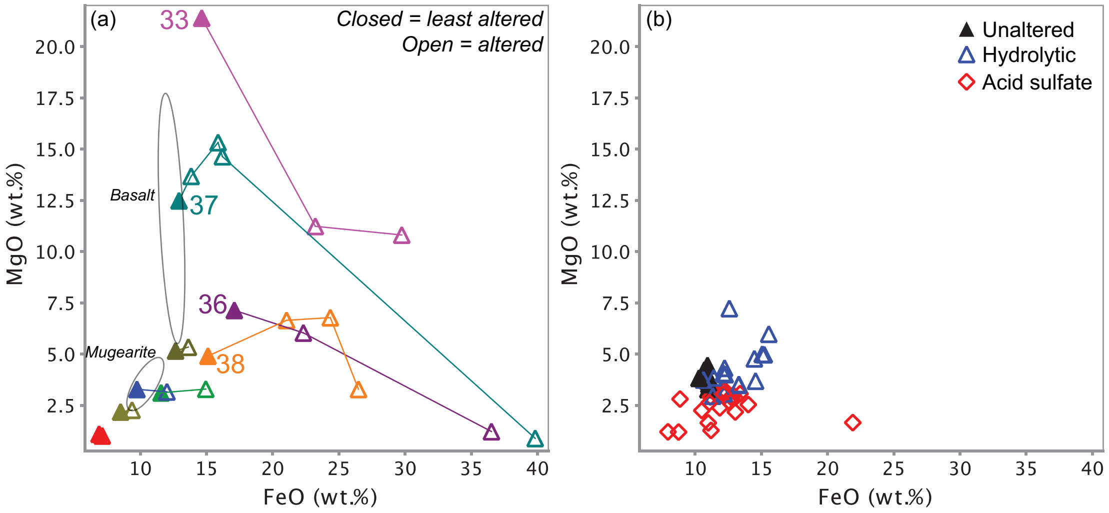

Figure 2-5: (a) MgO versus FeO for weathering profiles showing consistent, progressive increase in FeO. MgO is variable, decreasing regularly in some profiles (MK15-33, MK15-36) but increasing initially, and then decreasing in other profiles (MK15-37, MK15-38). (b) Maunakea summit tephra, showing increases in FeO and MgO due to hydrolytic alteration and variable FeO concentrations in acid sulfate altered tephra. Tielines in (a) connect weathering profiles, and least altered samples for selected sites are indicated by site number (MK15 prefix omitted for clarity). Maunakea basaltic and mugearitic compositional ranges are shown by ellipses (p = 0.5 contour).

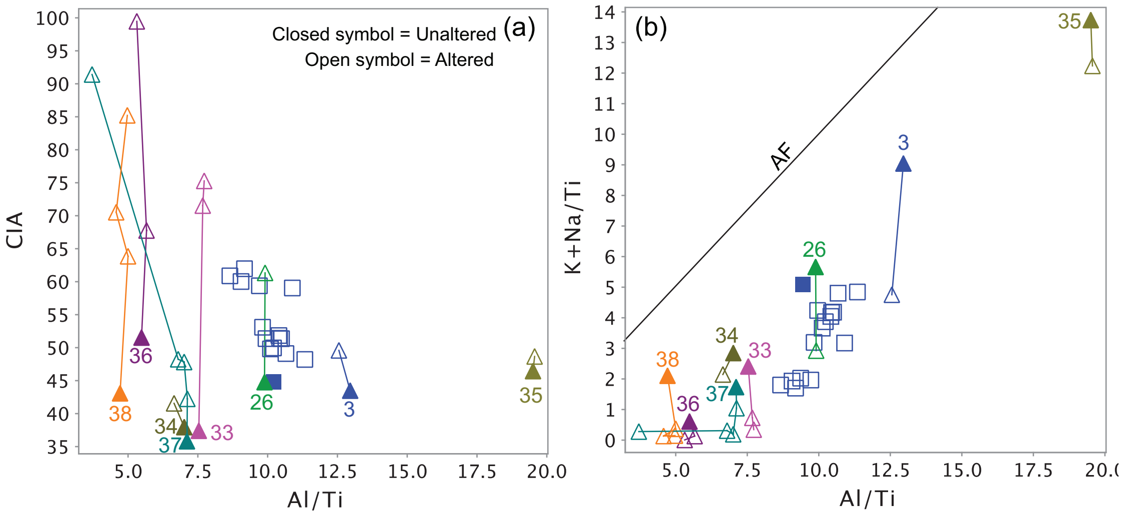

Figure 2-6: Hydrolytic alteration indicators (a) chemical index of alteration (CIA) [*Nesbitt and Young*, 1982] and (b) Ti normalized total alkali versus Al. Hydrolytic Maunakea summit tephra (squares) are shown with weathering profiles (triangles) labelled with site numbers (MK15 prefix omitted for clarity). The alkali feldspar control line (AF; 1:1) is shown.

2.4.2. Hydrolytically Altered Tephra

Geochemical and mineralogical results for the Maunakea summit tephra and Kilauea acid sulfate rind have been reported previously [*Morris et al.*, 2000b, 2000a; *Hamilton et al.*, 2008] and we provide a brief summary here. Unaltered tephra is hawaiitic and has relatively limited variability (Appendix 2-2; Figure 2-6), and to determine relative mobility, we use the average unaltered hawaiitic tephra of *Morris et al.* [2000b]. Hydrolytic alteration results in element mobility with characteristics similar to the weathering profiles (Figure 2-7). The greatest oxide depletion is in alkalis, with K_2O more depleted than Na_2O. Silica and CaO are also consistently depleted, but to a lesser extent. TiO_2, Al_2O_3, FeO, MnO, and P_2O_5 are all constant or enriched. An apparent depletion of 11% in TiO_2 in one sample (HWMK720) may be attributable to variability in the parent material, although it does fall outside of the standard deviation of 5% for TiO_2 in the fresh tephra samples. MgO is enriched in some samples (Figure 2-5), but a depletion of the element in the <2 μm size fraction led *Morris et al.* [2000b] to conclude that it is kinetically slow to dissolve, then is readily leached away. The hydrolytically altered tephra retains primary minerals plagioclase feldspar, Fe-Ti spinel, and trace pyroxene and olivine. The samples are relatively oxidized, having nanophase oxides (np-ox; determined by Mössbauer spectroscopy) and variable amounts of hematite.

Hydrolytic tephra from the Maunakea summit [*Morris et al.*, 2000b; *Hamilton et al.*, 2008] share bulk chemical and mineralogical characteristics with the pedogenic weathering profiles. The high LOI, low SO_3 hydrolytic tephra found at the Maunakea summit have been referred to as "palagonitic" [e.g., *Bell et al.*, 1993; *Morris et al.*, 2000b]. *Schiffman et al.* [2002] argue for a distinction between pedogenically altered and palagonitized tephra, with three criteria for a palagonite designation: 1) it has ash with palagonitized rinds, 2) deposits are usually consolidated tuff, and 3) it contains smectite. Four Maunakea summit samples contain phyllosilicate minerals smectite ± kaolinite (HWMK720, 741, 904, 911). These four are lower in MgO and Al_2O_3 than most of the other hydrolytic tephra, but do not deviate from the general chemical trends. They follow the same trend as the weathering profiles, which are all examples of pedogenic alteration with rock disaggregation, ferrihydrite and allophane formation, and tendency to be desilicated and aluminous [*Schiffman et al.*, 2002].

We ask here if *Curiosity* would be able to resolve differences between the end products of pedogenic weathering (weathering profiles) and palagonitic alteration (hydrolytic tephra)? The first proposed criterion for palagonite is not testable by *Curiosity's* instruments because it can't prepare samples to examine fine textures smaller than ~100 µm. The second is difficult to apply in Gale Crater's sedimentary deposits, particularly because transport of the sediment removes the original geologic context. The third is testable with CheMin, and smectite has been discovered in Gale at Yellowknife Bay [*Vaniman et al.*, 2014]. Because the bulk geochemical compositions are similar, we maintain that differences between pedogenic and palagonitic alteration wouldn't be discernable in APXS data. We therefore group these samples together under the "hydrolytic" type of alteration.

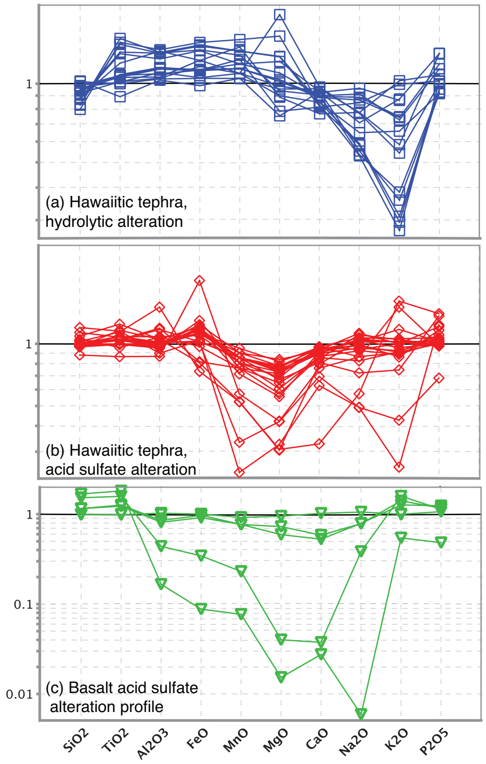

Figure 2-7: Oxide and trace element ratios to the least altered parent material. (a) Hydrolytic alteration has similar element mobility trends to weathering profiles (Figure 2-4), whereas acid sulfate altered (b) tephra and (c) basalt rind have distinct element

mobilities (see text). Data in (a, b) are from [*Morris et al.*, 2000b; *Hamilton et al.*, 2008] and in (c) are from [*Morris et al.*, 2000a].

2.4.3. Acid Sulfate Altered Tephra

Acid sulfate altered tephra is distinct from the weathering profiles and hydrolytic tephra in major and minor element composition (Appendix 2-2, Figure 2-7b). First, whereas silica is leached by up to 20% in all hydrolytic tephra, in acid sulfate samples, silica ranges from 3% depletion to a 10% enrichment. One sample is depleted 10% (HWMK24). Similar ranges are found in TiO_2, Al_2O_3, and FeO, Na_2O, K_2O, and P_2O_5, which are all both enriched and depleted within ~10% for many samples. Exceptions in the alkali elements include two cristobalite- and smectite-bearing samples with strong alkali depletions, and interpreted to be hydrothermal, mild acid sulfate alteration products (HWMK30, 31) [*Hamilton et al.*, 2008]. Elements that show depletions in all samples are MnO, MgO, and CaO. Plagioclase feldspar is usually the dominant mineral in XRD, and secondary phases include jarosite, alunite, and hematite, with smectite and trace kaolinite in some phyllosilicate-bearing tephra.

The profile of an acid sulfate altered rind on a Kilauea basalt from Sulfur Banks [*Morris et al.*, 2000a] shares characteristics with the acid sulfate tephra. Relative to the least altered interior of the rock (Figure 2-7c), incipient alteration also shows a retention of most elements except MnO, MgO, and CaO. XRD indicates sulfates (gypsum and alunite) are present as secondary phases in the incipient alteration. With extensive acid sulfate alteration, significant depletions of most elements, excepting silica and TiO_2, corresponds with the removal of primary minerals and increasing contributions of amorphous silica and anatase.

The acid sulfate altered tephra from the Maunakea summit [*Morris et al.*, 2000b; *Hamilton et al.*, 2008] and altered basalt rind from Kilauea [*Morris et al.*, 2000a] illustrate the characteristic bulk chemistry and the products of interaction with low pH, high SO_3 fluids. The common feature is the retention, or passive enrichment of silica (Figures 2-12b, 2-12c). MgO is readily leached, while K_2O is retained by secondary sulfates. Thus, K_2O/MgO is a good indicator for hydrolytic alteration (lower K_2O/MgO) versus acid sulfate alteration (higher K_2O/MgO) [*Morris et al.*, 2000b]. In the highly altered rock, most elements may be leached, but SiO_2 and TiO_2 are retained in amorphous silica and anatase [*Morris et al.*, 2000a].

2.4.4. Maunakea Sedimentary Deposits

Sedimentary deposits on Maunakea represent a range of alluvial, colluvial, glacial, aeolian, and volcanic processes [*Porter*, 1997; *Wolfe et al.*, 1997]. The deposits are a varied mixture of interbedded ash, lapilli, aeolian sand deposits, debris flows, and diamict. Diamicts are weakly to moderately indurated, but all other deposits are unconsolidated or weakly consolidated. *Wolfe et al.* [1997] describe a reference section for slope deposits that illustrates the complexity of the deposits. We sampled eight bedded deposits and 24 unconsolidated sand and pebble deposits, removing clasts larger than coarse pebbles, but otherwise preserving the qualitative proportions of different clast sizes. Figures 2-8 and 2-9 show representative field sites where sediments were sampled.

The mineralogy of the unconsolidated sediment is nearly indistinguishable from incipiently weathered hawaiites in XRD analyses, having peaks attributed to primary minerals plagioclase feldspar, pyroxene, and Fe-Ti spinel. Secondary red, white, yellow, and green alteration products were observed in the sediment, primarily as oxidized red tephra (~20% by volume). This includes yellow/white breccia clasts found to contain alunite and jarosite with μXRD. Neither these nor other secondary products were detectable in the bulk powder XRD. The secondary products are thus either below the XRD detection limit, obscured by peak overlap, or are X-ray amorphous.

The bulk chemical compositions of the sediment samples indicate two trends linked to sedimentological processes: 1) deviation from igneous parent compositions due to alteration and 2) physical mixing of material derived from the two different volcanic units: Laupahoehoe and Hamakua. Relative degrees of alteration can not be reliably estimated using the ratio technique used for the weathering profiles (Figures 2-4) because parent compositions are unknown. Therefore, we turn to the chemical index of alteration (CIA) [*Nesbitt and Young*, 1982] to estimate degrees of weathering. Unaltered Hamakua volcanics have a CIA ~36 and unaltered Laupahoehoe volcanics have a CIA ~44, and alteration by removal of Na, K, and Ca and retention of Al causes this number to increase (Figure 2-10a). A similar index is the ratio [K + Na]/Ti which decreases in value with alkali leaching, and is sensitive to incipient weathering (Figure 2-10b). These two indices, plotted versus the ratio of Al/Ti, demonstrates that the sediment reflects its parent volcanic compositions and altered products. Leaching of mobile elements Na, K, and Ca, with the retention of immobile elements Ti and Al, is consistent with hydrolytic alteration of the sediment.

The sediment compositions also bridge the compositional gap between the basaltic Hamakua and evolved alkaline Laupahoehoe compositions, consistent with physical mixing of material derived from the two volcanic units. The 'bridging' compositions are relatively rare in Maunakea rocks (Figure 1-3) and is thus not a realistic igneous composition for the volcano. The mixing process is well illustrated by Figure 2-10c, where sediment sampled from above 3050 m, above which Laupahoehoe outcrop caps the volcano, the sediment is mugearitic. Below this elevation, where Hamakua basalts and diamict are exposed in gulches, the sediment compositions plot along a spectrum between the two volcanic units. This is simply because both units are integrated downslope into the unconsolidated alluvium and colluvium materials.

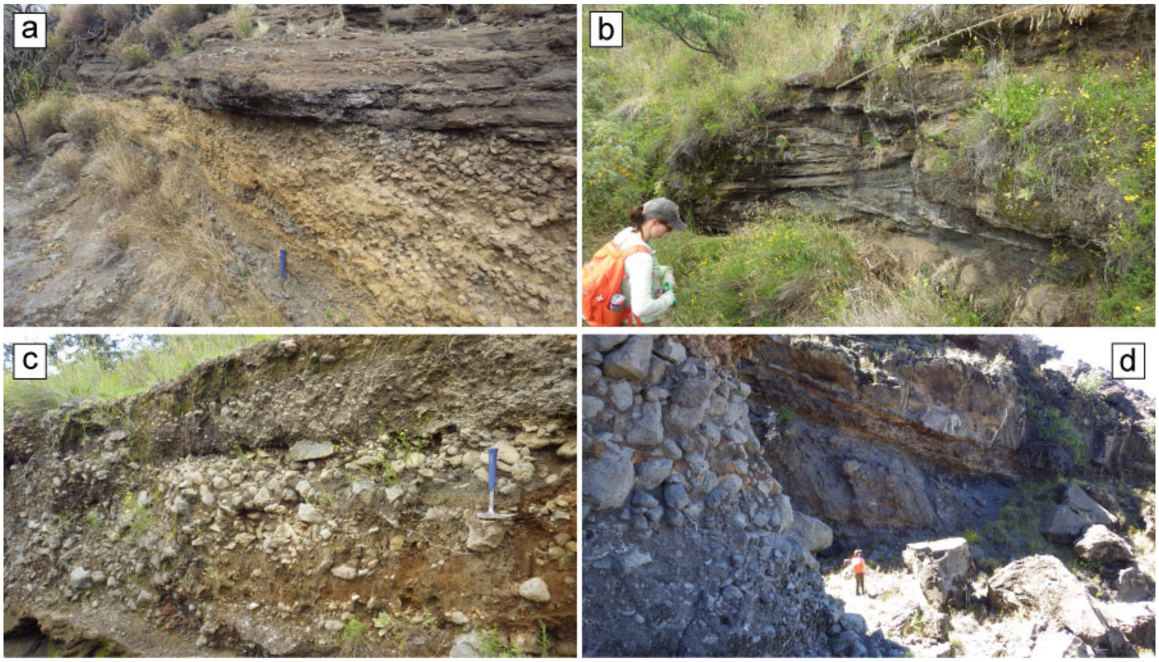

Figure 2-8: Common sedimentary deposits at Maunakea. (a) Palagonitized, subangular very coarse pebbles to small cobbles varying from matrix supported at the base to clast supported near the disconformably overlying bedded fine to coarse sand. The sand is interbedded with layers of angular 1-4 cm tephra clasts (blue hammer in center bottom of image for scale; site MK15-29). (b) Cross-bedded, coarse, subangular sand and fine pebble deposit underlying a flow (site MK15-50). (c) A sequence of gulch deposits overlying a cross-bedded sand deposit (i.e., Figure 2-8b) with subangular to subrounded cobbles and very coarse pebbles in a sand matrix. The upper bed is matrix supported and the middle bed (indicated by hammer) ranges from matrix to clast supported (site MK15-47). (d) Diamict overlain by flows at ~3100 m elevation on the southwest side of Maunakea. The material is minimally weathered, but shows evidence of palagonitization at the flow contact. Scale in the middle and right side of the images is provided by A. Thomas; the largest cobbles in the foreground on the left are ~40 cm (site MK15-53).

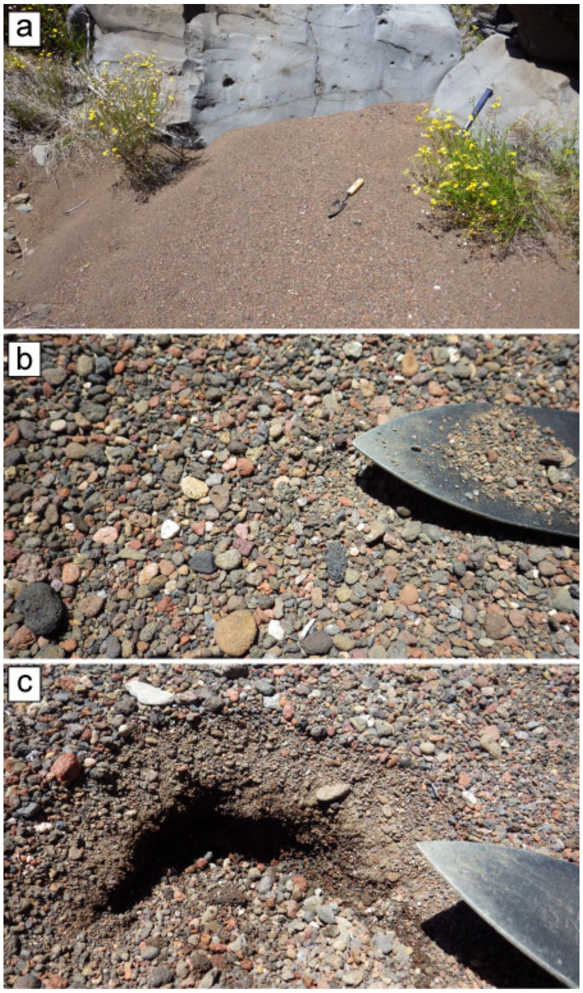

Figure 2-9: Representative outwash sand and pebble deposit on Maunakea (site MK15-56 at 3010 m elevation). (a) Context view of the deposit, which is in a low point within a gulch. (b) The undisturbed surface contains very fine to medium rounded to subrounded pebbles. The clasts consist of a poorly sorted mixture of lava fragments (gray/dark gray), moderately weathered lava fragments (yellow, brown, red), and tephra of the types described in sections 2.5 (brown, red, pink, yellow, white, green). (c) A pit in the deposit shows a cross section, with fine to coarse sand and fine pebbles overlain by a coarser lag deposit. The blade of the spade is 5.5 cm wide.

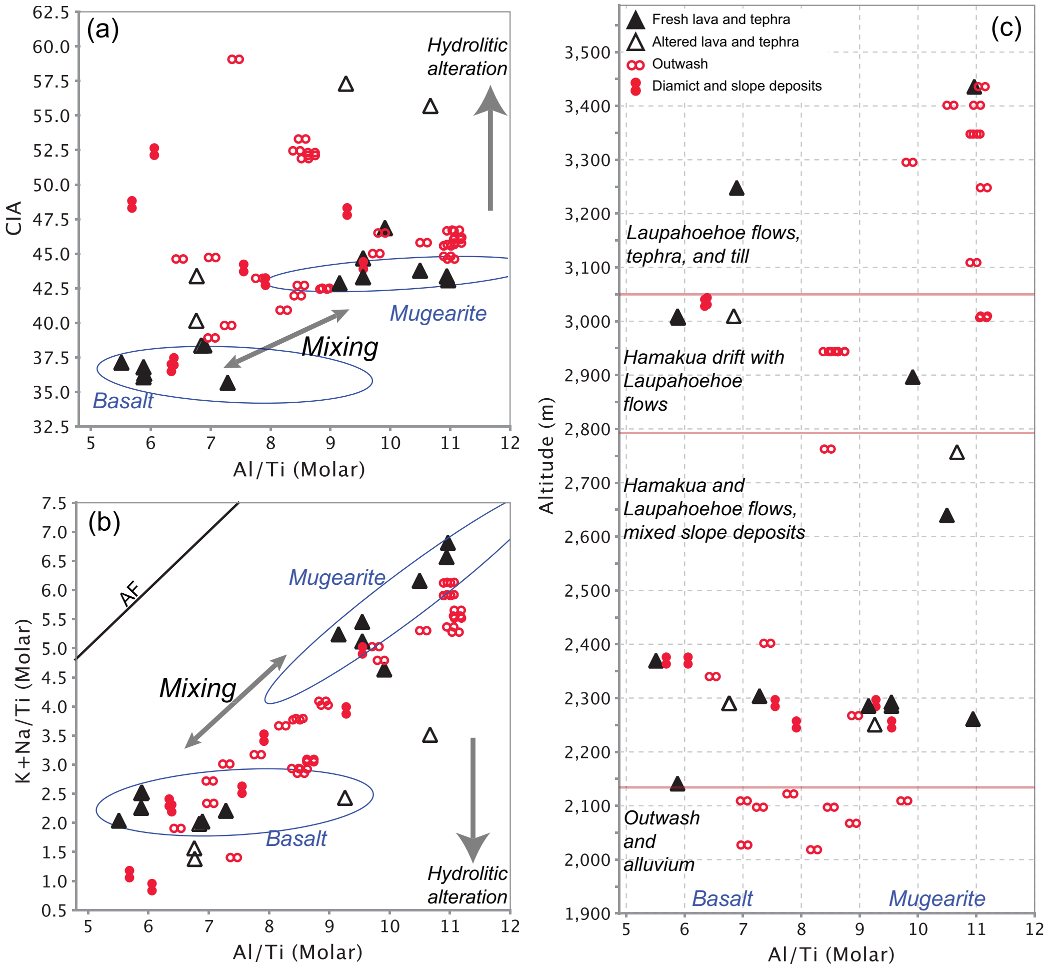

Figure 2-10: Sedimentary weathering and physical mixing trends relative to Al/Ti at Maunakea (excludes weathering profiles). (a) Hydrolytic alteration and leaching results in an increasing CIA and upward weathering vector. (b) Similarly, hydrolytic open system alteration leads to leaching of Na and K with retention of Al, resulting in a downward weathering vector. Physical mixing between sediment derived from the compositionally distinct basaltic and mugearitic parent volcanics (ellipses) follows a linear mixing trend that spans the compositional gap between the two parent compositions. (c) At elevations above 3000 m, Laupahoehoe lavas and till are extensive, while Hamakua basalts are only exposed in deep gulches. Thus, mugearitic compositions dominate the sediment at higher elevations. With decreasing elevation, Hamakua lavas and drift are commonly exposed, contributing basaltic sediment and resulting in a mixed basaltic and mugearitic sediment composition near the Maunakea/Mauna Loa saddle at ~2000 m.

2.5. Discussion: Application to Gale Crater

The geochemical and mineralogical trends observed on Hawai'i provide a framework to discuss *Curiosity's* Gale Crater dataset. This dataset encompasses the volcanic parent compositions at Maunakea and Kohala, consisting of two distinct, well-defined basaltic and alkalic units (Figure 1-7) formed by post-shield volcanism [*Lanphere and Frey*, 1987; *Wolfe et al.*, 1997]. We have also characterized alteration of these parental lithologies by 1) hydrolytic reactions in lava weathering profiles (Figure 2-4) and tephra (Figure 2-7a), and 2) by acid sulfate reactions in hawaiitic tephra and tholeitic basalt (Figures 2-12b, 2-12c). These materials were also eroded, physically mixed, and possibly subsequently altered, by sedimentary processes. Below, we apply insights from Hawaiian processes to aid interpretations of the geologic history of Gale Crater.

2.5.1. Diverse Igneous Provenance

The range in APXS compositions of the Bradbury group and the Stimson formation are broadly consistent with the basaltic to alkalic compositions of the post-shield volcanism on Hawai'i, and the mugearitic Jake_M class has particularly good overlap with the Laupahoehoe mugearites (Figure 2-S4) [*Stolper et al.*, 2013; *Schmidt et al.*, 2014b]. Some compositional differences between the ocean island basalts and the Gale basaltic groups are reflected in Martian meteorites, such as lower TiO_2 and higher FeO and MnO, and these may be characteristic features of the Mars crust [*McSween Jr. et al.*, 2009]. MgO is also higher in the Hamakua basalts due to olivine accumulation [*Wolfe et al.*, 1997]; this is not observed in Gale CheMin samples, which have relatively low olivine content (0-5 wt.%) [*Rampe et al.,* 2017; *Treiman et al.*, 2016; *Yen et al.,* 2017]. The provenance of the Murray formation is less clear due to the high silica component, which may be due to alteration, detrital high silica materials, or both.

Whereas Maunakea has two igneous types (basaltic and mugearitic), the Bradbury group likely has three igneous types (Table 1-1): basaltic (YKB), mugearitic (Jake_M), and potassic basalt (Bathurst Inlet) [*Schmidt et al.*, 2015; *Treiman et al.*, 2016]. The basaltic YKB samples suggest a source similar to the average Mars crustal composition [*McLennan et al.*, 2013; *Vaniman et al.*, 2014]. The Jake_M type has not been found in outcrop (i.e., float) and has not been drilled and analyzed by CheMin XRD, but the high Na_2O + K_2O (8.8 wt.%) suggests two possible formation pathways [*Stolper et al.*, 2013; *Schmidt et al.*, 2014b]. One possibility is mantle metasomatism and a second is low degrees of partial melting, followed by fractionation at high pressure [*Collinet et al.*, 2015]. The component of Gale sediment not produced at Hawai'i is the potassic Bathurst Inlet class, which is exemplified by the drill target Windjana (Table 1-1). These rocks have the same elevated range of K_2O as the Jake_M rocks (1.0-3.5 wt.%), but have low Na_2O (1.0-3.0 wt.%). They also have lower SiO_2 (39-46 wt.%) and higher FeO (13-21 wt%). CheMin XRD results for Windjana show that it contains 21 wt.% sanidine along with pyroxene, magnetite, olivine, and amorphous and smectitic material indicating it is a minimally altered sandstone of with a mixed igneous provenance [*Treiman et al.*, 2016]. The K_2O enrichment and high K_2O/Na_2O (3.3) may be consistent with an igneous protolith derived by partial melting of a phlogopite-bearing metasomatized mantle [*Treiman and Medard*, 2016].

An alternative hypothesis for the mafic/felsic trend in the Bradbury group (Figure 1-8a, 2-18b) suggests that it was produced by the hydrodynamic sorting of heavier mafic minerals from lighter felsic minerals during sediment transport into the crater via Peace Valles, and that the material was derived from a plagioclase-phyric basalt [*Siebach et al.*, 2017]. We find this hypothesis implausible for two reasons. First, sediment at Maunakea sampled from 2000 m had little evidence of sorting, being dominated by lithic fragments and having << 5 % separated, individual crystals (olivine and plagioclase). The composition of the sediments is also not correlated with mafic or felsic content; samples between 2000 and 2100 m elevation are not weighted toward either the basaltic or mugearitic endmembers (Figure 2-10c). This comparison of Gale to Maunakea is limited because the transport distance from Maunakea's summit to the Mauna Loa saddle is up to 9 km with 2000 m of relief, whereas the Peace Valles catchment (likely Gale source region) is about 55 km from *Curiosity's* traverse, with 2500 m of relief. Another analogue site with a more comparable sediment transport distance is the Askja sand sheet in Iceland, where aeolian processes transport high-FeO basaltic sand up to 30 km with a ~20% increase in MgO over the first ~5 km and with no change in MgO over the subsequent 25 km [*Sara et al.*, 2017]. This counter-indicates sorting of mafic/felsic minerals derived from basalt at that transport scale because the sorting hypothesis predicts a decrease in MgO due to a decrease in mafic minerals with distance.

A second argument against mineral sorting is based on the presence of potassic basalt (Bathurst Inlet). These basaltic sedimentary rocks have a high sanidine content (up to 21 wt% inferred from Windjana [*Treiman et al.*, 2016]). If the high alkali compositions in the Bradbury group were due to physical sorting and concentration of feldspar mineral grains, how could the transport of sediments from a source region containing the hypothesized two endmembers, a plagioclase-phyric basalt and a potassic basalt, yield a deposit containing alkalic rocks depleted in mafic minerals (Jake_M) and alkalic rocks *not* depleted in mafic minerals (Bathurst Inlet)? This requires heterogeneity in the sorting and distribution of the detrital minerals. That is, some parts of the deposit have not had the mafic minerals removed while others have, which is inconsistent with the averaging effect and predicted mafic/felsic gradient with transport distance (and/or transport energy) in the crater. We suggest that generation of sediment composition by mixing of three igneous endmembers (basaltic, mugearitic, and potassic basalt) follows the law of parsimony better than the mineral sorting hypothesis.

2.5.2. Sedimentary Mixing in the Bradbury Group

All bedrock units in Gale Crater are sedimentary, ranging from mudstone to conglomerate [*Grotzinger et al.*, 2015], and the compositions of Bradbury group rocks reflect the diverse provenance. The APXS and CheMin evidence suggests the Bradbury group experienced minimal, isochemical weathering [*McLennan et al.*, 2013; *Vaniman et al.*, 2014; *Treiman et al.*, 2016], thus variations not attributable to processes that formed the source material are likely a result of sedimentary mixing. By comparing Bradbury variation with Maunakea and Kohala, we can test the relative contributions of aqueous alteration and sediment mixing. First, limited hydrolytic weathering is likely for YKB or Bathurst Inlet because the decrease in (K+Na)/Ti observed in Hawaiian samples due to hydrolytic alteration is not apparent (Figure 2-11a, 15c). In comparing Ti normalized plots, note that TiO_2 is lower in Martian samples than at Maunakea, leading to different absolute numbers, but the relationships between K, Na, and Al are consistent and can be compared across Gale and Hawai'i [*Stolper et al.*, 2013]. The positive correlation of

(K+Na)/Ti with Al/Ti with a slope of ~1 is indicates the preservation of the primary alkali feldspar compositions. This conclusion is less certain for the Jake_M rocks with higher, more variable (K+Na)/Ti because they fall farther away from the alkali feldspar control line. We note that the CIA should not be applied to test for evidence of weathering in Gale Crater because salts are present [*Vaniman et al.*, 2014; *Rampe et al.,* 2017; *Yen et al.,* 2017] and element solubility and mobility (K ≈ Na > Ca >> Al) are not the same in acidic fluids as they are in the circumneutral fluid weathering scenarios upon which the index was based (Figure 2-S5) [*Nesbitt and Young*, 1982]. Next, in the plot of (K+Na)/Ti versus Al/Ti (Figure 2-11c), the Bradbury group sediments cover a continuous range along the alkali feldspar control line. This is similar to the manner in which Maunakea sediments span the igneous compositional gap between hawaiites and mugearites. The Hawaiian sediments, which are a product of mechanical mixing, provide an analogue explanation for the mixing of two igneous endmembers.

Gale is distinct from Hawai'i, however, having a potassic component (Bathurst_Inlet) that is consistent with addition of a third igneous source. The three igneous endmembers described in section 2.6.1. are apparent in a plot of K/Ti versus Na/Ti (Figures 2-15b, 2-15d), where the YKB basalts and Jake_M mugearites have a similar positive correlation to Maunakea basalts and mugearites. The potassic endmember Bathurst Inlet however demonstrates an increase in K/Ti with no change or decreasing Na/Ti, likely reflecting its high concentration of K-feldspar. As with the two-component mixing of sediments at Maunakea, the three endmembers of the Bradbury group likely contribute materials to the sedimentary rocks and result in intermediate compositions ("Alkalic other"; Figure 2-11d, S5). Physical mixing of the three Bradbury endmembers likely occurred during transport to the crater floor.

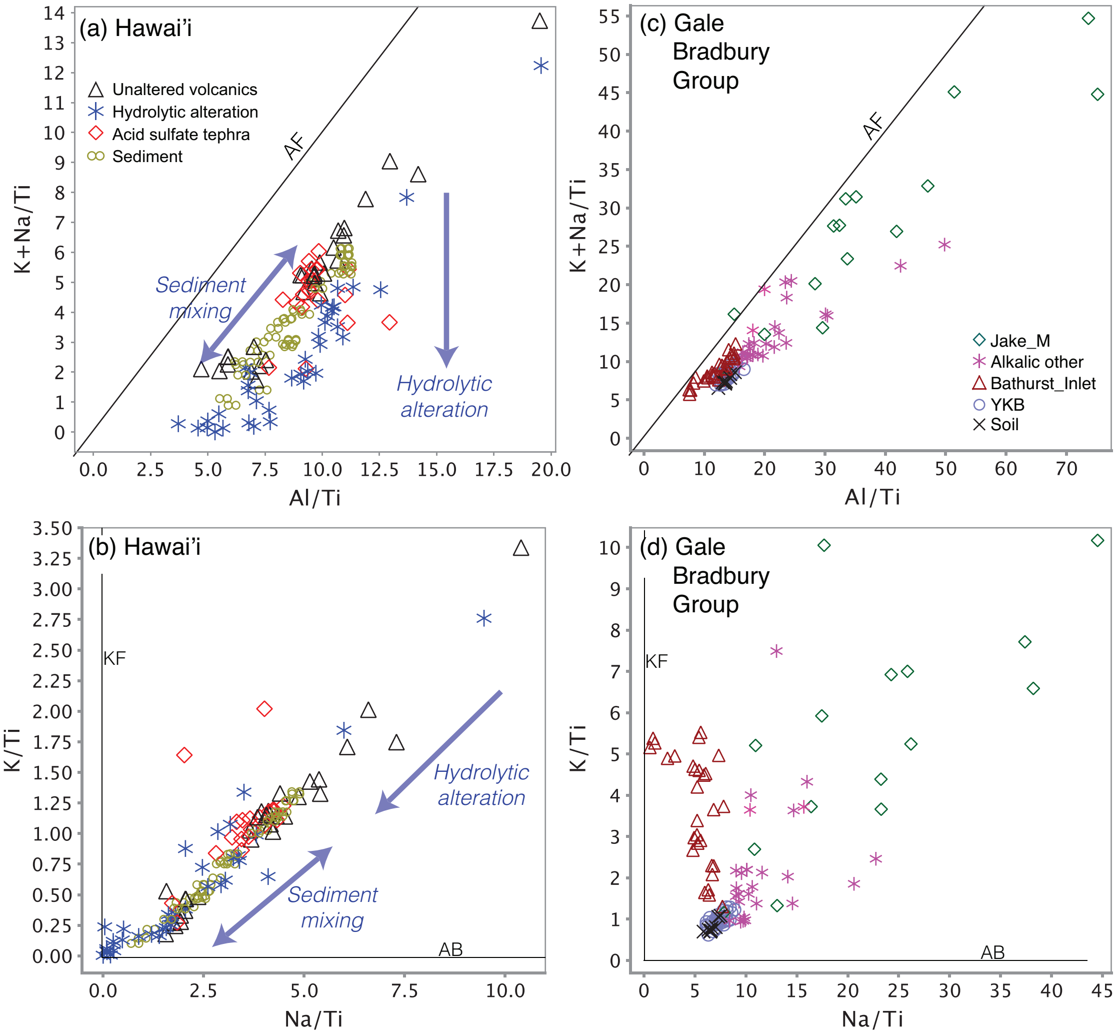

Figure 2-11: Molar alkali plots of (a, b) Hawaiian samples and (c, d) the Bradbury group in Gale. Vectors indicate mixing and alteration trends. Alkali feldspar control lines are shown (AF=alkali feldspar; KF = potassium feldspar; AB=albite). Note the absolute values are not comparable between the two sites because TiO_2 is lower in the Martian samples (Table 1-1). Nevertheless, the relative trends are plausibly compared.

2.5.3. Alteration Trends in the Mount Sharp Group

The most notable geochemical distinction among the Gale dataset is the trend toward high SiO_2 among Mt. Sharp rocks relative to the Bradbury Group (Figures 1-7, 1-8). Silica is elevated relative to average Mars in the Murray bedrock (50-57 wt.%) and to an even higher degree in the Buckskin unit (58-79 wt.%). High SiO_2 concentrations are also observed in light-toned, fracture-associated haloes in both the Stimson and Murray formations (up to 75 wt.%). While having similar chemistries, the link between high silica bedrock and later diagenetic haloes is not well constrained, but below we propose formation processes based on our observations at Hawai'i.

2.5.3.1. Fracture associated haloes

The unambiguous geologic occurrence of fracture-associated, light-toned haloes gives context for high silica (50-75 wt.%) alteration. Haloes are centered on fractures in the bedrock, and are defined by a lightening of the rock tone that decreases with distance from the fracture. They occur in both Murray and Stimson formations, but are limited in occurrence along Curiosity's traverse and not all fractures exhibit them. Haloes were not observed in the Bradbury group. The haloes cross-cut the Stimson/Murray disconformity and therefore formed after the overlying Stimson sandstone was emplaced and lithified. Haloes were investigated by APXS in Murray bedrock (Ferdig and Cody; Figures 2-12) and in detail by APXS and CheMin at two Stimson drill sites (Big Sky/Greenhorn; Okoruso/Lubango). At the Stimson sites, holes were drilled into light-toned rock near the fracture and in darker-toned rock farther from the fracture (< 2 m), effectively sampling the gradient from parent to altered material (Table 1-1). CheMin XRD found that the parent Stimson sandstone targets are composed primarily of basaltic minerals (plagioclase feldspar, pyroxene, magnetite) and X-ray amorphous material, whereas the haloes have reduced pyroxene abundance and a large increase in Ca-sulfates and amorphous silica [*Yen et al.,* 2017]. Multiple interpretations have been proposed for their formation, including acidic alteration [e.g., *Gellert et al.*, 2016; *Schmidt et al.*, 2016; *Yen et al.,* 2017] and simple silica addition by way of chemical precipitation [*Frydenvang et al.*, 2016; *Milliken et al.*, 2016].

Because the parental bedrock is known, we can directly compare its composition to the altered composition to infer halo alteration processes at Mt. Sharp (Figure 2-12). The haloes exhibit silica enrichment accompanied by high SO_3 (9.5-15.1 wt.%), ~2.5x increase in K_2O/MgO, and decreases in Al, Fe, and Mn. Titanium is enriched in Lubango and Cody, but does not change in Greenhorn. Calcium is enriched in the drill targets Greenhorn and Lubango, which is attributed to the formation of the Ca-sulfates detected by CheMin [*Yen et al.,* 2017]. In addition, Ni and Zn, which are soluble and commonly mobile at low pH [*Drever*, 1997], are strongly depleted in the haloes.

Element trends in the haloes are more consistent with trends in the Hawaiian samples that were altered by acid sulfate processes (Figures 2-7b, 2-7c) than those altered by hydrolytic processes (Figures 2-4, 2-6, 2-7a). Enriched SiO_2 and TiO_2 retention with depleted cations are common fingerprints for acidic alteration because the solubility of SiO_2 and TiO_2 remains low in acidic solutions capable of dissolving Fe, Al, Mg, and Zn [e.g., *Squyres et al.*, 2008]. Highly soluble in circumneutral waters, K_2O removed from primary components may be retained by sulfates (K-jarosite) that are stable and insoluble at low pH [e.g., *Lindsay*, 1979].

An alternative explanation for the composition of the haloes is the precipitation of silica and Ca-sulfate from a neutral to alkaline fluid [e.g., *Frydenvang et al.*, 2016; *Milliken et al.*, 2016]. In the simplest form of this process, the addition of silica and sulfate would cause the other components to be reduced proportionally. This is not apparent in the fracture haloes, in which Ti increases and other elements decrease disproportionately [*Gellert et al.*, 2016]. For example, molar K/Mg in altered Hawaiian samples decreases with hydrolytic alteration and increases with acid sulfate alteration (Figure 2-13). An acid sulfate altered rind on basalt from Kilauea exhibits a similar silica and TiO_2 enrichment and cation depletion pattern (decreasing Al, Fe, Mn, Mg, Na) as observed in the Mt. Sharp haloes (Figures 2-12c, 2-16) and also has increasing K/Mg with higher silica. We find the most plausible alteration process to be via acidic fluids.

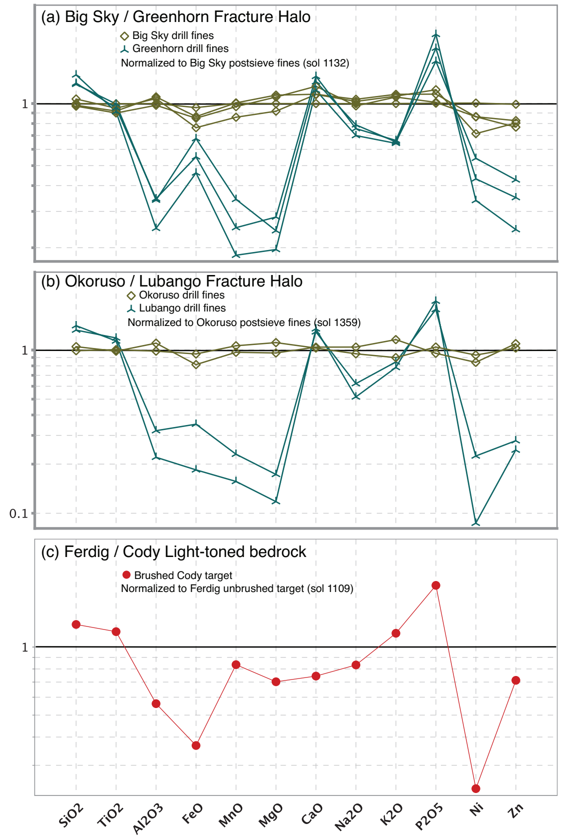

Figure 2-12: APXS results for light-toned haloes associated with fractures at Mt. Sharp, normalized to the adjacent (< 2 m), less altered parent rock. In the Stimson formation, (a) Big Sky and (b) Okoruso are drill targets representing less altered parent, and (a) Greenhorn and (b) Lubango are respective drill targets in the light-toned material. (c) Ferdig and Cody are a paired measurement of darker and lighter toned Murray bedrock, respectively.

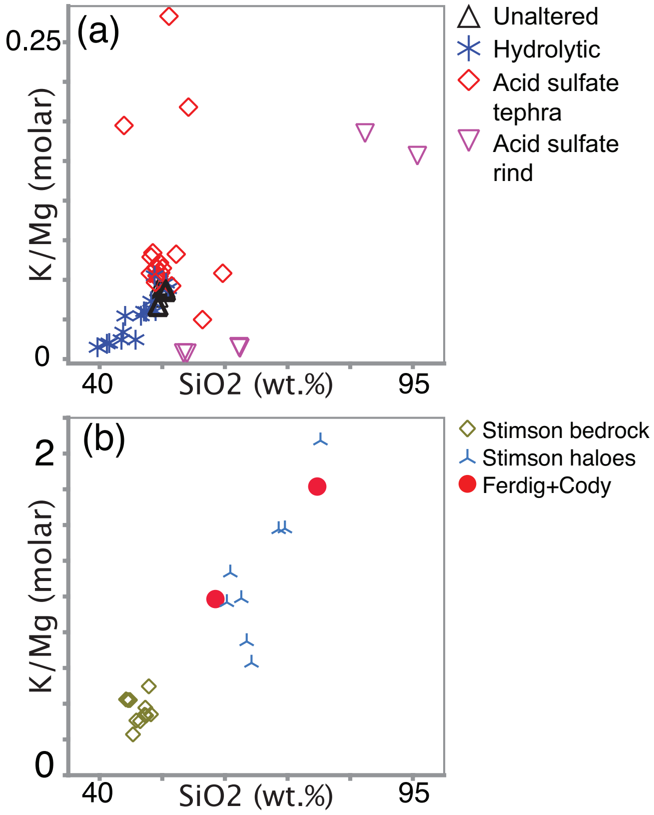

Figure 2-13: Variation of molar K/Mg with silica in (a) Maunakea tephra and Kilauea acid sulfate altered basalt rind and (b) Mt. Sharp fracture associated haloes.

2.5.3.2. Silica enrichment in Murray formation bedrock

The Murray formation bedrock has characteristics similar to the fracture haloes, but differences point to a more complex history. Although the unaltered parent composition of the Murray sediments is unknown, elemental variations can reasonably be compared to average Mars crust, or soil (Figure 2-15). Relative to soil, Murray bedrock has elevated silica, the same or greater TiO_2, K_2O, and P_2O_5, and depleted MnO, MgO, and CaO. The high silica Buckskin unit of Murray has even greater depletions in these elements, as well as lower Al_2O_3 and Na_2O. The silica enrichment and the associated depletion in MgO in Buckskin rocks leads to lower Mg/Si, deviating from mafic/felsic mineral trends in Mg/Si and Al/Si (Figure 2-14). CheMin analyses show variability in Murray mineralogy, but most bedrock, with the exception of Buckskin, consists of ~40% basaltic minerals (plagioclase, pyroxene, < 1% olivine), ~15% opaline silica, and ~15% X-ray amorphous material [*Rampe et al.,* 2017]. Additional components are variable phyllosilicates (0-7%), hematite (1-7%), magnetite (3-8%), and crystalline silica (opal-CT and cristobalite; 0-18%). Jarosite (1-4%) and apatite (~1-2%) are also detectable [*Rampe et al.,* 2017]. Buckskin is unique, containing 25% feldspar and 40% high-Si amorphous material, with a tridymite component (17%) interpreted to have a high temperature volcanic source [*Morris et al.*, 2016].

The silica and TiO_2 enrichment with Mg and Mn depletion is a trend that is consistent with fracture haloes in Gale (Figure 2-12) and the acid sulfate altered samples of Hawai'i (Figures 2-12b, 2-12c), thus, extending the acid sulfate alteration interpretation to the Murray formation bedrock is plausible [e.g., *Gellert et al.*, 2016; *Ming et al.*, 2016; *Rampe et al.,* 2017; *Schmidt et al.*, 2016; *Yen et al.,* 2017]. The Buckskin silica enrichment is partially attributed to the addition of volcanic tridymite; however, because Fe, Mg, and Al are depleted and Ti, K, and P are enriched, simple silica addition alone does not explain the enrichment [*Morris et al.*, 2016]. The presence of jarosite is also a strong indicator of low pH fluids because it precipitates at pH < 4, and commonly coprecipitates with phyllosilicates and hematite in acidic sedimentary systems [e.g., *Baldridge et al.*, 2009]. The geochemical and mineralogical evidence led *Rampe et al.* [2017] to propose a model for the Murray formation in which acidic groundwater interacted with the sediment and mobilized Al, Fe, Mn, Zn, and Ni. Buckskin is leached of these elements, and they precipitated down-section in lower Murray due to buffering by the bedrock, causing Al, Zn, and Ni enrichment (Figure 2-15).

One challenge for the acid sulfate alteration model for Murray is the presence of ~1-2% apatite, which is soluble at low pH and likely would not have been stable. Apatite is the most likely primary P-bearing phase, assuming the Murray parent was basaltic. In the hydrolytic alteration regimes on Hawai'i, P_2O_5 is retained (Figures 2-4, 2-12a), and we interpret this to be due to the low solubility and persistence of apatite in the altered samples, although this is not confirmed; apatite was below the detection limit in most samples. Phosphate is also retained in the acid sulfate altered Maunakea tephra, where primary apatite was likely dissolved, then P reprecipitated in secondary Fe-phosphates with low solubility at low pH [e.g., *Hausrath et al.*, 2013]. If apatite interacted with acidic fluids in the Murray formation sediments, secondary Fe-phosphate would be more stable than apatite. *Berger et al.* [2016b] proposed a mechanism for preserving apatite via the formation of Fe-phosphate armor around apatite grains that prevented complete dissolution [e.g., *Johnson and Hallberg*, 2005]. We propose an alternative explanation, whereby apatite occurs as inclusions in plagioclase feldspar, which is sufficiently resistant to acidic alteration that it could have protected the apatite from dissolution. Apatite occurs as acicular inclusions in olivine and plagioclase in Kohala and Maunakea lavas. Plagioclase is also apparent in thin sections and XRD patterns in jarosite- and alunite-rich tephra on Maunakea, although those samples did not contain apatite inclusions in plagioclase. Apatite occurs in maskelynite as inclusions in Martian meteorites [*McCubbin and Nekvasil*, 2015], and as clasts in less-shocked Martian meteorite NWA 7034 [McCubbin et al. 2016], so it is possible that the primary apatite in Murray bedrock was within inclusions, and was ‘armored’ in acidic solutions.

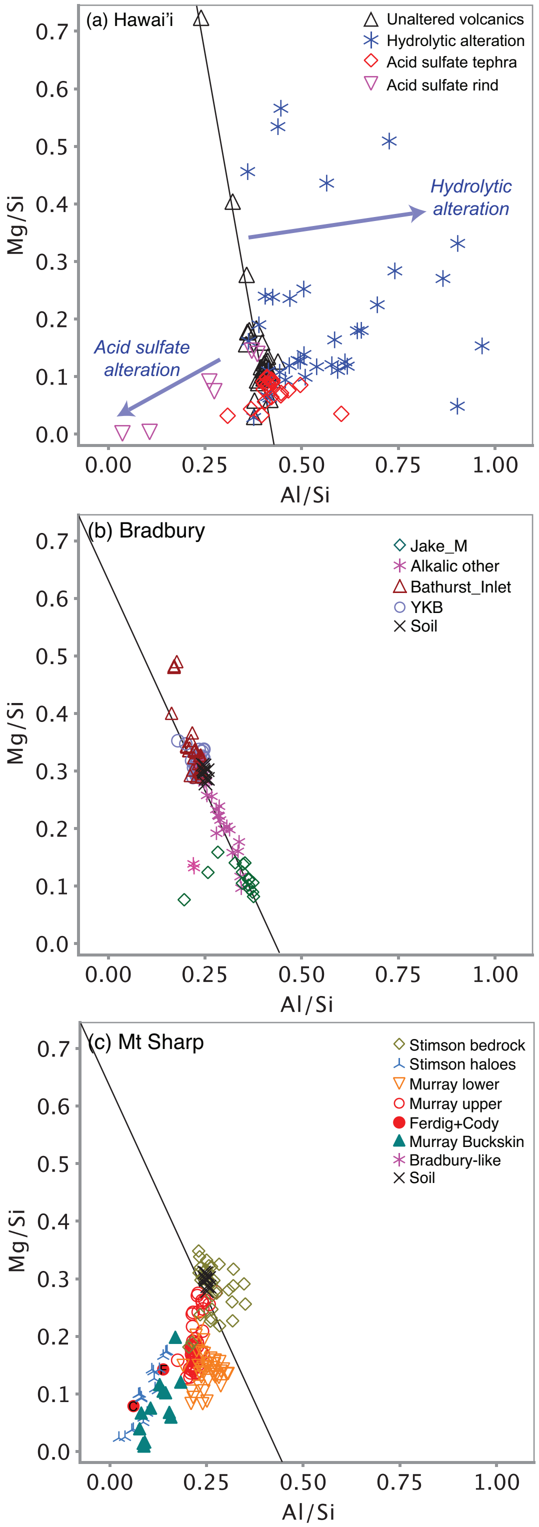

Figure 2-14: Variation of Mg/Si and Al/Si at (a) Hawai'i and (b, c) Gale. Lines indicate a mafic/felsic igneous trend; deviation from this trend is consistent with open system alteration (arrows).

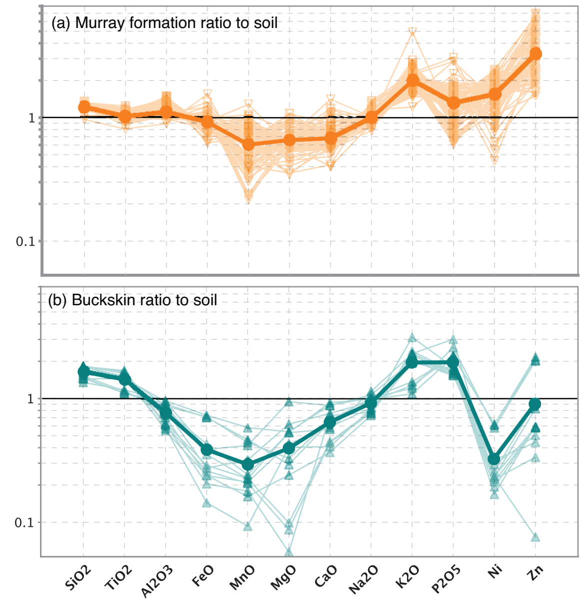

Figure 2-15: APXS results normalized to average Mars (soil) for (a) Murray formation bedrock and (b) the Buckskin unit within the Murray formation. Bold lines denote mean values and light lines denote individual targets.

2.6. Conclusion

Maunakea and Kohala represent a unique opportunity to investigate relative contributions of igneous, sedimentary, and aqueous alteration processes that are analogous to those that affected rocks observed by *Curiosity* in Gale Crater on Mars. Chemical and mineralogical compositions at the two sites overlap over a wide range of basaltic and alkalic rocks, with remarkably similar mugearitic compositions shared by the Laupahoehoe Volcanics of Maunakea and the Jake_M class in Gale Crater. The large precipitation gradient across Hawai'i resulted in a wide range of pedogenic weathering rates, enabling the comparison of incipient through extensive weathering in rocks with the same compositions. Volcanic activity also caused acid sulfate and palagonitic alteration, illustrating element mobility and secondary mineralogy under different fluid conditions. Sedimentary processes on Maunakea, although on a smaller scale than Gale Crater (~1/6), also demonstrate trends in provenance resulting from the mixing of the two parent lithologies.

By comparison to the observations at Maunakea and Kohala, we evaluated interpretations for sedimentary bedrock compositions in Gale Crater. The Bradbury group is consistent with a physical mixture of detritus from multiple igneous lithologies, including basaltic and mugearitic as found at Maunakea, but additionally containing a potassic basalt component. These Gale rocks lack the element mobility indicative of open system hydrolytic and acid sulfate alteration found on Hawai'i, and are thus minimally and/or isochemically altered. High silica rocks in the Mt. Sharp group have element mobilities and mineralogies most consistent with the acid sulfate altered material at Hawai'i, and we interpret this to be evidence of extensive acid sulfate alteration in the Murray formation bedrock, and localized acid sulfate alteration along Stimson formation fractures.

2.7. References

Baldridge, A. M., S. J. Hook, J. K. Crowley, G. M. Marion, J. S. Kargel, J. L. Michalski, B. J. Thomson, C. R. de Souza Filho, N. T. Bridges, and A. J. Brown (2009), Contemporaneous deposition of phyllosilicates and sulfates: Using Australian acidic saline lake deposits to describe geochemical variability on Mars, *Geophys. Res. Lett.*, *36*(19), doi:10.1029/2009GL040069.

Bell, J. F., R. V. Morris, and J. B. Adams (1993), Thermally altered palagonitic tephra: A spectral and process analog to the soil and dust of Mars, *Journal of Geophysical Research: Planets*, *98*(E2), 3373–3385, doi:10.1029/92JE02367.

Berger, J. A., M. E. Schmidt, M. R. M. Izawa, R. Gellert, D. W. Ming, E. B. Rampe, S. J. VanBommel, and A. C. McAdam (2016b), Phosphate Stability in Diagenetic Fluids Constrains the Acidic Alteration Model for Lower Mt. Sharp Sedimentary Rocks in Gale Crater, Mars, in *Lunar Planet. Sci. Conf. 47*, p. Abstract 1652.

Bishop, J. L., P. Schiffman, and R. Southard (2002), Geochemical and mineralogical analyses of palagonitic tuffs and altered rinds of pillow basalts in Iceland and applications to Mars, *Geological Society, London, Special Publications*, *202*(1), 371–392, doi:10.1144/GSL.SP.2002.202.01.19.

Capo, R. C., C. E. Whipkey, J. R. Blachère, and O. A. Chadwick (2000), Pedogenic origin of dolomite in a basaltic weathering profile, Kohala peninsula, Hawaii, *Geology*, *28*(3), 271–274, doi:10.1130/0091-7613(2000)28<271:POODIA>2.0.CO;2.

Collinet, M., E. Médard, B. Charlier, J. Vander Auwera, and T. L. Grove (2015), Melting of the primitive Martian mantle at 0.5–2.2 GPa and the origin of basalts and alkaline rocks on Mars, *Earth and Planetary Science Letters*, *427*, 83–94.

Colman, S. M. (1982), *Chemical weathering of basalts and andesites; evidence from weathering rinds*, Professional Paper, USGS Numbered Series, U.S. G.P.O.

Cornell, R. M., and U. Schwertmann (2006), *The iron oxides: structure, properties, reactions, occurrences and uses*, John Wiley & Sons.

Drever, J. I. (1997), *The Geochemistry of Natural Waters: Surface and Groundwater Environments*, 3rd ed., Prentice Hall.

Eggleton, R. A., C. Foudoulis, and D. Varkevisser (1987), Weathering of basalt: changes in rock chemistry and mineralogy, *Clays and Clay Minerals*, *35*(3), 161–169.

Ehlmann, B. L., D. L. Bish, S. W. Ruff, and J. F. Mustard (2012), Mineralogy and chemistry of altered Icelandic basalts: Application to clay mineral detection and understanding aqueous environments on Mars, *Journal of Geophysical Research: Planets*, *117*(E10), n/a–n/a, doi:10.1029/2012JE004156.

Farr, T. G., and J. B. Adams (1984), Rock coatings in Hawaii, *Geological Society of America Bulletin*, *95*(9), 1077–1083, doi:10.1130/0016-7606(1984)95<1077:RCIH>2.0.CO;2.

Frydenvang, J. et al. (2016), Discovery of Silica-Rich Lacustrine and Eolian Sedimentary Rocks in Gale Crater, Mars, in *Lunar Planet. Sci. Conf. 47*, p. Abstract 2349.

Gay, P., and R. W. LeMaitre (1961), Some observations on iddingsite, *American Mineralogist*, *46*(1–2), 92–111.

Gellert, R. et al. (2016), Chemical Evidence for an Episode of Acidic Leaching at the Base of Mount Sharp, Gale Crater, Mars, as seen by the APXS, in *Lunar Planet. Sci. Conf. 47*, p. Abstract 2368.

Gislason, S. R., S. Arnorsson, and H. Armannsson (1996), Chemical weathering of basalt in Southwest Iceland; effects of runoff, age of rocks and vegetative/glacial cover, *Am J Sci*, *296*(8), 837–907, doi:10.2475/ajs.296.8.837.

Grotzinger, J. P. et al. (2014), A Habitable Fluvio-Lacustrine Environment at Yellowknife Bay, Gale Crater, Mars, *Science*, *343*(6169), 1242777, doi:10.1126/science.1242777.

Grotzinger, J. P. et al. (2015), Deposition, exhumation, and paleoclimate of an ancient lake deposit, Gale crater, Mars, *Science*, *350*(6257), aac7575, doi:10.1126/science.aac7575.

Hadnott, B. A., B. L. Ehlmann, and B. L. Jolliff (2017), Mineralogy and chemistry of San Carlos high-alkali basalts: Analyses of alteration with application for Mars exploration, *American Mineralogist*, *102*(2), 284–301, doi:10.2138/am-2017-5608.

Hamilton, V. E., R. V. Morris, J. E. Gruener, and S. A. Mertzman (2008), Visible, near-infrared, and middle infrared spectroscopy of altered basaltic tephras: Spectral signatures of phyllosilicates, sulfates, and other aqueous alteration products with application to the mineralogy of the Columbia Hills of Gusev Crater, Mars, *J. Geophys. Res.*, *113*, 30 PP., doi:200810.1029/2007JE003049.

Hausrath, E. M., and S. L. Brantley (2010), Basalt and olivine dissolution under cold, salty, and acidic conditions: What can we learn about recent aqueous weathering on Mars?, *Journal of Geophysical Research: Planets*, *115*(E12), n/a–n/a, doi:10.1029/2010JE003610.

Hausrath, E. M., and O. Tschauner (2013), Natural Fumarolic Alteration of Fluorapatite, Olivine, and Basaltic Glass, and Implications for Habitable Environments on Mars, *Astrobiology*, *13*(11), 1049–1064, doi:10.1089/ast.2013.0985.

Hausrath, E. M., A. K. Navarre-Sitchler, P. B. Sak, C. I. Steefel, and S. L. Brantley (2008), Basalt weathering rates on Earth and the duration of liquid water on the plains of Gusev Crater, Mars, *Geology*, *36*(1), 67–70, doi:10.1130/G24238A.1.

Hausrath, E. M., D. C. Golden, R. V. Morris, D. G. Agresti, and D. W. Ming (2013), Acid sulfate alteration of fluorapatite, basaltic glass and olivine by hydrothermal vapors and fluids: Implications for fumarolic activity and secondary phosphate phases in sulfate-rich Paso Robles soil at Gusev Crater, Mars, *J. Geophys. Res. Planets*, *118*(1), 1–13, doi:10.1029/2012JE004246.

Herdianita, N. R., K. A. Rodgers, and P. R. L. Browne (2000), Routine instrumental procedures to characterise the mineralogy of modern and ancient silica sinters, *Geothermics*, *29*(1), 65–81, doi:10.1016/S0375-6505(99)00054-1.

Johnson, D. B., and K. B. Hallberg (2005), Acid mine drainage remediation options: a review, *Science of The Total Environment*, *338*(1–2), 3–14, doi:10.1016/j.scitotenv.2004.09.002.

Johnson, D. M., P. R. Hooper, R. M. Conrey, and G. Laboratory (1999), XRF analysis of rocks and minerals for major and trace elements on a single low dilution Li-tetraborate fused bead, in *Advances in X-ray Analysis, v, 41, p. 843–867 Le Bas, M.J*, pp. 745–750.

Kurtz, A. C., L. A. Derry, and O. A. Chadwick (2002), Germanium-silicon fractionation in the weathering environment, *Geochim. Cosmochim. Acta*, *66*(9), 1525–1537, doi:10.1016/S0016-7037(01)00869-9.

Lanphere, M. A., and F. A. Frey (1987), Geochemical evolution of Kohala volcano, Hawaii, *Contributions to Mineralogy and Petrology*, *95*(1), 100–113.

Le Deit, L. L., E. Hauber, F. Fueten, M. Pondrelli, A. P. Rossi, and R. Jaumann (2013), Sequence of infilling events in Gale Crater, Mars: Results from morphology, stratigraphy, and mineralogy, *J. Geophys. Res. Planets*, *118*(12), 2012JE004322, doi:10.1002/2012JE004322.

Lindsay, W. L. (1979), *Chemical equilibria in soils*, Wiley.

McCubbin, F. M., and H. Nekvasil (2015), Maskelynite-hosted apatite in the Chassigny meteorite: Insights into late-stage magmatic volatile evolution in martian magmas, *American Mineralogist*, *93*(4), 676–684, doi:10.2138/am.2008.2558.

McLennan, S. M. et al. (2013), Elemental Geochemistry of Sedimentary Rocks at Yellowknife Bay, Gale Crater, Mars, *Science*, 1244734, doi:10.1126/science.1244734.

Milliken, R. E., J. A. Hurowitz, D. L. Bish, J. P. Grotzinger, and R. Wiens (2016), The Chemical and Mineralogical Stratigraphy of Lower Mt. Sharp: Relating Rover Observations to Orbital Predictions, vol. 47, p. 1495.

Ming, D. W., A. S. Yen, R. Gellert, B. Sutter, J. A. Berger, L. M. Thompson, M. E. Schmidt, R. V. Morris, and A. H. Treiman (2016), Elemental Gains/Losses Associated with Alteration Fractures in an Eolian Sandstone, Gale Crater, Mars, in *AGU Fall Meeting*, vol. P11B–1860, p. P11B–1860.

Minitti, M., C. Weitz, M. Lane, and J. Bishop (2007), Morphology, chemistry, and spectral properties of Hawaiian rock coatings and implications for Mars, *J. Geophys. Res.*, *112*(E5), E05015, doi:10.1029/2006JE002839.

Morris, R. V., T. Graff, M. D. Lane, D. C. Golden, C. S. Schwandt, T. D. S. D. W. Ming, S. A. Mertzman, J. F. Bell III, J. Crisp, and P. R. Christensen (2000a), Acid Sulfate Alteration Products of a Tholeiitic Basalt: Implications for Interpretation of Martian Thermal Emission Spectra, in *Lunar and Planetary Science Conference*, vol. 31, p. 2014.

Morris, R. V. et al. (2000b), Mineralogy, composition, and alteration of Mars Pathfinder rocks and soils: Evidence from multispectral, elemental, and magnetic data on terrestrial analogue, SNC meteorite, and Pathfinder samples, *J. Geophys. Res.*, *105*(E1), 1757–1817, doi:10.1029/1999JE001059.

Morris, R. V., D. C. Golden, D. W. Ming, T. D. Shelfer, L. C. Jorgensen, J. F. Bell, T. G. Graff, and S. A. Mertzman (2001), Phyllosilicate-poor palagonitic dust from Mauna Kea Volcano (Hawaii); a mineralogical analogue for magnetic Martian dust?, *Journal of Geophysical Research*, *106*(E3), 5057–5083, doi:http://dx.doi.org.proxy1.lib.uwo.ca/10.1029/2000JE001328.

Morris, R. V. et al. (2016), Silicic volcanism on Mars evidenced by tridymite in high-SiO2 sedimentary rock at Gale crater, *PNAS*, *113*(26), 7071–7076, doi:10.1073/pnas.1607098113.

Nakamura, M. T. (Martha T., G. D. (George D. Sherman, and 1904- (1965), Genesis of halloysite and gibbsite from mugearite on the island of Maui,

Nesbitt, H. W., and R. E. Wilson (1992), Recent chemical weathering of basalts, *Am J Sci*, *292*(10), 740–777, doi:<p>10.2475/ajs.292.10.740</p>.

Nesbitt, H. W., and G. M. Young (1982), Early Proterozoic climates and plate motions inferred from major element chemistry of lutites, *Nature*, *299*(5885), 715–717.

Óskarsson, B. V., M. S. Riishuus, and Ó. Arnalds (2012), Climate-dependent chemical weathering of volcanic soils in Iceland, *Geoderma*, *189–190*, 635–651, doi:10.1016/j.geoderma.2012.05.030.

Pokrovsky, O. S., J. Schott, D. I. Kudryavtzev, and B. Dupré (2005), Basalt weathering in Central Siberia under permafrost conditions, *Geochimica et Cosmochimica Acta*, *69*(24), 5659–5680, doi:10.1016/j.gca.2005.07.018.

Poppe, L. J., V. F. Paskevich, J. C. Hathaway, and D. S. Blackwood (2000), *A Laboratory Manual for X-Ray Powder Diffraction*, U.S. Geologic Survey Open-File Report, U. S. Geological Survey Open-File Report, U.S. Geological Survey, Coastal and Marine Geology Team, Woods Hole Field Center, Woods Hole, MA.

Porter, S. C. (1979), Quaternary Stratigraphy and Chronology of Mauna Kea, Hawaii: A 380,000-yr Record of Mid-Pacific Volcanism and Ice-Cap Glaciation, *Geological Society of America Bulletin*, *90*(7 Part II), 980–1093, doi:10.1130/GSAB-P2-90-980.

Porter, S. C. (1997), Late Pleistocene Eolian Sediments Related to Pyroclastic Eruptions of Mauna Kea Volcano, Hawaii, *Quaternary Research*, *47*(3), 261–276, doi:10.1006/qres.1997.1892.

Rampe, E. B. et al. (2017), Mineralogy of an ancient lacustrine mudstone succession from the Murray formation, Gale crater, Mars, *Earth and Planetary Science Letters*, doi:10.1016/j.epsl.2017.04.021.

Salvatore, M. R., J. F. Mustard, J. W. Head, R. F. Cooper, D. R. Marchant, and M. B. Wyatt (2013), Development of alteration rinds by oxidative weathering processes in Beacon Valley, Antarctica, and implications for Mars, *Geochimica et Cosmochimica Acta*, *115*, 137–161, doi:10.1016/j.gca.2013.04.002.

Sara, M. J., I. Uksins Peate, M. S. Riishuus, R. A. Yingst, M. E. Schmidt, J. A. Berger, and T. Hartsock (2017), Askja Sand Sheet, Iceland, as a Depositional Analog for the Stimson Fm. in Gale Crater, Mars, vol. 48, p. 2638.

Schiffman, P., R. J. Southard, D. D. Eberl, and J. L. Bishop (2002), Distinguishing palagonitized from pedogenically-altered basaltic Hawaiian tephra: mineralogical and geochemical criteria, *Geological Society, London, Special Publications*, *202*(1), 393–405, doi:10.1144/GSL.SP.2002.202.01.20.

Schiffman, P., R. Zierenberg, N. Marks, J. L. Bishop, and M. D. Dyar (2006), Acid-fog deposition at Kilauea volcano: A possible mechanism for the formation of siliceous-sulfate rock coatings on Mars, *Geology*, *34*(11), 921–924, doi:10.1130/G22620A.1.

Schmidt, M. E., J. A. Berger, D. Blaney, R. Gellert, J. P. Grotzinger, O. Forni, P. L. King, and N. Mangold (2014a), Geochemical Classification of Rocks in Gale Crater with APXS to Sol 360: Sediment Provenance, Mixing, and Diagenetic Processes, in *Lunar Planet. Sci., XLV*, p. Abstract 1504.

Schmidt, M. E. et al. (2014b), Geochemical diversity in first rocks examined by the Curiosity Rover in Gale Crater: Evidence for and significance of an alkali and volatile-rich igneous source, *J. Geophys. Res. Planets*, *119*(1), 64–81, doi:10.1002/2013JE004481.

Schmidt, M. E., N. Mangold, M. Fisk, O. Forni, S. McLennan, D. W. Ming, D. Sumner, V. Sautter, A. J. Williams, and R. Gellert (2015), Classification Scheme for Diverse Sedimentary and Igneous Rocks Encountered by MSL in Gale Crater, in *Lunar and Planetary Science Conference*, 16-20 Mar. 2015, United States.

Schmidt, M. E., J. A. Berger, R. Gellert, M. R. M. Izawa, D. W. Ming, L. Thompson, E. Desouza, M. Fisk, and G. Perrett (2016), APXS Classification of Lower Mount Sharp Bedrock: Silica Enrichment and Acid Alteration, in *Lunar Planet. Sci. Conf. 47*, p. Abstract 2043.

Seelos, K. D., R. E. Arvidson, B. L. Jolliff, S. M. Chemtob, R. V. Morris, D. W. Ming, and G. A. Swayze (2010), Silica in a Mars analog environment: Ka'u Desert, Kilauea Volcano, Hawaii, *Journal of Geophysical Research: Planets (1991–2012)*, *115*(E4).

Siebach, K. L., M. B. Baker, J. P. Grotzinger, S. M. McLennan, R. Gellert, L. M. Thompson, and J. A. Hurowitz (2017), Sorting out Compositional Trends in Sedimentary Rocks of the Bradbury Group (Aeolus Palus), Gale Crater, Mars, *Journal of Geophysical Research: Planets*.

Smith, K. L., A. R. Milnes, and R. A. Eggleton (1987), Weathering of basalt: formation of iddingsite, *Clays and Clay Minerals*, *35*(6), 418–428.

Spengler, S. R., and M. O. Garcia (1988), Geochemistry of the Hawi lavas, Kohala volcano, Hawaii, *Contributions to Mineralogy and Petrology*, *99*(1), 90–104.

Squyres, S. W. et al. (2008), Detection of Silica-Rich Deposits on Mars, *Science*, *320*(5879), 1063–1067, doi:10.1126/science.1155429.

Stolper, E. M. et al. (2013), The Petrochemistry of Jake_M: A Martian Mugearite, *Science*, *341*(6153), 1239463, doi:10.1126/science.1239463.

Thompson, L. M. et al. (2016), Potassium-rich sandstones within the Gale impact crater, Mars: The APXS perspective, *J. Geophys. Res. Planets*, 2016JE005055, doi:10.1002/2016JE005055.

Treiman, A. H., and E. Medard (2016), MANTLE METASOMATISM IN MARS: POTASSIC BASALTIC SANDSTONE IN GALE CRATER DERIVED FROM PARTIAL MELT OF PHLOGOPITE-PERIDOTITE. Presented at Geological Society of America annual meeting, 2016.

Treiman, A. H. et al. (2016), Mineralogy, provenance, and diagenesis of a potassic basaltic sandstone on Mars: CheMin X-ray diffraction of the Windjana sample (Kimberley area, Gale Crater), *J. Geophys. Res. Planets*, *121*(1), 2015JE004932, doi:10.1002/2015JE004932.

VanBommel, S. J., R. Gellert, J. A. Berger, J. L. Campbell, L. M. Thompson, K. S. Edgett, M. J. McBride, M. E. Minitti, I. Pradler, and N. I. Boyd (2016), Deconvolution of distinct lithology chemistry through oversampling with the Mars Science Laboratory Alpha Particle X-Ray Spectrometer, *X-Ray Spectrom.*, doi:10.1002/xrs.2681.

Vaniman, D. T. et al. (2014), Mineralogy of a Mudstone at Yellowknife Bay, Gale Crater, Mars, *Science*, *343*(6169), 1243480, doi:10.1126/science.1243480.

Wolfe, E. W., and J. Morris (1996), *Geologic map of the Island of Hawaii*, IMAP, USGS Numbered Series.

Wolfe, E. W., W. S. Wise, and G. B. Dalrymple (1997), The Geology and Petrology of Mauna Kea Volcano, Hawaii: A Study of Postshield Volcanism, *US Geological Survey professional paper*, (1557), 1–129.

Yen, A. S. et al. (2017), Multiple stages of aqueous alteration along fractures in mudstone and sandstone strata in Gale Crater, Mars, *Earth and Planetary Science Letters*, doi:10.1016/j.epsl.2017.04.033.

Yesavage, T., A. Thompson, E. M. Hausrath, and S. L. Brantley (2015), Basalt weathering in an Arctic Mars-analog site, *Icarus*, *254*, 219–232, doi:10.1016/j.icarus.2015.03.011.

Yingst, R. A., K. S. Edgett, M. McBride, M. E. Minitti, K. Stack, and W. Goetz (2015), Sedimentary Early Mars Revealed at the Microscale: The Gale Crater Example, in *Lunar Planet. Sci. Conf. 46*, p. Abstract 1378.

2.8. Supplemental Materials

Supplementary information is presented in Figures 2-S1 through 2-S5 below.

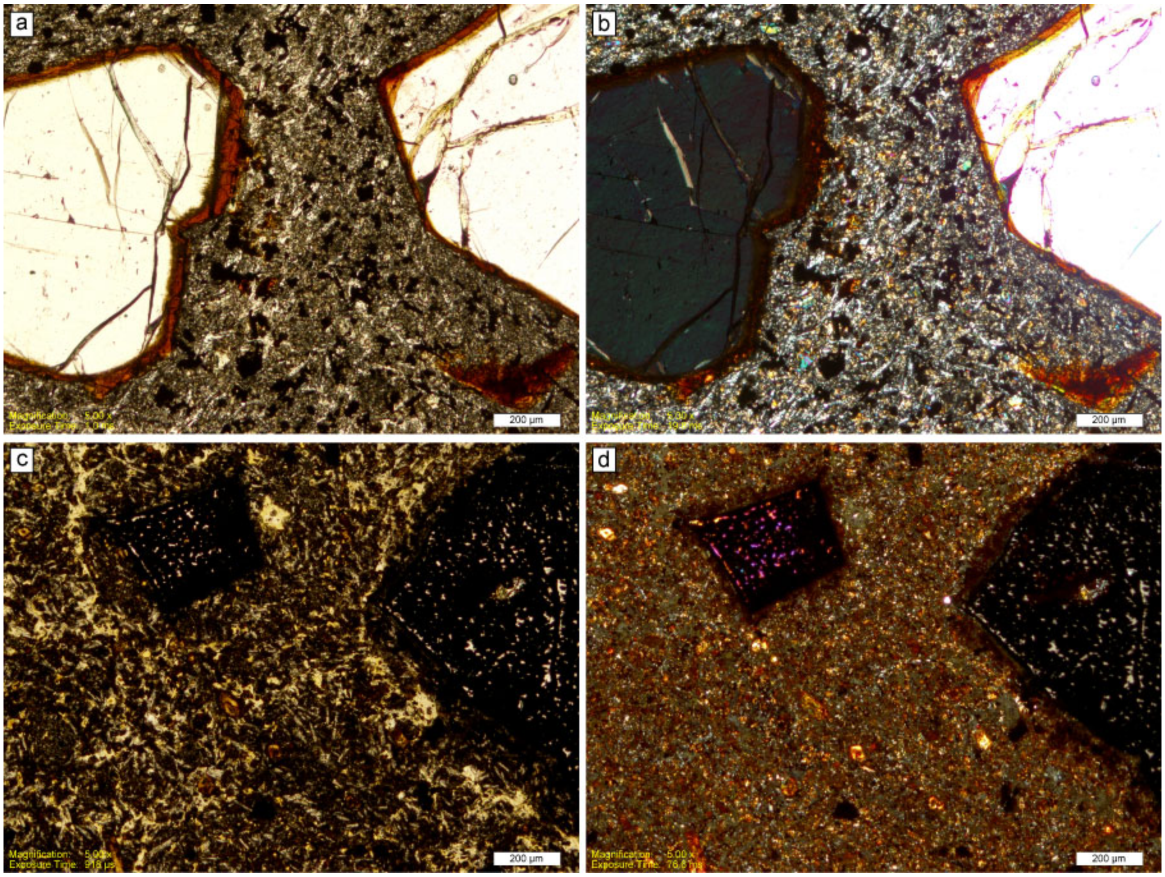

Figure 2-S1: Representative thin section micrographs showing progressive weathering in a Hamakua basalt profile (site MK15-37). (a) Incipient alteration begins with red rims around olivine (ol) due to iddingsite formation. (b) With crossed polarizers, plagioclase is birefringent and preserves an igneous texture. (c) Plane polarized and (d) cross polarized images of a moderate to highly weathered basalt. Olivine crystals have altered to Fe-Ti spinel pseudomorphs, preserving olivine birefringence within a swiss cheese texture. Most plagioclase grains maintain primary textures, but are altered such that they are isotropic.

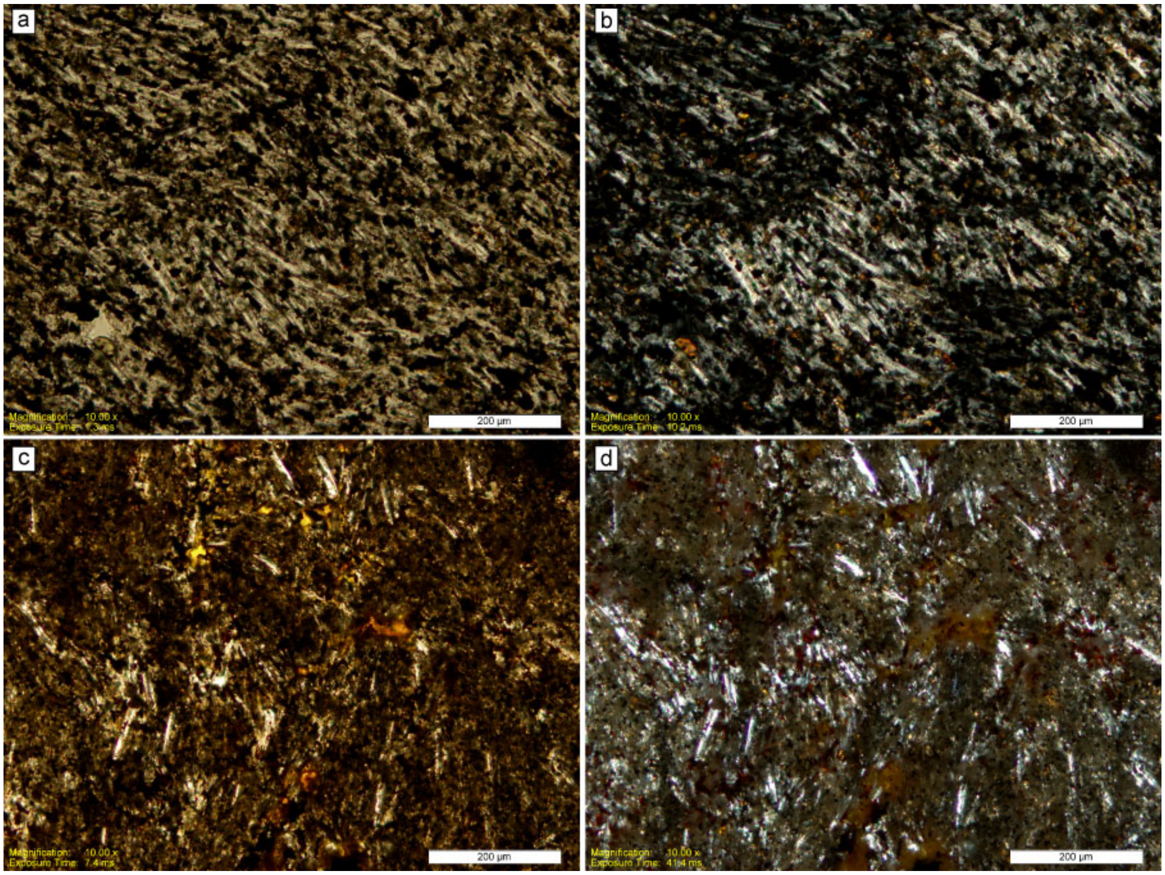

Figure 2-S2: Incipient weathering of a Laupahoehoe benmoreite (site MK15-35). (a) Plane polarized and (b) cross polarized images of unaltered benmoreite (35a) shows the typical trachytic texture and abundant salt and pepper oxides. (c) Plane polarized and (d) cross polarized images of an incipiently altered benmoreite (MK15-35b) shows red staining associated with the oxides and some fine-grained clay-like texture. Compare with the bulk composition of these two rocks (Figure 2-6; Appendix 2-1), which indicate only minimal leaching of K_2O and SiO_2.

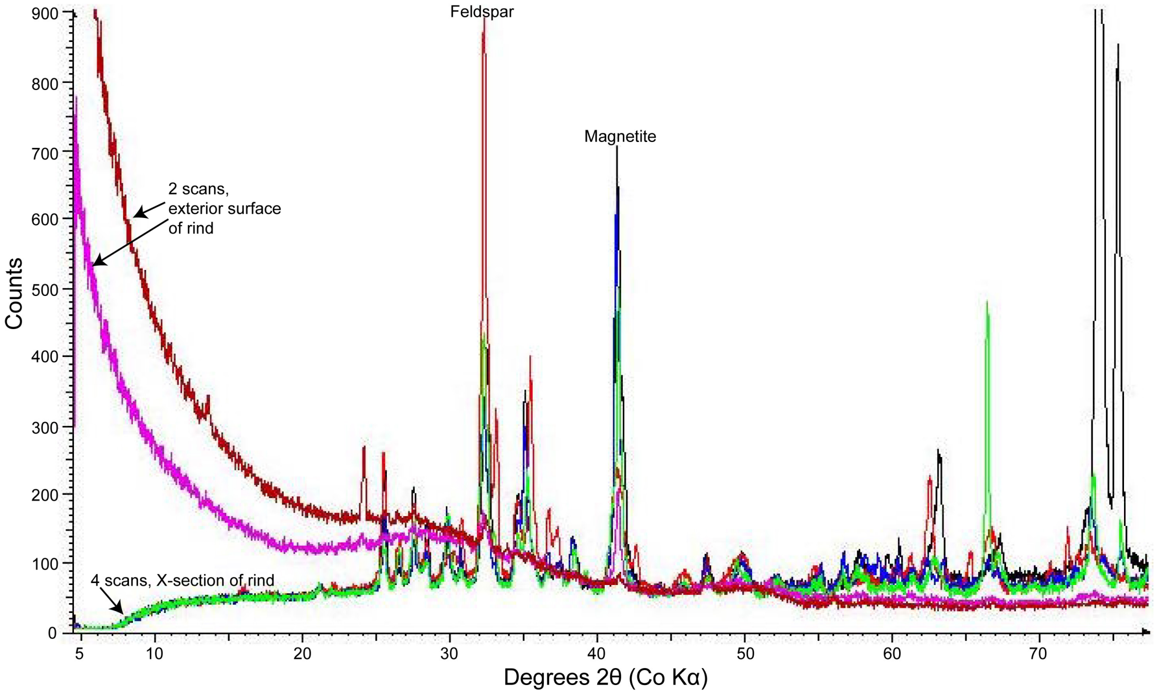

Figure 2-S3: Representative μXRD line scans showing a transect over a thin, incipient weathering rind of a mugearite (MK15-61B). The interior of the rock has varying relative amounts of magnetite and plagioclase feldspar, evident in inverse peak intensities at the feldspar line at 32.2° 2θ and magnetite peak at 41.5° 2θ. High intensity peaks at 66.5°, 74°, and 75.5 ° 2θ correspond with preferred orientation spots on the 2d pattern. The top exterior surface of the rind is X-ray amorphous with a large low 2θ background (possibly allophane) and broad amorphous silica hump (20-35° 2θ).

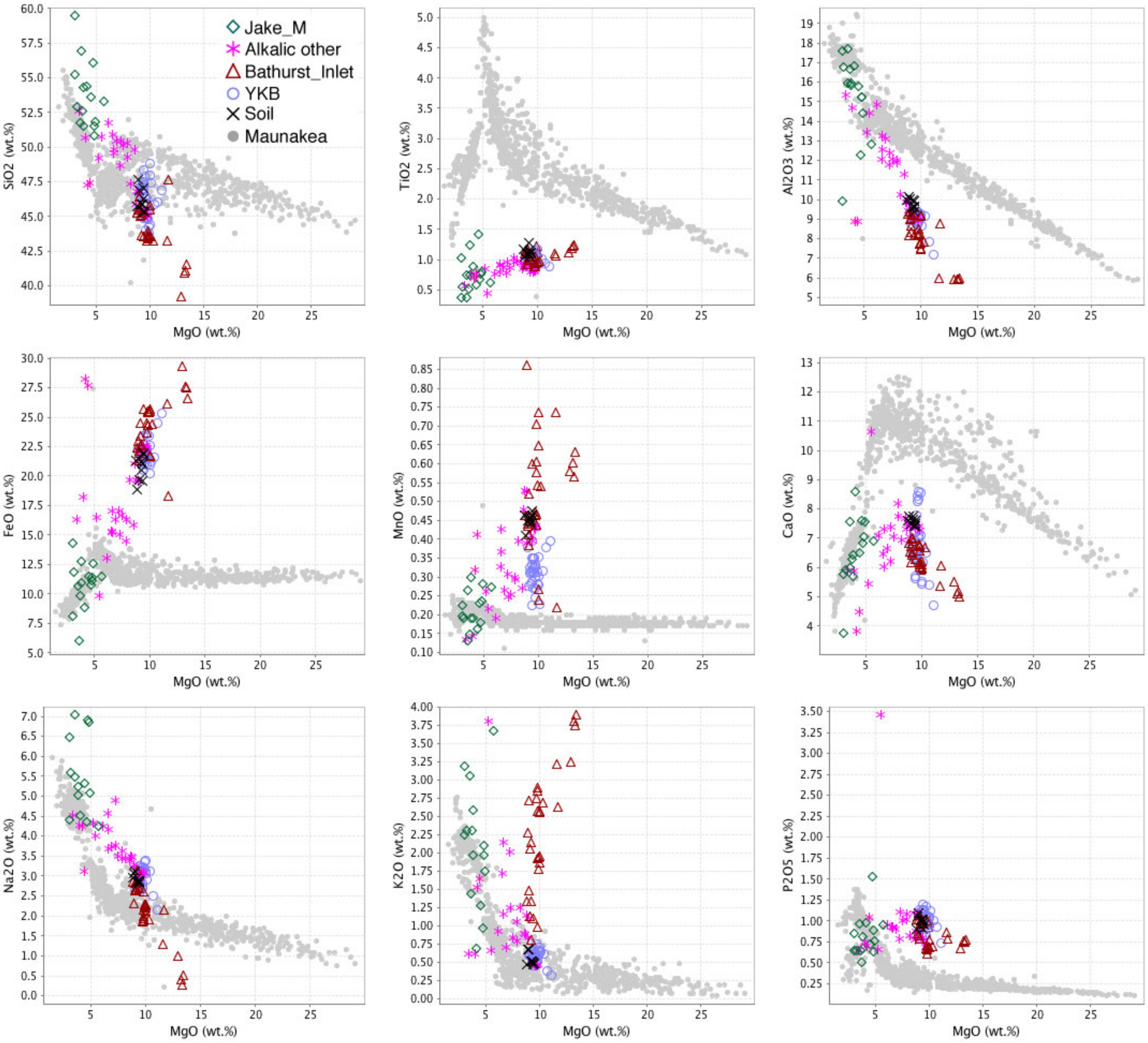

Figure 2-S4: MgO variation diagrams for fresh Maunakea whole rock volcanics (Georoc database) and the Bradbury group in Gale Crater. The Jake_M class overlaps in composition with the low MgO Laupahoehoe mugearites in all major and minor oxides except for TiO_2.

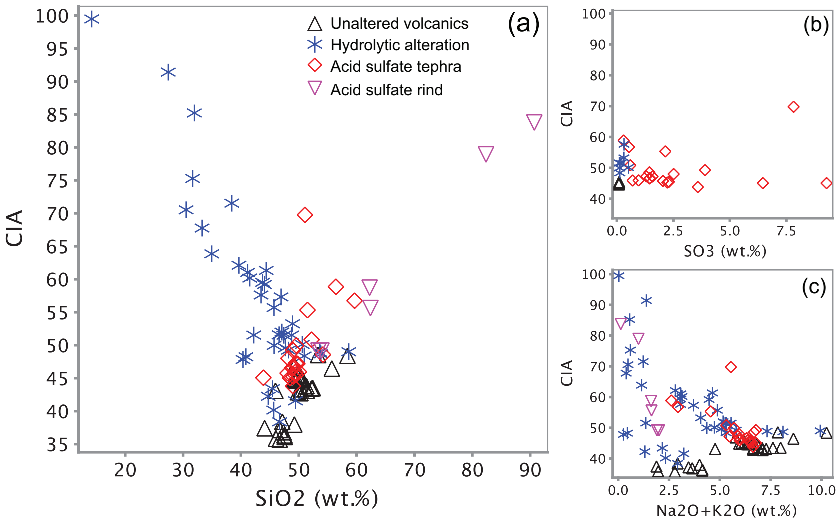

Figure 2-S5: Evaluation of CIA suitability as an indicator for alteration at Maunakea. (a) CIA increases regularly with progressive hydrolytic alteration and acid sulfate alteration in the rind from Kilauea. This is because, in circumneutral, low temperature waters, the elements K, Na, and Ca are soluble but Al is not [*Nesbitt and Young*, 1982]. However, CIA varies in the acid sulfate tephra. (b) Acid sulfate alteration of tephra with addition of sulfates and (c) retention of alkalis in sulfates can lead to highly altered materials without a predictable increase in CIA. CIA is not an appropriate indicator for alteration in all acid-sulfate systems, where retention of cations (K, Na, Ca) in secondary phases, and increased solubility of Al, invalidates the CIA assumptions (i.e., silicate components without secondary salts).

Chapter 3

3. Particle Induced X-ray Spectrometry of Hawaiian Materials: An APXS Analogue Study

3.1. Introduction

The Alpha Particle X-ray Spectrometer (APXS), a rover-based instrument used for measuring the chemical composition of Martian samples on the surface of Mars, is a combination of Particle Induced X-ray Emission spectrometry (PIXE) and X-ray Fluorescence spectrometry (XRF) [*Rieder et al.*, 2003; *Gellert et al.*, 2006, 2009]. Employing laboratory XRF analyses as an analogue for APXS on Mars is useful because XRF is sufficiently accurate [*Johnson et al.*, 1999] to make interpretations for analogue geologic materials on Earth that are relevant to Mars (see Chapter 2). However, differences in sample preparation and the physics of sample interrogation can lead to different results for XRF and APXS of the same material [*Campbell et al.*, 2009, 2011, 2012]. We thus turn to PIXE as a potential APXS analogue.

Micro-beam PIXE is well-established as an accurate (~1%) analytical method for geologic materials [e.g., *Johansson et al.*, 1995]; however, studies of geologic materials by broad beam PIXE methods are limited [*Flannigan and Campbell*, 2017]. Broad beam PIXE is better than micro-beam PIXE as an APXS analogue because it integrates the X-ray signal from a larger, more comparable area on the sample. The APXS interrogates a roughly circular area ~1.5 – 2.0 cm in diameter; broad beam PIXE typically interrogates an area up to 4 mm x 4 mm. The primary reason broad beam PIXE studies of geologic materials are uncommon is because accuracy is decreased by heterogeneous matrix effects [*Flannigan and Campbell*, 2017]. To determine elemental concentrations, the theoretical yield is calculated using matrix corrections that assume a homogeneous mix of elements on a sub-micrometer scale [*Gellert et al.*, 2006; *Campbell et al.*, 2009]. Most geologic samples are not homogeneous at this scale, even when milled into a powder.

The failure of the homogeneity assumption is linked to systematic offsets of elemental concentrations from well-known certificate values. These offsets found in PIXE analyses have also been identified in testbed APXS analyses [*Campbell et al.*, 2009, 2011, 2012]. The largest offsets are observed in Na, Mg, and Al, which are all light elements excited by the PIXE component of APXS. Empirical corrections based on geological reference materials account for heterogeneous matrix effects in APXS data [*Rieder et al.*, 2003; *Gellert et al.*, 2006], but studies of the effects on PIXE and APXS are limited [*Campbell et al.*, 2009, 2011, 2012; *Perrett et al.*, 2014].

Here, we expand on the work of *Flannigan and Campbell* [2017] to evaluate PIXE as an analogue method to emulate APXS. PIXE analyses of geological reference materials have reproduced testbed APXS results for the same materials [*Flannigan and Campbell*, 2017]. However, the geological reference materials were selected based on bulk chemical compositions and are not linked to each other in a geologically useful manner. Thus, the reference materials are not necessarily ideal as Mars analogue materials. In addition, they do not contain altered material and cover a limited range of FeO concentrations (3-20 wt.%). Our objective is to further evaluate PIXE as an APXS analogue by conducting broad beam PIXE analyses on a well-characterized Mars analogue sample set from Maunakea and Kohala volcanoes on Hawai'i (Chapter 2). In this chapter, we present PIXE analyses, derive empirical corrections, estimate error in accuracy, and evaluate the accuracy. The sample set includes new results for 19 samples from the summit of Maunakea, and we present those results and connect them to the discussion of Gale Crater in Chapter 2.

3.2. Methods

3.2.1. Hawaiian Sample Set

The 43 samples analyzed by PIXE for this study were collected from Maunakea and Kohala volcanoes on Hawai'i (Appendix 3-1). Of these samples, 24 were analyzed by XRF in previous studies, and the XRF results, XRD, petrography, and geologic context of the larger sample set that they were subsampled from is discussed in detail in Chapter 2. Subsampling was intended to represent the full range of rock types and alteration regimes investigated in Chapter 2. In particular, samples were selected that encompass the full range of Fe (as FeO total wt.%) contents found in the Hawaiian samples (Figure 3-1). Iron is a significant X-ray attenuating element in the matrix of many geologic samples and thus has a large effect on modeling the yield of other elements [*Campbell et al.*, 2012; *Flannigan and Campbell*, 2017]. As such, samples of weathering profiles include unaltered lava and progressively weathered samples with passive enrichment of FeO. Altered tephra from the summit of Maunakea was also subsampled for PIXE analysis because acid sulfate alteration led to the addition of S in most cases.

An additional 19 samples of tephra from Maunakea were analyzed with PIXE, and the first geochemical results are presented here. These represent a range of tephra altered under acid sulfate and palagonitic conditions. The tephra was subsampled from the collections of D. W. Ming and R. V. Morris at NASA Johnson Space Center. Hand samples and sieved (< 1mm) tephra were collected. Petrographic analysis was conducted on ~10 of the hand samples.

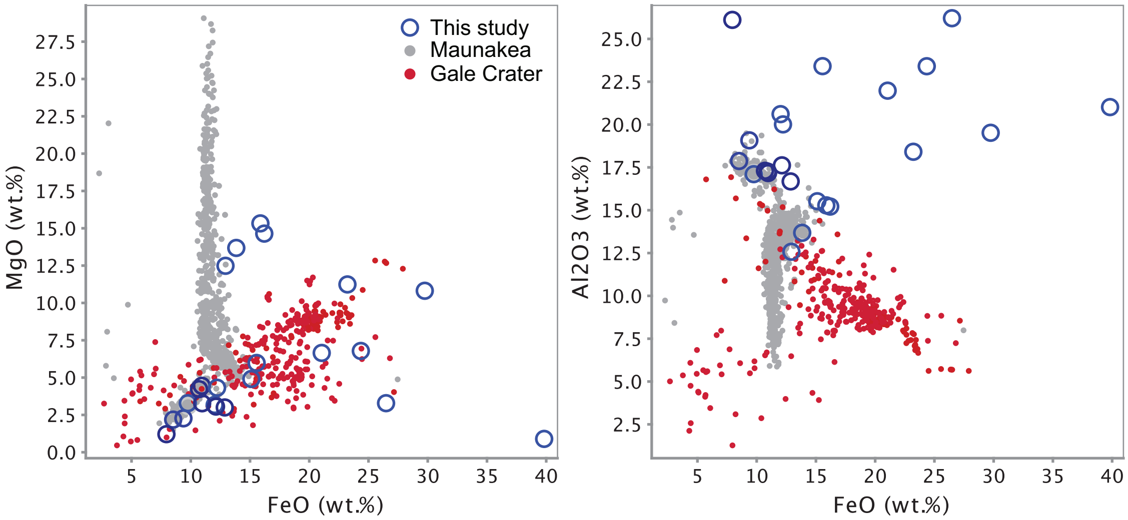

Figure 3-1: Overview of sample compositions (XRF results from previous studies) compared to relatively unaltered whole rock analyses of Maunakea volcanics (gray; data from GEOROC database) and APXS results from Gale Crater, Mars (red; data from Planetary Data System).

3.2.2. Sample Preparation and PIXE Analysis

PIXE analyses were conducted on pressed powder pellets. To create powders, subsamples of ~5-10 g were milled in an aluminum ball mill for 8-20 minutes. Unaltered and moderately altered samples were milled for 20 minutes because the crystalline material was more resistant to milling; highly altered samples were friable and milling for 8 minutes was adequate to create a powder. A previous study of the effect of milling time with the same experimental setup used here showed that compositions do not change with milling times longer than 20-30 minutes [*Flannigan and Campbell*, 2017]. That is, heterogeneous matrix effects that change PIXE yield as a function of grain sizes (discussed below) are not improved with longer milling times (30-60 m). Powders were then pressed into pellets (13 mm diameter) without binder. A carbon coating was applied to prevent charging and allow measurement of current off the sample. One duplicate pellet was made for sample PH201A.

The PIXE analyses were conducted according to the method of *Flannigan and Campbell* [2017] with a 2.5 MeV proton broad beam generated in a particle accelerator at the University of Guelph. The 4 mm x 4 mm beam was targeted normal to the sample surface with a SDD detector positioned 45° relative to the surface and incident beam. Counting times were determined by the preset total integrated beam charge of 10 μC, and counts per second were maintained at ~1200-2300 with a beam current of ~8.5-12 nA.

Determination of elemental concentrations was completed with the PIXE spectrum fitting software package GUPIX [*Maxwell et al.*, 1989, 1995]. The software uses a nonlinear least-squares fitting algorithm and converts peak areas to elemental concentrations by standardization based on fundamental parameters. Samples were treated as 'unknown', thus the matrix was calculated iteratively so that matrix effects and secondary fluorescence could be determined. An infinitely thick sample that is homogeneous on the sub-micrometer scale is assumed. Error in precision is taken to be the one sigma statistical fitting error.

3.2.3. Empirical Correction Factor

Systematic errors have been observed previously in analyses of powdered geologic samples in PIXE using the GUPIX approach [*Flannigan and Campbell*, 2017]. These errors coincide with systematic errors in testbed APXS analyses using GUPIX-based approaches [*Campbell et al.*, 2009, 2011, 2012]. Error found in the fundamental parameters approach to APXS calibration are attributable largely to heterogeneity on the sub-micrometer scale that violates the homogeneous matrix assumption [*Campbell et al.*, 2009]. We therefore applied an empirical correction factor (*ECF*) to the elemental concentrations to improve accuracy. This method is similar to that defined by *Campbell et al.* [2012] for APXS results. Because our approach is intended to evaluate samples with unknown mineralogy, composition, and limited geologic context, the *ECF* is determined independently of those factors. That is, while systematic errors may be attributable to certain rock characteristics (e.g., grain size, phenocryst abundance) or rock types [*Campbell et al.*, 2012], we assume that these characteristics are unknown. The *ECF* is related to the elemental concentrations determined by GUAPX by the equation

$$C_i^{Std} = ECF_i * C_i^{PIXE}$$

where C_i^{PIXE} is the concentration of element *i* as determined by GUPIX and C_i^{Std} is the concentration of element *i* in a standard. For this work, the standard for each sample is taken as a split sample that was measured by XRF (Chapter 2), thus we have 24 analyses from which *ECF* values can be calculated. All PIXE concentrations are recalculated as volatile-free to enable direct comparison with the volatile-free XRF results.

To calculate the *ECF*, the error in accuracy was first estimated by deviation of the PIXE result for each element from a standard using the value *R*, which is defined as

$$R_i = \frac{C_i^{PIXE}}{C_i^{Std}}$$

The mean *R* for each element is the average deviation of the 24 analyses from the standard and this is used to calculate the *ECF* by assuming

$$ECF_i = \frac{1}{R_i^{mean}}$$

We take the standard deviation of the R values of the 24 analyses to be the error in accuracy. The elemental concentrations determined by GUPIX for the full sample set (n = 42) were then corrected with ECF_i and then renormalized to 100 wt.% without volatiles.

3.3. Results

Representative PIXE spectra are presented in Figure 3-2, showing good resolution of Kα peaks and a consistent full width at half maximum (FWHM) of ~130 eV for the Mn Kα peak. GUPIX concentrations are compared to the XRF results for 24 samples as R-values in Figure 3-3 and Table 3-1. The largest deviations from the XRF results (i.e., greatest difference from unity) in major and minor elements are seen in Al_2O_3, MgO, and P_2O_5. This is reflected in the larger accuracy error, as estimated from the standard deviation in R. Trace element and SO_3 R-values are shown in Figures 3-4 and 3-5, respectively.

After correction by the *ECF* (Table 3-1) and renormalizing to 100 wt.% *without* volatiles, the PIXE results more accurately reflect the XRF results (Figure 3-6). Results for the 43 PIXE analyses and one duplicate analysis (PH201A) are presented in Appendix 3-1 as values corrected by the *ECF* for each element (Table 3-1). Sulfur, chlorine, and trace elements (Ni, Cr, Zn) are presented in Appendix 3-1 but are not included in the normalized analysis so that XRF and PIXE can be directly compared as volatile-free. Additionally, S, Cl, and trace elements Ni, Cr, and Zn were not *ECF* corrected because 1) no Cl analyses were available to determine R-values, 2) S, Ni, and Zn had fewer analyses (n = 6 to 14) and thus have higher uncertainty in R^{mean}, and 3) S and Cr have correlations between R and concentration that indicate that a mean correction is not valid for the full dataset.

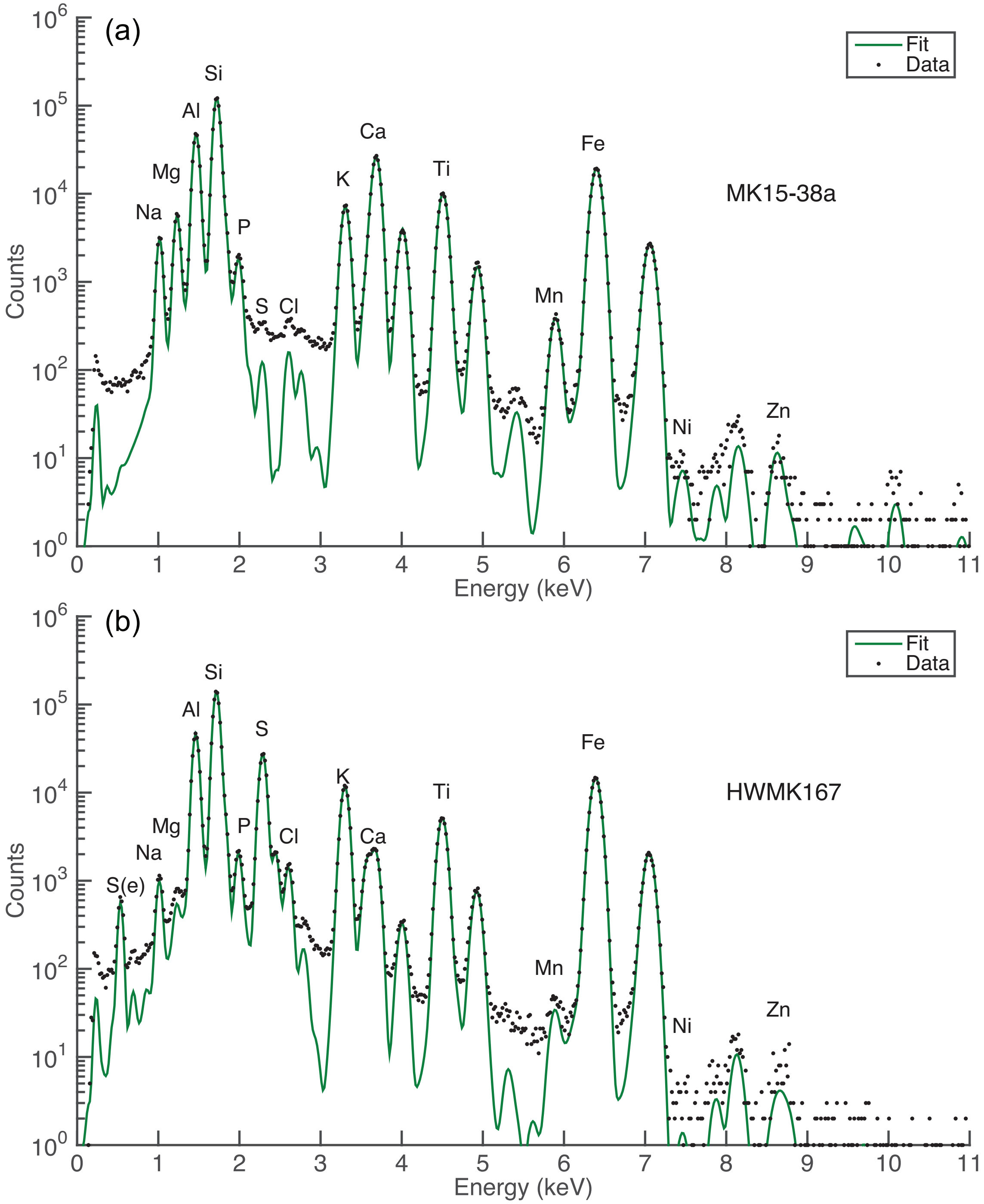

Figure 3-2: Representative PIXE spectra for (a) unaltered alkali basalt (MK15-38a) and (b) jarositic tephra (HWMK167). Select Kα peaks and the S escape peak [S(e)] are indicated.

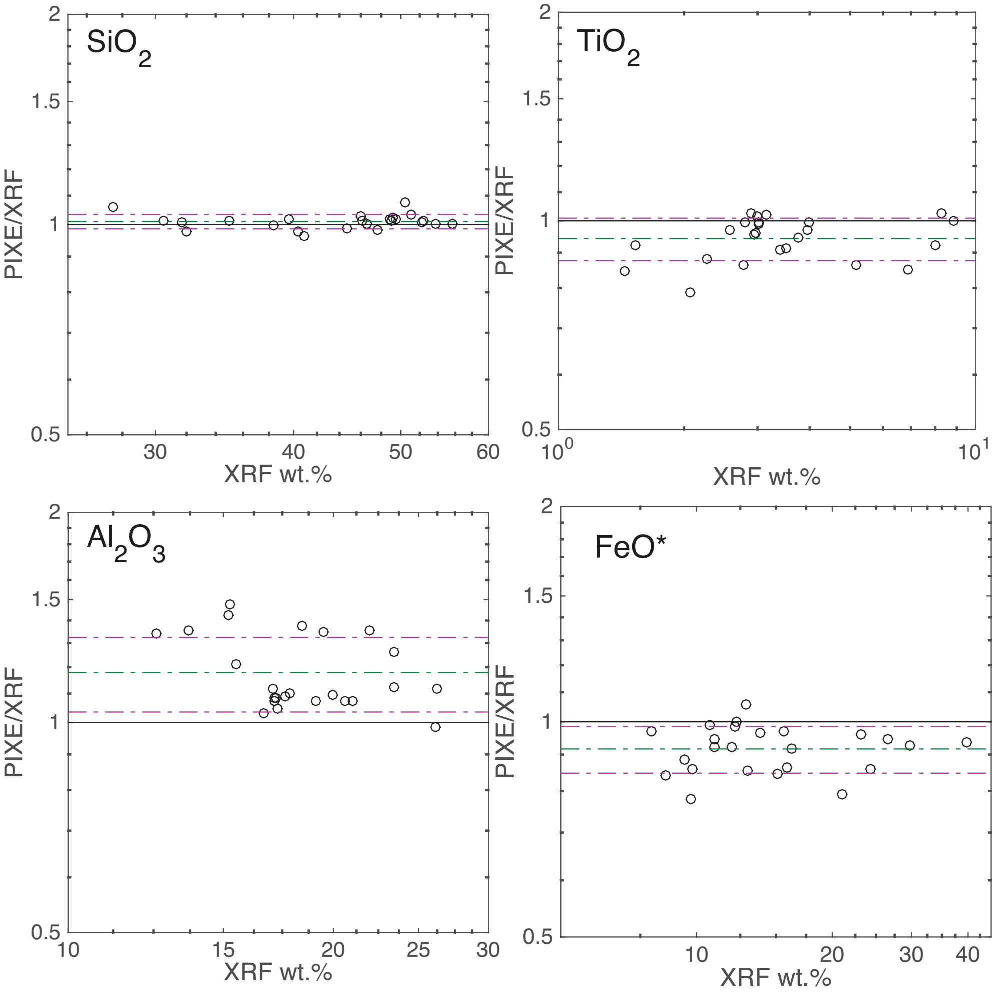

Figure 3-3: Uncorrected PIXE concentrations normalized to XRF concentrations (i.e., *R* value) plotted versus the log of the XRF concentration of the oxide. The mean *R* (green) and standard deviation (magenta) are indicated. Statistical fit error (2σ) is shown where larger than the symbol.

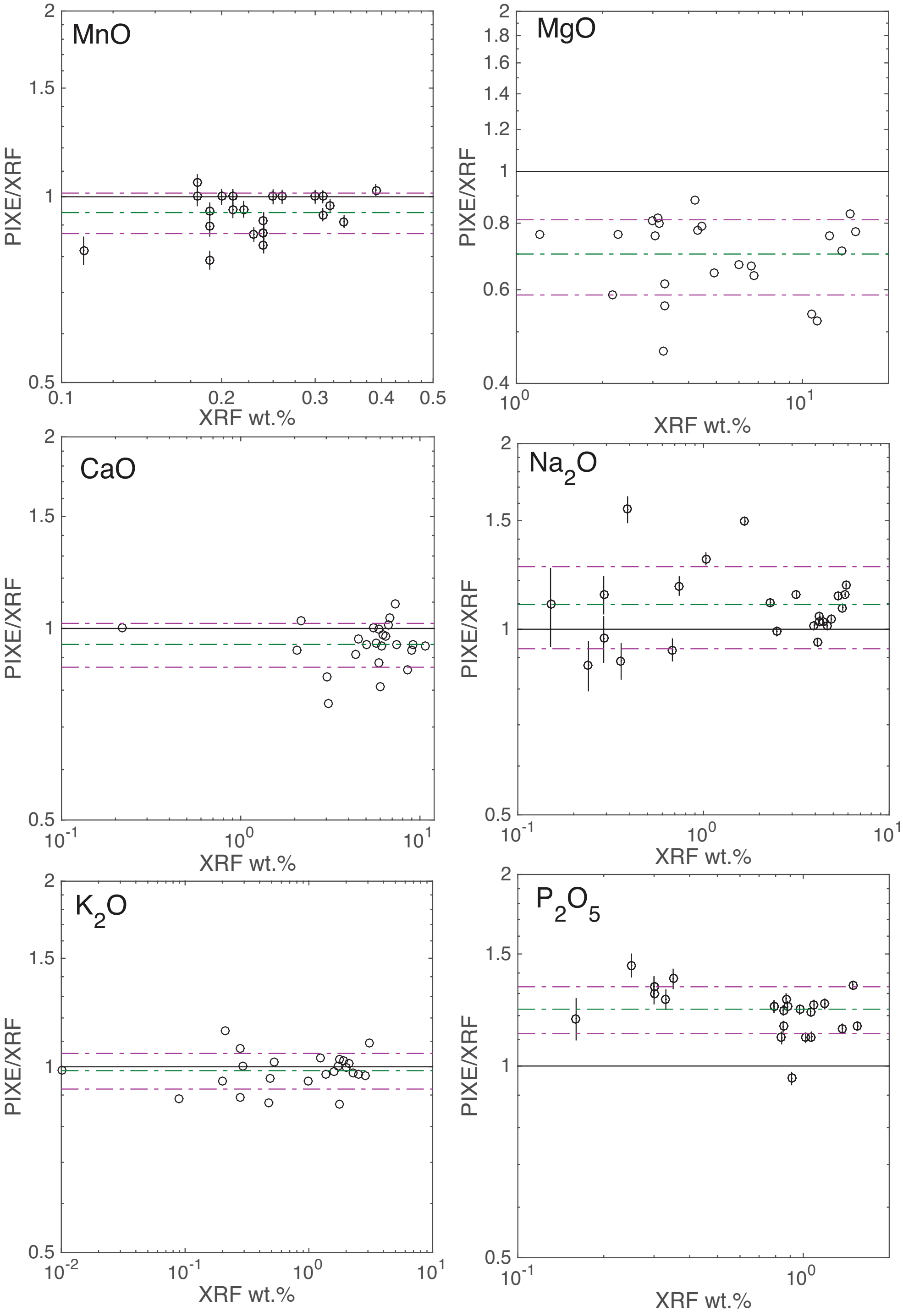

Figure 3-3 continued: Uncorrected PIXE concentrations normalized to XRF concentrations (i.e., *R* value) plotted versus the log of the XRF concentration of the oxide. The mean (green) and standard deviation (magenta) are indicated. Statistical fit error (2σ) is shown where larger than the symbol.

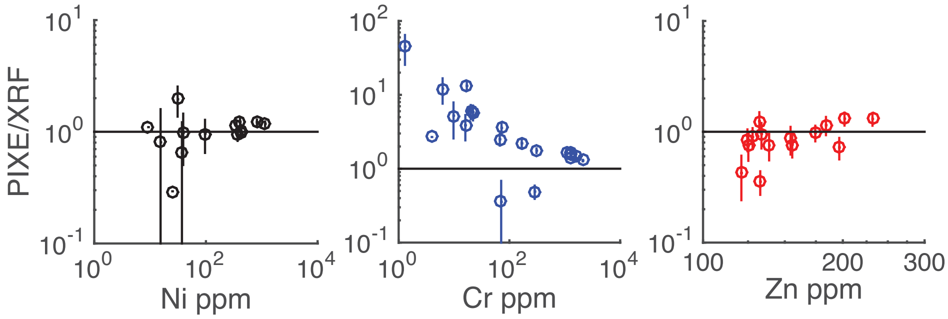

Figure 3-4: Uncorrected PIXE concentrations normalized to XRF concentrations (i.e., *R* value) for trace elements. Statistical fit error (2σ) is shown.

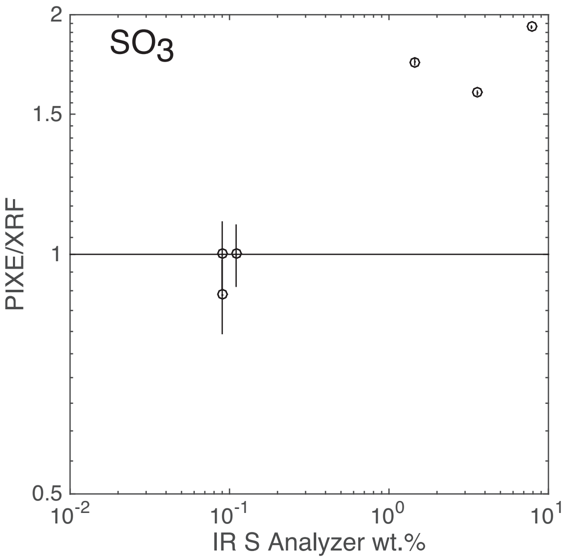

Figure 3-5: Uncorrected PIXE SO_3 concentration normalized to SO_3 concentrations (i.e., *R* value), as measured by a LECO IR-32 total sulfur analyzer [*Morris et al.*, 2000]. Statistical fit error (2σ) is shown.

Table 3-1: *R*-values, error correction factors (*ECF*), and estimates of PIXE error in accuracy for powdered geologic samples.

	R mean	*R* standard deviation	*ECF*	Accuracy error (%)
SiO_2	1.01	0.024	0.99	2
TiO_2	0.94	0.065	1.06	7
Al_2O_3	1.18	0.14	0.85	12
FeO	0.92	0.067	1.09	7
MnO	0.94	0.070	1.06	7
MgO	0.70	0.11	1.43	16
CaO	0.94	0.073	1.06	8
Na_2O	1.10	0.17	0.91	15
K_2O	0.99	0.065	1.01	7
P_2O_5	1.23	0.10	0.81	8
SO_3	1.36	0.41	0.74	30[1]
Cl	N/A	N/A	N/A	N/A
Ni[2]	0.90	0.47	N/A	52
Cr	5.43	9.5	N/A	175
Zn[2]	0.83	0.34	N/A	41

[1] Error for SO_3 is less certain than other elements and it is likely overestimated; see text.

[2] Ni and Zn have a smaller number of samples ($n = 16$).

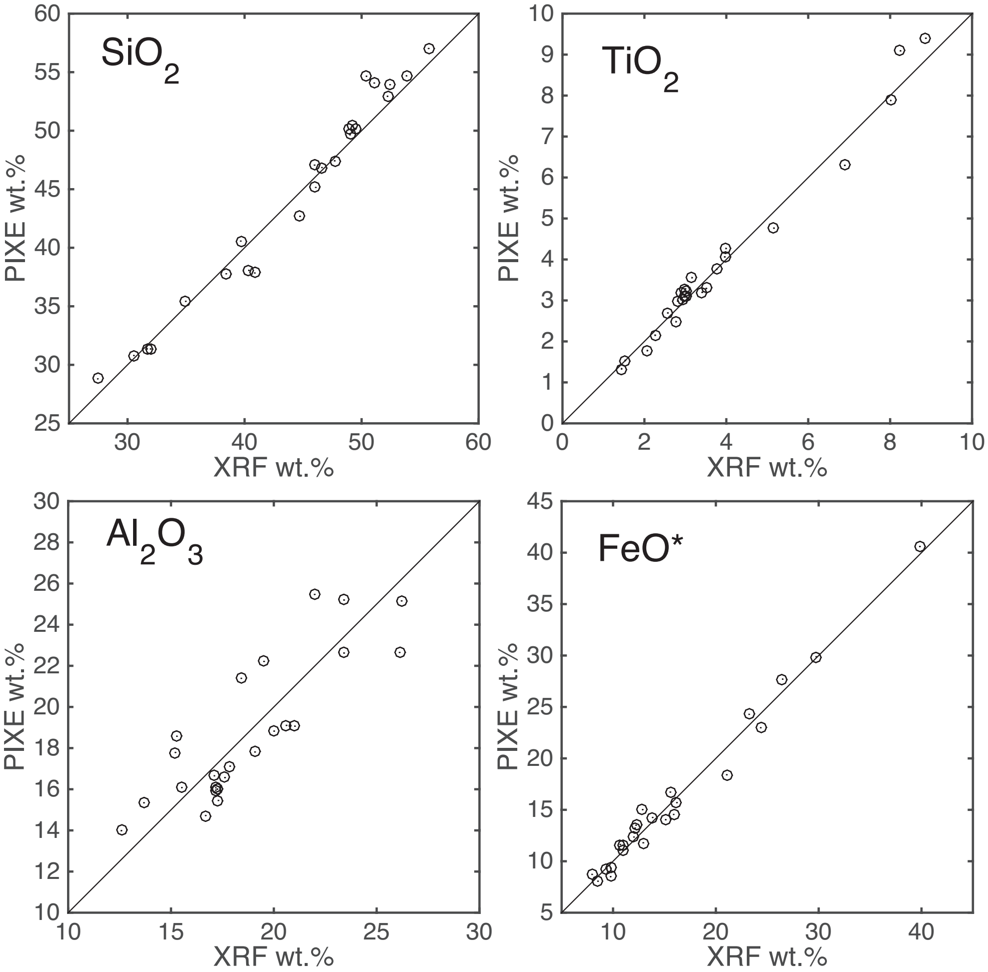

Figure 3-6: Corrected PIXE concentrations versus XRF concentrations for major and minor oxides. All are renormalized to volatile-free concentrations. Statistical fit error (2σ) is shown where larger than the symbol. The line indicates the 1:1 slope though the origin.

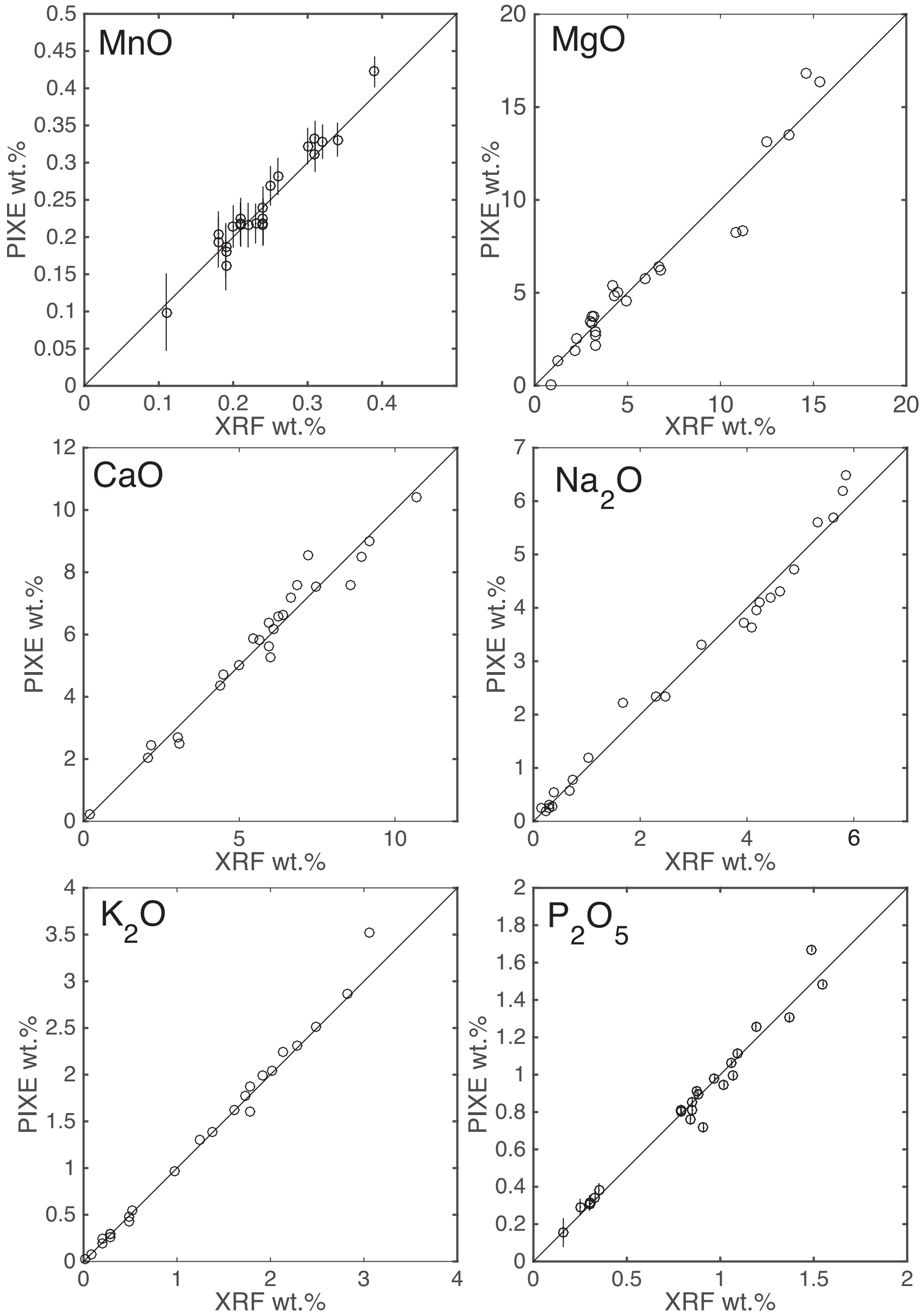

Figure 3-6 continued: Corrected PIXE concentrations versus XRF concentrations for major and minor oxides. All are renormalized to volatile-free concentrations. Statistical fit error (2σ) is shown where larger than the symbol. The line indicates the 1:1 slope though the origin.

3.4. Discussion

3.4.1. Comparing the PIXE and APXS Methods

The broad beam PIXE and APXS techniques are comparable, in part, because of the similarities in sample interactions of 5 MeV alpha-particles from the decay of ^{244}Cm (APXS) and 2.5 MeV protons from a particle accelerator (PIXE). As a result, X-ray counts, as a function of energy, lead to similar spectral features (Figure 3-7). *Flannigan and Campbell* [2017] investigated PIXE as an analogue for APXS and noted that the spectral resolution of PIXE (FWHM Mn $K\alpha$ = 130 eV) is nearer to the resolution of the MSL APXS on Mars (FWHM Mn $K\alpha \approx$ 140-150 eV) than the flight-equivalent testbed APXS unit on Earth (FWHM Mn $K\alpha$ = 170-180 eV). Errors in precision, which is based on statistical counting errors for elemental peak area, are thus also comparable between APXS and PIXE (Table 3-2). The precision of APXS is borne out in Martian data, for example, where multi-point APXS rasters over white Ca-sulfate veins have stoichiometric 1:1 variation of Ca and S [*VanBommel et al.*, 2016]. Evidence of this type of stoichiometric variation in PIXE is also apparent in the Maunakea samples, as presented below.

Error in accuracy of PIXE is compared to APXS in Table 3-2. Note that the error commonly cited for APXS is error in precision, or statistical fitting error, and it is typically lower than the accuracy error [e.g., *Ming et al.*, 2008; *Thompson et al.*, 2016]. The error analysis of the Hawaiian samples resulted in a PIXE error in accuracy that is qualitatively similar to APXS. *Flannigan and Campbell* [2017] presented evidence that the systematic offset and variance in PIXE (Figure 3-3) was comparable in APXS of the same georeference materials (Figure 3-S1). Notable differences are Al_2O_3 and SO_3, which have larger error than APXS. The sources of these errors are discussed in detail in the following sections. The accuracy errors of TiO_2, K_2O, and P_2O_5 are higher for APXS because they have been overestimated pending verification of distance dependent background corrections (R. Gellert, personal communication).

Differences between the two methods arise because the ^{244}Cm source in the APXS also emits Pu X-rays, which excite characteristic X-rays from the sample (XRF), leading to better counting statistics for elements with atomic numbers (Z) greater that Ti. A consequence of the XRF component of APXS is that detection limits are lower (~30 ppm) for trace elements heavier than Fe, such as Ni, Zn, and Ge (Figure 3-7; see Chapter 5). The XRF contribution to the APXS signal is also reflected in the fitting error, which is larger in PIXE for trace elements ($Z > 24$) because the XRF component of APXS causes a greater X-ray yield at energies above ~4.5 keV.

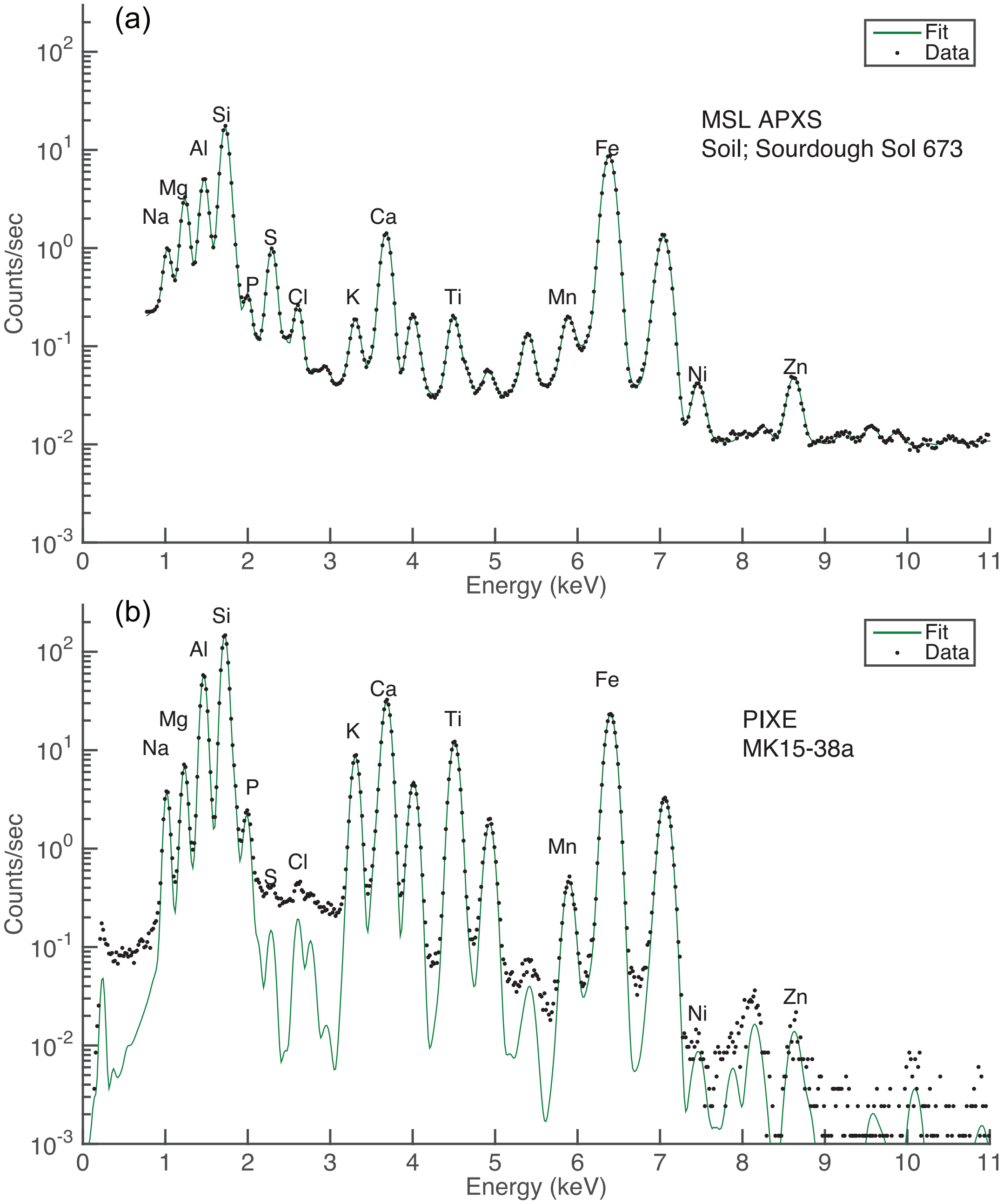

Figure 3-7: Comparison of APXS and PIXE spectra of geologic materials with similar compositions, normalized to counts per second and shown on the same scale. (a) An APXS spectrum of soil in Gale Crater (Sourdough; Sol 673) shows a basaltic composition, with elevated S, Cl, and Zn. The lifetime was 7.5 h and the FWHM of Mn is 147.7 eV. (b) The PIXE spectrum of Maunakea sample MK15-38a shows a transitional, high alkali basaltic composition. The lifetime was 827 s and the FWHM of Mn is 130.2 eV. Note the fitting methods used for APXS and PIXE are different, as discussed in the text. Selected Kα peaks are indicated. The full APXS spectrum (0.78-25 keV) is not shown.

Table 3-2: Comparison of PIXE and APXS error for powdered geologic samples.

	PIXE mean statistical fitting error (%)	PIXE relative accuracy error (%)	APXS typical[1] statistical fitting error (%)	APXS relative accuracy error (%)[2,3]
SiO_2	< 1	2	1	3
TiO_2	< 1	7	4	20
Al_2O_3	< 1	12	2	7
FeO	1	7	1	7
MnO	5	7	3	8
MgO	1	16	3	14
CaO	< 1	8	1	7
Na_2O	3	15	5	11
K_2O	1	7	6	15
P_2O_5	2	8	7	15
SO_3	9	30[4]	1	15
Cl	8	N/A	2	30
Ni	47	52	5	16
Cr	71	175	4	19
Zn	25	41	3	16

[2] Typical is taken to be soil and soil-like compositions with overnight integrations and FWHM <150 eV Mn Kα.

[2] Error determined by *Gellert et al.* [2006].

[3] Note caveats about APXS error in text.

[4] This error is likely overestimated (see section 3.4.2)

3.4.2. PIXE and Sulfur

Sulfur is a significant element on the surface of Mars because it is a fluid-mobile element that is enriched in the dust (see Chapter 4) and occurs commonly as sulfate veins, concretions, and cements [e.g., *Ming et al.*, 2008; *Arvidson et al.*, 2011; *Berger et al.*, 2015]. A key objective for the PIXE analysis of the expanded sample set from Maunakea is to investigate chemical trends related to acid sulfate alteration. Unlike common geochemical analytical methods used on Earth, APXS and PIXE analyze sulfur simultaneously with other elements. Because XRF sample preparation involves fusing the sample and volatiles are lost, S was measured separately with a LECO IR-32 total sulfur analyzer [*Morris et al.*, 2000]. The *R*-values for SO_3 indicate that PIXE and the infrared technique (IR S analyzer) agree at low concentrations (< 1 wt.%), but are very different at higher concentrations (1-10 wt.%; $R = 1.5\text{-}2$; Figure 3-5).

We can qualitatively test the precision and accuracy of PIXE sulfur concentrations because jarosite and alunite were detected in the altered tephra (Figure 3-8; Chapter 2).

Stoichiometric molar variation of S with common sulfate cations (Na^+, K^+, Mg^{2+}, Ca^{2+}) has been demonstrated to be a method for identifying sulfates in APXS measurements because the precision of the method is high [*VanBommel et al.*, 2016]. We can apply this to the PIXE dataset because the alkali jarosite and alunite content is predicted to result in stoichiometric variation of S and K+Na. Figure 3-9 demonstrates that the S-bearing tephra has two groups of data: 1) a group with K and Na concentrations that are similar to unaltered hawaiitic tephra and lava at the summit and 2) a group of K-enriched, Na-depleted tephra. The latter group is positively correlated in K+Na versus S with a slope of 0.73 and y-intercept close to the origin (Figure 3-9b). This is consistent with the stoichiometric addition of K-, Na-alunite group sulfates. The differences between the two compositional groups are confirmed texturally because samples with higher Na contain breccia clasts of moderately to incipiently altered tephra cemented with sulfates (Figure 3-8b), whereas the Na-depleted samples are dominated by fine-grained sulfates and ferric phases (Figure 3-8a).

The IR sulfur analyzer results used to calculate the *R*-values for SO_3 (Table 3-1; Figure 3-5) have lower absolute concentrations than determined by PIXE (Figure 3-10). As noted above, this discrepancy was the justification for *not* applying an *ECF* correction to the PIXE SO_3 results. We suggest that the PIXE results are more accurate because they are consistent with the textural observations and expected molar variation of Na+K and S. The three samples shown in Figure 3-10 were sieved (< 1mm) in the field and no samples were available for sectioning and thus textures are not known. However, the two samples with lower SO_3 (HWMK510 and HWMK940) contain lithic fragments and are darker in color than the pale yellow to white of sulfate-rich samples (Figure 3-11a, 3-11b). In contrast, the sample with higher concentrations of SO_3 (HWMK740) has fewer lithic fragments and is lighter in color (Figure 3-11c). These observations indicate that HWMK740 is accurately grouped with the Na-depleted, sulfate-rich samples on the red line in Figure 3-9b and Figure 3-10, and that the PIXE SO_3 analysis is reasonably accurate. Further work is needed to verify the accuracy of S analysis in geologic samples by PIXE. Nevertheless, we find that the PIXE results are self-consistent and we conclude that the SO_3 concentrations are qualitatively accurate.

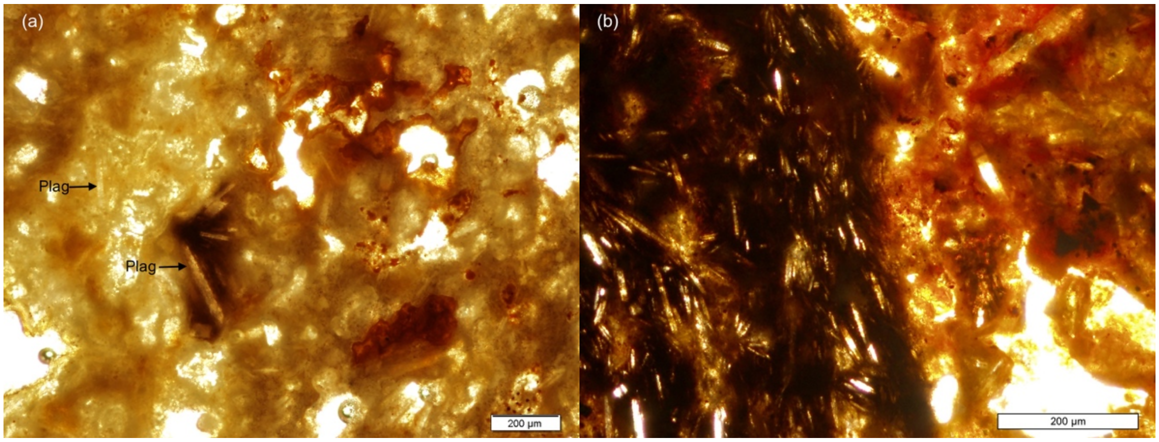

Figure 3-8: Thin section micrographs of acid sulfate altered tephra. (a) Highly altered tephra with very fine-grained pale yellow jarosite, pearly white alunite, and red ferric phases. Representative plagioclase phenocrysts are indicated. This texture is typical of the samples that fall on the red Na-depleted alkali sulfate line in Figure 3-9b. (b) Brecciated tephra showing a slightly altered hawaiite clast on the left, cemented with fine-grained sulfates on the right. The sulfate textures are the same as (a), with varying amounts of ferric phases and plagioclase crystals. The breccia texture (b) is typical of the samples containing higher Na in Figure 3-9a, which have less altered compositions than (a) but contain elevated SO_3.

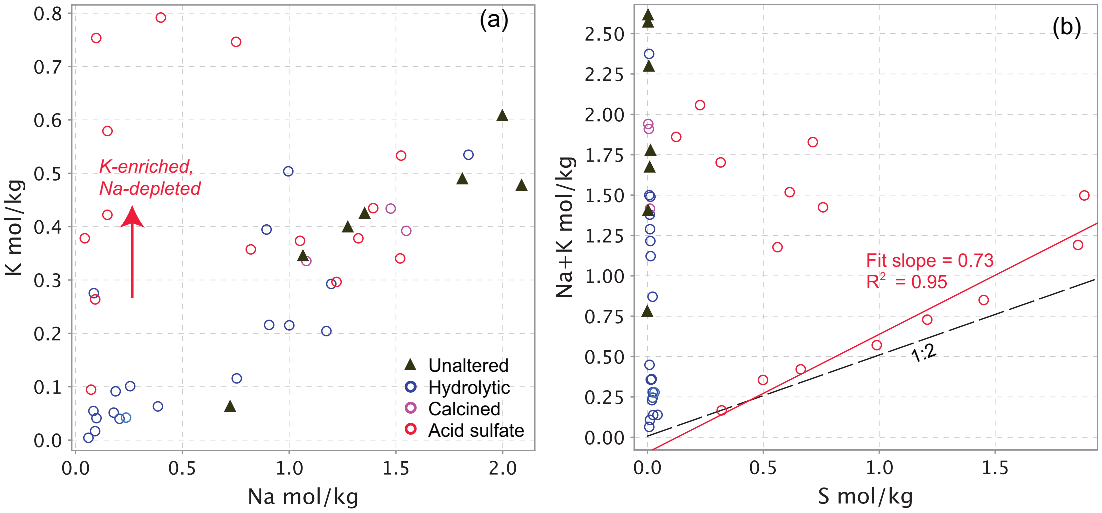

Figure 3-9: Molar variation of (a) K versus Na and (b) Na + K versus S in PIXE analyses of Maunakea summit samples. The eight K-enriched and Na-depleted samples indicated in (a) correspond with the eight low Na + K samples along the red line in (b). The red line in (b) is a linear fit to the lower alkali acid sulfate tephra. Black lines indicate the molar variation of K + Na versus S in a mixture of pure K- and Na-bearing alunite group

sulfates. That is, in K-, Na-jarosite and K-, Na-alunite, one mole of alkali elements will correspond with two moles of sulfur.

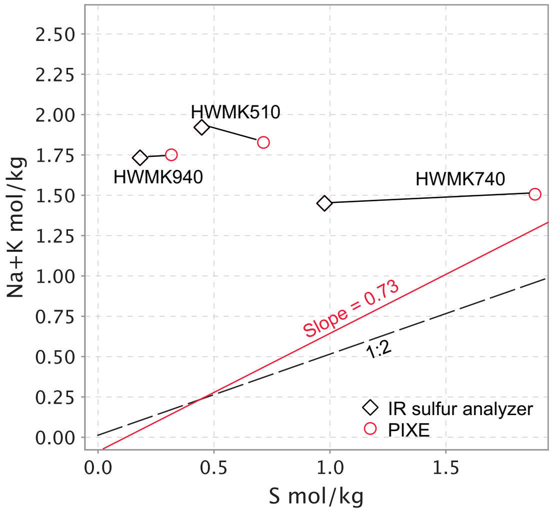

Figure 3-10: Comparison of IR sulfur analyzer results [*Morris et al.*, 2000; *Hamilton et al.*, 2008] and the PIXE sulfur results for the same samples, which were split from the original < 1 mm sieved tephra collected by R. V. Morris. The scale, red line, and black dashed line are the same as in Figure 3-9b. Tielines join the same sample, i.e., they join sample splits, which are numbered.

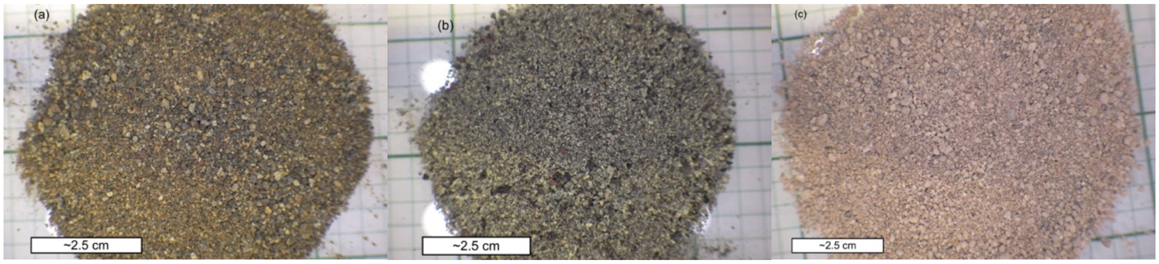

Figure 3-11: Images of sulfur-bearing tephra samples (sieved < 1 mm) from the Maunakea summit: (a) HWMK940, (b) HWMK510, and (c) HWMK740. Sulfur content, as determined by both PIXE and IR, increases from (a) to (c) as shown in Figure 3-10. The sample with the greatest sulfur content (c) has the fewest lithic fragments and lightest color.

3.4.3. Heterogeneous Matrix Effects

Analyses of powdered geologic materials on testbed APXS instruments have shown systematic offsets of light element concentrations (Na, Mg, Al), as determined by the fundamental parameters, GUPIX-based method [*Campbell et al.*, 2009, 2011, 2012; *Perrett et al.*, 2014]. Offsets that are not explained by instrument effects and peak overlap are attributed to heterogeneous matrix effects. In basaltic material, Al and Na are consistently higher than XRF concentrations, and Mg is consistently lower than XRF concentrations. That is, in basalts the *R*-values for Al and Na are higher than unity (1.19 ± 0.16 and 1.04 ± 0.18, respectively) and Mg *R*-values are lower than unity (0.84 ± 0.22) [*Campbell et al.*, 2012]. This deviation is smaller in samples with less Fe, such as dacite. These trends most likely occur because the Fe in the sample is not intimately mixed with all elements on the sub-micrometer scale; it is contained within mafic minerals and attenuates elements in mafic minerals more than elements contained in felsic minerals. The consequence of this is that Mg, which occurs primarily in Fe-bearing minerals (olivine, pyroxene), is attenuated more than predicted because the PIXE yield model assumes homogeneity on a sub-micrometer scale. Similarly, Al and Na, which are contained primarily in the Fe-free mineral feldspar, are not attenuated as much as predicted by the modeling. To account for these effects, empirical corrections similar to the *ECF* method used for this work are applied to the APXS concentrations [*Gellert et al.*, 2006]. However, the heterogeneous matrix effects are a source of error in APXS results. Similar effects are mitigated in XRF analyses on Earth by fusing geologic samples into glasses; this cannot be done by any of the Mars rovers so the effect must be considered in error estimations.

Heterogeneous matrix effects observed in testbed APXS analyses [*Campbell et al.*, 2011, 2012] have been reproduced previously in PIXE analyses of the same geological reference materials [*Flannigan and Campbell*, 2017]. The systematically low mean Mg *R*-values and high mean Na and Al *R*-values found in this work (Figure 3-3) also indicate that the heterogeneous matrix effects caused systematic errors in the PIXE analyses presented here. Three key trends identified in previous works, however, are not reproduced here with the Hawaiian sample set. Unlike previous APXS and PIXE studies, we have found 1) no correlation of FeO content with *R*-values of any element (Table 3-3; Figure 3-12) [cf. *Campbell et al.*, 2012; *Flannigan and Campbell*, 2017], 2) no correlation between the *R*-values of Al_2O_3 and Na_2O ($r = 0.24$) [cf. *Perrett et al.*, 2014], and 3) no effect of loss on ignition (LOI) on *R*-values (Table 3-3; Figure 3-12) [cf.

Campbell et al., 2010]. These three trends were identified in APXS calibration samples that were primarily unaltered, crystalline igneous rocks. Thus, FeO was contained primarily within mafic igneous minerals and *R*-values for Na, Mg, and Al were more likely to deviate from unity increasingly with higher FeO content. However, rock textures were not examined; only XRD analyses were used for evaluating heterogeneous matrix effects. The PIXE calibration samples presented here, in contrast, contain a mixture of unaltered and altered materials and the textures have been analyzed along with XRD (Chapter 2). Below, we propose an extension of the previous calibration discussions of heterogeneous matrix effects to include altered materials and textural observations. Note that we do not necessarily dispute the conclusions of the previous works.

Trends in the Maunakea and Kohala weathering profiles indicate that olivine content has an important effect on the accuracy of PIXE for geologic samples. We first use the Chemical Index of Alteration (CIA) to examine chemical trends in the weathering profiles. The CIA is calculated with the equation

$$\mathrm{CIA} = [\mathrm{Al_2O_3} / \mathrm{Al_2O_3} + \mathrm{CaO} + \mathrm{Na_2O} + \mathrm{K_2O}] \times 100$$

using molecular proportions [*Nesbitt and Young*, 1982]. This index is sensitive to weathering in open-system circumneutral regimes because Al_2O_3 is insoluble and forms secondary clay minerals and/or hydroxides in weathered residue, whereas CaO, Na_2O, and K_2O are soluble and leach out of weathered rocks (see Chapter 2). Thus, an unweathered basalt has a CIA of ~40 to 50 and the index increases with weathering. The CIA of the Maunakea and Kohala weathering profiles are plotted versus MgO/FeO in Figure 3-13, which demonstrates a passive enrichment of MgO and FeO with moderate weathering, followed by a decrease in MgO in the highly weathered samples. This MgO trend is also apparent in Figure 3-14, which shows that MgO increases with moderate weathering, then drops to below 1 wt. % in the most highly weathered sample (MK15-37e).

The MgO trend is consistent with rock textures: olivine alters in situ and converts to magnetite pseudomorphs (Figure 3-15). Olivine and magnetite will both cause the perturbation in *R*-values as described above because both are Fe-bearing phases that are not intimately mixed with the Al- and Na-bearing feldspar. Therefore, the olivine and magnetite pseudomorphs cause inaccurate calculation of Al and Mg concentrations because the attenuation of Mg by Fe is underestimated and the attenuation of Al by Fe is overestimated. The most altered samples are friable, having few or no remaining discrete grains of olivine, magnetite pseudomorphs, or primary magnetite; the only X-ray diffracting phases are hematite, chromite, ilmenite, and quartz (see Chapter 2). Thus, the FeO in the most altered samples may be abundant (28-40 wt. %), but it is intimately mixed with the Al_2O_3, which is most likely contained in an X-ray amorphous hydroxide, and the heterogeneous matrix effect is lessened. The relationship between Al_2O_3 *R*-values and MgO content for the full calibration sample set is shown in Figure 3-16, demonstrating the difference in *R*-values between olivine-rich and olivine-poor samples.

Changes in MgO content of the weathered mugearite (MK15-3) and benmoreite (MK15-35) are different than observed in the basalts (Figures 3-13, 3-14), and are likely related to different trends in *R*-values. The alkalic protoliths have lower olivine abundance and smaller olivine crystals that are approximately the same size as primary magnetite grains (Figure 3-17a). With incipient weathering and a small increase in CIA, MgO decreases with K_2O, Na_2O, and SiO_2 (Chapter 2). The passive enrichment of MgO seen in the basalts is not apparent in the alkalic rocks. The weathered alkalic rocks also have *R*-values that are closer to unity than the unweathered protoliths, that is, they display a lesser heterogeneous matrix effect. This is so despite the passive increase in FeO content, suggesting that the Fe-bearing olivine grains are breaking down due to alteration and the Fe is more homogeneously distributed in the sample. Supporting petrographic observations include red staining in the incipiently altered samples, which indicate oxidation of the primary Fe-bearing phases (Figure 3-17b).

An alternative explanation for the changes in *R*-values with weathering is differences in mineral grain durability with weathering. The altered Hawaiian rocks are significantly more friable than the volcanic protoliths, likely due to the disruption of the feldspar crystal structure (evident in isotropic plagioclase; see Chapter 2), the conversion of olivine to iddingsite and magnetite, and the formation of fine-grained secondary phases (hematite, gibbsite, amorphous Fe-oxides and oxyhydroxides). Increased alteration has been previously linked with smaller grain sizes at Maunakea [*Morris et al.*, 2000]. This change in grain size and possible decrease in mineral hardness could lead to significantly finer mean grain sizes in altered samples, relative to unaltered samples, after the samples are milled into a powder. If so, the highly-altered material may contain a more intimate mixture of Fe with Al and Na, as well as a dilution of Mg in Si and Al. This would reduce the heterogeneous matrix effects. This conclusion is uncertain, however, because the powder grain sizes were not measured for this work. We find the effect of olivine discussed above is better supported by the textural evidence, and is a more significant cause of *R*-value perturbation.

Table 3-3: Correlation coefficients (*r*) for PIXE/XRF ratios (*R* values) with selected parameters.

	XRF[1]	FeO XRF	LOI
SiO_2	0.06	0.092	-0.12
TiO_2	0.18	0.21	0.46
Al_2O_3	-0.37	0.32	0.14
FeO	0.014	0.014	0.23
MnO	0.3	0.15	0.045
MgO	0.0016	-0.43	-0.055
CaO	0.069	-0.27	0.032
Na_2O	-0.1	0.25	-0.23
K_2O	0.17	0.044	0.091
P_2O_5	-0.44	0.28	0.26
SO_3	0.83	-0.29	0.73
Cl			
Ni	0.36	0.29	0.16
Cr	-0.29	-0.27	-0.38
Zn	0.59	0.64	0.62

[1] Correlation of the *R* values for each oxide with the corresponding XRF results for that oxide (wt. %). That is, these coefficients quantify the correlations in the plots in Figures 3-3 and 3-12.

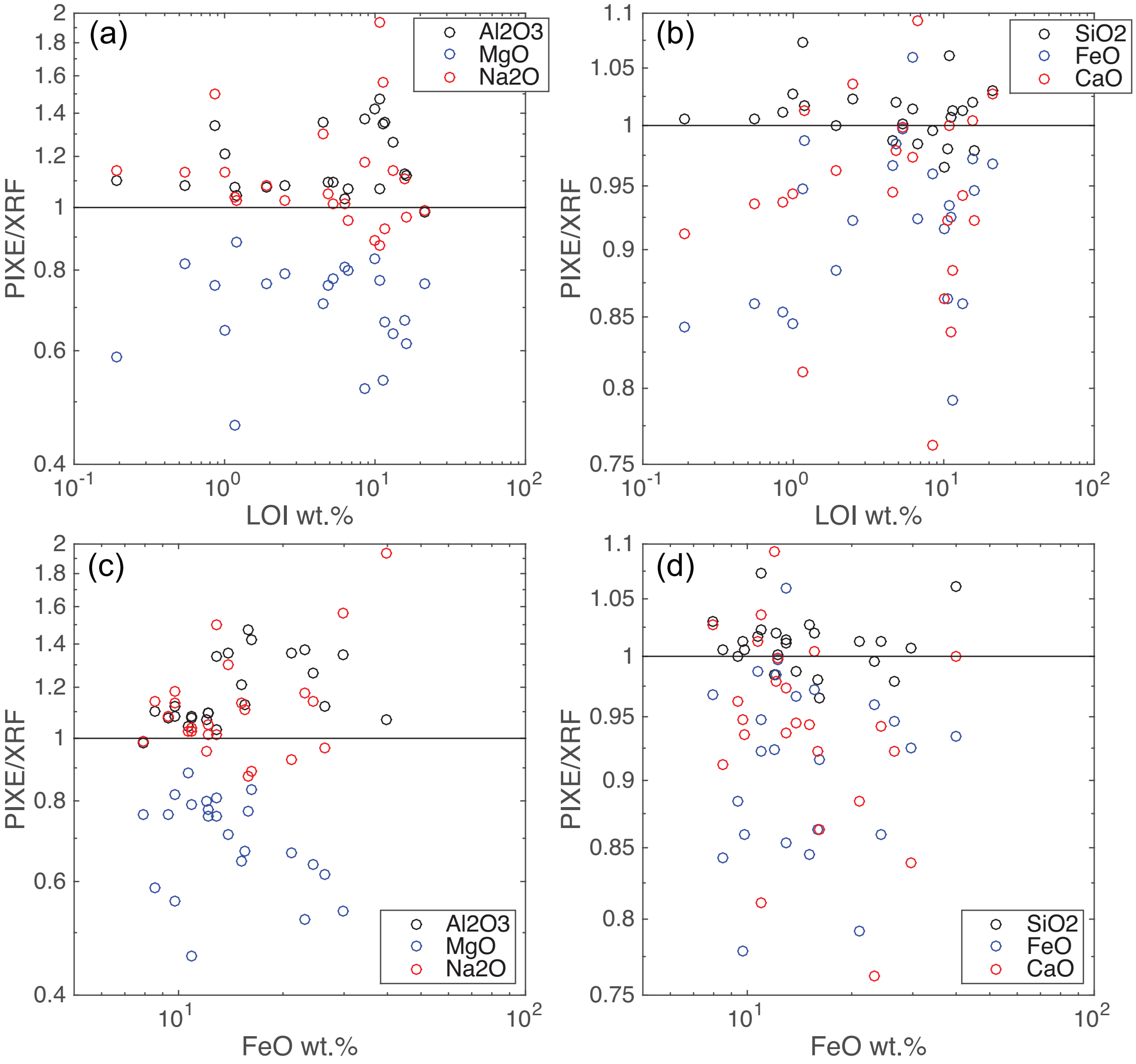

Figure 3-12: Major oxide PIXE concentration normalized to XRF concentrations (i.e., *R* value) plotted versus (a, b) the log of LOI and (c, d) the log of XRF FeO concentrations. As quantified by correlation coefficients in Table 3-3, *R* values do not correlate with LOI or FeO content. Note that correlations are apparent in subsets of the data, as discussed in the text.

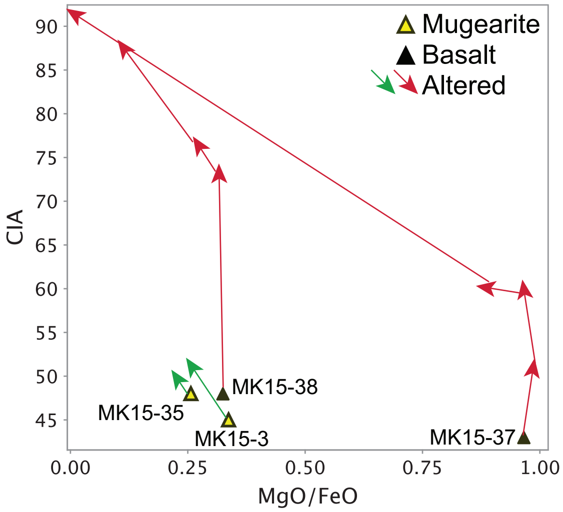

Figure 3-13: Changes in Chemical Index of Alteration (CIA) with weathering, using XRF results. Lines connect samples from the same weathering profile, the weathering profile site number is shown (Appendix 3-1), and the arrowheads are plotted at values that correspond to weathered samples. Note that MK15-35 is classified as a benmoreite but labeled as a mugearite for simplicity.

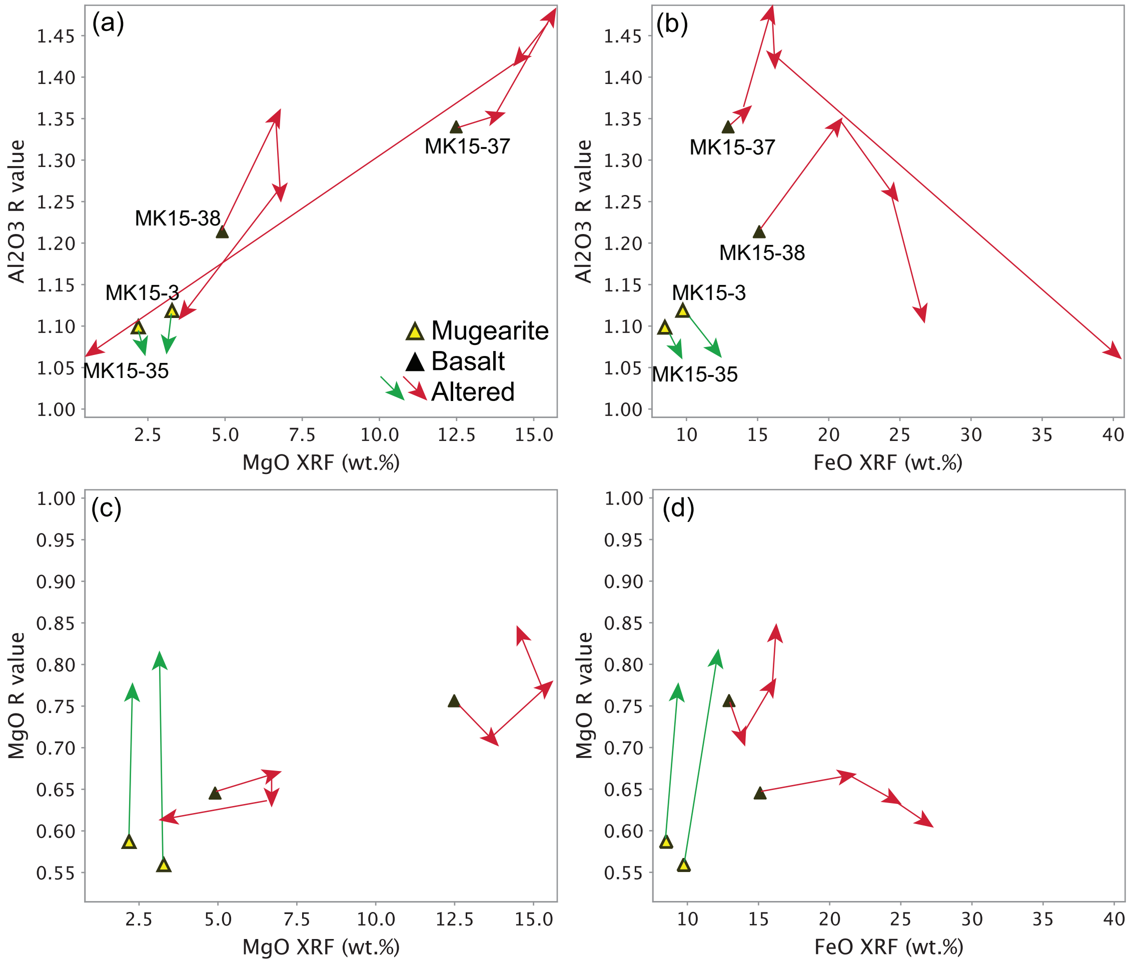

Figure 3-14: Changes in *R* value with weathering. Lines connect samples from the same weathering profile, the weathering profile site number is shown in (a) and (b) (Appendix 3-1), and the arrowheads are plotted at values that correspond to weathered samples. The most highly weathered sample of profile MK15-37 is not plotted in (c) and (d) because the MgO result for PIXE was below the detection limit and an *R*-value could not be calculated.

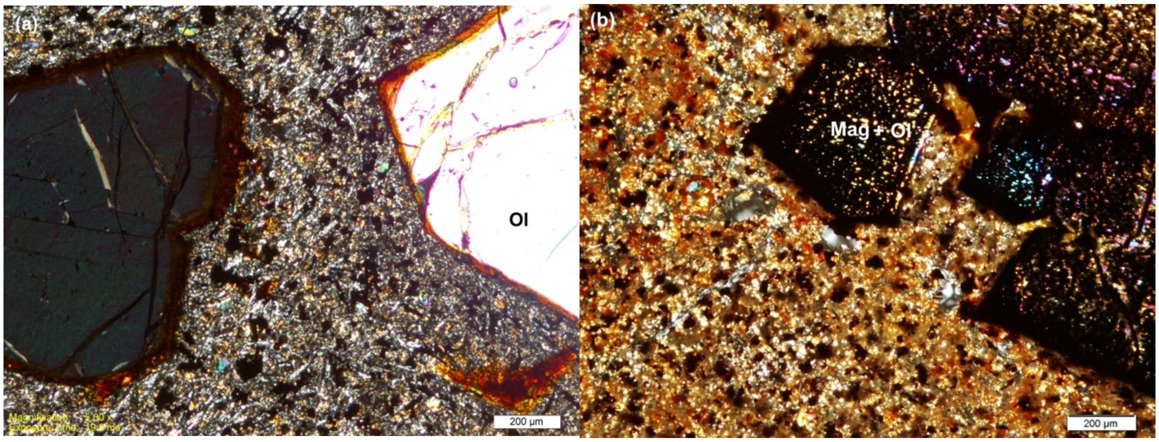

Figure 3-15: Cross-polarized thin section micrographs of (a) the least weathered sample of profile MK15-37 (sample ID MK15-37a) and (b) a moderately weathered sample from the same profile (ample ID MK15-37d). The olivine phenocrysts in (a) have red rims indicating incipient weathering and iddingsite formation. The olivine phenocrysts in (b) have altered to secondary magnetite, identified by µXRD (Chapter 2), but olivine interference colors are still visible in the interior of the grain. Note that most of the plagioclase in (b) is isotropic, indicating alteration.

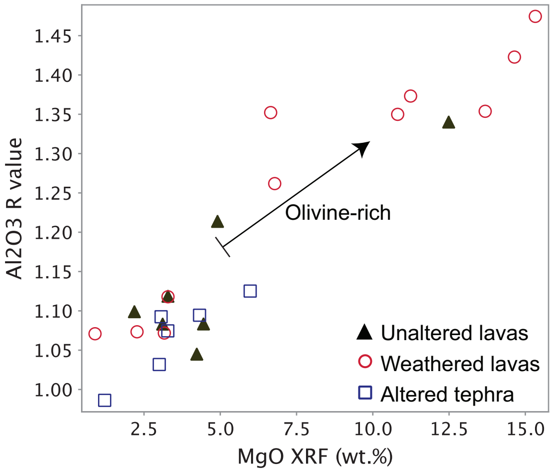

Figure 3-16: *R*-values for Al_2O_3 versus MgO XRF concentrations for all 24 calibration samples, showing a correlation $r = 0.93$. All samples with *R* greater than 1.2 are basaltic and have olivine or magnetite pseudomorphs after olivine. Samples with *R* less than 1.2 are either mugearite/benmoreite or their alteration products, including palagonitic and acid sulfate altered tephra and lavas with pedogenic alteration.

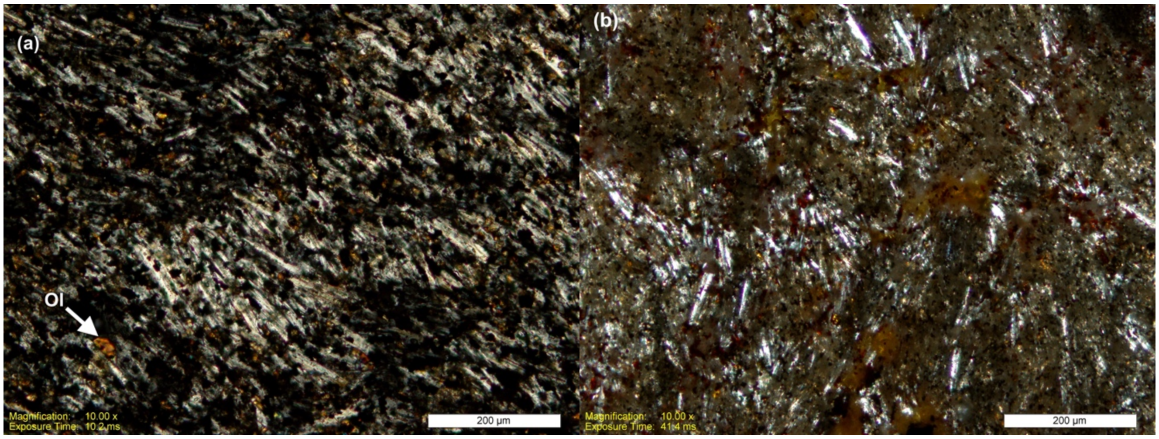

Figure 3-17: Cross-polarized thin section micrographs of (a) a relatively unaltered benmoreite and its (b) incipiently weathered product (weathering profile MK15-35). An olivine crystal is indicated in (a), showing that the mineral occurs at approximately the same size as the opaque magnetite grains. Red staining in (b) is consistent with oxidation of Fe due to weathering. In addition, roughly 20% of the plagioclase crystals are isotropic in (b), consistent with alteration.

3.4.4. Implications of Heterogeneous Matrix Effects

The consequences of the heterogeneous matrix effects on the PIXE results are apparent in a plot of Al_2O_3 content calculated by XRF and PIXE (Figure 3-18). To reiterate, the *ECF* correction was determined without considering the mineral composition of the samples. The result is that the olivine-rich basalts and moderately weathered products have under-corrected Al_2O_3, whereas the olivine-poor mugearites and benmoreites have over-corrected Al_2O_3. Therefore, this calibration dataset, having samples with and without olivine, has a greater error in accuracy than a calibration that evaluates rock types and mineralogy separately.

We find that, despite the greater error, combining olivine-rich and olivine-poor samples in the PIXE calibration dataset is better as an APXS analogue than evaluating samples separately based on rock type. This is because the mineralogy of most targets measured by the APXS on Mars is poorly constrained. Basalts with olivine and magnetite have been discovered in Gusev Crater [*Morris et al.*, 2006]. Olivine-bearing soil [*Blake et al.*, 2013] and sedimentary rock [*Vaniman et al.*, 2014; *Treiman et al.*, 2016] has been discovered in Gale Crater along with olivine-poor sedimentary rock [*Yen et al., 2017*]. In theory, different empirical corrections could be applied to APXS samples when mineralogy is better constrained (with CheMin or Mössbauer). However, the error in accuracy would only be improved for Al_2O_3, changing from 12% to ~7%, assuming that the PIXE error determined here is applicable to APXS. Because of these considerations, basing empirical corrections on mineralogy when the olivine content and textures are unknown is not recommended for APXS analyses.

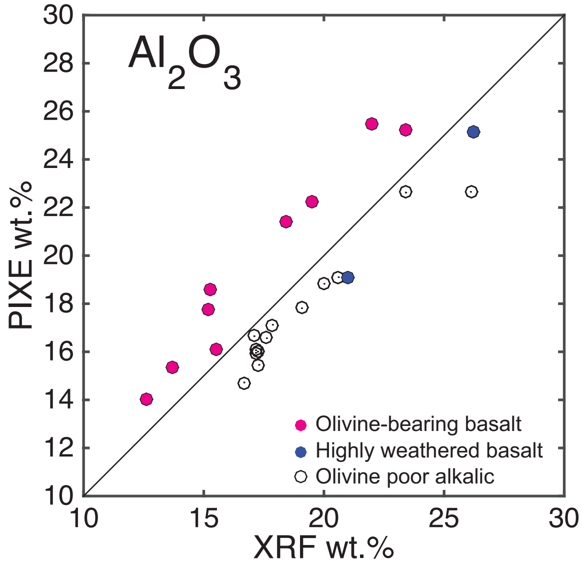

Figure 3-18: Corrected PIXE versus XRF concentrations of Al_2O_3. Olivine bearing basalts and their weathered products are indicated in magenta and blue (weathering profiles MK15-33, MK15-38, and MK15-37). The black line indicates the 1:1 slope through the origin. The modeled PIXE yield of Al is higher in the samples with olivine and magnetite pseudomorphs after olivine because those Fe-bearing phases cause a highly heterogeneous distribution of Fe in the sample and the attenuation of Al by Fe is over-estimated. The two highly weathered basalt samples that lie below the 1:1 line are the most weathered samples in profiles MK15-37 and MK15-38 (see Figure 3-13).

3.4.5. Relevance to Gale Crater

Of the 43 PIXE analyses presented in this chapter, 19 represent new results from tephra collected at the summit of Maunakea (Appendix 3-1), and they are relevant to hypotheses about acid sulfate alteration in Gale Crater (Chapters 2, 5). Sulfur-bearing samples, interpreted to contain sulfates of the alunite group (Chapter 2), share geochemical characteristics with the Stimson fracture haloes and the Murray Fm. (Figures 3-19, 3-20). Notably, the Maunakea tephra is enriched in silica with a corresponding decrease in FeO, MnO, MgO, CaO, and Na_2O. These trends are mirrored in the Murray Fm. and Stimson fracture haloes. Exceptions include Al_2O_3, which is enriched in several Maunakea samples (HWMK976), and higher CaO in the Stimson haloes, which is accounted for in Ca-sulfates.

The characteristics of the Maunakea tephra are consistent with the acid sulfate alteration interpretation. Silica has low solubility and is often passively enriched in open-system acidic alteration regimes. Under these conditions, Fe is soluble and can be leached out along with other metals that otherwise have low solubility in circumneutral fluids (Mn, Al). Further, K is retained in secondary sulfates. The primary P-bearing mineral, apatite, is also soluble in low pH fluids, but can form secondary, insoluble Fe-phosphates [*Hausrath et al.*, 2008]. The geochemical indicators of these processes are found in the Stimson fracture haloes and in the Murray Fm., thus an acid sulfate alteration scenario is plausible for those units. This hypothesis is discussed further in Chapters 2 and 5.

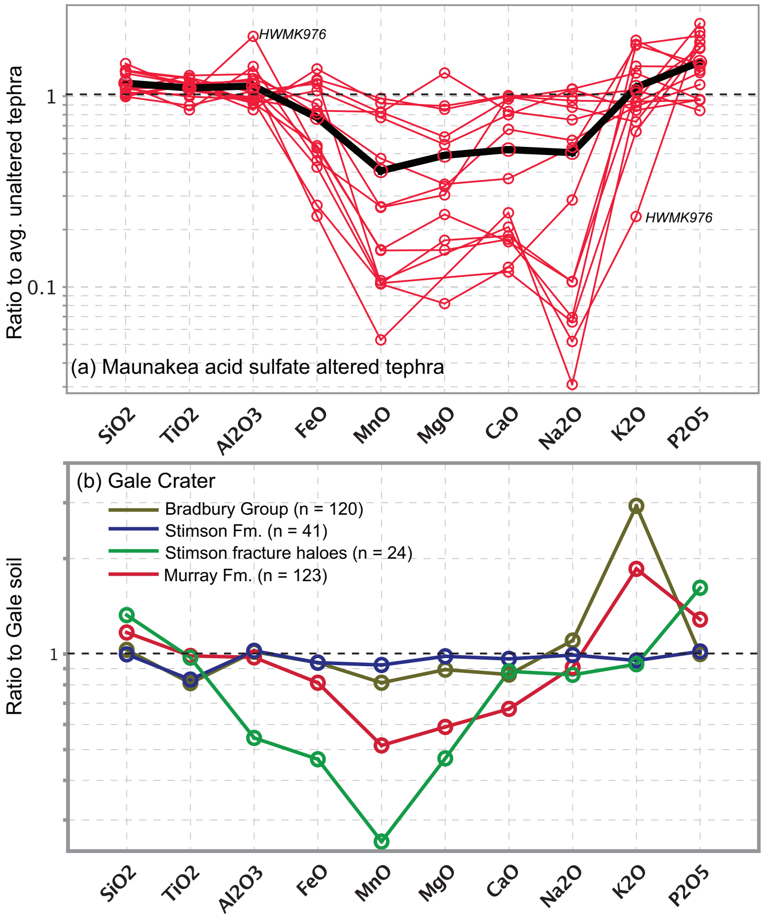

Figure 3-19: Element ratios for (a) Maunakea acid sulfate altered tephra and (b) Gale Crater. In (a), the altered tephra is normalized to concentrations for average unaltered tephra from the Maunakea summit [*Morris et al.*, 2000]. The mean values are denoted by the black line and the Al-rich, K-poor sample HWMK976 is indicated. The Gale Crater ratios are mean values for targets measured up to sol 1514, except for veins, with the number of targets (n) indicated in the legend. See Chapters 2 and 5 for descriptions of the Gale Crater sample groups.

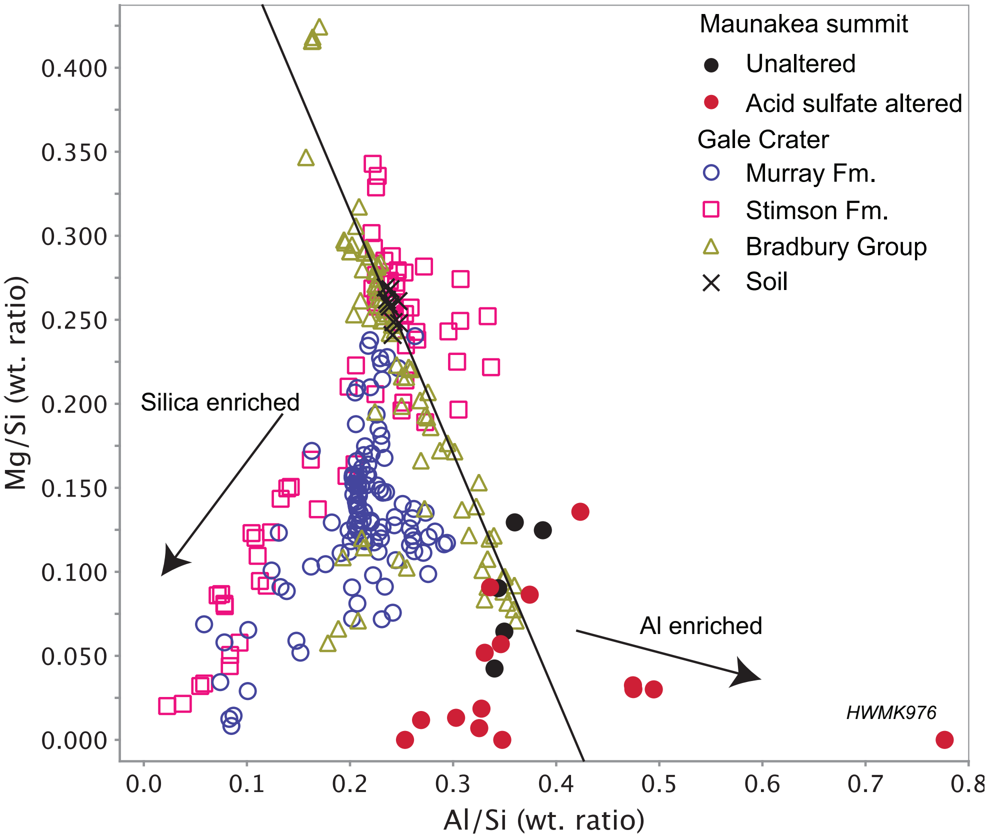

Figure 3-20: Variation of Mg/Si versus Al/Si in Gale Crater APXS data and in Maunakea PIXE data. All Gale Crater APXS data up to sol 1514 are shown, except for veins. Only unaltered and acid sulfate altered Maunakea summit samples are shown. The black line indicates a mafic/felsic igneous compositional trend. The silica-enriched, Mg-depleted acid sulfate altered Maunakea tephra display a similar trend away from the igneous control line as the Stimson fracture haloes and Murray Fm. bedrock. However, the Maunakea altered tephra does not decrease in Al/Si in all cases; an Al-enrichment is indicated.

3.5. Conclusions and Future Work

We have demonstrated here that broad beam PIXE is an appropriate analogue for APXS analyses, with accuracy and precision comparable to APXS. Empirical corrections are straightforward and improve accuracy without introducing systematic errors. Very high FeO content (up to 40 wt.%) does not perturb analyses, provided that the Fe is distributed in the sample in poorly crystalline, fine grained phases. The simultaneous measurement of major, minor, and trace elements with volatile elements S and Cl is important because it allows for the analysis of S and Cl by one method without heating the sample. We therefore concur with the conclusion of *Flannigan and Campbell* [2017] that PIXE should be investigated further as an APXS emulating method.

Two issues call for further work to improve the PIXE broad beam technique as an APXS analogue. First, while the error in Al_2O_3 can be qualitatively linked to olivine phenocrysts in unaltered samples and to magnetite (after olivine) in altered samples, a quantitative demonstration of the effect is needed. This could be done with fabricated samples that vary olivine content in a controlled manner. For example, basaltic glass samples could be prepared such that olivine phenocrysts could be added at different proportions, maintaining the same bulk composition. The working hypothesis would be: increasing olivine phenocryst content causes Al to have an increasingly positive R value.

The second issue for future investigation is S analysis. We presented a line of reasoning that the S analysis of PIXE is accurate because it follows the stoichiometric variation expected for alunite group sulfates. This could be tested by adding increasing amounts of a pure sulfate, such as K_2SO_4 to a basalt. If the PIXE results show S concentrations that match the amount added, and/or molar K:S variation of 2:1, then accuracy can be determined and corrections calculated as needed.

3.6. References

Arvidson, R. E. et al. (2011), Opportunity Mars Rover mission: Overview and selected results from Purgatory ripple to traverses to Endeavour crater, *Journal of Geophysical Research: Planets*, *116*(E7).

Berger, J. A. et al. (2015), Chemical Composition of Diagenetic Features at Lower Aeolis Mons, Mars as Measured by Curiosity's APXS, in *AGU Fall Meeting*, vol. P43B–2121.

Blake, D. F. et al. (2013), Curiosity at Gale Crater, Mars: Characterization and Analysis of the Rocknest Sand Shadow, *Science*, *341*(6153), 1239505, doi:10.1126/science.1239505.

Campbell, J. L., M. Lee, B. N. Jones, S. M. Andrushenko, N. G. Holmes, J. A. Maxwell, and S. M. Taylor (2009), A fundamental parameters approach to calibration of the Mars Exploration Rover Alpha Particle X-ray Spectrometer, *J. Geophys. Res.*, *114*(E04006), doi:200910.1029/2008JE003272.

Campbell, J. L., S. M. Andrushenko, S. M. Taylor, and J. A. Maxwell (2010), A fundamental parameters approach to calibration of the Mars Exploration Rover Alpha Particle X-ray Spectrometer: 2. Analysis of unknown samples, *J. Geophys. Res.*, *115*(E04009), doi:201010.1029/2009JE003481.

Campbell, J. L., A. M. McDonald, G. M. Perrett, and S. M. Taylor (2011), A GUPIX-based approach to interpreting the PIXE-plus-XRF spectra from the Mars Exploration rovers: II geochemical reference materials, *Nucl. Instrum. Methods Phys. Res. B*, *269*(1), 69–81, doi:10.1016/j.nimb.2010.09.014.

Campbell, J. L., G. M. Perrett, R. Gellert, S. M. Andrushenko, N. I. Boyd, J. A. Maxwell, P. L. King, and C. D. M. Schofield (2012), Calibration of the Mars Science Laboratory Alpha Particle X-ray Spectrometer, *Space. Sci. Rev.*, *170*(1–4), 319–340, doi:10.1007/s11214-012-9873-5.

Flannigan, E. L., and J. L. Campbell (2017), Emulating the Mars APXS with Accelerator-Based PIXE, M.Sc. thesis, University of Guelph, http://atrium.lib.uoguelph.ca/.

Gellert, R. et al. (2006), Alpha Particle X-Ray Spectrometer (APXS): Results from Gusev crater and calibration report, *J. Geophys. Res.*, *111*(E02S05), doi:200610.1029/2005JE002555.

Gellert, R., J. L. Campbell, P. L. King, L. A. Leshin, G. W. Lugmair, J. G. Spray, S. W. Squyres, and A. S. Yen (2009), The Alpha-Particle-X-Ray-Spectrometer (APXS) for the Mars Science Laboratory (MSL) Rover Mission, in *Lunar Planet. Sci., XL*, p. Abstract 2364.

Hamilton, V. E., R. V. Morris, J. E. Gruener, and S. A. Mertzman (2008), Visible, near-infrared, and middle infrared spectroscopy of altered basaltic tephras: Spectral signatures of phyllosilicates, sulfates, and other aqueous alteration products with application to the mineralogy of the Columbia Hills of Gusev Crater, Mars, *J. Geophys. Res.*, *113*, 30 PP., doi:200810.1029/2007JE003049.

Hausrath, E. M., D. C. Golden, R. V. Morris, and D. W. Ming (2008), Phosphate alteration on Mars, *Geochimica et Cosmochimica Acta Supplement*, *72*, 357.

Johansson, S. A. E., J. L. Campbell, and K. G. Malmqvist (1995), *Particle-Induced X-Ray Emission Spectrometry (PIXE)*, John Wiley & Sons.

Johnson, D. M., P. R. Hooper, R. M. Conrey, and G. Laboratory (1999), XRF analysis of rocks and minerals for major and trace elements on a single low dilution Li-tetraborate fused bead, in *Advances in X-ray Analysis, v, 41, p. 843–867 Le Bas, M.J*, pp. 745–750.

Maxwell, J. A., J. L. Campbell, and W. J. Teesdale (1989), The Guelph PIXE software package, *Nuclear Instruments and Methods in Physics Research Section B: Beam Interactions with Materials and Atoms*, *43*(2), 218–230, doi:10.1016/0168-583X(89)90042-6.

Maxwell, J. A., W. J. Teesdale, and J. L. Campbell (1995), The Guelph PIXE software package II, *Nuclear Instruments and Methods in Physics Research Section B: Beam Interactions with Materials and Atoms*, *95*(3), 407–421, doi:10.1016/0168-583X(94)00540-0.

Ming, D. W. et al. (2008), Geochemical properties of rocks and soils in Gusev Crater, Mars: Results of the Alpha Particle X-Ray Spectrometer from Cumberland Ridge to Home Plate, *J. Geophys. Res.*, *113*(E12S39), 28 PP., doi:200810.1029/2008JE003195.

Morris, R. V. et al. (2000), Mineralogy, composition, and alteration of Mars Pathfinder rocks and soils: Evidence from multispectral, elemental, and magnetic data on terrestrial analogue, SNC meteorite, and Pathfinder samples, *J. Geophys. Res.*, *105*(E1), 1757–1817, doi:10.1029/1999JE001059.

Morris, R. V., G. Klingelhöfer, C. Schröder, D. S. Rodionov, A. Yen, D. W. Ming, P. A. De Souza, I. Fleischer, T. Wdowiak, and R. Gellert (2006), Mössbauer mineralogy of rock, soil, and dust at Gusev crater, Mars: Spirit's journey through weakly altered olivine basalt on the plains and pervasively altered basalt in the Columbia Hills, *Journal of Geophysical Research: Planets (1991–2012)*, *111*(E2).

Nesbitt, H. W., and G. M. Young (1982), Early Proterozoic climates and plate motions inferred from major element chemistry of lutites, *Nature*, *299*(5885), 715–717.

Perrett, G. M., J. L. Campbell, S. Glasauer, and R. Pardo (2014), Quantitative determination of mineral phase effects observed in APXS analyses of geochemical reference materials, *X-Ray Spectrometry*, *43*(6), 359–366.

Rieder, R., R. Gellert, J. Brückner, G. Klingelhöfer, G. Dreibus, A. Yen, and S. W. Squyres (2003), The new Athena alpha particle X-ray spectrometer for the Mars Exploration Rovers, *J. Geophys. Res.*, *108*(E12), 8066, doi:200310.1029/2003JE002150.

Thompson, L. M. et al. (2016), Potassium-rich sandstones within the Gale impact crater, Mars: The APXS perspective, *J. Geophys. Res. Planets*, 2016JE005055, doi:10.1002/2016JE005055.

Treiman, A. H. et al. (2016), Mineralogy, provenance, and diagenesis of a potassic basaltic sandstone on Mars: CheMin X-ray diffraction of the Windjana sample (Kimberley area, Gale Crater), *J. Geophys. Res. Planets*, *121*(1), 2015JE004932, doi:10.1002/2015JE004932.

VanBommel, S. J., R. Gellert, J. A. Berger, J. L. Campbell, L. M. Thompson, K. S. Edgett, M. J. McBride, M. E. Minitti, I. Pradler, and N. I. Boyd (2016), Deconvolution of distinct lithology chemistry through oversampling with the Mars Science Laboratory Alpha Particle X-Ray Spectrometer, *X-Ray Spectrom.*, doi:10.1002/xrs.2681.

Vaniman, D. T. et al. (2014), Mineralogy of a Mudstone at Yellowknife Bay, Gale Crater, Mars, *Science*, *343*(6169), 1243480, doi:10.1126/science.1243480.

Yen, A. S. et al. (2017), Multiple stages of aqueous alteration along fractures in mudstone and sandstone strata in Gale Crater, Mars, *Earth and Planetary Science Letters*, doi:10.1016/j.epsl.2017.04.033.

3.7. Supplemental Materials

Supplementary information is presented in Figure 3-S1 below.

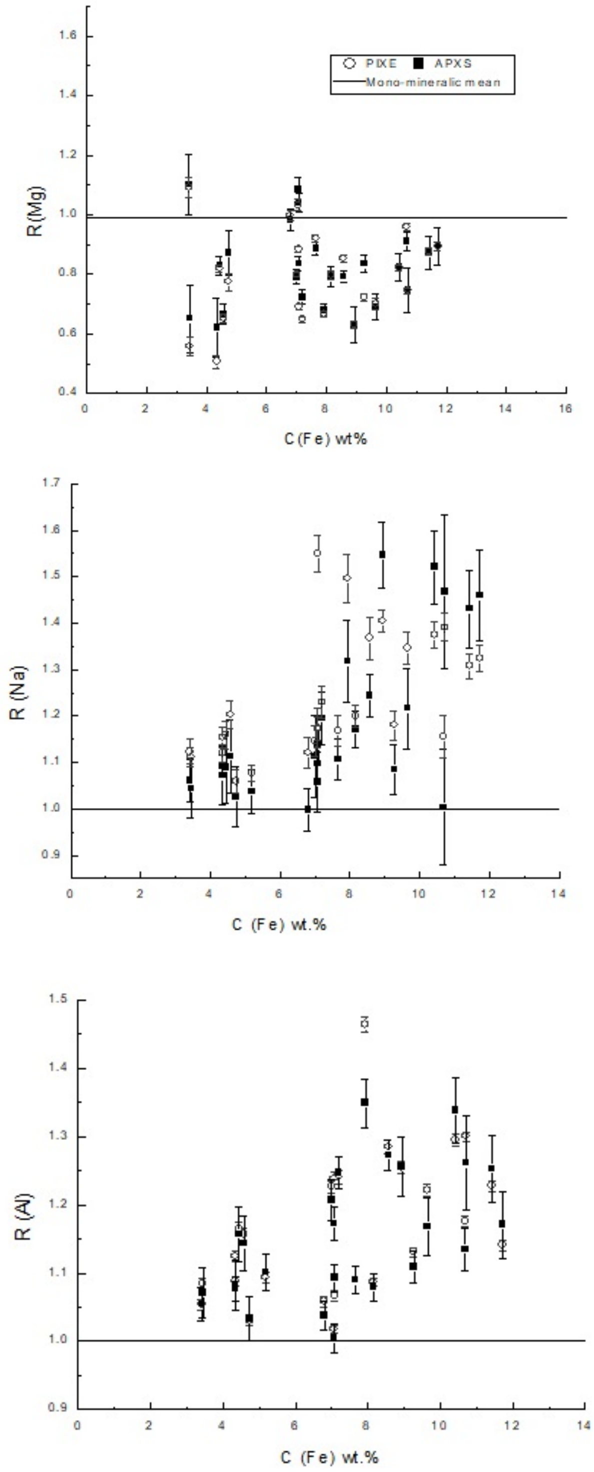

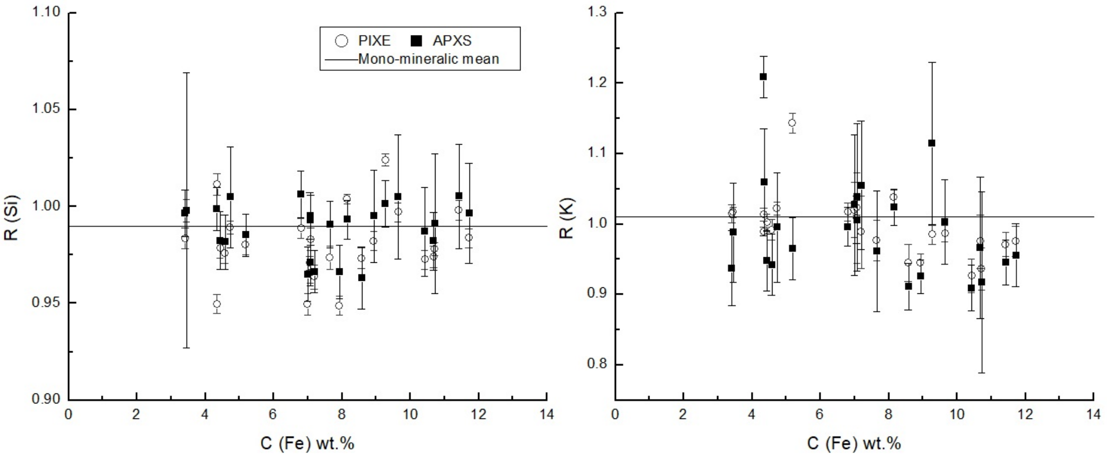

Figure 3-S1: Comparison of *R*-values for PIXE (open symbols) and APXS (closed symbols) analyses of the same georeference materials (reproduced with permission from *Flannigan and Campbell* [2017]). Hetergeneous matrix effects are apparent in the light elements Na, Mg, and Al, whereas Si and K are less affected. The attenuation of Na and Al by Fe is overestimated with higher Fe concentrations because the two elements are located within felsic minerals; they are not intimately mixed with Fe on a sub-µm scale. Similarly, the attenuation of Mg is under-estimated. Mg is located in the mafic minerals and is not dispersed in the felsic minerals, thus the attenuation calculated based on the assumption of homogeneity contains additional error.

Chapter 4

4. A Global Mars Dust Composition Refined by the Alpha Particle X-ray Spectrometer in Gale Crater

4.1. Chapter Summary and Key Points

Modern Martian dust is similar in composition to the global soil unit and bulk basaltic Mars crust, but it is enriched in S and Cl. The Alpha Particle X-ray Spectrometer (APXS) on the Mars Science Laboratory *Curiosity* rover analyzed airfall dust on the Science Observation Tray (o-tray) in Gale Crater to determine dust oxide compositions. The o-tray dust has the highest concentrations of SO_3 and Cl measured in Mars dust (SO_3 8.3%; Cl 1.1 wt.%). The molar S/Cl in the dust (3.35 ± 0.34) is consistent with previous studies of Martian dust and soils (S/Cl = 3.7 ± 0.7). Fe is also elevated ~25% over average Mars soils and the bulk crust. These enrichments link airfall dust with the S-, Cl-, and Fe-rich, X-ray amorphous component of Gale Crater soil. Dust and soil have the same S/Cl, constraining the surface concentrations of S and Cl on a global scale.

4.2. Introduction

Airfall dust is pervasive on Mars as suspended particulates in the atmosphere and as airfall deposits that coat many rock, soil, and given time, spacecraft hardware surfaces. The Martian dust cycle is closely linked to soil homogenization, with aeolian and other processes producing and mixing fine S- and Cl-rich material to form a globally homogeneous unit [*Yen et al.*, 2005, 2013]. The chemical and mineralogical make-up of the dust is therefore critically important for interpreting modern S and Cl cycles on the surface of Mars and for analyzing dusty surfaces both in situ and from orbit.

The chemical composition of Martian dust was previously estimated from Alpha-particle X-ray Spectrometer (APXS) measurements of accumulated surface dust or airfall dust captured by rover magnets by the Pathfinder and Mars Exploration Rover (MER) missions [*Rieder et al.*, 1997; *Goetz et al.*, 2005; *Yen et al.*, 2005, 2013]. These in situ observations of Martian dust indicate a S- and Cl-rich basaltic composition with a constant molar S/Cl of 3.7 ± 0.7 (Table 4-1). An ambiguity in deriving dust compositions from APXS measurements of surface dust is the possible contribution from admixed aeolian fines sourced from local rocks that do not represent the airfall dust. MER magnets more likely sampled the suspended atmospheric dust and had elevated Ti, Cr, Fe, S, and Cl relative to soil; however, larger saltated grains unrepresentative of dust were observed on the magnets [*Madsen et al.*, 2003; *Bertelsen et al.*, 2004; *Goetz et al.*, 2005]. The aluminum hardware over the MER magnets prevented Al analysis as well as calculation of oxides [*Goetz et al.*, 2005].

New APXS measurements of airfall Martian dust have been possible in Gale Crater on the titanium Science Observation Tray (o-tray), which is mounted horizontally on the front of the Mars Science Laboratory (MSL) rover, *Curiosity* (Fig. S1) [*Anderson et al.*, 2012]. The standard APXS calibration does not apply to the o-tray because the dust layer is thinner than the APXS sampling depth. The depth within a sample from which 90% of the X-rays are emitted (D_{90}) increases predictably with increasing atomic number (Z), ranging from ~2 µm for Na to ~90 µm for Fe in a basaltic matrix [*Rieder et al.*, 2003; *Brückner et al.*, 2008]. Airfall dust on the o-tray is uniform in thickness and composition and thus oxides are calculated by directly comparing the observed and modeled X-ray yields from the APXS. Here, we expand on the *Curiosity* dust measurements by modeling the APXS X-ray yields of a thin sample on the o-tray in order to calculate the oxide concentrations of airfall dust in Gale Crater.

Table 4-1: Elemental compositions of in situ soil and o-tray dust in Gale Crater and related Mars compositions

	Gale Crater			MER		
	Soil[a]	O-tray dust Sol 177	O-tray dust Sol 571	Gusev Crater Dust[b]	Meridiani Planum Dust[c]	Average Martian Soil[d]
SiO_2	43.0 ± 0.5[e]	38.6 ± 4.0	39.3 ± 1.7	45.0 ± 0.5	45.0 ± 0.3	45.41
TiO_2 [f]	1.10 ± 0.03	1.05 ± 0.18	1.06 ± 0.09	0.89 ± 0.08	1.01 ± 0.07	0.90
Al_2O_3	9.41 ± 0.19	9.32 ± 0.77	8.91 ± 0.39	9.56 ± 0.16	9.14 ± 0.09	9.71
FeO*	20.1 ± 0.3	21.6 ± 4.2	21.0 ± 2.2	16.5 ± 0.15	17.5 ± 0.04	16.73
MnO	0.42 ± 0.01	0.46 ± 0.25	0.42 ± 0.10	0.31 ± 0.02	0.34 ± 0.01	0.33
MgO	8.27 ± 0.17	8.08 ± 0.53	8.31 ± 0.38	8.25 ± 0.15	7.57 ± 0.08	8.35
CaO	7.17 ± 0.08	7.13 ± 1.23	7.04 ± 0.60	6.17 ± 0.07	6.54 ± 0.04	6.37
Na_2O	2.78 ± 0.14	2.73 ± 0.37	2.75 ± 0.22	2.9 ± 0.3	2.22 ± 0.19	2.73
K_2O	0.45 ± 0.02	0.44 ± 0.25	0.47 ± 0.09	0.49 ± 0.07	0.48 ± 0.06	0.44
P_2O_5	0.85 ± 0.05	n.d.	n.d.	0.91 ± 0.09	0.93 ± 0.09	0.83
SO_3	5.12 ± 0.07	8.01 ± 0.94	8.34 ± 0.42	7.61 ± 0.13	7.28 ± 0.07	6.16
Cl	0.64 ± 0.01	1.06 ± 0.27	1.08 ± 0.12	0.88 ± 0.03	0.78 ± 0.01	0.68

[a]Disturbed soil target Sourdough Sol 673 (Fig. 1). [b]Gobi1_soil, Sol 71 [*Gellert et al.*, 2006]. [c]MontBlanc_LesHauches Sol 60 [*Morris et al.*, 2006]. [d]From [*Taylor and McLennan*, 2010]. [e]The relative percent error shown is the larger of either the 2σ statistical fit error or the range in simulated APXS yield (Fig. 2a). [f]The Ti signal from the o-tray precludes Ti analysis; Ti in the dust is assumed to be the same as the soil (before renormalization). *Total iron reported as FeO.

4.3. Methods

Airfall dust on the o-tray was measured by APXS on Sols 177 and 571 (Sol = 24.6 h; Figure 4-1, 4-S1). Upon landing on August 6, 2012, the MSL skycrane retrorockets lofted surface fines from a depth of several cm, and a thin layer settled onto the o-tray. Navigation camera (Navcam) images [*Maki et al.*, 2012] confirmed that these fines were subsequently cleaned off of the center of the o-tray by the vibration and movement of fines scooped from the Rocknest sand shadow and portioned to the o-tray for analysis (sols 91-95) [*Berger et al.*, 2014]. The vibration and movement of fines was due to *Curiosity's* sampling subsystem vibration mechanism, which also caused the Rocknest fines to vibrate off the tray by Sol 129 [*Anderson et al.*, 2012]. On Sol 284, drill fines from a drilled mudstone target named Cumberland were portioned to the center of the tray. The drilled material had a finer grain size and was more cohesive than the scooped Rocknest fines [*Minitti et al.*, 2013], and neither wind, sampling subsystem vibrations, or rover tilt caused measureable movement of the drill fines on the o-tray. To exclude these fines from the APXS field of view (FOV) on Sol 571, the instrument was positioned ~2 cm laterally from the center of the o-tray (Fig. 1b). The total dust accumulation time as of the Sol 571 measurement was between 442 and 471 sols.

Particle-induced X-ray emission (PIXE) and X-ray fluorescence (XRF) spectrometry are the basis of the APXS technique [*Gellert et al.*, 2006; *Campbell et al.*, 2012]. The MSL APXS and its related spectrum fitting code, GUAPX, are described previously [*Gellert et al.*, 2009; *Campbell et al.*, 2011a, 2011b, 2012]. Element peak areas, which are directly proportional to elemental abundances in the sample, were calculated from APXS spectra with GUAPX. Peak areas are obtained using a non-linear least-squares spectrum fitting method, and are converted to element concentrations using matrix corrections, then converted to oxide concentrations whose sum is then normalized to 100 wt.%. Iterations are repeated until the concentrations are consistent. Error is reported as 2σ fit error.

Because the GUAPX approach requires an infinitely thick (bulk) sample (≥ 1 mm), we instead derived dust oxide concentrations from the simulated X-ray yield of a thin layer of bulk soil composition on the o-tray. To do this, we used the computer code APX-Yield [*Schmidt et al.*, 2014; *Campbell et al.*, 2014; *Berger et al.*, 2014], which employs GUAPX sub-routines to calculate the yield of characteristic X-rays for elements from layered samples using fundamental PIXE and XRF principles. The compositions of the thin layer and substrate are input to calculate the X-ray yield from each at a given layer thickness. Conversion of these calculated absolute X-ray yields to spectral peak areas would then require knowledge of instrumental effects such as geometric efficiency. This is not practical, and so we employ the ratios of thin samples to bulk samples, thereby removing instrumental effects. Deviations of observed thin/bulk peak area ratios from the modeled thin/bulk yield ratios are directly proportional to enrichment (or depletion) of elements in the thin sample (dust), relative to the bulk sample (soil). This is quantified by the dust correction factor *DCF* for each element *i.* We can thus compare elemental APXS spectral peak areas to the element APX-Yield modeled yields by the relationship

$$DCF_i \left(\frac{PA_D}{PA_S}\right)_i = f_A \left(\frac{Y_D}{Y_S}\right)_i \qquad \text{eq. 1}$$

where *PA* is the peak area, *Y* is the modeled yield, and subscripts *D* and *S* denote airfall dust and soil, respectively. The areal correction factor f_A is discussed below. This relationship allows the derivation of a dust oxide correction factor *DCF*

$$DCF_i = f_A \left(\frac{Y_D}{Y_S}\right)_i \left(\frac{PA_S}{PA_D}\right)_i \qquad \text{eq. 2}$$

which we used to calculate each dust oxide based on corresponding soil oxides by

$$Dust\ oxide = \frac{Soil\ oxide}{DCF}. \qquad \text{eq. 3}$$

At a given thickness, f_A is the same for all oxides. These oxide values were then renormalized to 100%. The disturbed soil target Sourdough (Sol 673; Figure 4-S2) was used as the bulk soil because it had a shorter standoff distance than most other overnight soil targets, and thus had better counting statistics and relatively smaller fitting error. Soil was employed as the bulk sample because it is the best, first approximation of the dust composition. Any bulk sample with a similar composition would yield the same dust oxides within error; therefore, the accuracy of the technique is not sensitive to the bulk composition from which the modeled layer composition is derived.

Several assumptions were necessary to apply the APX-Yield model to measurements of dust on the o-tray. The code assumes that the layers have uniform thickness and homogeneous composition at the micrometer scale, which is reasonable for the airfall dust. Although the dust sample likely has only partial areal coverage, previous work shows that the APXS signal varies across the spectrum with changes in areal coverage, and is approximately proportional to the percent areal coverage of the particulate according to the areal coverage correction factor f_A [*Berger et al.*, 2014]. We derived f_A from the Na peak area ratio (Figure 4-2), assuming the dust was thick with respect to the D_{90} of Na (~3 μm) [e. g., *Rieder et al.*, 2003]. The Martian dust probably formed sub-mm scale porous aggregates as it was deposited [e.g., *Johnson et al.*, 2002], which we assumed had a uniform mean thickness across the larger-scale ~1.7 cm diameter APXS FOV. The APXS signal also varies predictably with differences in instrument standoff distance, which were corrected with geometric normalization factors [*Gellert et al.*, 2006].

APXS measurements of the o-tray have additional considerations. The Ti signal from the o-tray precludes analysis of Ti in the dust, so we assumed the TiO_2 concentrations of the dust and the soil were the same (1.1 wt.%), which is consistent with apparent TiO_2 content in MER dust [*McGlynn et al.*, 2012]. Increased yields due to secondary fluorescence of Ca (6-7% increase) and K (3-4% increase) in the thin dust sample by the Ti substrate [e.g., *Berger et al.*, 2014] were modeled and corrected using APX-Yield software. Secondary fluorescence of chlorine and lighter elements due to Ti are modeled at <1% and were not corrected. APXS and Laser Ablation Inductively Coupled Plasma Mass Spectrometry analyses of the Ti metal used for the o-tray were reported previously [*Berger et al.*, 2014]. Iron (0.24 counts/s) and nickel (0.03 counts/s) were the only trace elements in the Ti metal detectable by the testbed flight-equivalent APXS, and these are subtracted from the dusty o-tray peak areas.

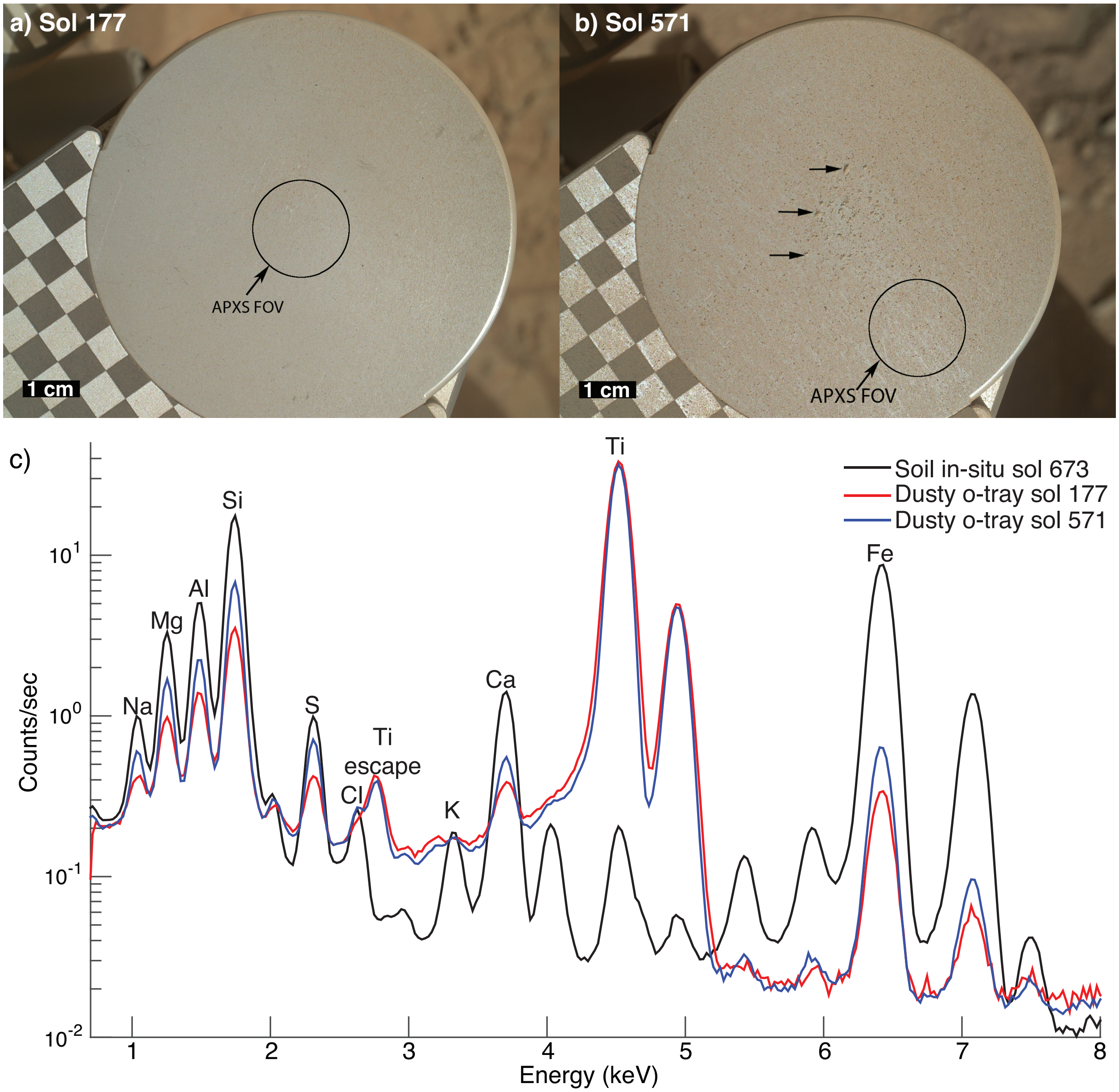

Figure 4-1: MAHLI images of the o-tray on sols (a) 177 [0177MH0001320010102444E01] and (b) 571 [0571MH0003600010201899C00] and (c) APXS spectra of the dusty o-tray and in situ soil. Selected Kα and the Ti escape peaks are labeled. The ~1.7 cm diameter APXS FOV was shifted 2 cm to the right on Sol 571 to avoid the Sol 284 Cumberland drill fines in the center of the o-tray (representative drill fine aggregates indicated with smaller arrows).

4.4. Results

Camera observations of the dusty o-tray on Sols 177 and 571 are consistent with a thin layer of airfall dust that increased in areal coverage, and possibly thickness, over time. Mars Hand Lens Imager (MAHLI) [*Edgett et al.*, 2012] images of the o-tray, obtained before APXS measurements during daylight hours (13:50 on Sol 177; 13:35 on Sol 571), show the dull red-brown hue of the layer of dust (Figure 4-1). The o-tray appears darker on Sol 571, likely due to a greater areal coverage of dust obscuring more of the light-gray titanium metal. Much of the dust texture is smaller than the 60.4 µm/pixel MAHLI resolution at a 15.2 cm working distance; however, uniformly distributed rounded dust aggregates (less than ~300 µm in diameter) are apparent. At this resolution, we cannot confirm whether saltating sand particles < 200 µm were on the tray; however, modeling suggests saltating grains ≤ 500 µm on Mars are unlikely to exceed 0.5 m in height [*Renno et al.*, 2014]. The Sol 571 o-tray image also includes linear streaks of unknown origin in the dust and indicates a change in coverage relative to Sol 177. Streaking may be evidence of aeolian pushing or rolling of dust aggregates, similar to "nick-like disturbances" observed by MER on dusty surfaces at Gusev Crater [*Sullivan et al.*, 2008]. The relative Si and Fe yields constrain the uniformity of the dust relief because they have contrasting D_{90} (~7 µm and ~90 µm, respectively). Si/Fe drops from 8.7 ± 0.3 on sol 177 to 8.1 ± 0.2 on sol 571, which is consistent with the modeled yield and indicates an increase in thickness with uniform coverage. Nevertheless, we increased the modeled thickness range to encompass this change in Si/Fe ratio, thus increasing the reported error to include uncertainty due to deviations in uniformity.

The APXS results indicate that the dust on the o-tray has a composition similar to that of Martian soil, but with elevated FeO, SO_3, and Cl (Table 4-1; Figures 4-1 and 4-2). We report Fe, S, and Cl as FeO, SO_3, and Cl, respectively, in keeping with previous literature on Martian APXS chemistry; oxidation state cannot be determined by APXS. The APXS signal of Sol 571 dust is higher than that of Sol 177 consistent with a larger sample volume due to greater areal coverage and increased thickness. Figure 4-2a presents the Kα peak area ratios between the dusty o-tray and the bulk soil. For a given thickness, the progressive drop in peak area ratio with increasing Z results from the sample being thin with respect to the interrogation depth D_{90}. The Kα peak area ratios fit within the modeled yield of a layer with thicknesses 0.65 – 1.00 mg/cm^2 with f_A = 0.26 (Sol 177) and 0.95 – 1.20 mg/cm^2 with f_A = 0.38 (Sol 571) (Figure 4-2). Notable exceptions are S (enriched by 65 – 69%) and Cl (enriched by 75 – 76%), which have the same S/Cl value observed in the soil (Figure 4-2b). Trace elements (e. g., P, Ni, Zn, Br) are below detection limits owing to the small sample volume. The Sol 177 and 571 peak area ratios are within error and therefore show no significant differences between the two o-tray measurements and no evidence of contribution from the nearby Cumberland drill fines.

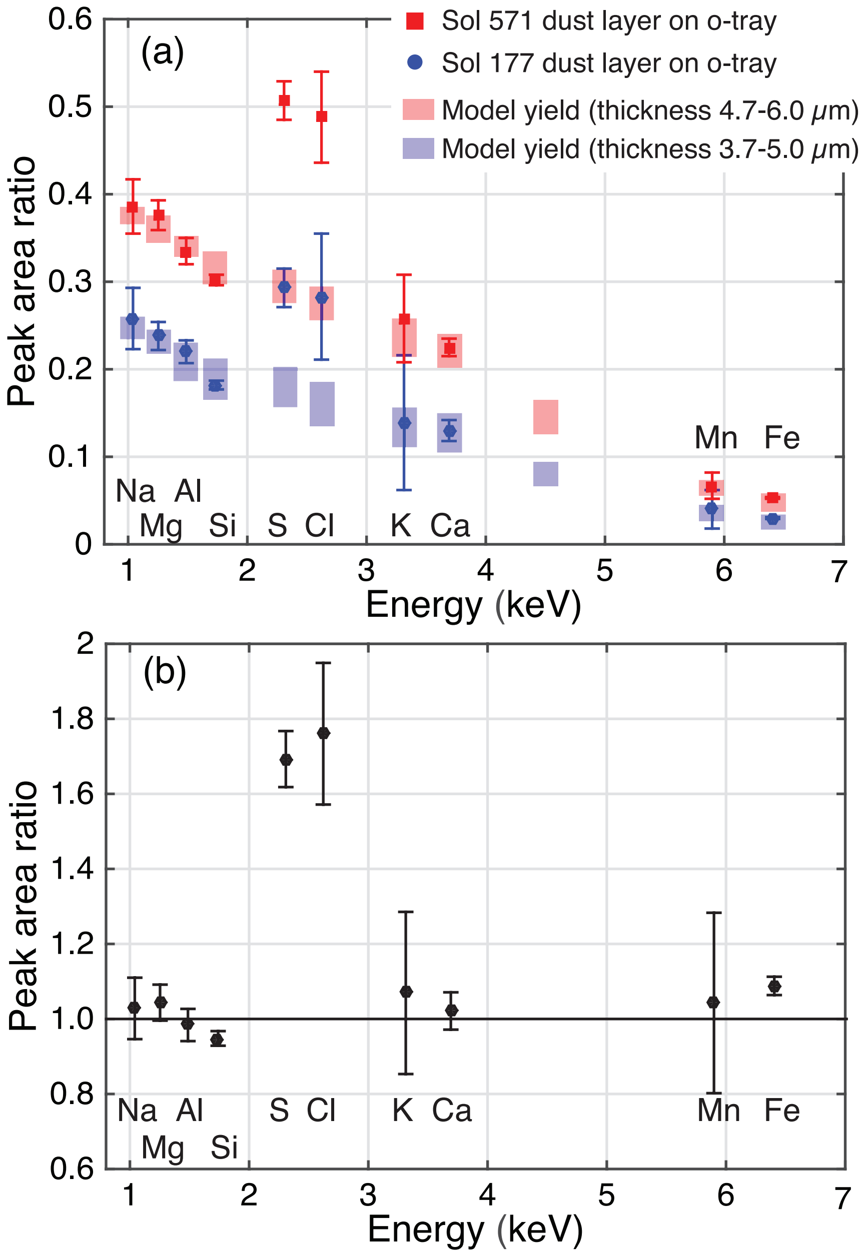

Figure 4-2: APXS peak areas of the dust on the o-tray, shown as ratios to (a) the peak areas of in situ, bulk soil (Sourdough; sol 673) and (b) the modeled APXS yield of a thin layer of soil with the composition of Sourdough and a thickness of 1.1 mg/cm^2. The blue and red boxes in (a) show the modeled APXS yield of a layer with soil composition. All detected elements are within the 5-10% error of the modeled yield, with the exceptions Fe, S, and Cl, which are enriched, maintaining the same S/Cl ratio as the soil.

4.5. Discussion

APXS results for the dust on the o-tray in Gale Crater are congruent with the Martian dust and soil compositions observed by previous Mars rover missions [*Foley et al.*, 2003b; *Goetz et al.*, 2005; *Yen et al.*, 2005]. O-tray dust oxide values are similar to widespread, basaltic soil types examined in Gale Crater, Gusev Crater, and Meridiani Planum (e.g., Laguna Class Soil) [*Ming et al.*, 2008; *Morris et al.*, 2008; *Yen et al.*, 2013], as well as by the Viking [*Clark et al.*, 1982] and Pathfinder missions [*Foley et al.*, 2003a]. Similar to six MER undisturbed soil targets at Gusev Crater and Meridiani Planum classified as "bright dust" (MER dust) [*Yen et al.*, 2005], the MSL o-tray dust also has elevated S and Cl relative to common soils and the same molar S/Cl (3.7 ± 0.7). The o-tray dust, however, has 12 ± 3% greater SO_3 and 31 ± 11% greater Cl than typical MER dust targets (Figure 4-3a; Table 4-1). Compared to MER dust and average soils, FeO is also enriched in the o-tray dust by ~25% (Figure 4-3b; Table 4-1). The Fe enrichment is smaller when compared to Gale Crater soils, which have higher FeO content (17.3 – 20.8 wt.%) than the average value (16.7 wt.%) determined from previous missions [*Taylor and McLennan*, 2010] owing to the generally higher FeO in Gale bedrock [*Schmidt et al.*, 2014]. Compositional differences between the o-tray dust and MER dust likely result from the different sampling and measurement conditions. The MER dust was measured on undisturbed ground surfaces that had accumulated dust over an unknown amount of time; it is uncertain how accurately the surface dust represents atmospheric dust because saltating and creeping fines may have mixed with the surface dust [e. g., *McGlynn et al.*, 2011]. The influence of local materials is also evident in the skew of the MER dust oxide values toward the local soils (Figure 4-3). Nonetheless, the compositional similarities of the o-tray airfall dust, surface dust, and typical Martian soils link the materials on a global scale.

Curiosity's investigation of the aeolian sand shadow named Rocknest (Sols 57 – 100) constrains the dust chemistry and mineralogy because the scooped and sieved material (< 150 μm) delivered to onboard instruments likely contained a fraction of dust. Such accumulations of aeolian sediment are commonly a mixture of sand and dust that retain the compositional characteristics of local and regional rocks as well as atmospheric dust [e.g., *Bagnold*, 1941; *Bishop et al.*, 2002; *Bridges and Muhs*, 2012]. In the o-tray dust, no elements quantified by APXS ($Z \geq 11$) exhibit the same magnitude of enrichment as S and Cl (Figure 4-2b), indicating that the two are not each bonded with a single cation (Na^+, K^+, Mg^{2+}, Ca^{2+}, Fe^{2+}, Fe^{3+}) in one salt phase. S and Cl may instead be adsorbed ions, coordinated with lighter elements (e.g., perchlorate), and/or distributed in a mixture of multiple salt phases (e.g., Mg-, Ca-sulfates, halite). One S-bearing crystalline phase, anhydrite (1.5 ± 0.7 wt.%), was detected in the Rocknest deposit by the Chemistry and Mineralogy (CheMin) XRD instrument, but it does not account for all of the SO_3 measured by APXS (5.5 ± 0.1 wt.%) [*Bish et al.*, 2013]. Similarly, evolved gas analysis (EGA) by the Sample Analysis at Mars instrument (SAM) yielded the equivalent of 0.5 – 3.5 wt.% SO_3 in both oxidized and reduced sulfur compounds consistent with minor amounts of sulfides and sulfates/sulfites [*McAdam et al.*, 2014]. The remaining ~3 wt.% SO_3 could be associated with an X-ray amorphous phase (see below) [*McAdam et al.*, 2014]. Oxychlorine compounds (e.g., perchlorates, chlorates) detected by SAM in the Rocknest deposit at 0.3 – 0.5 wt.% ClO_4^- account for much, but not all of the Cl detected by APXS (0.69 ± 0.03 wt.%) [*Glavin et al.*, 2013; *Leshin et al.*, 2013]. Neither halides nor Ca- or Mg-perchlorates were present above the CheMin detection limit (1 – 2 wt.%) [*Bish et al.*, 2013]. Chlorine in APXS analyses of Gale Crater rocks is also correlated with oxychlorine compounds inferred from SAM measurements [*Archer et al.*, 2015], confirming they are stable at the Martian surface in modern aeolian deposits as well as in mudstones deposited before 1.6 Ga [*Farley et al.*, 2014]. Oxychlorine compounds can be formed via multiple pathways, including oxidation reactions in the atmosphere involving aerosols [*Catling et al.*, 2010], therefore they are a likely Cl-bearing phase in the dust.

A substantial fraction of the Rocknest sample (~45-50 wt.%) was amorphous (i.e., without coherent X-ray diffraction), as determined by CheMin [*Blake et al.*, 2013; *Morris et al.*, 2015]. The relative proportions of crystalline phases, along with the bulk chemistry of Rocknest (represented by the APXS target Portage; Sol 89 [*Gellert et al.*, 2013]), enable mass balance calculations which indicate that most of the S and Cl, and much of the Fe, are contained in the amorphous fraction (Figure 4-3) [*Blake et al.*, 2013; *Dehouck et al.*, 2014; *Morris et al.*, 2015]. The crystalline component of Rocknest accounts for

~50 wt.% of the Fe_{Total} ($Fe + FeO + Fe_2O_3$), primarily as FeO in basaltic minerals, and the remainder is associated with the amorphous fraction [*Bish et al.*, 2013]. Because the amorphous component of Rocknest contains most of the S and Cl in the aeolian deposit, and a significant fraction of the Fe, it is likely closely related to the airfall dust, which is also elevated in these three elements relative to typical Martian soils.

Approximately 20 wt.% of the amorphous component of Rocknest is Fe_{Total}, indicating the presence of an X-ray amorphous ferric nanophase oxide (npOx) [*Blake et al.*, 2013; *Morris et al.*, 2015]. This is consistent with the presence of npOx in soils at Gusev Crater and Meridiani Planum, where npOx in the dust is yet higher [*Morris et al.*, 2006, 2008, 2013]. Mössbauer mineralogy of MER soils shows a positive correlation of Fe^{3+}/Fe_{Total} with SO_3 in the basaltic Laguna Class soils at a ratio of 0.051 ± 0.009 ($R^2 = 0.52$) [*Morris et al.*, 2008]. *Curiosity* does not have a Mössbauer instrument, and the APXS cannot measure Fe oxidation state; however, assuming this relationship extends to Gale Crater soils and dust [e.g., *Morris et al.*, 2013], we extrapolated possible Fe^{3+}/Fe_{Total} values based on SO_3 content to calculate Fe_2O_3 for Gale Crater soils and the o-tray dust (Figure 4-S3). The estimated Fe_2O_3 values for Gale Crater indicate a positive correlation between ferric Fe and both SO_3 and Cl ($R^2 = 0.90$ and 0.82, respectively). This suggests the three elements are associated, maintaining consistent S/Fe^{3+} and Cl/Fe^{3+} ratios in the soil, dust, and amorphous fraction. The Fe, S, and Cl are most enriched in the amorphous material, with dust intermediate between that and soils. We emphasize that this conclusion is based on an assumption about oxidation state that cannot be verified with the APXS, and we do not infer that the dust and the amorphous material are necessarily the same. Nevertheless, the similarity of S/Cl at the three distant Mars rover sites couples the Fe, S, and Cl enrichments in the o-tray dust to the gradational positive correlations between S, Cl, and Fe^{3+}/Fe_{Total} in MER soils and dust. This is evidence that the global dust is enriched in npOx associated with S and Cl, which is mixed into the soils and, therefore, dust is a key part of soil-forming processes and the distribution of Fe, S, and Cl on the Martian surface.

The global compositional similarities of soil and dust support models of the dust cycle and soil formation that include the global circulation of dust [*McSween Jr. and Keil*, 2000; *Bishop et al.*, 2002; *McGlynn et al.*, 2011]. Aeolian processes suspend the finest fraction of surface fines (1.4 – 2.5 μm) [*Clancy et al.*, 2003], which is mixed in the atmosphere by local dust devils and seasonal, regional dust storms. Global dust storms are less well understood, but occur approximately every 1 – 3 Mars years [*Liu et al.*, 2003] (1 Mars year = 687 d). The dust is re-deposited to the surface by settling where it can be re-mixed into the soil by aeolian processes [e. g., *McGlynn et al.*, 2011]. The arid Martian climate enhances dust availability, in contrast to Earth where it is restricted by widespread liquid water, preventing global dust storms [*Rafkin et al.*, 2013]. On Mars, the dust distributes the S- and Cl-bearing fines globally and thus is an active S and Cl cycling process at the surface.

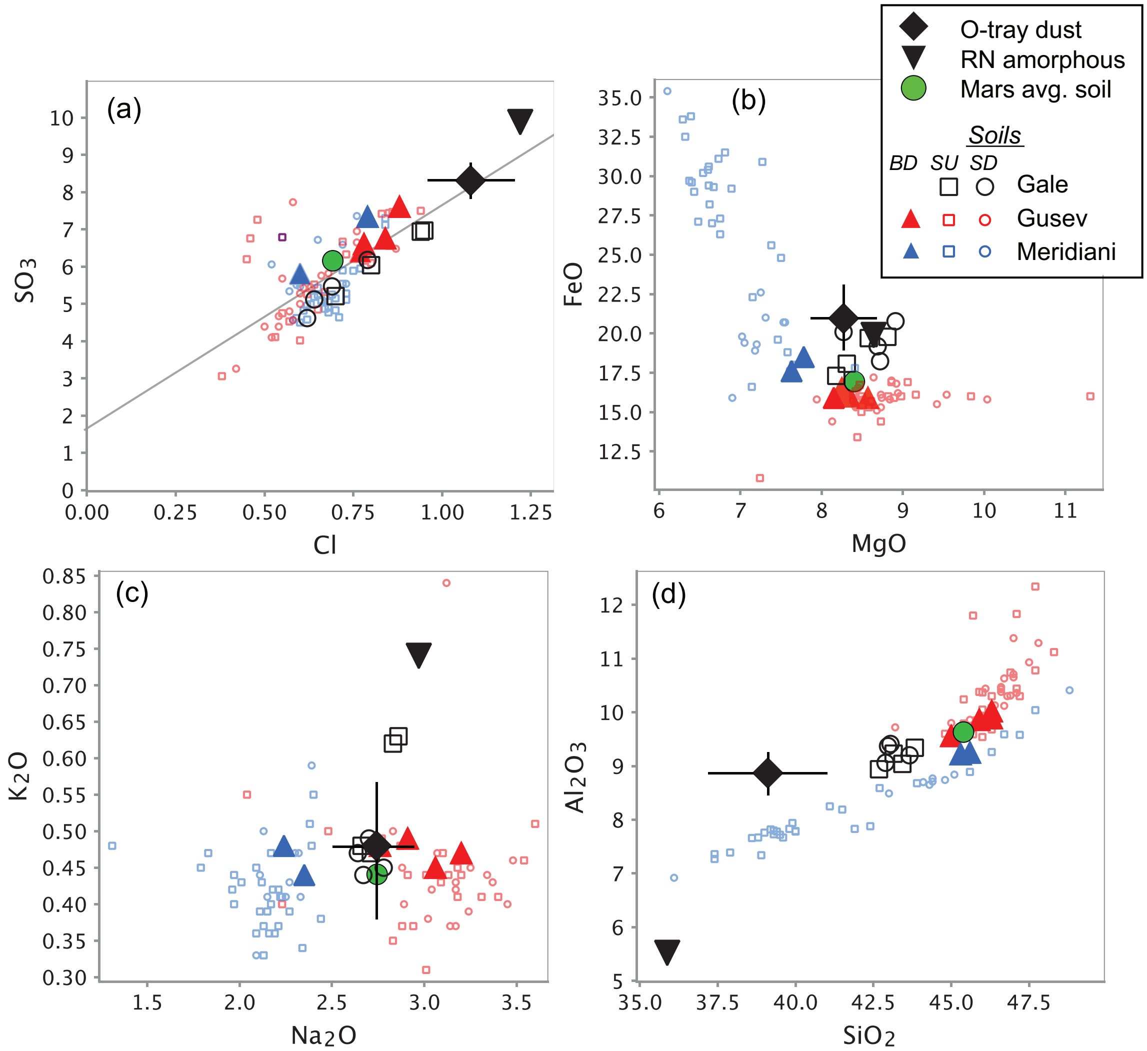

Figure 4-3: Martian dust composition relative to soils in Gale Crater, Gusev Crater, and Meridiani Planum (wt. %). The estimated XRD amorphous component of Rocknest aeolian fines (RN amorphous) is plotted [*Morris et al.*, 2015]. Bright dust (BD), undisturbed soil (SU), and disturbed soil (SD) are indicated. The estimated average Mars soil composition is shown (green circle) [*Taylor and McLennan*, 2010]. Silica- and sulfate-rich MER soils are omitted. Error is shown for the o-tray dust and is contained within the symbols for Gale soils and MER bright dust. Error is not shown for MER soils, but is similar to Gale soils.

4.6. Conclusion

APXS results for the dust on the *Curiosity* rover o-tray in Gale Crater represent a refinement of the Martian global dust compositions observed by previous Mars missions. As observed around the planet, Martian dust has a globally uniform composition related to soils. The dust is enriched in S, Cl, and Fe relative to typical soils, but with the same S/Cl ratio (~3.7). These observations support models that link the global dust cycle and soil formation, where the fine dust is globally distributed by aeolian processes and is input to the surface where it becomes a component of the soil. The dust is thus an important agent for distributing S and Cl globally to the surface of modern Mars.

4.7. References

Anderson, R. C. et al. (2012), Collecting Samples in Gale Crater, Mars; an Overview of the Mars Science Laboratory Sample Acquisition, Sample Processing and Handling System, *Space Sci. Rev.*, *170*(1-4), 57–75, doi:10.1007/s11214-012-9898-9.

Archer, P. D. et al. (2015), Oxychlorine Species on Mars: The Gale Crater Story, vol. 46, p. 2971.

Bagnold, R. A. (1941), *The Physics of Blown Sand and Desert Dunes*, Methuen & Company : William Morrow.

Berger, J. A. et al. (2014), MSL-APXS titanium observation tray measurements: Laboratory experiments and results for the Rocknest fines at the Curiosity field site in Gale Crater, Mars, *J. Geophys. Res. Planets*, 2013JE004519, doi:10.1002/2013JE004519.

Bertelsen, P. et al. (2004), Magnetic Properties Experiments on the Mars Exploration Rover Spirit at Gusev Crater, *Science*, *305*(5685), 827–829, doi:10.1126/science.1100112.

Bish, D. L. et al. (2013), X-ray Diffraction Results from Mars Science Laboratory: Mineralogy of Rocknest at Gale Crater, *Science*, *341*(6153), 1238932, doi:10.1126/science.1238932.

Bishop, J. L., S. L. Murchie, C. M. Pieters, and A. P. Zent (2002), A model for formation of dust, soil, and rock coatings on Mars: Physical and chemical processes on the Martian surface, *J. Geophys. Res.*, *107*(5097), doi:10.1029/2001JE001581.

Blake, D. F. et al. (2013), Curiosity at Gale Crater, Mars: Characterization and Analysis of the Rocknest Sand Shadow, *Science*, *341*(6153), 1239505, doi:10.1126/science.1239505.

Bridges, N. T., and D. R. Muhs (2012), Duststones on Mars: source, transport, deposition, and erosion, *Sedimentary Geology of Mars*, *102*, 169–182.

Brückner, J., G. Dreibus, R. Gellert, S. W. Squyres, H. Wänke, A. Yen, and J. Zipfel (2008), Mars Exploration Rovers: chemical composition by the APXS, in *The Martian Surface*, vol. 1, edited by J. F. Bell III, pp. 58 – 101, Cambridge University Press, New York.

Campbell, J. L., J. A. Maxwell, S. M. Andrushenko, S. M. Taylor, B. N. Jones, and W. Brown-Bury (2011a), A GUPIX-based approach to interpreting the PIXE-plus-XRF spectra from the Mars Exploration Rovers: I. Homogeneous standards, *Nuclear Instruments and Methods in Physics Research Section B: Beam Interactions with Materials and Atoms*, *269*(1), 57–68, doi:10.1016/j.nimb.2010.10.004.

Campbell, J. L., A. M. McDonald, G. M. Perrett, and S. M. Taylor (2011b), A GUPIX-based approach to interpreting the PIXE-plus-XRF spectra from the Mars Exploration rovers: II geochemical reference materials, *Nuclear Instruments and Methods in Physics Research Section B: Beam Interactions with Materials and Atoms*, *269*(1), 69–81, doi:10.1016/j.nimb.2010.09.014.

Campbell, J. L., G. M. Perrett, R. Gellert, S. M. Andrushenko, N. I. Boyd, J. A. Maxwell, P. L. King, and C. D. M. Schofield (2012), Calibration of the Mars Science Laboratory Alpha Particle X-ray Spectrometer, *Space. Sci. Rev.*, *170*(1-4), 319–340, doi:10.1007/s11214-012-9873-5.

Campbell, J. L. et al. (2014), The Mars Science Laboratory APXS calibration target: Comparison of Martian measurements with the terrestrial calibration, *Nucl. Instrum. Methods Phys. Res. B*, *323*, 49–58, doi:10.1016/j.nimb.2014.01.011.

Catling, D. C., M. W. Claire, K. J. Zahnle, R. C. Quinn, B. C. Clark, M. H. Hecht, and S. Kounaves (2010), Atmospheric origins of perchlorate on Mars and in the Atacama, *J. Geophys. Res. Planets*, *115*(E00E11), doi:10.1029/2009JE003425.

Clancy, R. T., M. J. Wolff, and P. R. Christensen (2003), Mars aerosol studies with the MGS TES emission phase function observations: Optical depths, particle sizes, and ice cloud types versus latitude and solar longitude, *J. Geophys. Res.*, *108*(E9), 5098, doi:10.1029/2003JE002058.

Clark, B. C., A. K. Baird, R. J. Weldon, D. M. Tsusaki, L. Schnabel, and M. P. Candelaria (1982), Chemical composition of Martian fines, *J. Geophys. Res.*, *87*(B12), 10059–10067, doi:10.1029/JB087iB12p10059.

Dehouck, E., S. M. McLennan, P.-Y. Meslin, and A. Cousin (2014), Constraints on abundance, composition, and nature of X-ray amorphous components of soils and rocks at Gale crater, Mars, *J. Geophys. Res. Planets*, 2014JE004716, doi:10.1002/2014JE004716.

Edgett, K. S. et al. (2012), Curiosity's Mars Hand Lens Imager (MAHLI) Investigation, *Space Sci. Rev.*, *170*(1-4), 259–317, doi:10.1007/s11214-012-9910-4.

Farley, K. A. et al. (2014), In Situ Radiometric and Exposure Age Dating of the Martian Surface, *Science*, *343*(6169), 1247166, doi:10.1126/science.1247166.

Foley, C. N., T. E. Economou, R. N. Clayton, and W. Dietrich (2003a), Calibration of the Mars Pathfinder alpha proton X-ray spectrometer, *J. Geophys. Res.*, *108*(E12), 8095, doi:10.1029/2002JE002018.

Foley, C. N., T. Economou, and R. N. Clayton (2003b), Final chemical results from the Mars Pathfinder alpha proton X-ray spectrometer, *J. Geophys. Res.*, *108*(E12), 8096, doi:10.1029/2002JE002019.

Gellert, R. et al. (2006), Alpha Particle X-Ray Spectrometer (APXS): Results from Gusev crater and calibration report, *J. Geophys. Res.*, *111*(E02S05), doi:200610.1029/2005JE002555.

Gellert, R., J. L. Campbell, P. L. King, L. A. Leshin, G. W. Lugmair, J. G. Spray, S. W. Squyres, and A. S. Yen (2009), The Alpha-Particle-X-Ray-Spectrometer (APXS) for the Mars Science Laboratory (MSL) Rover Mission, in *Lunar Planet. Sci., XL*, Abstract 2364.

Gellert, R. et al. (2013), Initial MSL APXS activities and observations at Gale crater, Mars, in *Lunar Planet. Sci., XLIV*, Abstract 1432.

Glavin, D. P. et al. (2013), Evidence for perchlorates and the origin of chlorinated hydrocarbons detected by SAM at the Rocknest aeolian deposit in Gale Crater, *J. Geophys. Res.*, *118*(10), 1955–1973, doi:10.1002/jgre.20144.

Goetz, W. et al. (2005), Indication of drier periods on Mars from the chemistry and mineralogy of atmospheric dust, *Nature*, *436*(7047), 62–65, doi:10.1038/nature03807.

Johnson, J. R., P. R. Christensen, and P. G. Lucey (2002), Dust coatings on basaltic rocks and implications for thermal infrared spectroscopy of Mars, *J. Geophys. Res.*, *107*, 5035, doi:10.1029/2000JE001405.

Lee, R. E., M. E. Schmidt, R. Gellert, J. L. Campbell, P. L. King, and K. S. Edgett (2014), Linking MAHLI and APXS to analyze dust coverage on Yellowknife Bay rock targets, in *Lunar Planet. Sci., XLV*, Abstract 2144.

Leshin, L. A. et al. (2013), Volatile, Isotope, and Organic Analysis of Martian Fines with the Mars Curiosity Rover, *Science*, *341*(6153), 1238937, doi:10.1126/science.1238937.

Liu, J., M. I. Richardson, and R. J. Wilson (2003), An assessment of the global, seasonal, and interannual spacecraft record of Martian climate in the thermal infrared, *J. Geophys. Res.*, *108*(E8), 5089, doi:10.1029/2002JE001921.

Madsen, M. B. et al. (2003), Magnetic Properties Experiments on the Mars Exploration Rover mission, *J. Geophys. Res.*, *108*(E12), 8069, doi:10.1029/2002JE002029.

Maki, J., D. Thiessen, A. Pourangi, P. Kobzeff, T. Litwin, L. Scherr, S. Elliott, A. Dingizian, and M. Maimone (2012), The Mars Science Laboratory Engineering Cameras, *Space Sci Rev*, *170*(1-4), 77–93, doi:10.1007/s11214-012-9882-4.

McAdam, A. C. et al. (2014), Sulfur-bearing phases detected by evolved gas analysis of the Rocknest aeolian deposit, Gale Crater, Mars, *J. Geophys. Res*, *119*(2), 373–393, doi:10.1002/2013JE004518.

McGlynn, I. O., C. M. Fedo, and H. Y. McSween (2011), Origin of basaltic soils at Gusev crater, Mars, by aeolian modification of impact-generated sediment, *J. Geophys. Res.*, *116*(E7), E00F22, doi:10.1029/2010JE003712.

McGlynn, I. O., C. M. Fedo, and H. Y. McSween (2012), Soil mineralogy at the Mars Exploration Rover landing sites: An assessment of the competing roles of physical sorting and chemical weathering, *J. Geophys. Res.*, *117*(E1), E01006, doi:10.1029/2011JE003861.

McSween Jr., H. Y., and K. Keil (2000), Mixing relationships in the Martian regolith and the composition of globally homogeneous dust, *Geochimica et Cosmochimica Acta*, *64*(12), 2155–2166, doi:10.1016/S0016-7037(99)00401-9.

Ming, D. W. et al. (2008), Geochemical properties of rocks and soils in Gusev Crater, Mars: Results of the Alpha Particle X-Ray Spectrometer from Cumberland Ridge to Home Plate, *J. Geophys. Res.*, *113*(E12S39), doi:200810.1029/2008JE003195.

Minitti, M. E. et al. (2013), MAHLI at the Rocknest sand shadow: Science and science-enabling activities, *J. Geophys. Res.: Planets*, *118*(11), 2338–2360, doi:10.1002/2013JE004426.

Morris, R. V. et al. (2006), Mössbauer mineralogy of rock, soil, and dust at Meridiani Planum, Mars: Opportunity's journey across sulfate-rich outcrop, basaltic sand and dust, and hematite lag deposits, *J. Geophys. Res.*, *111*(E12S15), doi:10.1029/2006JE002791.

Morris, R. V. et al. (2008), Iron mineralogy and aqueous alteration from Husband Hill through Home Plate at Gusev Crater, Mars: Results from the Mössbauer instrument on the Spirit Mars Exploration Rover, *J. Geophys. Res.: Planets*, *113*(E12), doi:10.1029/2008JE003201.

Morris, R. V. et al. (2013), The amorphous component in martian basaltic soil in global perspective from MSL and MER missions, in *Lunar Planet. Sci., XLIV*, Abstract 1653.

Morris, R. V. et al. (2015), Update on the Chemical Composition Of Crystalline, Smectite, and Amorphous Components for Rocknest Soil and John Klein and Cumberland Mudstone Drill Fines at Gale Crater, Mars, in *Lunar Planet. Sci., XLVI*, 16-20 Mar. 2015, United States.

Rafkin, S. C. R., J. L. Hollingsworth, M. A. Mischna, C. E. Newman, and M. I. Richardson (2013), Mars: Atmosphere and climate overview, *Comparative Climatology of Terrestrial Planets*, *1*, 55–89.

Renno, N. O., D. Halleaux, H. Elliott, and J. F. Kok (2014), The Lifting of Aerosols and Their Effects on Atmospheric Dynamics, *Comparative Climatology of Terrestrial Planets*, 355.

Rieder, R., T. Economou, H. Wänke, A. Turkevich, J. Crisp, J. Brückner, G. Dreibus, and H. Y. McSween (1997), The Chemical Composition of Martian Soil and Rocks Returned by the Mobile Alpha Proton X-ray Spectrometer: Preliminary Results from the X-ray Mode, *Science*, *278*(5344), 1771–1774, doi:10.1126/science.278.5344.1771.

Rieder, R., R. Gellert, J. Brückner, G. Klingelhöfer, G. Dreibus, A. Yen, and S. W. Squyres (2003), The new Athena alpha particle X-ray spectrometer for the Mars Exploration Rovers, *J. Geophys. Res.*, *108*(E12), 8066, doi:200310.1029/2003JE002150.

Schmidt, M. E. et al. (2014), Geochemical diversity in first rocks examined by the Curiosity Rover in Gale Crater: Evidence for and significance of an alkali and volatile-rich igneous source, *J. Geophys. Res. Planets*, *119*(1), 64–81, doi:10.1002/2013JE004481.

Sullivan, R., R. Arvidson, J. F. Bell, R. Gellert, M. Golombek, R. Greeley, K. Herkenhoff, J. Johnson, S. Thompson, and P. Whelley (2008), Wind ‐ driven particle mobility on Mars: Insights from Mars Exploration Rover observations at “El Dorado” and surroundings at Gusev Crater, *J. Geophys. Res.: Planets*, *113*(E6), doi:10.1029/2008JE003101.

Taylor, S. R., and S. McLennan (2010), *Planetary Crusts: Their Composition, Origin and Evolution*, 1st ed., Cambridge University Press.

Yen, A. S. et al. (2005), An integrated view of the chemistry and mineralogy of martian soils, *Nature*, *436*(7047), 49–54, doi:10.1038/nature03637.

Yen, A. S. et al. (2013), Evidence for a global martian soil composition extends to Gale crater, in *Lunar Planet. Sci., XLIV*, Abstract 2495.

4.8. Supplemental Materials

Supplementary information is presented in Figures 4-S1 through 4-S3 below.

Figure 4-S1. Location of the Ti Science Observation Tray (o-tray) on *Curiosity*. The MAHLI mosaic [after JPL Photojornal http://www.nasa.gov/jpl/msl/pia18390] shows the o-tray mounted on the right-front of the rover, coated with dull red-brown dust, which covers most of the surfaces of the rover. These images were acquired on Sol 613, 42 sols

after the Sol 571 APXS measurement of the dusty o-tray. For scale, the o-tray is 7.5 cm in diameter and the wheels are 40 cm in width.

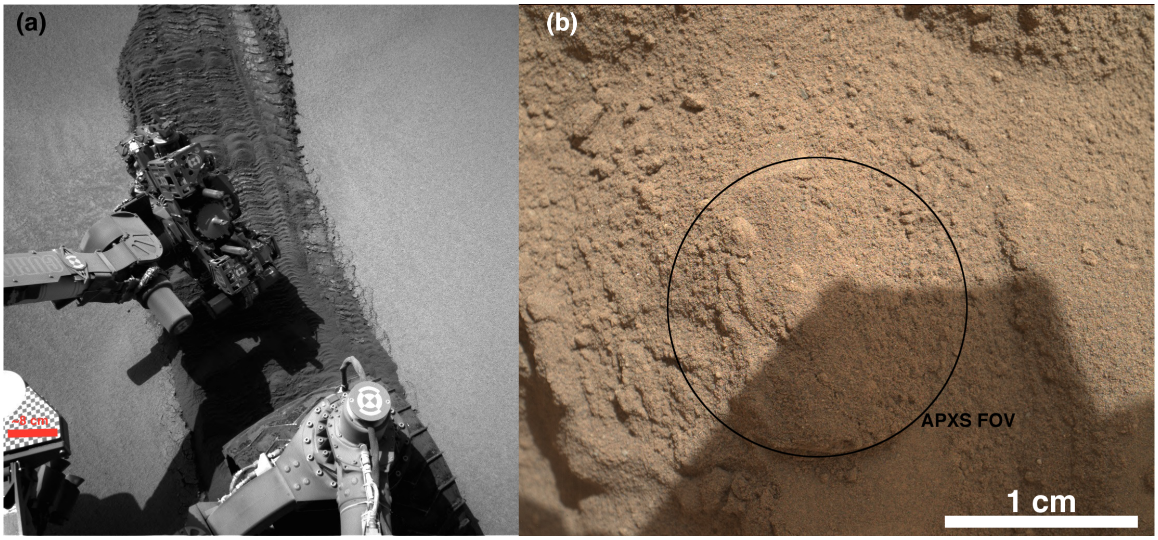

Figure 4-S2. (a) Navcam image [NRB_457239783RADLF0380000NCAM00320M1] of the Sol 673 APXS deployment to the disturbed soil target Sourdough in a track made by *Curiosity's* wheel. The wheel disturbed the lighter-toned, dusty bedform armor, which is typically enriched in SO_3 and Cl relative to the darker interior of the bedform. (b) MAHLI image [0674MH0002910010203939C00] of Sourdough showing the APXS FOV.

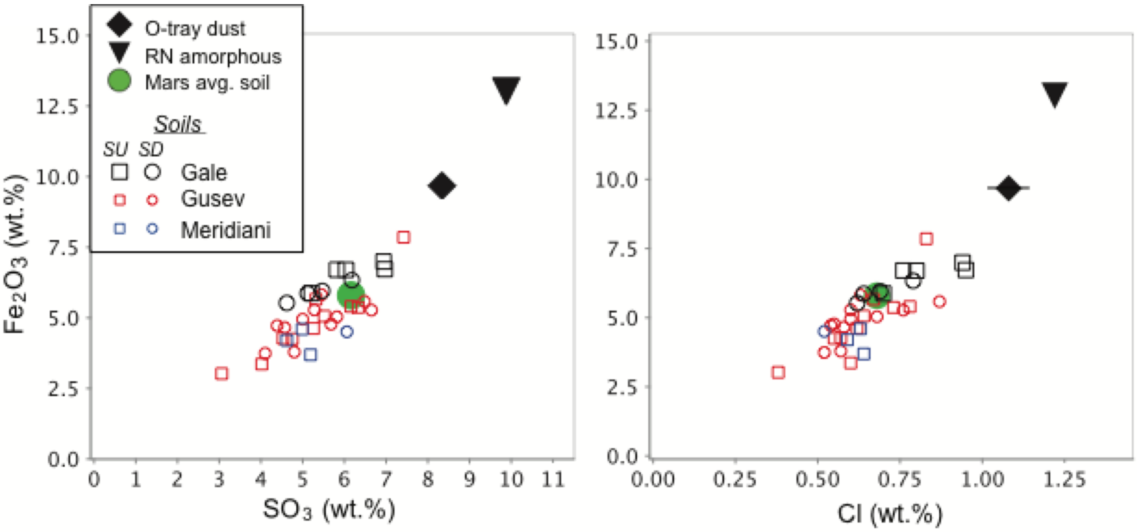

Figure 4-S3. Inferred Fe_2O_3 content in Martian soils, o-tray dust, and amorphous fraction of the Rocknest aeolian deposit (RN). Undisturbed (SU) and disturbed (SD) soils are indicated. MER Fe_2O_3 values were calculated from Mössbauer and APXS data. The RN

amorphous values are from a model by [*Morris et al.*, 2015]. APXS is not sensitive to Fe oxidation state, so Fe_2O_3 values for Gale Crater soils and the o-tray dust were calculated assuming a positive correlation of Fe^{3+}/Fe_{Total} with SO_3 in the basaltic Laguna Class MER soils at a ratio of 0.051 ± 0.009 ($R^2 = 0.52$) [*Morris et al.*, 2008].

Chapter 5

5. Zinc and Germanium in the Sedimentary Rocks of Gale Crater on Mars Indicate Hydrothermal Enrichment Followed by Diagenetic Fractionation

5.1. Chapter Summary and Key Points

Zinc and germanium enrichments have been discovered in sedimentary rocks in Gale Crater, Mars, by the Alpha Particle X-ray Spectrometer (APXS) on the rover *Curiosity*. Concentrations of Zn (910 ± 840 ppm) and Ge (65 ± 58 ppm) are tens to hundreds of times greater than in Martian meteorites and estimates for average silicate Mars. Enrichments occur in diverse rocks including minimally to extensively altered basaltic and alkalic sedimentary rocks. The magnitude of the enrichments indicates hydrothermal fluids, but *Curiosity* has not discovered unambiguous hydrothermal mineral assemblages. We propose that Zn- and Ge-rich hydrothermal deposits in the source region were dispersed in siliciclastic sediments during transport into the crater. Subsequent diagenetic mobilization and fractionation of Zn and Ge is evident in a Zn-rich sandstone (Windjana; Zn ~4000 ppm, Ge ~85 ppm) and associated Cl-rich vein (Stephen; Zn ~8000 ppm, Ge ~60 ppm), in Ge-rich veins (Garden City; Zn ~2200 ppm, Ge ~650 ppm), and in silica-rich alteration haloes leached of Zn (30-200 ppm). In moderately to highly altered silica-rich rocks, Ge remained immobile relative to leached elements (Fe, Mn, Mg, Ca), consistent with fluid interaction at $\mathrm{pH} \ll 7$. In contrast, cross-cutting Ge-rich veins at Garden City suggest aqueous mobilization as Ge-F complexes at $\mathrm{pH} < 2.5$. Multiple jarosite detections by the CheMin X-ray diffractometer and variable Zn concentrations indicate diagenesis of lower Mt. Sharp bedrock under acidic conditions. The enrichment and fractionation of Zn and Ge constrains fluid events affecting Gale sediments and can aid in unraveling fluid histories as *Curiosity's* traverse continues.

5.2. Introduction

Sedimentary rocks enriched in Zn and Ge have been discovered in Gale Crater, Mars, by the Alpha Particle X-ray Spectrometer (APXS) on the Mars Science Laboratory (MSL) rover *Curiosity.* Zinc and germanium concentrations in Gale Crater sedimentary rocks are commonly one to two orders of magnitude greater than the concentrations predicted for the Martian mantle and crust (Table 5-1). Models of the composition of the Martian mantle suggest moderately volatile elements, including Zn and Ge, are enriched ~2X relative to Earth, but do not directly account for the scale of enrichment observed in Gale Crater [*Dreibus and Wanke*, 1985; *Treiman et al.*, 1986; *Lodders and Fegley Jr.*, 1997]. High Zn and Ge point to enrichment processes involving fluids and thus have important implications for the aqueous history of Gale Crater. Understanding this history is a main objective of the MSL mission [*Grotzinger et al.*, 2012].

Enrichments in Zn and Ge are not unique to Gale Crater. High concentrations of both elements were also discovered by APXS instruments onboard Mars Exploration Rovers (MER) in Gusev Crater near Home Plate (≤ 2270 ppm Zn; ≤ 190 ppm Ge) and at Meridiani Planum (≤ 6200 ppm Zn; ≤ 850 ppm Ge) [*Gellert et al.*, 2006; *Ming et al.*, 2008; *Schmidt et al.*, 2008; *Squyres et al.*, 2012; *Mittlefehldt et al.*, 2016]. Although the high concentrations observed at the two MER sites are localized rather than dispersed in widespread sediments as in Gale Crater, such enrichments at three distant sites (1000s of km apart) on Mars suggest these elements are mobile and may be evidence of similar aqueous processes preserved on the surface of Mars [*Gellert et al.*, 2006; *Ming et al.*, 2008; *Schmidt et al.*, 2008; *Mittlefehldt et al.*, 2016].

The contrasting geochemical affinities of Zn and Ge make them a useful pair for bracketing fluid conditions and for tracing geochemical processes. By examining Zn and Ge in sedimentary rocks at Gale Crater, we contribute to understanding the behavior of these elements on the surface of Mars. Here, we describe the geologic context for Zn and Ge enrichments observed at Gale Crater and present a model comprising hydrothermal deposits in the sediment source region and subsequent trace element remobilization by fluids during diagenesis.

Table 5-1: Concentrations of Zn and Ge in Earth and Mars (Mantle and Crust)

	Zn (ppm)	Ge (ppm)	Reference
Earth			
Avg. crust	77	1.4 ± 0.4	1, 3
Basalt	110 - 130	1.4 ± 0.3	1, 2
Silicate sediment	20 - 90	1.4 ± 1.2	1
Mars			
Avg. crust + mantle	83	0.14	4
Martian meteorites	40 - 90	1 - 3	5
Laguna class soils (MER)	270 ± 80	< 30	6
Gale Crater soils	320 ± 40	< 30	This work

[1] [*Bernstein*, 1985]
[2] [De Argollo and Schilling, 1978]
[3] [Heinrichs et al., 1980]
[4] [Lodders and Fegley Jr., 1997]
[5] [Treiman et al., 1986; Warren et al., 1999; Yang et al., 2015; Humayun et al., 2016]
[6] [Rieder et al., 2004; Gellert et al., 2006; Ming et al., 2008]

5.2.1. Zn and Ge Geochemistry and Tracer Potential

The usefulness of Zn and Ge as a tracer pair for the Martian surface begins with their tendency to be enriched together by high temperature fluids. Evidence from Martian meteorites and planetary formation models suggests that Zn and Ge are dispersed as trace elements in the igneous crust, such as they are on Earth (Table 5-1) [e.g., *Dreibus and Wanke*, 1985; *Treiman et al.*, 1986; *Lodders and Fegley Jr.*, 1997]. In the Martian crust, it is likely that much of the Zn occurs at trace levels in magnetite and silicates, substituting for Fe^{2+} or Mg^{2+} [*Heinrichs et al.*, 1980]. Similarly, Ge^{4+} follows Si^{4+} in silicates in igneous systems [*De Argollo and Schilling*, 1978; *Bernstein*, 1985] and Zn and Ge are likely a trace component of silicate minerals in the Martian crust as they are in Martian meteorites [*Humayun et al.*, 2013, 2016; *Yang et al.*, 2015]. However, both Zn and Ge are volatile elements and can be concentrated by high temperature fluids (roughly > 150° C). For example, Zn and Ge often occur together on Earth in hydrothermal sulfide deposits due to a shared chalcophile affinity [*Bernstein*, 1985]. A common pathway to Ge enrichment on Earth (100s-1000s ppm) is through hydrothermal precipitation of sphalerite. Germanium occurs in the mineral via coupled substitution of Ge^{4+} for Zn^{2+} (and Fe^{2+}), with charge balanced by vacancy or other trace elements (e.g., Ag^{+}, Cu^{+}) [*Bernstein*, 1985; *Cook et al.*, 2015]. Oxidative weathering of sulfide deposits may concentrate Zn and Ge to higher levels [e.g., *Heyl and Bozion*, 1964; *Heinrichs et al.*, 1980; *Bernstein and Waychunas*, 1987]. Sulfides are not necessary for enrichment; Zn and Ge may also be concentrated in volcanic emanations, hydrothermal fluids, and related precipitates [e.g., *Thomas et al.*, 1982; *Arnórsson*, 1984; *Froelich et al.*, 1985; *Mortlock et al.*, 1993; *Evans and Derry*, 2002; *Hamade et al.*, 2003]. The co-enrichment of Zn and Ge is thus a potential indicator for high temperature fluid processes on Mars.

Zinc and germanium are further useful as tracers of low temperature fluid conditions (roughly < 150° C), where their volatility has a lesser effect on mobility than acidity and redox potential. This is particularly important for Gale Crater, which contains abundant geologic evidence of liquid surface water [*Williams et al.*, 2013; *Grotzinger et al.*, 2014, 2015] and textural, chemical, and mineralogical evidence of diagenetic fluids [e.g., *Gellert et al.*, 2015; *Rampe et al.*, 2017; *Thompson et al.*, 2016; *Yen et al.,* 2017]. In diagenetic fluids on Earth, Zn solubility is controlled largely by acidity and redox potential, and although it is influenced by ionic strength, temperature, and sediment composition, mobility is usually high at pH < 7 under non-reducing conditions (Figure 1) [e.g., *Mann and Deutscher*, 1980; *McBride*, 1994; *Drever*, 1997; *Tingzong et al.*, 1997; *McPhail et al.*, 2003]. Zinc is thus mobile in acidic fluids and may be subject to leaching and enrichment. In contrast, the fate of Ge in low temperature sedimentary fluids is largely controlled by its speciation as germanic acid in water [*Pokrovsky et al.*, 2006; *Wood and Samson*, 2006], following silica solubility (Figure 5-1) as predicted by their similar geochemical properties [*Froelich et al.*, 1985; *Mortlock and Froelich*, 1987; *Murnane and Stallard*, 1990]. Unlike Si, however, Ge is effectively redox sensitive because it tends to be concentrated by adsorption and coprecipitation in Mn-, Fe-oxides [*King et al.*, 2000; *McManus et al.*, 2003; *Pokrovsky et al.*, 2006]. In summary, Zn and Ge have overlapping, but contrasting properties that can be used to constrain geochemical conditions.

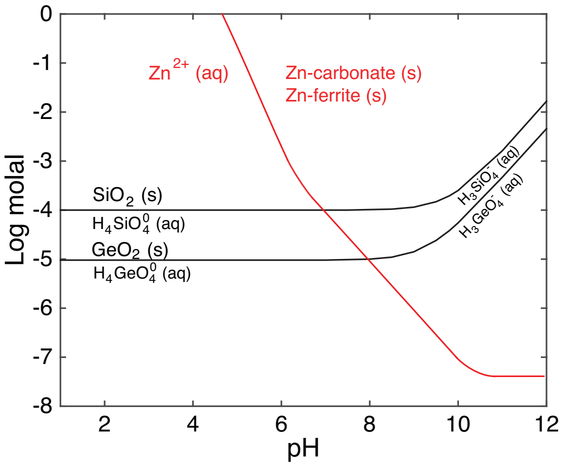

Figure 5-1: Schematic solubility of GeO_2, SiO_2, and Zn at 25° C. Zinc is commonly soluble at low pH [e.g., *McBride*, 1994; *Drever*, 1997], whereas Ge has low solubility [*Pokrovski and Schott*, 1998].

5.2.2. Overview of Gale Crater Geologic Setting

Curiosity's first ~1340 sols ('sol' = 24.6 h; Martian solar day since landing) in Gale Crater on Mars (hereafter also referred to as Gale) were spent roving ~12 km through eroded sedimentary rocks, gaining ~100 m in elevation on a traverse toward Aeolis Mons (informally named Mt. Sharp; Figure 2). The sedimentary rocks record ancient aqueous processes on Mars, and reconstructing the paleoclimate at Gale is one of the primary mission goals of *Curiosity* [*Grotzinger et al.*, 2012]. To accomplish this, the rover has investigated outcrops along the traverse and at waypoints selected largely from orbital observations. APXS target locations and informal geographic names are summarized in Figure 5-2; a chronology of recent rover operations and exploration was presented previously [*Grotzinger et al.*, 2015; *Rice et al.,* 2017].

After the Late Noachian-Early Hesperian Gale Crater impact ~3.7-3.5 Ga [*Thomson et al.*, 2011; *Le Deit et al.*, 2013], the raised crater rim and crater walls provided sediment that mantled the crater floor via mass wasting and localized valley incision with alluvial fan formation. Models of the initial crater depth and rim height indicate that 1-2 km of sediment may currently lie above the post-impact basement [*Grotzinger et al.*, 2015]. In situ K-Ar dating constrains the age of a mudstone comprised of a mixture of detrital and authigenic components to 4.21 ± 0.35 Ga [*Farley et al.*, 2014] and, based on crater counts, the sediment was deposited before 3.3 - 3.1 Ga [*Grant et al.*, 2014; *Grotzinger et al.*, 2015].

Lithified sediment preserves diverse textures, with grain sizes ranging from below imager resolution (~16-32 μm per pixel for Mars Hand Lens Imager; MAHLI) up to sand and medium pebbles/fine gravel [e.g., *Grotzinger et al.*, 2015; *Rice et al.,* 2017]. Porphyritic igneous textures have been observed in individual clasts in pebbly sandstone, conglomerate, and float [e.g., *Sautter et al.*, 2015]; evidence of widespread igneous outcrop (e.g., tuff, lava, impact melt) has not been discovered in Gale. Veins, concretions, haloes, and apparent replacement textures demonstrate early and late diagenetic fluid interaction with the Gale rocks [e.g., *Grotzinger et al.*, 2014; *Berger et al.*, 2015; *Kah et al.*, 2015; *Yen et al.,* 2017]. Most units are laminated and/or bedded, and relationships between sedimentary structures and stratigraphy, among other evidence, led *Grotzinger et al.* [2014, 2015] to the interpretation that Gale contained at least one standing body of water for thousands to millions of years. According to this model, fine-grained sediment was deposited in a lacustrine setting, and a sequence of coarser sandstone and conglomerate records a fluvial deltaic depositional system sourced from the crater rim. Recent aeolian erosion in the drier Amazonian climate exposed the current surface. The surface exposure of one unit, the Sheepbed mudstone at Yellowknife Bay, has been dated at 78 ± 30 Ma [*Farley et al.*, 2014].

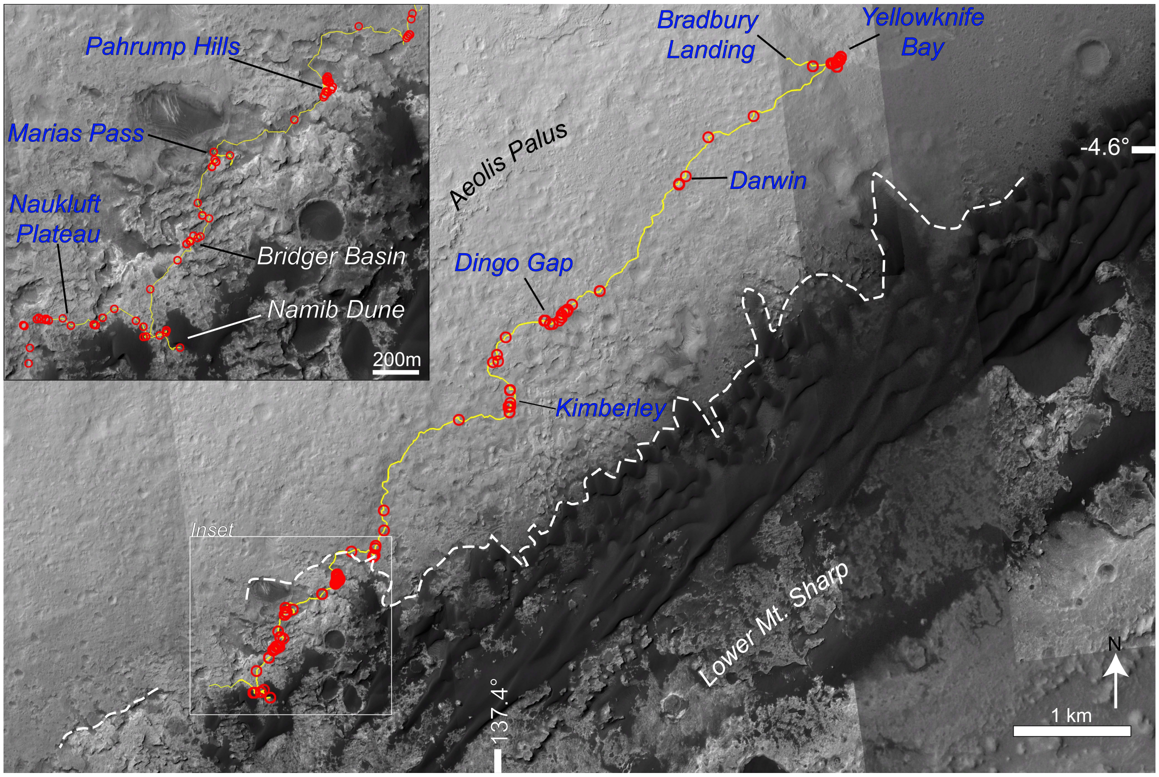

Figure 5-2: Map of *Curiosity*'s traverse over ~1350 sols with APXS target locations (red circles) and key waypoints indicated. The approximate division between Aeolis Palus (Bradbury Group) and lower Mt. Sharp rock units is shown (dashed line). Orbital image credit NASA, JPL, and the University of Arizona.

5.3. Methods

The MSL APXS is mounted on *Curiosity*'s robotic arm and measures characteristic X-rays from Martian samples interrogated by α particles and Pu L X-rays emitted from a ^{244}Cm radioisotope source [*Gellert et al.*, 2006, 2009]. This combination of particle-induced X-ray emission (PIXE) and X-ray fluorescence (XRF) enables the quantification of major, minor, and many trace elements with atomic number $Z \geq 11$ [*Gellert et al.*, 2006, 2009; *Campbell et al.*, 2010, 2011, 2012]. The APXS data were reduced using empirical peak fitting and calibration designed for the MER APXS [*Gellert et al.*, 2006]. The procedure employs a nonlinear least squares fit routine [*James and Roos*, 1989] and adjustments appropriate for the APXS method, including background contributions, escape peaks, and scatter peaks. Differences in the MSL APXS detector response, source intensity, and instrument geometry are incorporated. Germanium was originally not included in the principal MER APXS calibration of *Gellert et al.* [2006]; however, the APXS response curve from 7-12 keV is well established by Ni, Zn, and Br, allowing for the interpolation of Ge response [*Ming et al.*, 2008]. Pure GeO_2 powder has also been included in the MSL calibration sample suite. Representative spectra of Gale samples are presented in Figure 5-3.

Under typical deployment conditions, the detection limit of Zn and Ge is approximately 30 ppm with $\geq$ 1 h integrations at low temperatures ($<$ -20° C). This increases to ~50 ppm for shorter integrations and warmer temperatures, and beyond that for larger standoff distances from the APXS detector. Statistical fitting errors (2σ) decrease with increasing spectral intensity and resolution and therefore encompass the length of integration, standoff distance, and sensor head temperature. This represents error in precision, and is the error value reported herein, enabling comparison between different targets. The analytical uncertainty (accuracy) for Zn and Ge is ± 15-20% [*Campbell et al.*, 2012]. High Z elements (i.e., $Z = 26$ through 32) have low background, high sensitivity and good accuracy. The signal of these elements comes from a depth of ~100 μm and the XRF absorption correction using the average composition of the sample is a good approximation, less prone to heterogeneous absorption by specific minerals.

Mineralogical data discussed herein is derived from published results from *Cuirosity's* Chemistry and Mineralogy instrument (CheMin), which is an X-ray Diffractometer (XRD) mounted in the rover's body [*Blake et al.*, 2012]. Samples are delivered from the drill and scoop, and as such the number of samples is smaller than the number of APXS targets. As such, all drilled and scooped targets have corresponding APXS analyses, but not all APXS targets have CheMin analyses.

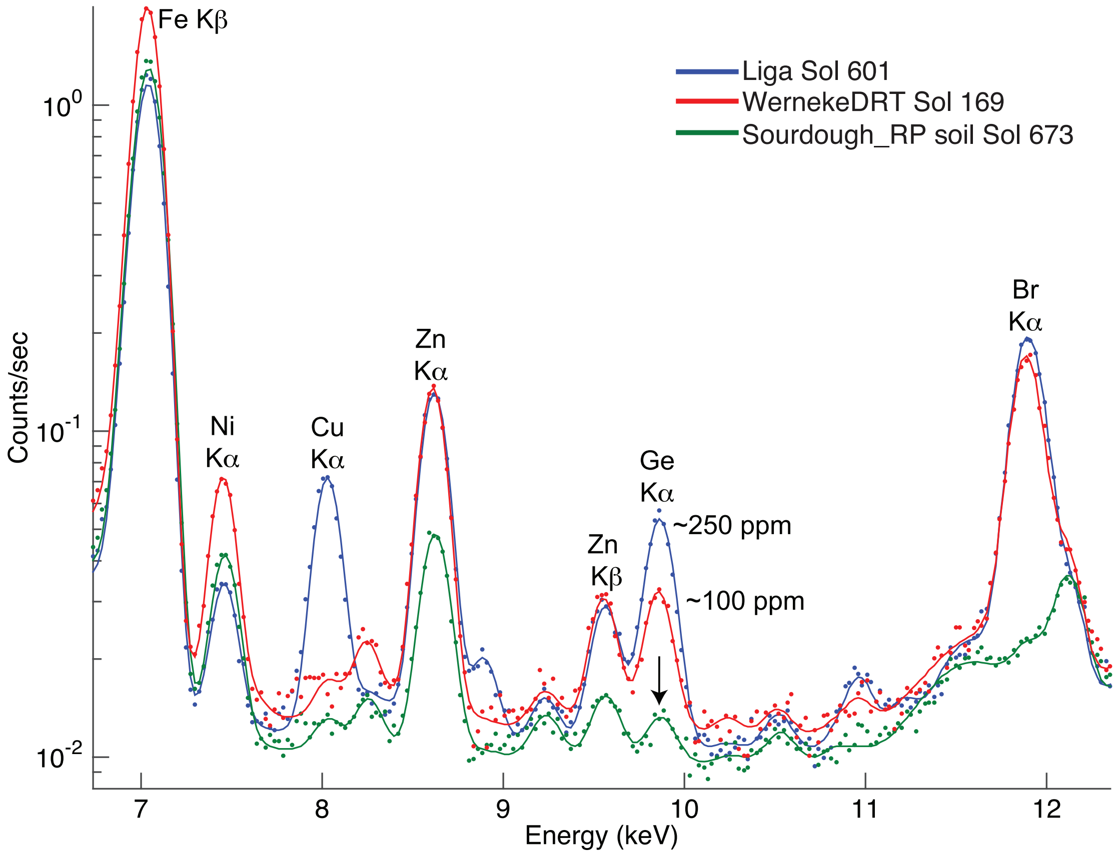

Figure 5-3: Representative APXS spectra showing the data (dots) and fits (lines) for overnight targets with a range of Ge content. Selected peaks and the Ge concentrations are labelled. The Sourdough_RP soil shows a Ge Kα peak at 9.886 keV (arrow) near the detection limit of 30 ppm. The full APXS spectrum (~700 eV - 25 keV) is not shown.

5.4. Results

5.4.1. APXS Dataset

APXS results for sols 0-1340 show variable Zn and Ge levels (Tables 2, S1; Figures 4, 5) that are commonly elevated above the average Martian crust + mantle (Table 5-1). For this work a general detection limit of 30 ppm was applied and samples marked with NQ for "not quantifiable" if they are below this limit. For near surface contact with the APXS and good quality spectra, Ge above ~50 ppm is quantifiable within approximately 20 minutes measuring time. Germanium is above the detection limit for many APXS deployments, and Ge values for targets with similar compositions (e.g., rasters comprising multiple spots < 5 cm apart) are consistent between long and short integrations. For these reasons, we include targets with shorter integrations in our discussion below. The added uncertainty is represented in the larger statistical error, which is also presented as error bars in plots herein. Correlations between compositional variables have been quantified using linear correlation coefficients (*r*). It is recognized that the fact that compositional data are closed means that *r*-values and other measures normally used for 'open' data do not have their usual meanings [*Aitchison*, 1982]. Nevertheless, given the various other uncertainties, the linear correlation coefficients reported here can still provide a qualitative guide to interpreting the co-variations between elements in the rocks studied here. All APXS data discussed here, except for Ge, are curated by the Planetary Data System where they are publicly available (https://pds.nasa.gov). This work is the first full presentation of APXS results for Ge over sols 0 – 1360.

Dust on sample surfaces is a consideration for APXS measurements because the effective sample interrogation depth, defined as the depth from which 90% of the signal is detected (D_{90}) [*Rieder et al.*, 2003; *Brückner et al.*, 2008; *Campbell et al.*, 2009], is on the order of dust thickness [e.g., *Campbell et al.*, 2014; *Schmidt et al.*, 2014b]. The rover's Dust Removal Tool (DRT) brushes dust off targets, reducing its contribution to the APXS signal, but this tool cannot be deployed for every target. Since D_{90} increases with atomic number (Z), the effect of dust is significantly less for Zn and Ge ($D_{90} > 180$ µm) than for lighter elements such as Na and Mg ($D_{90} < 5$ µm). This is evident in the three targets that have good quality APXS measurements before and after brushing (Ekwir, Wernecke, and Windjana), where Zn and Ge are the same within error for the brushed and unbrushed surfaces (Appendix 5-1).

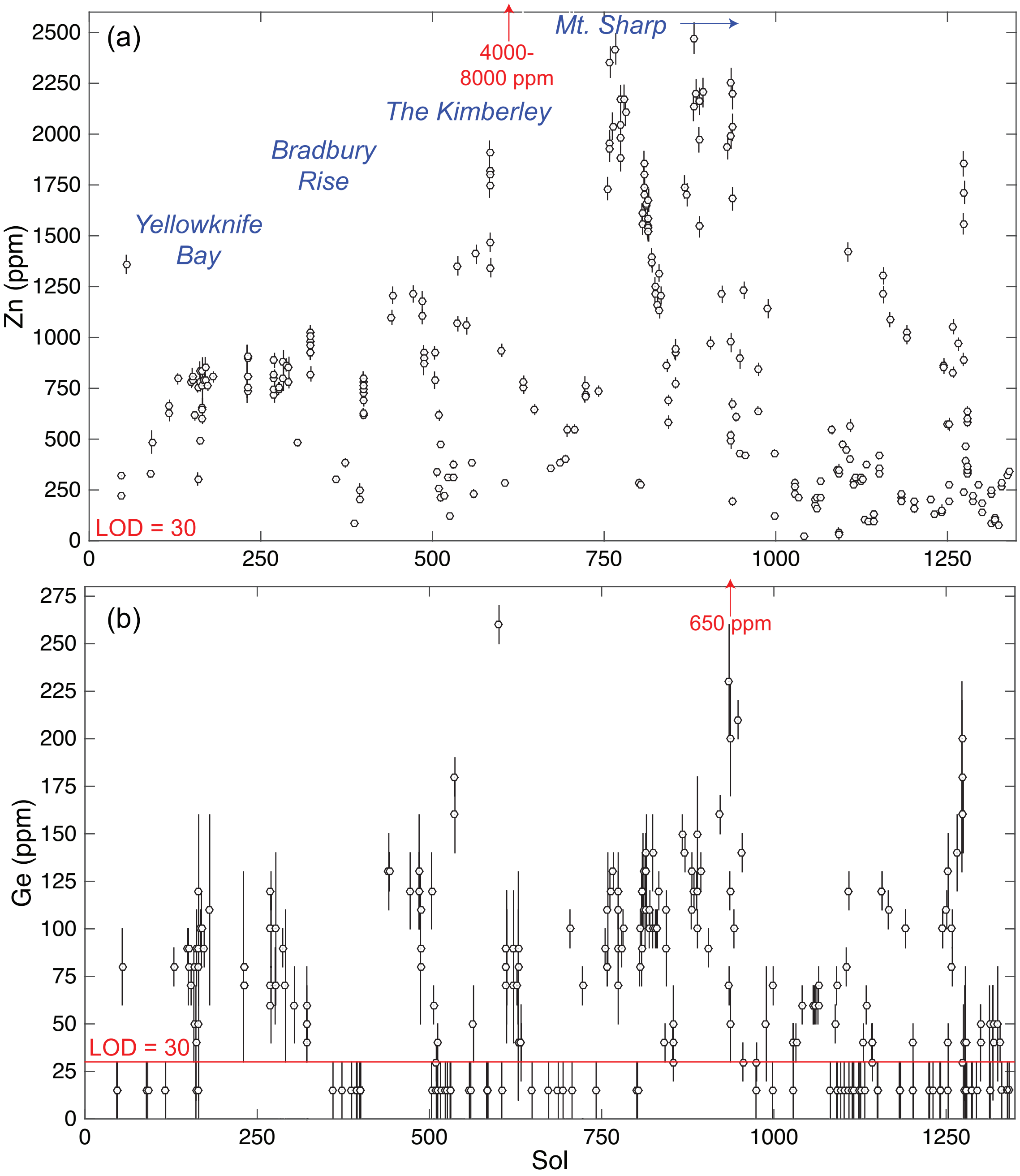

Figure 5-4: (a) Zinc and (b) germanium APXS results for Gale Crater over the first 1340 sols. Larger error indicates larger standoff, shorter lifetime, and/or warmer sensor head temperatures. Highly enriched targets (Windjana, Stephen, and Garden City) are not shown but are indicated with arrows (see Fig 5c). Targets below the Ge limit of detection (LOD; 30 ppm) are plotted as 15 ± 15 ppm. Geographic waypoints (see Fig. 5-2) are indicated. In this and all plots herein, multiple APXS targets on one outcrop are plotted as individual points, except where noted.

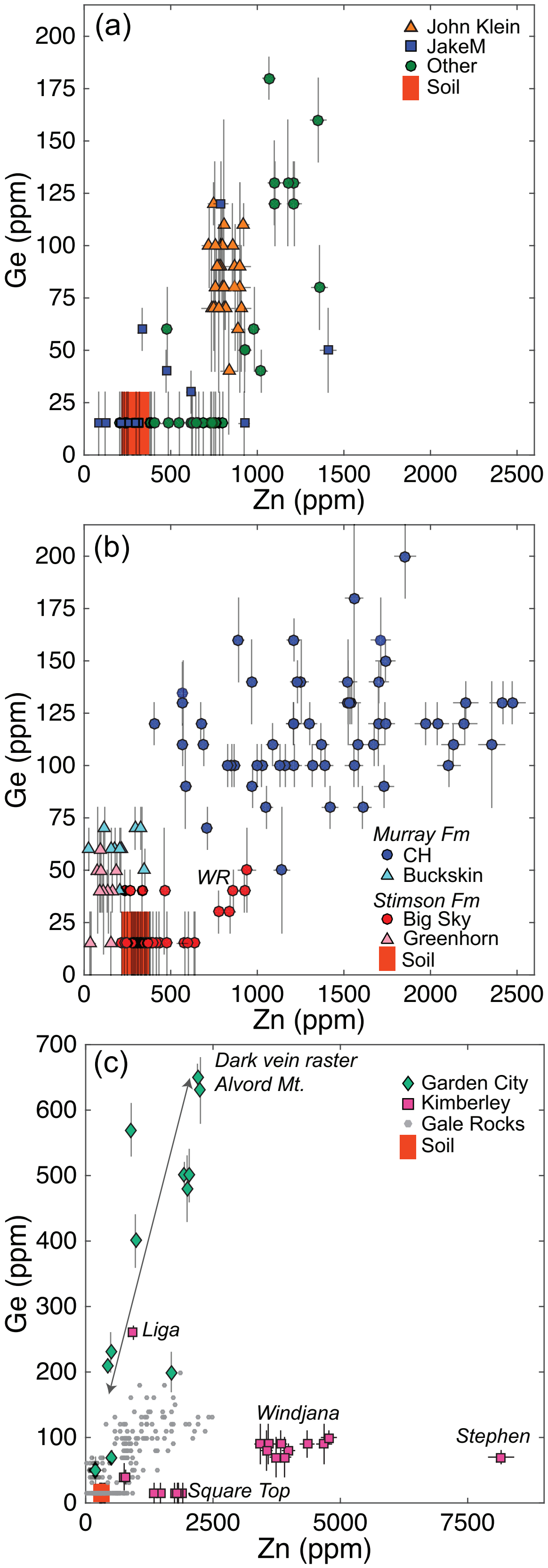
(a)
John Klein
JakeM
Other
Soil
Ge (ppm)
Zn (ppm)
0
25
50
75
100
125
150
175
200
0
500
1000
1500
2000
2500
(b)
WR
Murray Fm
CH
Buckskin
Stimson Fm
Big Sky
Greenhorn
Soil
Ge (ppm)
Zn (ppm)
(c)
Dark vein raster
Alvord Mt.
Garden City
Kimberley
Gale Rocks
Soil
Liga
Windjana
Stephen
Square Top
Ge (ppm)
Zn (ppm)
0
100
200
300
400
500
600
700
0
2500
5000
7500

Figure 5-5: Zinc and germanium results for (a) the Bradbury Group (excluding the Kimberley formation) and (b) lower Mt. Sharp Group rocks and soils, excluding veins and concretions. The Whale Rock and Bigfork/Albert outcrops of the Stimson formation are indicated (WR). (c) Zinc and germanium in The Kimberley and Garden City with all other Gale APXS targets plotted for reference. The arrow indicates the APXS raster over the Garden City veins containing two phases: 1) high Ge, low SO_3 dark material and 2) low Ge, high SO_3 Ca-sulfate. Other targets with sulfate-bearing veins and concretions (Mavor and Morrison classes; Appendix 5-1) are not plotted.

Table 5-2: Diagnostic Zn and Ge characteristics in Gale Crater[1]

Unit / feature name	Representative APXS rock class	Description	Typical Zn (ppm)	Typical Ge (ppm)	Zn and Ge characteristics
Bradbury Group					
Yellow-knife Bay	John Klein*	Basaltic, isochemically altered	800 ± 50	80 ± 20	Enriched Zn and Ge, low variance
Bradbury Rise	Jake_M	Mugearitic	440 ± 350	< 40	Not enriched, igneous-like composition
	Bathurst Inlet	Potassic basaltic sandstone and conglomerate	1150 ± 180	110 ± 50	Enriched Zn and Ge Higher variance
Kimberley	Windjana*	Bathurst Inlet-like potassic basaltic sandstone, minimal alteration	1440 ± 460 ~4000 in Windjana	70 ± 60 ~85 in Windjana	Highly enriched Zn Highly variable Ge High Ge (~260 ppm) and Cu (~580 ppm) in one sandstone (Liga)
	Stephen	Vein / Fracture fill a few cm from Windjana	~8000	~60	Highly enriched Zn Same Ge as adjacent bedrock
Mt. Sharp Group					
Murray Fm.	Confidence Hills* (CH)	Altered, basaltic, with elevated Al_2O_3, SiO_2, and Mn/Fe	1400 ± 500	110 ± 20	Enriched Zn, high variance Enriched Ge, low variance
	Buckskin* (BK)	High SiO_2 (75 wt%) and TiO_2 (1.7 wt%) with low Fe, Mn, Mg, Ca Acidic silica-retaining alteration	170 ± 100	50 ± 20	Depleted Zn Elevated Ge, but ~half of CH
Garden City	Alvord Mountain	Vein cluster near Pahrump with dark Ca-rich precipitate	~2500	~650	Zn elevated ~ 500 ppm over CH bedrock Very highly enriched Ge 6X over CH host bedrock
Stimson Fm.	Big Sky* Okoruso*	Soil-like basaltic with elevated Cl	310 ± 30	< 30	Soil-like Zn Ge below LOD diagnostic of Stimson parent
Stimson fracture haloes	Greenhorn* Lubango*	High SiO_2 (65 wt%) with low Fe, Mn, Mg, Al, Na Acidic silica-retaining alteration	80 ± 60	40 ± 10	Depleted Zn Elevated Ge relative to parent Stimson
Soils and Sand					
Soils	Portage	Basaltic soils	320 ± 40	< 30	Zn enriched in dust component Ge below LOD
Bagnold sand	Gobabeb	Basaltic sand, slightly elevated Cl	190 ± 30	< 30	Zn depleted due to smaller dust component Ge below LOD

---

[1] Rock classes are not comprehensive; representative end-members are included and are based on [*Schmidt et al.*, 2016; *Mangold et al.,* 2017].

*Denotes drilled targets

5.4.2. Zn and Ge Occurrence and Distribution

Zinc and Ge enrichments occur in diverse rock types along *Curiosity*'s traverse. Zinc depletions have also been observed in Mt. Sharp rocks. Here, we define *enriched* and *depleted* relative to the range observed in Gale soils (Table 5-2). Because Ge is below or around the APXS limit of detection (LOD) in all soil measurements, Ge depletion by this definition is not observable. The Gale rocks are geochemically and mineralogically diverse (Figure 5-6) [e.g., *McLennan et al.*, 2013; *Schmidt et al.*, 2014b; *Rampe et al.,* 2017; *Treiman et al.*, 2016]. As such, in this section we present the Zn and Ge characteristics of the units and outcrops explored by *Curiosity* (Figure 5-2). The APXS targets are grouped broadly by stratigraphic unit and assigned classification names using the APXS geochemical compositional classes defined previously [*Schmidt et al.*, 2014a, 2016; *Thompson et al.*, 2016] to subgroup and describe rocks with similar chemical composition (Appendix 5-1; Figure 5-S1). Table 5-2 summarizes the Zn and Ge characteristics of Gale Crater materials in context with the stratigraphic grouping and geochemical classification. Outcrops and units were named and described previously [*Grotzinger et al.*, 2014, 2015; *Treiman et al.*, 2016].

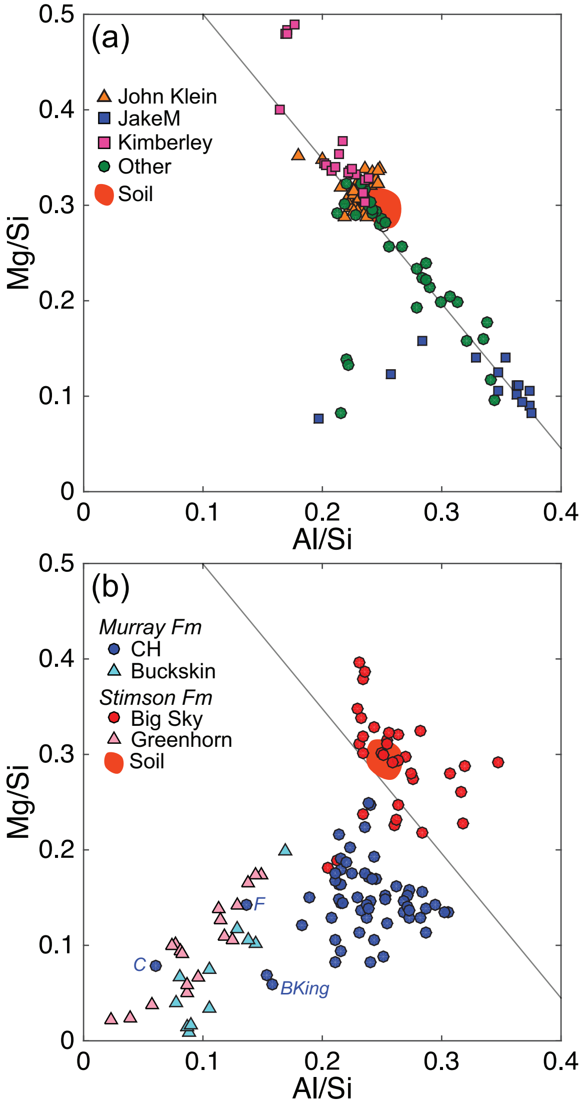

Figure 5-6: Composition of (a) Bradbury Group and (b) lower Mt. Sharp Group rocks and soils. The line indicates a typical trend for unaltered compositions, indicating variation in igneous mafic and felsic mineral mixtures. Deviation from this trend toward lower Al/Si indicates alteration with silica retention and cation leaching. Confidence Hills (CH) outliers Bonanza King (BKing), Ferdig (F), and Cody (C) are indicated (see text). Veins and concretions (Stephen, Alvord_Mt., Mavor and Morrison classes) are not shown.

5.4.2.1. Soils and Sand

Curiosity investigated soils (Portage class) and sand dunes (Gobabeb class), including detailed studies of an inactive sand shadow named Rocknest [*Bish et al.,* 2013; *Blake et al.*, 2013; *McAdam et al.*, 2014] and the active Bagnold Dunes at the foot of Mt. Sharp

[*Achilles et al.*, 2017; *Ehlmann et al.*, 2017; *O'Connell-Cooper et al.*, 2017]. Nine soil and ~12 sand targets were measured by the APXS in Gale [*O'Connell-Cooper et al.*, 2017]. In soils, Zn ranges from 275±10 to 380±15 ppm, whereas the Bagnold Dune sands are consistently lower at 130±10 to 230±10 ppm. In the sand and soils, Ge is near or below the 30 ppm level at which it can be quantified with reasonable certainty (Figure 5-3).

5.4.2.2. Ca-Sulfate Veins

Widespread white sulfate veins and concretions (Mavor class) have been investigated throughout most units by the APXS in Gale [*McLennan et al.*, 2013; *Nachon et al.,* 2017; *VanBommel et al.*, 2016, 2017]. The veins crosscut bedding planes and thus represent late diagenetic fluids. Rasters over these features show they are Ca- and S-rich, with 1:1 stoichiometric Ca-S variation consistent with pure Ca-sulfate [*VanBommel et al.*, 2016]. Vein targets are typically small with respect to the ~1.5 cm APXS field of view (some veins are thicker but were not measured by the APXS). A deconvolution of the five point raster on the target Sayunei (sol 165) using the method of VanBommel et al. [2016] yields effectively zero Zn and Ge in the pure Ca-sulfate veins. All other white veins similarly do not contain evidence of trace element enrichments (Ni, Zn, Ge).

In APXS targets containing Ca-sulfate veins, the analysis is usually a combination of bedrock and vein. To simplify the evaluation of bedrock, we omit targets containing Ca-sulfate veins and concretions from the discussion below, except where noted. That is, Mavor class targets (Appendix 5-1) were not included in any of the plots or calculation of correlations.

5.4.2.3. Bradbury Group (Aeolis Palus)

Yellowknife Bay and Bradbury Rise

The rocks of the Bradbury Group (BG), which includes every target from the Bradbury Rise landing site up to the contact of Aeolis Palus and lower Mt. Sharp (Figure 5-2), have a wide range of compositions, consisting of eight distinct geochemical classes based on APXS data (Figures 6, S1a, S1b) [*Schmidt et al.*, 2014a; *Thompson et al.*, 2016]. A key distinguishing characteristic is total alkali content, which is at basaltic levels (2.3-3.8 wt% Na_2O+K_2O) in the Sheepbed mudstone of the Yellowknife Bay formation (John Klein class) [*McLennan et al.*, 2013] and elevated to hawaiitic and mugearitic levels (5.0-9.5 wt% Na_2O+K_2O) in the overlying BG sandstone and conglomerate (Figure 5-S1a) [*Thompson et al.*, 2016]. CheMin XRD analyses show the Sheepbed drill samples John Klein and Cumberland (sols 230-291) contain minerals common in basalt (plagioclase, pyroxene, olivine, magnetite) and Ca-sulfates, Fe-oxides, smectite, and X-ray amorphous material [*Vaniman et al.*, 2014]. The overlying BG sedimentary rocks are more alkali-rich, likely mixing Al-rich, mugearitic (Jake_M class) and Fe-rich, potassic (Bathurst Inlet class) endmembers (Figure 5-S2) [*Schmidt et al.*, 2014a, 2014b]. Chemical weathering was probably not extensive; hawaiitic and mugearitic igneous compositions are generally preserved in major and minor elements (e.g., Figure 5-6). Exceptions are two similar float targets (Et_Then, sol 91; Secure, sol 560) with elevated FeO (26-27 wt%) indicating Fe-oxide cement [*Schmidt et al.*, 2014b]. Overall, the compositions of BG units are consistent with the physical mixing of sediment derived from three endmember lithologies: 1) the basaltic John Klein class, 2) the mugearitic Jake_M class, and 3) the potassic basalt Bathurst Inlet class (Figure 5-S2) [*Treiman et al.*, 2016].

Overall, Zn and Ge have a broadly positive correlation ($r = 0.66$) in the BG rocks, although Ge is more variable (Tables 2, S1, Figure 5-5a). Zinc and germanium tend to be near soil levels in the low Fe, high Al classes (Jake_M and Nova) and enriched in the high Fe, low Al classes (Bathurst Inlet, John Klein). The high K_2O, low Na_2O Bathurst Inlet rocks are consistently elevated in Zn (1000-2000 ppm), whereas most other rocks, except for the mugearitic Jake M class, are less enriched (400-1000 ppm). Et_Then and Secure have high FeO, but approximately the same Zn, as soil. Germanium is also low in Secure, but Et_Then had large ~5 cm instrument standoff distance and Ge could not be determined. Many of the Bradbury Rise targets were pieces of float found along the rover traverse, particularly those in the high alkali Jake_M and Bathurst Inlet classes, limiting geologic inferences about the relationships between the two rock types, which have distinct Zn and Ge content (i.e., Jake_M has igneous concentrations and Bathurst Inlet is enriched).

The Kimberley Formation

The Kimberley formation (sols 574-634) is part of a widespread unit with east-west trending striations that is intermittently exposed in southern Aeolis Palus. It consists of a ~10 m section of southward dipping interbedded sandstone and conglomerate strata overlain by cross-stratified sandstone [*Grotzinger et al.*, 2015; *Treiman et al.*, 2016; *Rice et al.*, 2017]. Sedimentary textures vary widely, including fine, well-cemented sandstone, coarse sandstone, variable pebble content, and moderately to poorly cemented conglomerate [*Grotzinger et al.*, 2015; *Rice et al.*, 2017]. All Kimberley targets share similar chemical characteristics with each other and with the Bathurst Inlet class of the BG rocks [*Thompson et al.*, 2016]. All have elevated FeO and lower Al_2O_3 and SiO_2, and all have the high K_2O, but low Na_2O, that distinguishes them from the other high alkali rocks of the Jake_M class. The Windjana drill target in the Dillinger member of the Kimberley formation shares these trends but to a greater extent, with yet higher K_2O, lower Na_2O, and elevated FeO and MnO (Figures S1b, S2, S3a) [*Thompson et al.*, 2016].

Zinc is elevated in all Bathurst Inlet class rocks, but it is highest in the Kimberley formation (Figure 5-5c). APXS analyses of the Windjana drill target, including the pre- and post-DRT surface, fines ejected by the drill, and fines dumped from the sampling subsystem, show a consistently high concentration of ~4000 ppm from the surface down to ~5 cm depth in the drill hole. The Dillinger member typified by Windjana [*Treiman et al.*, 2016] is the only highly enriched bed measured by APXS in the formation; it is 2-4X higher in Zn than other Kimberley APXS targets. An exception, however, is a fin feature named Stephen (sols 627, 629) about ~10 cm from Windjana (Figure 5-7). Stephen has a Mn-rich layer detected by ChemCam that is consistent with a veinlet or vein alteration halo [*Lanza et al.*, 2016]. Stephen has the highest Zn measured by APXS in Gale (8160 ± 245 ppm). Removal of the dust signal in the APXS data by deconvolving dust and clean rock surface in a five spot raster over the target revealed very high values for a number of elements in Stephen, including MgO (18.6 ± 0.3 wt%), MnO (4.8 ± 0.1 wt%), Ni (1460 ± 75 ppm), Zn (8960 ± 245 ppm), Cl (3.3 ± 0.1 wt%), and Br (1790 ± 60 ppm) [*VanBommel et al.*, 2016]. The target also has the first detectable Co enrichment found in Gale (~300 ppm) [*Lanza et al.*, 2016]. The composition is otherwise consistent with the potassic basalt Windjana, with low SiO_2 (33.4 ± 0.3 wt%) and Na_2O (1.0 ± 0.1 wt%) but high FeO (20.8 ± 0.2 wt%) and K_2O (2.4 ± 0.1 wt%) [*Thompson et al.*, 2016]. This magnitude of Zn concentration in bedded outcrop (Windjana) and veins (Stephen) has not been discovered elsewhere on *Curiosity's* traverse.

Germanium is highly variable in the Kimberley formation (Tables 2, S1, Figure 5-5c). The lowest stratigraphic member, named Liga, contains a single APXS target (also named Liga; sol 601) with 250 ± 10 ppm Ge. Liga also has elevated Cu (580 ± 10 ppm). Targets in the overlying Square Top member are all below the Ge LOD (30 ppm). Above that in the Dillinger member, both the drill target Windjana and the nearby fin Stephen have Ge (~85 and ~60 ppm, respectively), which falls into the same range as other Bathurst Inlet rocks. Zinc and germanium are not correlated in the Kimberley formation. In particular, the Zn-rich Stephen target does not have a corresponding Ge enrichment relative to the host bedrock and the Ge-rich Liga target has a Zn concentration similar to other Bathurst Inlet rocks.

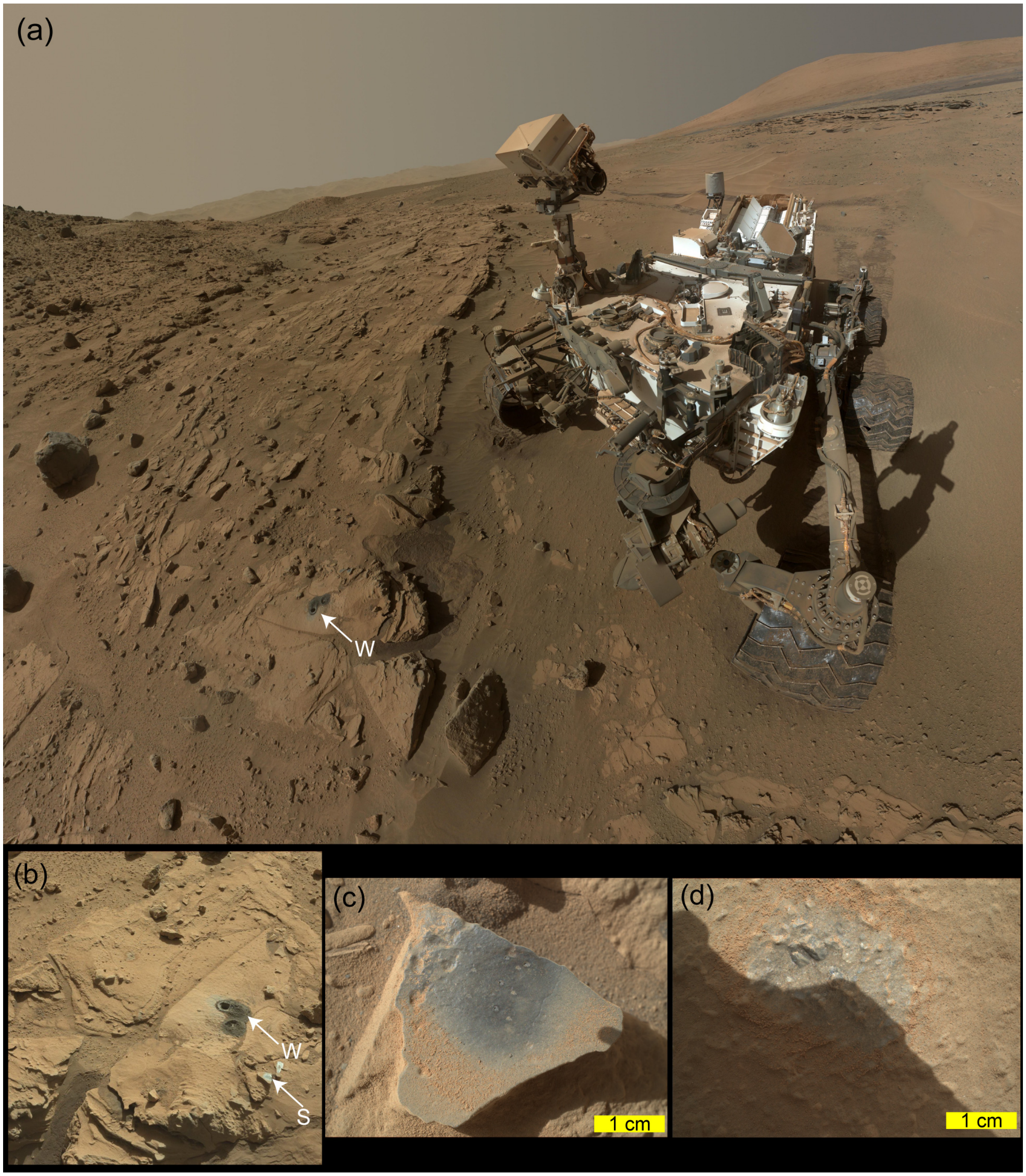

Figure 5-7: Images of Zn and Ge enriched targets in the Kimberley formation. (a) MAHLI mosaic of the Windjana drill site (W) in the Dillinger unit of the Kimberley formation. (sols 612-629; from NASA image PIA18390). (b) Mastcam of the Windjana drill site (hole width 16 mm) next to the target Stephen (S). (c) MAHLI image of the Zn-rich Stephen target (sol 627). (d) MAHLI image of the Ge- and Cu-rich Liga target about 30 m north of the Kimberley drill site (site 31/0724). In (c) and (d), dust was cleared from the center of the image by the ChemCam laser. Images from NASA, JPL, and Malin Space Science Systems.

5.4.2.4. Lower Mount Sharp Group (Aeolis Mons)

Curiosity arrived at lower Mt. Sharp shortly after sol 700 (Figure 5-2), where it began investigating the Murray and unconformably overlying Stimson formations. The two formations are distinguishable in orbital images in part because Murray is lighter toned and smoother than Stimson. Rover analyses demonstrate that the two formations have very distinct chemical characteristics, including differing Zn and Ge, but each formation maintains consistent and quite homogeneous compositions along the traverse of >2 km. Both units contain lighter-toned, fracture-associated haloes linked to one or more later cross-cutting fluid alteration events.

Murray Formation

Curiosity has examined the Murray formation extensively over ~2.2 km of the lower Mt. Sharp traverse, gaining ~45 m in elevation, measuring ~100 APXS targets, and drilling four holes over sols 750-1091[*Rampe et al.*, 2017; *Thompson et al.*, 2016]. The Murray formation is comprised largely of fine-grained (smaller than the typical 16-32 μm per pixel resolution of MAHLI images), finely laminated sedimentary rock. Textures vary and include rounded coarse sand (or concretions) and lenticular mineral pseudomorphs within the finer-grained matrix [*Kah et al.,* 2015]. Compositionally, Murray rocks differ from the BG (Figures S1, S3). Four CheMin XRD samples in the lower Murray formation contain ~17-27 wt% plagioclase feldspar, ~20-50 wt% X-ray amorphous material, varying amounts of pyroxene, phyllosilicate and hematite, and minor amounts of magnetite, apatite, and jarosite [*Rampe et al.,* 2017]. APXS results show the rocks have consistently lower alkalis and elevated silica (SiO_2 48-74 wt%; Figure 5-6; Appendix 5-1, Figure 5-S1c) [*Thompson et al.*, 2016]. As a whole, major and minor elements (Na, Mg, Al, Ca, Mn, and Fe) decrease with increasing silica (Figure 5-S4) [*Thompson et al.,* 2016]. There is also a trend toward high Al_2O_3 and MnO with moderate SiO_2 in the Mojave subclass. Important exceptions include: 1) a positive correlation between TiO_2 and SiO_2 ($r = 0.86$), and 2) variable P_2O_5 and K_2O (Figure 5-S4) [*Gellert et al.*, 2016; *Yen et al.*, 2017]. Silica and iron content are useful to classify Murray rocks as Confidence Hills class ($SiO_2 < 55$ wt%; FeO > 11wt%) and Buckskin class ($SiO_2 > 55$

wt%; FeO < 11wt%), using the names of representative drill targets [*Schmidt et al.,* 2016; *Thompson et al.*, 2016]. Exceptions include Cody, a high silica Murray target discussed below, and Bonanza King (BKing in Figures 6, 8), a higher silica target we have provisionally grouped as a subclass of Confidence Hills, rather than Buckskin, because it has higher Zn (~710 ppm) and is stratigraphically disconnected from the Buckskin unit (i.e., lower elevation of -4457 m and laterally ~800 m distant). Silica and iron contents are useful discriminants for classification [*Schmidt et al.*, 2014a, 2016; *Thompson et al.*, 2016; *Mangold et al.*, 2017].

Murray formation rocks, which include the Confidence Hills (CH) and Buckskin (BK) classes, exhibit a wide range in Zn and Ge concentrations (Figure 5-8a, 5-8b). Zinc concentrations in CH ranges from soil-like levels of 400 ppm up to 2470 ppm, and the mean (1380 ppm) represents a ~4X enrichment over soil. In contrast, the mean Zn content of BK is lower than soil at 210 ppm, including one Si-rich target, Lamoose, which has very low Zn concentrations (30 ± 5 ppm). Germanium is elevated in all Murray rocks relative to soil (30-155 ppm). Among the high-silica BK targets, Ge is roughly half (~55 ppm) the lower silica CH targets (~110 ppm). BK is thus lower than CH in both Zn and Ge concentrations and the two elements do not correlate within each class (Figure 5-5b).

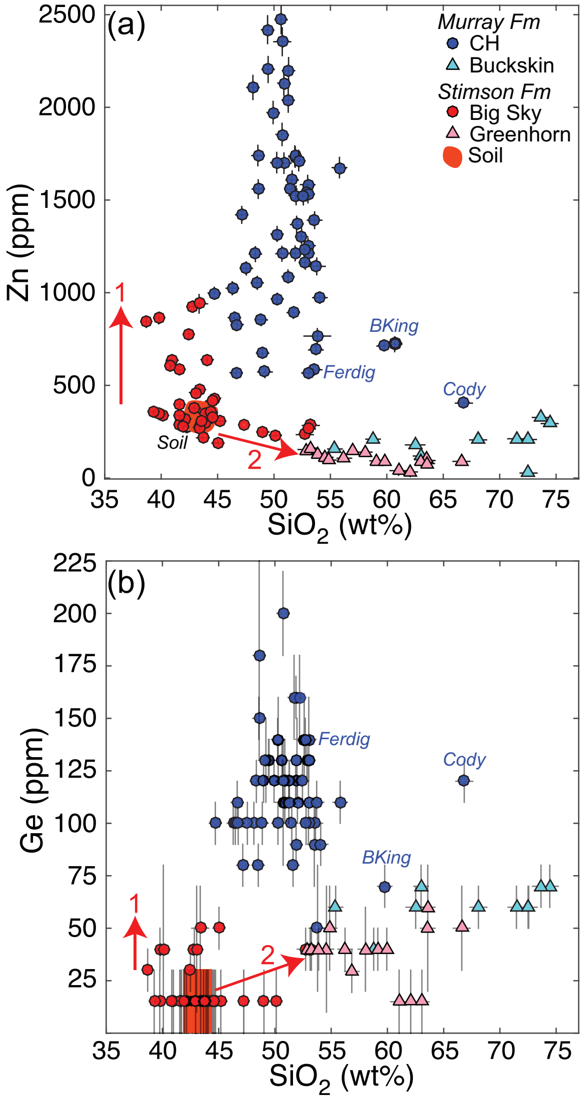

Figure 5-8: Variation of (a) Zn and (b) Ge with silica in lower Mt. Sharp rocks. Vector 1 indicates Stimson targets near the Stimson/Murray contact, interpreted to be enriched in Zn and Ge due to physical incorporation of Murray into the overlying Stimson. Vector 2 indicates the Zn and Ge trends between parent (Big Sky) and altered (Greenhorn) Stimson at high silica fracture haloes.

Diagenetic Features of the Murray Formation

Very high Ge concentrations (up to 650 ppm) were discovered by the APXS in a cluster of veins named Garden City (also known as Alvord_Mountain class) in the Murray formation (sols 930-948) ~50 m south of the Pahrump outcrop. Most veins are ~1-6 cm thick, standing in positive relief a few centimeters above the host rock (Figure 5-9). The veins contain discrete white and dark gray precipitates representing at least two fluid events, with the dark material apparently brecciated and entrained by the white material. Because the two phases were small with respect to the APXS field of view (~1.5 cm), an APXS and MAHLI raster of 7 spots was conducted to enable deconvolution of the compositions using the method of *VanBommel et al.* [2016]. In the raster, the white phase exhibits a 1:1 molar variation of Ca and S, consistent with the nearly pure Ca-sulfates common in veins in Gale. The dark phase is distinct; after deconvolving the compositions of the white and dark phases using APXS rasters over the vein [*VanBommel et al.*, 2017], we find that SO_3 is low (6.4 wt%) in the dark material and it is composed primarily of CaO (23 wt%), SiO_2 (35 wt%), and FeO (17 wt%), with enrichments in MnO (1 wt%), Zn (2400 ppm), and Ge (650 ppm). The host bedrock, represented by the target Hyrum, is like the CH class of Murray rocks, but with relatively low Zn (673 ± 25 ppm). A fin-shaped target next to the vein (Kern Peak), interpreted to be altered bedrock within the vein halo, has low CaO (2.9 ± 0.04 wt%), high FeO (23.4 ± 0.3 wt%), high Ge (205 ± 5 ppm), and the second highest P_2O_5 measured in Gale (2.7 ± 0.14 wt%) [*Berger et al.*, 2016b]. Additional studies of the vein included a MAHLI ultraviolet illumination experiment [*Fisk et al.*, 2015] and ChemCam LIBS, which detected high levels of Ca and a related molecular emission Ca-F peak [*Nachon et al.*, 2017].

Evidence of Ni-rich Mg-sulfates was found in concretions in the Murray formation in the lower Pahrump Hills outcrop (Morrison class) [*VanBommel et al.*, 2016]. An analysis of rasters over concretions by *VanBommel et al.* [2016] demonstrated 1:1 stoichiometric Mg-S variation, indicating Mg-sulfates. Unlike the Ca-sulfates, these concretions are not pure; they are a mixture of ~10% Ni-, Mg-sulfate and the host bedrock. Zinc and Ge levels in the Mg-sulfates are similar to the host rock with no detectable enrichment or depletion.

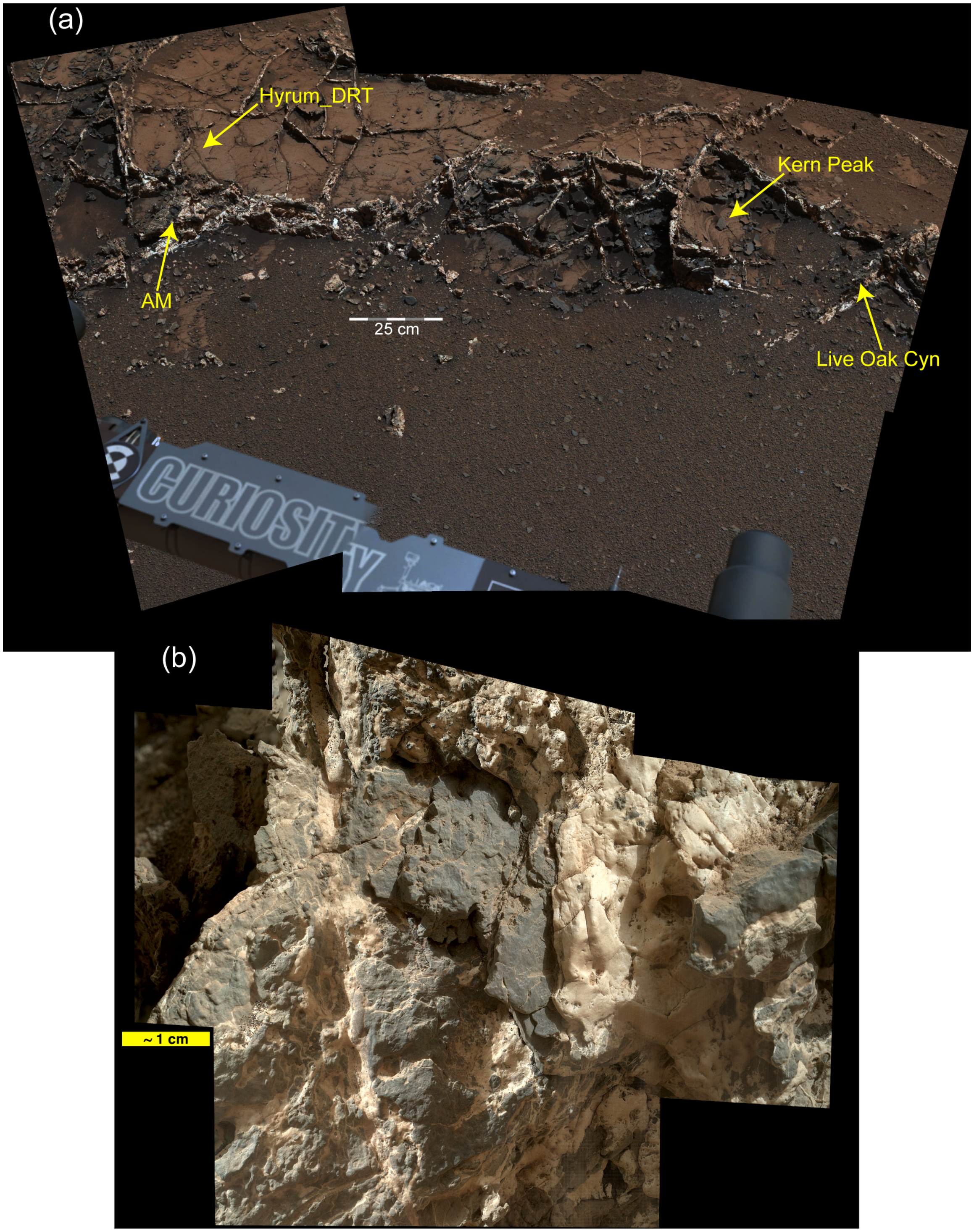

Figure 5-9: Images of Ge enriched veins at Garden City in the Murray formation (site 45/0852). (a) Mastcam context mosaic of the vein cluster with APXS targets indicated and (b) MAHLI mosaic of Alvord Mountain site (AM in 9a) containing six Alvord Mountain raster points, Coalville, and Indianola targets. The white material is Ca-sulfate and the dark material is composed primarily of Ca and Si, with Mn and Ge enrichments. Images and from NASA, JPL, and Malin Space Science Systems.

Stimson Formation

Curiosity's investigation of the Stimson formation up to sol 1340 has included ~48 APXS targets and four drill holes. The Stimson includes the Whale Rock, Bigfork/Albert, and Ronan outcrops near the Pahrump Hills, several targets near Bridger Basin where the Big Sky and Greenhorn drill targets were located, and the Okoruso and Lubango drill targets on the Naukluft Plateau (Figure 5-2). The Stimson formation contains thinly-bedded sandstone with uniform, recessive interbeds and intermittent cross-bed structures. Grain sizes are primarily medium sand with varying amounts of rounded coarse sand and usually a recessive cementing matrix. Beds within the Stimson near the Murray formation contact have centimeter-scale, secondary knobby structure. Parent Stimson bedrock (Big Sky class; formerly known as Ronan class [cf. *Thompson et al.*, 2016]) has a narrower range of compositions than is found in Murray rocks, and has a consistent, soil-like SiO_2 (~43 wt%; Figure 5-S1, 5-S4) and Fe/Mn (~47). White Ca-sulfates along veins and filling voids are common, although qualitatively different than in the Murray formation, occurring less frequently in fractures and more often along bedding planes (e.g., Rossing sol 1287). Stimson deviates from the soil-like composition significantly in light-toned haloes that are usually less than ~1 m in width and associated with bedrock fractures [*Yen et al.*, 2017]. The haloes have elevated silica (53-64 wt%; Greenhorn class), and two were investigated in the Big Sky/Greenhorn (sols 1114-1143) and Okoruso/Lubango (sols 1318-1359) drill campaigns (Figure 5-S4) [*Yen et al.*, 2017]. Paired measurements by the APXS of fracture-associated halos and nearby host bedrock were conducted to capture chemical gradients. Paired measurements in the Stimson (and Murray) are summarized in Table 5-3.

Relative to most of the Murray formation targets, Zn and Ge are present at lower concentrations in the Stimson formation, and this contrast is a diagnostic feature of Stimson. In Stimson outcrop, Zn and Ge are both within range of soil (Figure 5-8c, 5-8d). There are two exceptions. First, three outcrops have elevated Zn (640-940 ppm) and Ge (30-45 ppm) denoted by vector 1 in Figure 8. These outcrops include Whale Rock (San Andreas, Tecoya, and Sierra Nevada targets; sols 842-854), Bigfork/Albert (sols 974-975), and the Khomas raster target (sols 1279-1280). Here, we group Whale Rock and

Bigfork/Albert with the Stimson formation [cf. *Grotzinger et al.*, 2015] because they are chemically similar to other Stimson targets, having 39-44 wt% SiO_2 and soil-like Fe/Mn of 44, and, unlike the fine-grained Murray, the outcrops are dark, coarsely-bedded and cross-bedded sandstones [*Grotzinger et al.*, 2015; *Thompson et al.*, 2016]. Based on sedimentological observations, *Grotzinger et al.* [2015] described Whale Rock and Bigfork/Albert alternatively as intercalated sandstones in the Murray formation. Khomas is on Stimson outcrop at the Naukluft Plateau ~2 m west of the contact of Stimson with the Murray formation (Figure 5-2). The second deviation in Zn and Ge trends occurs in the light-toned, silica-rich Stimson halo targets (Figure 5-8, vector 2), where Ge is elevated (25-60 ppm) and Zn is depleted well below soil levels (< 200 ppm) [*Yen et al.*, 2017].

Table 5-3: Paired Alteration Halo Targets in Mt. Sharp Units

Unit name	Sol	Less altered target (SiO_2 in wt %)	More altered target (SiO_2 in wt %)
Murray Fm.	1109	Ferdig (53)	Cody (67)
Stimson Fm.	1091-1092	Ledger (44)	Devon (61) Ivanhoe (62)
	1114-1143	Big Sky (42-45)*	Greenhorn (53-59)* Pilgrim (64) Vandalia (59)
	1313-1314	Onesi (50) Kasane (49)	Uau (67)
	1318-1359	Okoruso (45)*	Lubango (60)*

*Denotes drill targets

5.5. Discussion

5.5.1. Enriched Global Soil and Dust

Although the bulk chemical compositions of Martian soils reflect the largely basaltic crust, Zn is enriched in the soils relative to crustal values predicted from Martian meteorites (Table 5-1). Gale soils are similar in composition to the basaltic soils analyzed by APXS in Gusev Crater and Meridiani Planum (e.g., Laguna Class soils) [*Yen et al.*, 2005, 2013; *Gellert et al.*, 2006; *Ming et al.*, 2008; *O'Connell-Cooper et al.*, 2017]. Mean Zn in Gale soil (320 ± 40 ppm) is in range with basaltic soils at Meridiani Planum (320 ± 80) and Gusev Crater (270 ± 80). Because Ge is near or below the 30 ppm detection limit in soils, we cannot conclude with certainty if they are enriched relative to the bulk crust and Martian meteorites.

Fluid-mobile element enrichments (S, Cl, Zn) in Martian soils have been linked, in part, to enrichments in Martian dust [*Yen et al.*, 2005; *Ming et al.*, 2008; *Berger et al.*, 2016a]. Lower Zn, S, and Cl in the active Bagnold sand dune compared to Gale soil (Tables 2, S1) agrees with MER APXS analyses of the El Dorado sand sheet in Gusev Crater, which is also lower in Zn (~130 ppm) than local basaltic soils (270 ± 80) [*Ming et al.*, 2008]. MER APXS also found elevated Zn in undisturbed, dusty soil surfaces relative to disturbed soils, which led to the interpretation that the Martian dust is enriched in Zn [*Yen et al.*, 2005; *Ming et al.*, 2008]. An MSL APXS study of airfall dust on the science observation tray could not quantify Zn or Ge because the sample volume was too small [*Berger et al.*, 2016a]. Nevertheless, the correlation of Zn with S and Cl in the sand and soils is consistent with and enrichment of Zn in the dust, as observed by the MER rovers.

These observations support models of global Mars soil formation that describe soils as having varying amounts of three main components: (1) S-, Cl-, and Zn-enriched global dust, (2) regional fines, and (3) local gravel, sand, and finer material [e.g., *McSween Jr. and Keil*, 2000; *Bishop et al.*, 2002; *McGlynn et al.*, 2011; *Berger et al.*, 2016a]. Active sand sheets are depleted in the global dust component and dominated by components 2 and 3, as indicated by low S, Cl, and Zn. Assuming the global dust unit represents a well-mixed sampling of the Martian crust, the S, Cl, and Zn enrichments indicate that fluid-mobile element enrichments are a widespread feature of the modern Martian surface. These elements have been added to the crustal materials that have been physically broken down into dust particles. The enrichment was likely due to volcanic emissions and/or fluids that mobilized these elements to the surface where they were distributed with the igneous dust particles.

5.5.2. Primary Enrichment Processes

The widespread occurrence of Zn and Ge in the diverse sedimentary rocks of Gale at concentrations significantly greater than those of the Martian meteorites and modeled crust (Table 5-1) points toward primary enrichment processes involving fluids. We define these as *primary* enrichment processes to distinguish them from secondary diagenetic processes that also affected Zn and Ge. We propose below that the magnitude of the Zn and Ge enrichment was most likely due to hydrothermal activity, but we first examine the amount of meteoritic input and the possible presence of magmatic sulfides in the parent rocks.

Inferring the Zn and Ge enrichment process(es) from *Curiosity's* dataset includes uncertainty for four main reasons. (1) *Curiosity* has been investigating rocks in a sedimentary system, which can induce varying degrees of mixing, averaging, and sorting of the source rocks. (2) Zn is readily mobilized by fluids in sediment at low temperatures [e.g., *McBride*, 1994; *Degryse et al.*, 2009; *Mertens and Smolders*, 2013]. These first two processes likely diluted and obscured concentrated primary Zn and Ge deposits. (3) The APXS detection limit for Ge (30 ppm) is 10X higher than the levels in Martian meteorites and crustal models (< 3 ppm), thus the relative magnitude of Ge enrichment and Ge mobility below 30 ppm is uncertain. (4) We cannot unambiguously determine the Zn- and Ge-bearing phases, or whether they are associated with crystalline minerals or the substantial X-ray amorphous fraction observed by CheMin [*Vaniman et al.*, 2014; *Morris et al.*, 2015; *Treiman et al.*, 2016; *Rampe et al.,* 2017; *Yen et al.,* 2017]. Despite these sources of uncertainty, we discuss plausible enrichment pathways for Zn and Ge in Gale.

5.5.2.1. Meteoritic Input

Much of the surface of Mars preserves impacts dating back to the Noachian period [e.g., *Carr and Head*, 2010], and Zn- and Ge-bearing impactor material is likely a component of the modern surface [e.g., *Yen et al.*, 2006]. The meteoritic components of lunar and Martian soils have been linked compositionally to CI chondrites [*Taylor,* 1982; *Yen et al.*, 2006], which contain average Zn (310 ± 12 ppm) and Ge (33.2 ± 0.3 ppm) concentrations [*Lodders*, 2003] that are enriched ~3X and ~10X, respectively, over Martian meteorites.

Thus, chondritic input of Zn and Ge may constitute part of the Gale enrichment. Nickel is a useful tracer for meteoritic material on Mars with APXS [*Yen et al.*, 2006] because CI chondrites contain 10640 ± 210 ppm Ni [*Lodders*, 2003] and the element is quantifiable by the MER and MSL APXS instruments at > 50 ppm [*Gellert et al.*, 2006]. *Yen et al.* [2006] estimated a 1% to 3% chondritic contribution to soil based on elevated Ni in MER APXS analyses. Based on MSL APXS Ni values, a 1% to 4% meteoritic input was estimated for Yellowknife Bay mudstones in Gale [*McLennan et al.*, 2013]. We note that CM and CR chondrite impactor clasts are common in howardite meteorites and may represent the chondritic component of Martian soils more accurately than CI chondrites [*Zolensky et al.*, 1996]. However, compared to CI chondrites, CM and CR chondrites contain more Ni (12300 – 13100 ppm), less Zn (100-180 ppm), and less Ge (18-26 ppm) [*Lodders and Fegley*, 1998]. Therefore, the chondritic Zn and Ge component may be over-estimated by CI chondrites. We also emphasize that the apparent mobilization of Ni in Gale sediments (e.g., in Ni-rich Mg-sulfates [*VanBommel et al.*, 2016]) adds uncertainty to estimates of meteoritic input.

We find that the magnitude of the Zn and Ge enrichments cannot be accounted for by meteoritic material alone. The molar ratio Ge/Ni is 0.0025 in CI chondrites and 0.17 in Gale (excluding the Ge-rich Garden City vein and Ni-rich Mg-sulfates). Molar Zn/Ni in CI chondrites is 0.26 and 1.4 in Gale. Therefore, the mean Ni in Gale (500 ppm) does not represent sufficient meteoritic material to account for the elevated Zn and Ge. The 1-4% addition of chondritic material predicted by Ni content amounts to an addition of 0.3-1.3 ppm Ge and 3-12 ppm Zn, which is relatively insignificant.

5.5.2.2. Magmatic Sulfides

Both Zn and Ge are chalcophile when sulfur activity is elevated, and they can be accommodated in magmatic sulfide minerals. Estimated Sulfide Concentrations at Sulfide Saturation (SCSS) values for Gale Crater melts range from ~6000 ppm for Jake_M class samples to ~13500 ppm for some Bathurst Inlet class samples [*Izawa et al.*, 2016]. Melts with compositions similar to Bathurst Inlet class rocks may have been particularly efficient carriers of sulfides and chalcophile elements, due to their high FeO* (up to 23 wt%), which correlates with both high SCSS and low viscosity [*Izawa et al.*, 2016]. Melts with compositions similar to Jake_M and Bathurst Inlet may also have contributed to sulfide mineralization through assimilation of crustal S during emplacement in a manner analogous to some terrestrial magmatic sulfide deposits [*Burns and Fisher*, 1990; *Baumgartner et al.*, 2015]. A further source of magmatic enrichment in Zn, Ge, and other chalcophile elements may be the Martian mantle source for these magmas. Elevated alkalis in Bathurst Inlet and Jake_M rocks indicate metasomatic events in the source mantle [*Stolper et al.*, 2013; *Schmidt et al.*, 2014b], and Zn and Ge may have been concentrated by associated processes.

Although magmatic sulfide mineralization may have provided an important source of initial enrichment in chalcophile elements, including Zn and Ge, further enrichment by another secondary process would have been necessary to reach the Zn and Ge concentrations observed by the APXS. Evidence for sulfide minerals on the Martian surface comes from pyrolysis results from the Sample Analysis at Mars (SAM) instrument [*McAdam et al.*, 2014], but sulfide minerals have not been confirmed above 1 wt% by CheMin. Pyrrhotite is present in Martian meteorites, including the regolith breccia samples of the NWA 7034 group [*Agee et al.*, 2013], but concentrations of both Zn and Ge in specific mineral phases are poorly constrained for Martian meteorites, with some exceptions [*Humayun et al.*, 2013, 2016], and are almost always below the detection limit of electron probe microanalysis (100 ppm).

5.5.2.3. Hydrothermal Fluids

Hydrothermal activity is a plausible enrichment pathway for Zn and Ge (and other volatiles) in Gale. Volcanism and impacts, especially the Gale Crater forming impact, potentially triggered hydrothermal systems in the region [*Schwenzer et al.*, 2012; *Newsom et al.*, 2014; *Morris et al.*, 2016]. Zinc and germanium are readily mobilized by hydrothermal fluids under a wide range of geochemical conditions [e.g., *Bernstein*, 1985; *Höll et al.*, 2007]. Zinc, in particular, has few constraints on its overall mobility in hydrothermal systems and is commonly one of the most enriched metals in associated fluids [e.g., *Óskarsson*, 1981; *Symonds et al.*, 1987; *Zelenski et al.*, 2014]. The magnitude of the Gale Zn and Ge enrichment is realistic for hydrothermal systems, whereas it is not for meteoritic input or magmatic sulfides (sections 4.2.1-4.2.2). We therefore propose a hydrothermal fluid enrichment model for Gale.

The occurrence and distribution of Zn and Ge are key to evaluating a hydrothermal enrichment model. Several overlapping lines of evidence indicate that Zn- and Ge-rich deposits are a feature of the sediment source region:

1. The lack of unambiguous hydrothermal alteration mineral assemblages [cf. *Schwenzer and Kring*, 2013] and high temperature fluid mineral precipitates in CheMin samples counter-indicates in situ hydrothermalism in the sediment.

2. The modeled geothermal profile for the greatest possible Gale Crater fill was unlikely to have exceeded 150° C [*Borlina et al.*, 2015], so metasomatic concentration of volatiles is effectively precluded *after deposition*.

3. Zn and Ge are not correlated with any particular secondary mineral assemblage; they are elevated in diverse basaltic and alkalic rock classes. This indicates that Zn and Ge are distributed in the sediment source region (i.e., crater rim), and are not linked to one rock type or massive ore-like deposit. Rather, the widespread, but variable Zn and Ge concentrations seen by APXS suggest primary enrichment occurs as veins, breccias, and (or) disseminated deposits that crosscut different rock units in the crater rim. The Zn and Ge in the sediment therefore include contributions from heterogeneously distributed hydrothermal deposits within the catchment.

4. Liga, the Ge- and Cu-rich sandstone target (section 3.2.2.2), is an isolated enrichment that we interpret to be pebbly sandstone containing a detrital nugget of a hydrothermal precipitate from the source region.

5. Zn-enriched (~6200 ppm) and Ge-enriched (~850 ppm) breccia was discovered in separate targets in the rim of Endeavor Crater by *Opportunity* [*Squyres et al.*, 2012; *Mittlefehldt et al.*, 2016] and may be an analogue for primary Zn- and Ge-rich deposits in the Gale sediment source. That is, this may be a common feature associated with impact hydrothermal alteration on the Martian surface.

Curiosity's instrument payload has not yet identified host phases for Ge and Zn, and so the primary Zn- and Ge-bearing phases can only be partially constrained. Hydrothermal deposits are complex, reflecting variability in temperature, fO_2, fS_2, and halide concentrations. On Earth, Zn and Ge are commonly enriched together in sulfide deposits when S_2 activity is high, with as much as 100s - 1000s ppm Ge in sphalerite [e.g., *Bernstein*, 1985; *Höll et al.*, 2007; *Frenzel et al.*, 2016]. However, no evidence of extensive sulfide deposits has been found in Gale; CheMin has not confirmed sulfides above 1 wt%, which is consistent with SAM analyses [*Ming et al.*, 2014].

Given the relatively low abundance of sulfide minerals (< 1 wt%), Zn and Ge may be associated with oxidized phases. This could be by direct precipitation in an oxidizing environment or by oxidative alteration of primary sulfides and/or silicates [e.g., *Heyl and Bozion*, 1964]. Autometasomatism (i.e. alteration by magmatic water), later hydrothermal alteration, or oxidized groundwater could yield Fe-oxides, oxide-hydroxides, and hydroxysulfates that retain and often concentrate the Ge and Zn [*Heyl and Bozion*, 1964; *Bernstein*, 1985; *Bernstein and Waychunas*, 1987]. Oxidative weathering of sulfide minerals leads to the formation of acidic solutions which may have played a role in the further mobilization and redistribution of chalchophile elements including Zn and Ge, possibly into ferric oxyhydroxide minerals or by adsorption on Fe-oxides. In Gale, crystalline Fe-oxides and Fe-bearing amorphous material are present in all drilled targets analyzed by CheMin XRD [*Vaniman et al.*, 2014; *Treiman et al.*, 2016; *Rampe et al., 2017*]. These are plausible Ge- and Zn-bearing host phases as they are commonly associated with enrichments on Earth [e.g., *Heyl and Bozion*, 1964; *Bernstein*, 1985; *Bernstein and Waychunas*, 1987].

Other trace elements are commonly enriched with Zn and Ge in hydrothermal fluids [*Bernstein*, 1985], and it is reasonable to expect that they would likely be enriched in the Gale rocks. Trace elements likely to follow Zn and Ge in hydrothermal fluids, but with concentrations below ~200 ppb in the Martian mantle + crust (e.g., Ag, Cd, In, Sn) [*Lodders and Fegley Jr.*, 1997], are unlikely to be detectable in APXS spectra if they are enriched only 10-100X. Trace elements with greater predicted Martian abundances include Cu (2-5 ppm), Ga (4-7 ppm), and Pb 380 ppb) [*Lodders and Fegley Jr.*, 1997].

No systematic enrichment of Ga or Pb has been discovered, but work is ongoing. Two Cu-rich targets have been discovered by the APXS in the Kimberley: one with 580 ppm Cu (Liga) and another with 270 ppm Cu (Stephen) [*Lanza et al.*, 2016]. APXS results also indicate the Windjana bedrock drill sample next to the Stephen target (Figure 5-7) has 40-60 ppm Cu [*Lanza et al.*, 2016]. All of these targets are enriched relative to the Cu concentrations predicted for the Martian mantle + crust (2-5 ppm) [*Lodders and Fegley Jr.*, 1997]. Thus, a Cu enrichment of up to 10X would likely be near or below the APXS detection limit, which can be qualitatively estimated to be ~30 ppm. Further work is ongoing to characterize Cu in the APXS dataset. We conclude that the Cu enriched targets support the interpretations proposed here based on Zn and Ge; however, Cu is not as consistently elevated as Zn and Ge (above a rough detection limit of ~30 ppm).

We reemphasize that the Zn and Ge enrichments occur in rocks with diverse chemical and mineralogical compositions, and unambiguous hydrothermal alteration mineral assemblages have not been detected in CheMin samples (n = 12 over sols 0 - 1340) [*Vaniman et al.*, 2014; *Rampe et al.,* 2017; *Treiman et al.*, 2016]. For example, *Schwenzer and Kring* [2013] modeled hydrothermal mineral assemblages likely for the Martian crust, and minerals predicted to occur up to more than 50 wt% under a range of conditions (e.g., serpentine, chlorite, and zeolites) have not been detected above 1 wt% in CheMin measurements. However, other minerals that can form by hydrothermal processes have been detected by CheMin, including amorphous silica, cristobalite, tridymite, magnetite, hematite, sulfates, and clay minerals [*Vaniman et al.*, 2014; *Morris et al.*, 2016; *Treiman et al.*, 2016; *Rampe et al.,* 2017]. These phases can be formed by a number of distinct processes other than hydrothermal, including low temperature diagenesis and igneous melting, thus the ambiguity.

This ambiguity means we cannot rule out in situ hydrothermal enrichment. A possible pathway to enrichment within the sediment after emplacement is via hydrothermal fluids, perhaps from a magmatic body that mobilized Zn and Ge from a sulfide reservoir into the sediment, and precipitated the elements after changes in chemical composition (e.g., pH, Eh, S content) and temperature due to interaction with the sediment. We find this model to be possible, but less likely than an enrichment in the source region with subsequent dilution in siliciclastic sediment. Evidence against in situ enrichment is primarily 1) the lack of a clear source of heat after sediment emplacement (although *Churchill et al.* [2017] propose a possible volcano north of Gale) 2) alteration characteristics of enriched rock types are different (section 3.2), counter-indicating a wholesale influx of hydrothermal fluid into the sediment, and 3) *Treiman et al.* [2016] argue that Windjana (Bathurst Inlet) has no detectable hydrothermal alteration minerals (above ~1 wt%), yet the sample is enriched in Zn, Ge, and Cu.

5.5.3. Diagenetic Mobilization and Fractionation

Zinc and germanium are a practical element pair for tracing diagenetic processes because they have contrasting solubilities and geochemical affinities that can lead to fractionation in diagenetic fluids (Figure 5-1). Unambiguous evidence of Zn and Ge fractionation in Gale has been found by the APXS in alteration haloes and veins, providing in situ examples of element mobility with clear geologic context and allowing inferences of fluid conditions. In contrast with the primary hydrothermal enrichment proposed above, haloes and veins most likely involved fluids at the diagenetic temperatures predicted for the Gale sediment (< 150° C [*Borlina et al.*, 2015]). Below we first discuss Ge/Si fractionation observed in silicate weathering on Earth. Then we discuss evidence for diagenetic mobility of Zn and Ge in Gale in the Kimberley formation of the BG, in the fracture-associated alteration haloes of lower Mt. Sharp, and in the Murray formation.

5.5.3.1. Silicate Weathering and Ge/Si Fractionation

Low temperature, circumneutral silicate weathering has been shown to fractionate Ge and Si on Earth, increasing Ge/Si and absolute Ge values in weathering residue [*Kurtz et al.*, 2002; *Scribner et al.*, 2006]. For example, a study of Hawaiian soil profiles, with a basalt protolith relevant to Mars, demonstrated an increase in Ge (1.6 ppm to 5.6 ppm) and Ge/Si (2.5 µmol/mol to 10-25 µmol/mol) in soils with progressive weathering [*Kurtz et al.*, 2002]. The fate of the Ge in the residual material is debated; as Ge is released from weathering of silicate minerals, it may concentrate in clay minerals [*Kurtz et al.*, 2002; *Scribner et al.*, 2006] or coprecipitate in oxides [*King et al.*, 2000; *McManus et al.*, 2003; *Pokrovsky et al.*, 2006], while the silica is preferentially leached in solution.

Two characteristics of Ge/Si fractionation via silicate weathering make it an unlikely scenario for the primary Ge enrichment in Gale. First, the magnitude of absolute Ge enrichment is only ~3X greater than the protolith in the most weathered sediment on Earth. In contrast, the mean enrichment in Gale is ~25-40X greater than Martian meteorites (a plausible protolith composition). Second, the Hawaiian weathering regime studied by Kurtz et al. [2002] includes extensive leaching of silica ($SiO_2 < 20$ wt%) and precipitation of abundant secondary oxides/hydroxides (e.g., FeO > 40 wt%; $Al_2O_3 > 30$ wt%). Evidence for this type of weathering has not been observed in Gale [e.g., *McLennan et al.*, 2013, 2015; *Treiman et al.*, 2016]. That is, if the elevated Ge/Si in Gale (75-250 µmol/mol) was achieved by circumneutral weathering of an igneous silicate with 1-3 ppm Ge, or even a soil-like precursor with ~10-20 ppm Ge, extensive silica leaching would also be evident.

5.5.3.2. Zinc Mobility in the K-rich Kimberley Formation

The Kimberley formation demonstrates the diagenetic, in situ fractionation of Zn and Ge in the Gale sediment. The Windjana drill target in the Dillinger unit is enriched in Zn (~4000 ppm) at levels that are roughly 4X greater than the other Kimberley APXS targets and the BG Bathurst Inlet class (Figure 5-5c). The nearby Stephen vein/fracture fill has an unusual precipitate composition and is even more enriched in Zn (8160 ± 245 ppm). We interpret this enrichment to be caused by a fluid that mobilized Zn in the BG sediment and concentrated it in the Dillinger bed and associated fractures [*Thompson et al.*, 2016]. Elevated Cl in Stephen (up to 3.4 wt%) indicates that chloride compounds may have facilitated the highly localized Zn, Mn, Ni, Cu, and Co enrichment detected by APXS [cf. *Lanza et al.*, 2016]. The distribution of the Zn enrichment in units overlying Dillinger is not well constrained because they were not reachable with APXS, although ChemCam found evidence of more widespread, very high Zn concentrations (>5 wt%) in scattered, small (~1 mm^2) points in the Kimberley [*Lasue et al.*, 2016].

Unlike Zn, Ge is not enriched in Windjana and Stephen (Figure 5-5c) relative to related BG rocks. The apparent immobility of Ge in the Dillinger bed and fractures is evidence that the Zn was carried in a fluid at a low temperature (<< 250° C) and without sufficient dissolved fluoride to facilitate Ge solubility [*Benoit and Place*, 1963; *Ciavatta et al.*, 1990; *Pokrovski and Schott*, 1998]. The fluid conditions are further constrained to pH < 7, in which Zn is mobile and Ge is relatively insoluble at low temperatures (Figure 5-1). Whereas complexation with Cl^- likely increased Zn mobility, Ge-Cl compounds have very low solubility and Ge was probably immobile in the Zn-mobilizing fluid. Experimental work shows that very low pH (< 2.5) and elevated F are necessary for low temperature Ge mobilization [*Ciavatta et al.*, 1990], suggesting that the fluid was buffered to higher pH and/or F concentrations were low. Lanza et al. [2016] argue further that high Mn in Stephen (MnO ~5 wt%) indicates an oxidizing fluid, which has implications for the Zn-bearing phase (possibly pyrolusite or hematite), but specific Zn phases cannot be confirmed with the rover dataset.

5.5.3.3. Lower Mt. Sharp Fracture Haloes

Several interpretations have been proposed for the formation of light-toned fracture haloes in Mt. Sharp units (Tables 2, S1, S4) [e.g., *Gellert et al.*, 2016; *Schmidt et al.*, 2016; *Yen et al.*, 2017]. Yen et al., [2017] provide the detailed mineralogical and geochemical compositions for these fracture haloes and discuss formation models. Our preferred model invokes leaching by acidic fluids along fractures, which is indicated by high silica (50-75 wt%) and depletions in fluid mobile cations (Na, K, Mg, Ca, Ni, Zn) as well as cations usually insoluble in circumneutral fluids but mobile in acidic fluids (Fe, Mn, Al). A key observation supporting this is that not all cations are depleted. TiO_2 is retained with SiO_2 as a residue, likely due to low solubility of both oxides at low pH [*Squyres et al.*, 2007]. P_2O_5 is also variable, and may have been retained (or added) due to the precipitation of secondary insoluble P-bearing phases in acidic, high ionic strength fluids [*Berger et al.*, 2016b]. Titanium and phosphorous retention, in particular, counter-indicates simple silica addition via chemical precipitation [cf. *Frydenvang et al.*, 2017; *Milliken et al.*, 2016].

The light-toned haloes provide in situ alteration gradients, wherein Zn and Ge have trends that are consistent with the acidic alteration scenario. In most of the paired alteration halo analyses (Table 5-3), as silica increases, Zn decreases and Ge increases (Figure 5-8, vector 2). Leaching of Zn by acidic fluids with retention of insoluble Ge in residue is consistent with the differing solubilities of the two elements (Figure 5-1). If the fluids had neutral to high pH, Zn would likely be insoluble as Zn-carbonate or Zn-ferrite [e.g., *Mann and Deutscher*, 1980]. Alkaline silica-precipitating fluids, an alternative interpretation for the haloes [*Milliken et al.*, 2016; *Frydenvang et al.*, 2017], cannot entirely account for the increase in SiO_2. In the Big Sky/Greenhorn pair, Zn/Si and Ge/Si have a negative correlation ($r = -0.81$) and as silica increases by 45%, Zn decreases by 67%. Neither of these changes can occur if simple silica addition alone is controlling the composition. Other trace elements (e.g., Ni) also have depletions too large to be explained by silica addition [*Gellert et al.*, 2016; *Schmidt et al.*, 2016; *Yen et al.,* 2017].

The acidic leaching proposed for the light-toned haloes contrasts with the nine APXS analyses on the Whale Rock, Bigfork/Albert, and Khomas outcrops. In these targets, both Zn and Ge have concentrations that are elevated over average Stimson (Figure 5-8, vector 1). All nine of these Stimson targets are in outcrops < 2 m from exposed Stimson/Murray contacts, but they are separated by up to 1200 m on *Curiosity's* traverse. We therefore interpret the elevated Zn and Ge to be due to the physical inclusion of Murray sediment in the Stimson sandstone when it was deposited.

The germanium, silica, and iron characteristics of the alteration haloes aid in constraining the likely host phase for Ge. GeO_2 and SiO_2 have similar solubility curves with respect to temperature and pH, whereby GeO_2 is about one order of magnitude less soluble than SiO_2 at pH < 9 and below 150° C (Figure 5-1). Solubilities of Ge and Si are independent of pH in solutions with pH < 9, and germanic acid, like silicic acid, is the dominant Ge species in solution (at low H_2S and low F^- activities) [*Bernstein and Waychunas*, 1987]. If Ge concentrations are controlled by GeO_2 solubility in germanates (silicates) and amorphous GeO_2 (silica), then Ge/Si is unlikely to change at low temperature and neutral to acidic pH [*Pokrovski and Schott*, 1998] between the host rock and halo; passive enrichment of both elements together would preserve the Ge/Si of the parent rock. This is not the case for Mt. Sharp haloes: Ge/Si decreases from 200 ± 20 to 150 ± 5 μmol/mol in the Cody – Ferdig alteration pair, stays below the LOD in the Ledger – Devon/Ivanhoe pair (< 55 μmol/mol), and increases variably from < 55 μmol/mol to ~40-70 μmol/mol in the Big Sky/Greenhorn and Okoruso/Lubango haloes. We find the apparent uncoupling of Ge and Si in the haloes demonstrates that Ge is less likely to be associated with the silica phases.

In Earth soils and sediment, Ge is preferentially adsorbed and coprecipitated with Fe oxides and oxyhydroxides during redox reactions, often leading to higher Ge concentrations and higher Ge/Si [e.g., *King et al.*, 2000; *Kurtz et al.*, 2002; *McManus et al.*, 2003; *Pokrovsky et al.*, 2006]. In the light-toned haloes, the addition of secondary Fe-bearing minerals (magnetite and/or hematite) is evident because the amount of Fe-oxides is higher in the crystalline fraction of the altered halo relative to the parent bedrock [*Yen et al.,* 2017]. The dissolution of Fe-bearing pyroxene along with the apparent leaching of Fe from the amorphous fraction of the parent bedrock resulted in a relative net gain in FeO of up to ~25% in the crystalline fraction of the altered halo [*Yen et al.,* 2017]. Since about half of the unaltered, soil-like Stimson targets have Ge near the detection limit (20-40 ppm), it is plausible that the Stimson formation rocks are elevated well above the Ge values of the Martian meteorites (1-3 ppm). Thus, the Ge enrichment in the alteration haloes may be a factor of 2 to 3 relative to the parent Stimson bedrock. Secondary Fe-oxide- and (oxy)hydroxide-forming environments have been shown to enrich Ge on Earth in circumneutral regimes [e.g., *King et al.*, 2000; *Kurtz et al.*, 2002; *McManus et al.*, 2003] as well as acid sulfate regimes [*Bernstein,* 1985]. Thus we propose that the 2-3X Ge enrichment may be related to the formation of secondary Fe-bearing phases. We acknowledge that the acidic alteration interpretation may be oversimplified; magnetite is also found in Greenhorn, where it would be metastable at low pH, suggesting a more complex fluid history in the fractures [*Yen et al.,* 2017].

5.5.4. Models for The Murray Formation

The contrasting stabilities of Zn and Ge at low pH and under diagenetic temperature conditions (Figure 5-1) provide additional constraint to the history of the Murray formation, which has geochemical [e.g., *Gellert et al.*, 2016; *Schmidt et al.*, 2016, *Thompson et al.*, 2016] and mineralogical [*Rampe et al.,* 2017] characteristics consistent with interaction with acidic fluids. In the acid alteration model, low pH fluids leached soluble elements (e.g., Ni, Zn), while relatively insoluble elements (e.g., Si, Ti) were conserved in a manner similar to that proposed for the fracture associated haloes (section

4.3.3). Unlike the halo alteration, however, the initial Zn and Ge concentrations of the Murray formation are less well constrained because the mudstone is more pervasively altered and the protolith composition is less understood.

In the following sections, we present two plausible (not mutually exclusive) models for the Zn and Ge variations observed in the Murray formation: 1) A top-down acidic leaching model, and 2) variations in provenance during emplacement of Murray sediment.

5.5.4.1. Top-down Acidic Leaching Along the Elevation Profile

A negative correlation of Zn with elevation (a proxy for stratigraphic position) has been proposed as evidence of top-down acidic leaching in the Murray formation (Figure 5-10) [*Rampe et al.,* 2017]. This is further supported by decreasing Ni and Mn progressively up the stratigraphic section [*Rampe et al.,* 2017]. While Zn, Ni, and Mn are not correlated in the Bradbury group (with the possible exception of the Dillinger unit of the Kimberley formation), they are correlated in the Murray formation and Stimson formation fracture haloes (Figure S3). Other elements expected to be mobile at low pH (Mg, Ca, Fe) do not exhibit the same clear trend with elevation (Figure 5-S5); however, compared to average Mars (soil), Ca and Mg are ~40% lower and Fe is ~15% lower in the Confidence Hills class (Figure 5-S4) [*Thompson et al.*, 2016]. The Buckskin class is more depleted in Ca and Mg (45% and 65%, respectively) and Fe is notably low (75% lower) [*Thompson et al.*, 2016]. These major element depletions may be linked to acidic alteration in an open hydrologic system [*Rampe et al.,* 2017]. Top-down leaching by low pH groundwater may provide a mechanism to transport and enrich Zn, Ni, and Mn at depth in response to a change in the fluid carrying capacity. An acidic plume and/or groundwater could have caused this depth profile by interacting with the sediment below -4440 m, mobilizing the metals and precipitating them at lower levels. At higher elevations (> -4440 m), the APXS targets are not depleted in Zn, Mn, and Ni, suggesting less leaching or different fluid chemistry above that level. An unconformity within Murray above Buckskin could cause the break in the element profiles shown in Figure 5-10 at -4440 m; however, we suggest this is unlikely because the finely laminated mudstone facies of the Murray formation [*Grotzinger et al.*, 2015] is more or less continuous up to -4420 m elevation (with some intercalated sandstone), despite the high silica excursion in composition at the Buckskin unit [*Rampe et al.,* 2017].

Many examples of similar trace metal profiles with depth exist on Earth, where a sharp drop in concentrations marks the presence of an acidic groundwater table, and metals are concentrated down-profile, often at an intersection with more dilute groundwater or sediment with a pH and/or redox buffering capacity [e.g., *Paulson*, 1997; *Clemente et al.*, 2008]. Note that *Curiosity* traversed ~1200 m laterally over this profile with large gaps in the sampling intervals (up to 500 m), and it is not clear if the variation is dominated by vertical or lateral transport.

Consistent with its low solubility at low pH, Ge does not vary in the same manner with elevation, further constraining the top-down leaching model. In CH rocks, Ge concentrations span similar ranges (Figure 5-10). The high silica BK class rocks, however, have about half the Ge concentration of other Murray rocks. Assuming the BK precursor rocks had similar initial Ge concentrations to the other Murray mudstones, Ge could have been removed by leaching. Low pH leaching of Ge is plausible at diagenetic temperatures in at least two scenarios. First, Ge forms aqueous Ge-F complexes (more stable than Ge-Cl complexes) in the presence of dissolved fluorine. Thus, Ge solubility increases, but can only reach significant dissolved concentrations ($> 10^{-5}$ molal GeF_6^{2-}) at $pH < 2.5$ and with F activities above 7 millimolal [*Benoit and Place*, 1963; *Golovnev et al.*, 2003]. Fluorine concentrations at this level are seen in on Earth in fumaroles, for example; groundwater is usually more dilute (<1 millimolal) [e.g., *Hurwitz et al.*, 2003]. Second, surface adsorption of Ge on Fe-oxy/hydroxide mineral grains is pH dependent, and a fraction of the Ge could have been mobile in fluids at $pH < 4$ [*Pokrovsky et al.*, 2006].

Fluorine-bearing fluid in the Murray formation is plausible because unambiguous evidence of Ge mobilization and enrichment (~650 ppm) was found in the Garden City veins. In the dark material in Garden City (best represented by Alvord_Mountain_raster7; Appendix 5-1), Zn is ~2X higher (2480 ± 75 ppm) and Ge is ~7X enriched over typical CH bedrock. High CaO (23.2 ± 0.5 wt%; deconvolved concentration from *VanBommel et* *al.* [2017]) and Ca-F detection by ChemCam [*Nachon et al.*, 2017] suggest the presence of a fluorine-rich phase in the dark vein material at Garden City, although the mineralogy is not known and a MAHLI ultraviolet fluorescence experiment was inconclusive [*Fisk et al.*, 2015]. Fluorite has been proposed for the dark vein material [*Nachon et al.*, 2017]. If all of the Ca in Alvord_Mountain_raster7 (4 mol/kg) was coupled with F as CaF_2 (pure fluorite), then the F would be 8 mol/kg, which is ~13 wt% after renormalizing to 100 wt%. The lowest energy detectable in the APXS spectrum is ~630 eV, and the F Kα peak is at 676.8 eV, therefore F is detectable by APXS at high concentrations [cf. *Nachon et al.*, 2017]. We estimate that >10 wt% fluorine would be detectable by the APXS; however, there is no evidence of a F peak at the ~13 wt% level; which suggests that not all of the Ca in the vein is coupled with F. Because Garden City is ~3 m in elevation below BK and Marias Pass, acidic, F-bearing fluid could have mobilized Ge, Zn, and other mobile elements (Ni, Mn) downward and precipitated the components in the Garden City vein cluster.

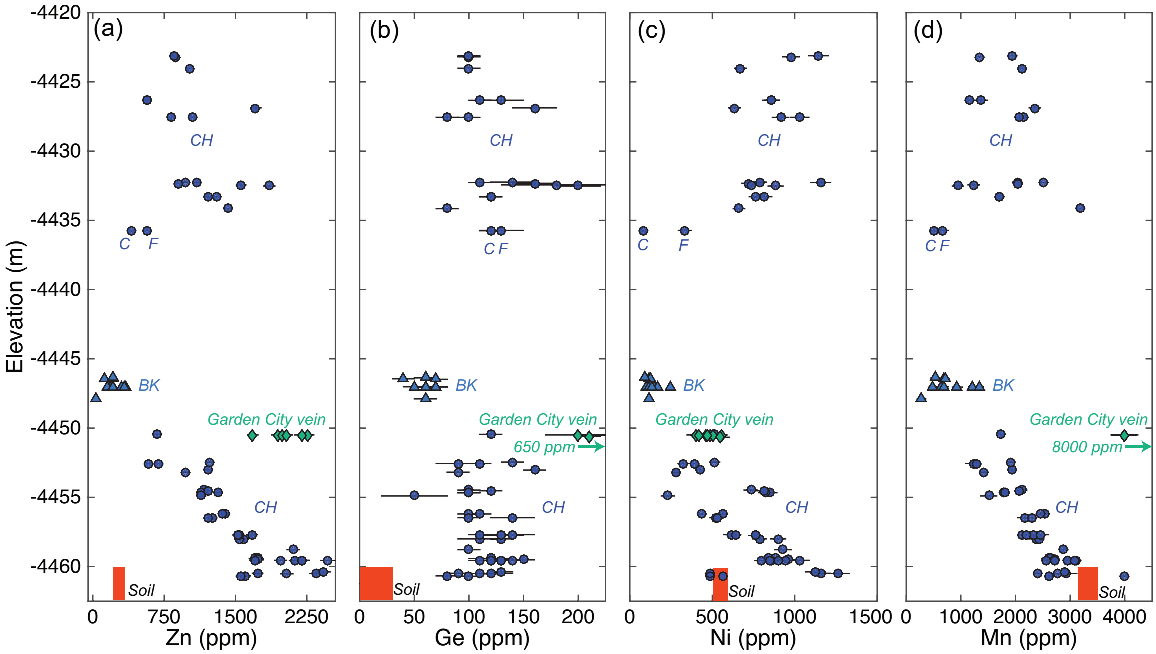

Figure 5-10: (a) Zn, (b) Ge, (c) Ni, and (d) Mn variation with elevation in the Murray formation. Above -4460 m, Zn, Ni, and Mn concentrations in the CH and BK classes decrease regularly with increasing elevation [*Rampe et al.*, 2017], whereas above Buckskin (-4445 m) the three elements do not correlate with elevation. Germanium does not vary with elevation in the CH rocks, and is about half of the CH concentrations in the

BK rocks. Compositional classes and the paired Ferdig (F) and Cody (C) targets (Table 5-3) are denoted and the symbols are as in Figure 5-5. Gale soil concentrations are indicated by the red box. Major element variation with elevation in the same units are presented in Figure 5-S5.

5.5.4.2. The Buckskin Class: Unique Provenance and/or Alteration History

Inconsistencies with the leached elevation profile model above call for an alternative model involving different provenance and/or alteration history for the BK class than the rest of the Murray formation. The elevation profiles of Zn and Ge (and Ni, Mn) obscure an important feature of the BK rocks. Silica ranges from 53-74 wt% in BK targets (Figure 5-8), which overlaps with CH targets (46-54 wt%). Assuming silica is an index for alteration, BK is *both* moderately and highly altered. Zinc is low over this full range of alteration, having no correlation with silica, which can be explained with the top-down model because Zn is readily mobile in moderately low pH fluids. However, Ge is also notably lower than CH in the moderately altered BK (30-60 ppm). Because Ge mobilization is unlikely without very low pH and F complexing, significant Ge leaching is inconsistent with the only moderately altered rocks. These observations support the interpretation that BK rocks had inherently lower Zn and Ge concentrations than CH, and that the two Murray classes did not necessarily have the same starting composition prior to diagenesis.

Mixing of a Zn and Ge depleted, silica-rich component into CH may explain some of the contrasting characteristics of BK and CH. BK has 17±1 wt% tridymite and a larger fraction of high silica amorphous material than the three CH class CheMin drilled samples [*Morris et al.*, 2016; *Rampe et al., 2017*]. If these components were low in Zn and Ge, then the addition of depleted, silica-rich material to an enriched CH-like rock might account for a decrease in Ge. However, such a two-component mixing model also has inconsistencies. The mixing would result in a linear relationship between the CH and BK endmembers in Figure 5-8, but this is not the case. This might indicate that the BK precursor/parent materials had lower Zn and Ge than the CH precursor/parent materials, or that Zn and Ge were removed from a CH-like precursor/parent.

5.6. Summary of Zn and Ge Enrichment and Fractionation Model

The APXS on *Curiosity* has discovered widespread Zn and Ge enrichments in the sedimentary rocks of Gale Crater on Mars. We interpret this enrichment to be a signature of the sediment source region, and that diagenetic fluids subsequently fractionated the two elements. Overall, Zn and Ge indicate a complex fluid history at Gale that we outline in a model below.

First, primary enrichment of Zn and Ge occurred in the Gale sediment source region. Hydrothermal fluids generated by impacts and volcanism mobilized and concentrated the elements near the Martian surface. Elevated Zn in soils measured by *Curiosity* and *Opportunity* and evidence of hydrothermal alteration in the Martian meteorite NWA 7034 [*McCubbin et al.*, 2016] may point to this process as a characteristic of the entire planet. These deposits were likely reworked and remobilized repeatedly during the early impact processing of the surface, but eventually were preferentially concentrated in fractures and breccia, possibly associated with the Gale Crater-forming impact and accompanying hydrothermal activity. Subsequent erosion of vein-bearing rock and breccia in the crater rim distributed the Zn- and Ge-rich hydrothermal precipitates as detrital material mixed with the host rock into the crater. Thus, *Curiosity* now observes sediment primarily composed of the dominant rock types of the source region, with a background signal elevated in Zn and Ge due to the primary hydrothermal deposits being physically mixed with the siliciclastic material during deposition.

Gale sediments experienced a complex history during and after deposition, with Zn and Ge recording evidence of provenance and fluid conditions. Zinc was mobilized and fractionated from Ge in the Kimberley formation, likely via Cl-rich fluids that caused minimal alteration of the bedrock. Acidic fluids with sufficiently low pH to mobilize Zn along with less soluble cations (Fe, Mn, Ca, Mg), while retaining silica, TiO_2, and Ge, altered the Murray formation. Most likely, both models discussed above (section 4.3.4) account for the Zn and Ge characteristics of Murray: the bedrock interacted with acidic fluids that mobilized Zn and other cations, but also experienced a change in provenance to incorporate materials with the lower Ge characterizing the BK rocks. The relative timing of these diagenetic interactions in the BG and lower Mt. Sharp is not clear. After a period of erosion of the Murray formation, the Stimson formation, possibly sourced from soil-like (low Ge) sands from outside of the crater, was emplaced. In one or more later fluid events within crosscutting fractures in lower Mt. Sharp units, Ge was concentrated, along with significant leaching of Zn, by acidic fluids.

We now ask if the Zn and Ge observations can illuminate the hypothesis of *Grotzinger et al.* [2014, 2015], who argue for the existence of a circumneutral lake in Gale Crater during the late Noachian and early Hesperian time. Lacustrine chemical processes are not likely to have been the direct cause of the primary Zn and Ge enrichment observed in mudstone deposits; at neutral pH and low temperature, both elements are relatively insoluble. Furthermore, the sediment lacks evidence of the extensive weathering or hydrothermal alteration necessary to extract high Zn and Ge concentrations from typical crustal materials (basalt) [e.g., *Kurtz et al.*, 2002; *Scribner et al.*, 2006]. As presented above, hydrothermal processes likely caused the enrichment of the elements in the source region, probably within Fe phases that were then delivered with clastic sediment to the lake. In neutral waters, Zn and Ge would favor solid phases. Periodic drying of a lake may have resulted in acidic brines capable of mobilizing the elements in solution, although lacustrine evaporite units have not yet been discovered (they may have been reworked or eroded away). We conclude that a neutral lake would not cause strong chemical fractionation of Zn and Ge in enriched sediment, and that diagenetic fractionation affected Zn and Ge to a degree that obscures lake chemistry. Further interpretation of paleolake chemistry based on Zn and Ge alone would be speculative.

Correlations between the Zn and Ge distribution and past fluvial, deltaic, and lacustrine depositional environments proposed for Gale Crater lake [*Grotzinger et al.,* 2014, 2015] are not clear. One distinction is apparent between the lacustrine mudstone (John Klein, CH, and Buckskin classes) and the fluvial deltaic sandstone deposits of the Bradbury Group (Bradbury classes excluding John Klein). The mudstone units have elevated Ge above ~40 ppm, whereas 39 of 76 targets in the fluvial deltaic deposits do not have detectable Ge, particularly most of the Jake_M class (Figure 5-5; Appendix 5-1). This may be due to change in provenance or a homogeneous averaging effect in the mudstones, but variability in the coarser sandstones could also be a consequence of cm-scale heterogeneity in the ~2 cm APXS field of view.

5.7. Conclusion

Discoveries by three APXS instruments on Mars hint that Zn and Ge enrichments are a common feature of the Martian surface [*Gellert et al.*, 2006; *Ming et al.*, 2008; *Mittlefehldt et al.*, 2016]. Concentrated Zn, Ge, and other fluid-mobile elements (e.g., S, Cl) on the surface may therefore preserve a record of fluid processes at many sites on the planet. In this work, we reasoned via the law of parsimony that the primary Zn and Ge enrichments in Gale Crater were in hydrothermal deposits in the source region, and these were subsequently dispersed in the sediment mantling the crater floor. We presented direct evidence of in situ diagenetic mobilization of Zn and Ge in Gale Crater, whereby the contrasting geochemical properties of the two elements led to fractionation, indicating different fluid conditions. Our model, based on geologic context and the natural geochemistry of Zn and Ge, constrains the geochemical fluid history of Gale Crater, and may provide a framework for understanding other sites on Mars that have similar fluid-mobile element enrichments.

5.8. Acknowledgements

All raw and reduced APXS data are available at the planetary data system, http://pds-geosciences.wustl.edu/missions/msl/apxs.htm. Results for Zn and Ge are available in this paper and as a supplementary .xlsx file (Appendix 5-1). This manuscript was improved by the insightful reviews of Munir Humayun and an anonymous reviewer as well as by comments from Neil Bannerjee, Lyudmila Goncharova, David Mittlefehldt, and Gordon Osinski. The MSL APXS was managed and financed by the Canadian Space Agency (CSA), with MacDonald Dettweiler and Associates (MDA) as prime contractor to build the instrument. Science team funding is provided by CSA and NASA/JPL-Caltech. A CSA MSL Participating Scientist Grant awarded to M. E. Schmidt supported J. A. Berger. We appreciate and acknowledge the unwavering support of dedicated engineers at MDA, CSA, and JPL during the development and operation of the APXS.

5.9. References

Achilles, C. N. et al. (2017), Mineralogy of an Active Eolian Sediment from the Namib Dune, Gale Crater, Mars, *J. Geophys. Res. Planets*, 2017JE005262, doi:10.1002/2017JE005262.

Aitchison, J. (1982), The Statistical Analysis of Compositional Data, *Journal of the Royal Statistical Society. Series B (Methodological)*, *44*(2), 139–177

Agee, C. B. et al. (2013), Unique Meteorite from Early Amazonian Mars: Water-Rich Basaltic Breccia Northwest Africa 7034, *Science*, doi:10.1126/science.1228858.

Arnórsson, S. (1984), Germanium in Icelandic geothermal systems, *Geochim. Cosmochim. Acta*, *48*(12), 2489–2502, doi:10.1016/0016-7037(84)90300-4.

Baumgartner, R. J., M. L. Fiorentini, D. Baratoux, S. Micklethwaite, A. K. Sener, J. P. Lorand, and T. C. McCuaig (2015), Magmatic controls on the genesis of Ni–Cu±(PGE) sulphide mineralisation on Mars, *Ore Geology Reviews*, *65, Part 1*, 400–412, doi:10.1016/j.oregeorev.2014.10.004.

Benoit, R. L., and J. Place (1963), Fluoride Complexes of Germanium (IV) in Aqueous Solution, *Can. J. Chem.*, *41*(5), 1170–1180, doi:10.1139/v63-165.

Berger, J. A. et al. (2015), Chemical Composition of Diagenetic Features at Lower Aeolis Mons, Mars as Measured by Curiosity's APXS, in *AGU Fall Meeting*, vol. P43B-2121.

Berger, J. A. et al. (2016a), A global Mars dust composition refined by the Alpha-Particle X-ray Spectrometer in Gale Crater, *Geophys. Res. Lett.*, 2015GL066675, doi:10.1002/2015GL066675.

Berger, J. A., M. E. Schmidt, M. R. M. Izawa, R. Gellert, D. W. Ming, E. B. Rampe, S. J. VanBommel, and A. C. McAdam (2016b), Phosphate Stability in Diagenetic Fluids Constrains the Acidic Alteration Model for Lower Mt. Sharp Sedimentary Rocks in Gale Crater, Mars, in *Lunar Planet. Sci. Conf. 47*, Abstract 1652.

Bernstein, L. R. (1985), Germanium geochemistry and mineralogy, *Geochim. Cosmochim. Acta*, *49*(11), 2409–2422, doi:10.1016/0016-7037(85)90241-8.

Bernstein, L. R., and G. A. Waychunas (1987), Germanium crystal chemistry in hematite and goethite from the Apex Mine, Utah, and some new data on germanium in aqueous solution and in stottite, *Geochim. Cosmochim. Acta*, *51*(3), 623–630, doi:10.1016/0016-7037(87)90074-3.

Bish, D. L. et al. (2013), X-ray Diffraction Results from Mars Science Laboratory: Mineralogy of Rocknest at Gale Crater, *Science*, *341*(6153), 1238932, doi:10.1126/science.1238932.

Bishop, J. L., S. L. Murchie, C. M. Pieters, and A. P. Zent (2002), A model for formation of dust, soil, and rock coatings on Mars: Physical and chemical processes on the Martian surface, *J. Geophys. Res.*, *107*(5097), 17, doi:doi:10.1029/2001JE001581.

Blake, D. et al. (2012), Characterization and Calibration of the CheMin Mineralogical Instrument on Mars Science Laboratory, *Space Sci. Rev.*, *170*(1–4), 341–399, doi:10.1007/s11214-012-9905-1.

Blake, D. F. et al. (2013), Curiosity at Gale Crater, Mars: Characterization and Analysis of the Rocknest Sand Shadow, *Science*, *341*(6153), 1239505, doi:10.1126/science.1239505.

Borlina, C. S., B. L. Ehlmann, and E. S. Kite (2015), Modeling the thermal and physical evolution of Mount Sharp's sedimentary rocks, Gale Crater, Mars: Implications for diagenesis on the MSL Curiosity rover traverse, *J. Geophys. Res. Planets*, *120*(8), 2015JE004799, doi:10.1002/2015JE004799.

Brückner, J., G. Dreibus, R. Gellert, S. W. Squyres, H. Wänke, A. Yen, and J. Zipfel (2008), Mars Exploration Rovers: chemical composition by the APXS, in *The Martian Surface*, vol. 1, edited by J. F. Bell III, pp. 58 – 101, Cambridge University Press, New York.

Burns, R. G., and D. S. Fisher (1990), Evolution of sulfide mineralization on Mars, *J. Geophys. Res. Solid Earth*, *95*(B9), 14169–14173.

Campbell, J. L., M. Lee, B. N. Jones, S. M. Andrushenko, N. G. Holmes, J. A. Maxwell, and S. M. Taylor (2009), A fundamental parameters approach to calibration of the Mars Exploration Rover Alpha Particle X-ray Spectrometer, *J. Geophys. Res.*, *114*(E04006), doi:200910.1029/2008JE003272.

Campbell, J. L., S. M. Andrushenko, S. M. Taylor, and J. A. Maxwell (2010), A fundamental parameters approach to calibration of the Mars Exploration Rover Alpha Particle X-ray Spectrometer: 2. Analysis of unknown samples, *J. Geophys. Res.*, *115*(E04009), doi:201010.1029/2009JE003481.

Campbell, J. L., A. M. McDonald, G. M. Perrett, and S. M. Taylor (2011), A GUPIX-based approach to interpreting the PIXE-plus-XRF spectra from the Mars Exploration rovers: II geochemical reference materials, *Nucl. Instrum. Methods Phys. Res. B*, *269*(1), 69–81, doi:10.1016/j.nimb.2010.09.014.

Campbell, J. L., G. M. Perrett, R. Gellert, S. M. Andrushenko, N. I. Boyd, J. A. Maxwell, P. L. King, and C. D. M. Schofield (2012), Calibration of the Mars Science Laboratory Alpha Particle X-ray Spectrometer, *Space. Sci. Rev.*, *170*(1-4), 319–340, doi:10.1007/s11214-012-9873-5.

Campbell, J. L. et al. (2014), The Mars Science Laboratory APXS calibration target: Comparison of Martian measurements with the terrestrial calibration, *Nucl. Instrum. Methods Phys. Res. B*, *323*, 49–58, doi:10.1016/j.nimb.2014.01.011.

Carr, M. H., and J. W. Head (2010), Geologic history of Mars, *Earth Planet. Sci. Lett.*, *294*(3–4), 185–203, doi:10.1016/j.epsl.2009.06.042.

Churchill, J. J. C., M. E. Schmidt, J. A. Berger, F. Fueten, L. L. Tornabene, L. E. Vargas, and J. Walmsley (2017), Possible Volcanic Avalanche Deposit North of Gale Crater, in *Lunar Planet. Sci. Conf. 48*, Abstract 2411.

Ciavatta, L., M. Iuliano, R. Porto, and E. Vasca (1990), Fluorogermanate(IV) equilibria in acid media, *Polyhedron*, *9*(10), 1263–1270, doi:10.1016/S0277-5387(00)86762-5.

Clemente, R., N. M. Dickinson, and N. W. Lepp (2008), Mobility of metals and metalloids in a multi-element contaminated soil 20 years after cessation of the pollution source activity, *Environmental Pollution (1987)*, *155*(2), 254–261, doi:http://dx.doi.org.proxy1.lib.uwo.ca/10.1016/j.envpol.2007.11.024.

Cook, N. J. et al. (2015), Distribution and Substitution Mechanism of Ge in a Ge-(Fe)-Bearing Sphalerite, *Minerals*, *5*(2), 117–132, doi:10.3390/min5020117.

De Argollo, R., and J.-G. Schilling (1978), Ge-Si and Ga-Al fractionation in Hawaiian volcanic rocks, *Geochim. Cosmochim. Acta*, *42*(6, Part A), 623–630, doi:10.1016/0016-7037(78)90007-8.

Degryse, F., E. Smolders, and D. R. Parker (2009), Partitioning of metals (Cd, Co, Cu, Ni, Pb, Zn) in soils: concepts, methodologies, prediction and applications – a review, *European Journal of Soil Science*, *60*(4), 590–612, doi:10.1111/j.1365-2389.2009.01142.x.

Dreibus, G., and H. Wanke (1985), Mars, a volatile-rich planet, *Meteoritics*, *20*, 367–381.

Drever, J. I. (1997), *The Geochemistry of Natural Waters: Surface and Groundwater Environments*, 3rd ed., Prentice Hall.

Ehlmann, B. L. et al. (2017), Chemistry, Mineralogy, and Grain Properties at Namib and High Dunes, Bagnold Dune Field, Gale Crater, Mars: A Synthesis of Curiosity Rover Observations, *J. Geophys. Res. Planets*, 2017JE005267, doi:10.1002/2017JE005267.

Evans, M. J., and L. A. Derry (2002), Quartz control of high germanium/silicon ratios in geothermal waters, *Geology*, *30*(11), 1019–1022, doi:10.1130/0091-7613(2002)030<1019:QCOHGS>2.0.CO;2.

Farley, K. A. et al. (2014), In Situ Radiometric and Exposure Age Dating of the Martian Surface, *Science*, *343*(6169), 1247166, doi:10.1126/science.1247166.

Fisk, M. R. et al. (2015), UV-Excited Fluorescence of Rocks in Gale Crater, Mars, in *AGU Fall Meeting*, vol. Abstract P51E-07.

Frenzel, M., T. Hirsch, and J. Gutzmer (2016), Gallium, germanium, indium, and other trace and minor elements in sphalerite as a function of deposit type — A meta-analysis, *Ore Geology Reviews*, *76*, 52–78, doi:10.1016/j.oregeorev.2015.12.017.

Froelich, P. N., G. A. Hambrick, M. O. Andreae, and R. A. Mortlock (1985), The Geochemistry of Inorganic Germanium, *J. Geophys. Res.*, *90*(C1), 1133–1141.

Frydenvang, J. et al. (2017), Diagenetic silica enrichment and late-stage groundwater activity in Gale crater, Mars, *Geophys. Res. Lett.*, *44*(10), 2017GL073323, doi:10.1002/2017GL073323.

Gellert, R. et al. (2006), Alpha Particle X-Ray Spectrometer (APXS): Results from Gusev crater and calibration report, *J. Geophys. Res.*, *111*(E02S05), doi:200610.1029/2005JE002555.

Gellert, R., J. L. Campbell, P. L. King, L. A. Leshin, G. W. Lugmair, J. G. Spray, S. W. Squyres, and A. S. Yen (2009), The Alpha-Particle-X-Ray-Spectrometer (APXS) for the Mars Science Laboratory (MSL) Rover Mission, in *Lunar Planet. Sci., XL*, Abstract 2364.

Gellert, R. et al. (2015), Chemical Evidence for an Aqueous History at Pahrump, Gale Crater, Mars, as Seen by the APXS, in *Lunar Planet. Sci., XLVI*, Abstract 1855.

Gellert, R. et al. (2016), Chemical Evidence for an Episode of Acidic Leaching at the Base of Mount Sharp, Gale Crater, Mars, as seen by the APXS, in *Lunar Planet. Sci. Conf. 47*, Abstract 2368.

Golovnev, N. N., V. B. Nogteva, and I. I. Golovneva (2003), Formation of Si (IV) and Ge (IV) fluoride complexes in dilute aqueous solutions, *Russian journal of general chemistry*, *73*(9), 1388–1394.

Grant, J. A., S. A. Wilson, N. Mangold, F. Calef, and J. P. Grotzinger (2014), The timing of alluvial activity in Gale crater, Mars, *Geophysical Research Letters*, *41*(4), 1142–1149, doi:10.1002/2013GL058909.

Grotzinger, J. P. et al. (2012), Mars Science Laboratory Mission and Science Investigation, *Space Sci Rev*, *170*(1-4), 5–56, doi:10.1007/s11214-012-9892-2.

Grotzinger, J. P. et al. (2014), A Habitable Fluvio-Lacustrine Environment at Yellowknife Bay, Gale Crater, Mars, *Science*, *343*(6169), 1242777, doi:10.1126/science.1242777.

Grotzinger, J. P. et al. (2015), Deposition, exhumation, and paleoclimate of an ancient lake deposit, Gale crater, Mars, *Science*, *350*(6257), aac7575, doi:10.1126/science.aac7575.

Hamade, T., K. O. Konhauser, R. Raiswell, S. Goldsmith, and R. C. Morris (2003), Using Ge/Si ratios to decouple iron and silica fluxes in Precambrian banded iron formations, *Geology*, *31*(1), 35–38, doi:10.1130/0091-7613(2003)031<0035:UGSRTD>2.0.CO;2.

Heinrichs, H., B. Schulz-Dobrick, and K. H. Wedepohl (1980), Terrestrial geochemistry of Cd, Bi, Tl, Pb, Zn and Rb, *Geochim. Cosmochim. Acta*, *44*(10), 1519–1533, doi:10.1016/0016-7037(80)90116-7.

Heyl, A. V., and C. N. Bozion (1964), *Oxidized zinc deposits of the United States*, Bulletin 1135, USGS Numbered Series, U.S. Government Printing Office.

Höll, R., M. Kling, and E. Schroll (2007), Metallogenesis of germanium—A review, *Ore Geology Reviews*, *30*(3–4), 145–180, doi:10.1016/j.oregeorev.2005.07.034.

Humayun, M. et al. (2013), Origin and age of the earliest Martian crust from meteorite NWA 7533, *Nature*, *503*(7477), 513–516, doi:10.1038/nature12764.

Humayun, M., S. Yang, K. Righter, B. Zanda, and R. H. Hewins (2016), The Germanium Dichotomy in Martian Meteorites, in *Lunar Planet. Sci. Conf. 47*, Abstract 2459.

Hurwitz, S., F. Goff, C. J. Janik, W. C. Evans, D. A. Counce, M. L. Sorey, and S. E. Ingebritsen (2003), Mixing of magmatic volatiles with groundwater and interaction with basalt on the summit of Kilauea Volcano, Hawaii, *J. Geophys. Res. Solid Earth*, *108*(B1), 2028, doi:10.1029/2001JB001594.

Izawa, M. R. M., M. E. Schmidt, J. A. Berger, and R. Gellert (2016), Evaluating the Influence of Magamatic Sulphides on Chalcophile Element Enrichments in the Bradbury Assemblage, Gale Crater, Mars, Using APXS Measurements, in *Lunar Planet. Sci. Conf. 47*, Abstract 2705.

James, F., and M. Roos (1989), MINUIT functional minimization and error analysis, *D506-Minuit, CERN.*

Kah, L. C., R. E. Kronyak, D. W. Ming, J. P. Grotzinger, J. Schieber, D. Y. Sumner, and K. S. Edgett (2015), Diagenetic Crystal Growth in the Murray Formation, Gale Crater, Mars, in *Geological Society of America Meeting*, Abstract 265770, Baltimore, MD, United States.

King, S. L., P. N. Froelich, and R. A. Jahnke (2000), Early diagenesis of germanium in sediments of the Antarctic South Atlantic: in search of the missing Ge sink, *Geochim. Cosmochim. Acta*, *64*(8), 1375–1390, doi:10.1016/S0016-7037(99)00406-8.

Kurtz, A. C., L. A. Derry, and O. A. Chadwick (2002), Germanium-silicon fractionation in the weathering environment, *Geochim. Cosmochim. Acta*, *66*(9), 1525–1537, doi:10.1016/S0016-7037(01)00869-9.

Lanza, N. L. et al. (2016), Oxidation of manganese in an ancient aquifer, Kimberley formation, Gale crater, Mars, *Geophys. Res. Lett.*, 2016GL069109, doi:10.1002/2016GL069109.

Lasue, J. et al. (2016), Observation of> 5 wt% zinc at the Kimberley outcrop, Gale crater, Mars, *J. Geophys. Res. Planets*, doi:10.1002/2015JE004946.

Le Deit, L. L., E. Hauber, F. Fueten, M. Pondrelli, A. P. Rossi, and R. Jaumann (2013), Sequence of infilling events in Gale Crater, Mars: Results from morphology, stratigraphy, and mineralogy, *J. Geophys. Res. Planets*, *118*(12), 2012JE004322, doi:10.1002/2012JE004322.

Le Maitre, R. W., P. Bateman, A. Dudek, J. Keller, J. Lameyre, M. J. Le Bas, P. A. Sabine, R. Schmid, H. Sorensen, and A. Streckeisen (1989), *A classification of igneous rocks and glossary of terms: Recommendations of the International Union of Geological Sciences Subcommission on the Systematics of Igneous Rocks*, Blackwell Oxford.

Lodders, K. (2003), Solar System Abundances and Condensation Temperatures of the Elements, *The Astrophysical Journal*, *591*, 1220–1247, doi:10.1086/375492.

Lodders, K., and B. Fegley Jr. (1997), An Oxygen Isotope Model for the Composition of Mars, *Icarus*, *126*(2), 373–394, doi:10.1006/icar.1996.5653.

Lodders, K., and B. Fegley (1998), *The planetary scientist's companion*, Oxford University Press.

Mangold, N. et al. (2017), Classification scheme for sedimentary and igneous rocks in Gale crater, Mars, *Icarus*, *284*, 1–17, doi:10.1016/j.icarus.2016.11.005.

Mann, A. W., and R. L. Deutscher (1980), Solution geochemistry of lead and zinc in water containing carbonate, sulphate and chloride ions, *Chemical Geology*, *29*(3-4), 293–311.

McAdam, A. C. et al. (2014), Sulfur-bearing phases detected by evolved gas analysis of the Rocknest aeolian deposit, Gale Crater, Mars, *J. Geophys. Res. Planets*, *119*(2), 373–393, doi:10.1002/2013JE004518.

McBride, M. B. (1994), *Environmental Chemistry of Soils*, Oxford University Press, New York.

McCubbin, F. M. et al. (2016), Geologic history of Martian regolith breccia Northwest Africa 7034: Evidence for hydrothermal activity and lithologic diversity in the Martian crust, *Journal of Geophysical Research: Planets*, *121*(10), 2120–2149, doi:10.1002/2016JE005143.

McGlynn, I. O., C. M. Fedo, and H. Y. McSween (2011), Origin of basaltic soils at Gusev crater, Mars, by aeolian modification of impact-generated sediment, *J. Geophys. Res.*, *116*(E7), E00F22, doi:10.1029/2010JE003712.

McLennan, S. M. et al. (2013), Elemental Geochemistry of Sedimentary Rocks at Yellowknife Bay, Gale Crater, Mars, *Science*, 1244734, doi:10.1126/science.1244734.

McLennan, S. M., E. Dehouck, J. P. Grotzinger, J. A. Hurowitz, N. Mangold, K. Siebach, and MSL Science Team (2015), Geochemical Record of Open-System Chemical Weathering at Gale Crater and Implications for Paleoclimates on Mars, in *Lunar Planet. Sci. Conf. 46*, Abstract 2533.

McManus, J., D. E. Hammond, K. Cummins, G. P. Klinkhammer, and W. M. Berelson (2003), Diagenetic Ge-Si fractionation in continental margin environments: further evidence for a nonopal Ge sink, *Geochim. Cosmochim. Acta*, *67*(23), 4545–4557, doi:10.1016/S0016-7037(03)00385-5.

McPhail, D. C., E. Summerhayes, S. Welch, and J. Brugger (2003), The geochemistry and mobility of zinc in the regolith, *Advances in Regolith*, 287–291.

McSween Jr., H. Y., and K. Keil (2000), Mixing relationships in the Martian regolith and the composition of globally homogeneous dust, *Geochimica et Cosmochimica Acta*, *64*(12), 2155–2166, doi:10.1016/S0016-7037(99)00401-9.

Mertens, J., and E. Smolders (2013), Zinc, in *Heavy Metals in Soils*, edited by B. J. Alloway, pp. 465–493, Springer Netherlands.

Milliken, R. E., J. A. Hurowitz, D. L. Bish, J. P. Grotzinger, and R. Wiens (2016), The Chemical and Mineralogical Stratigraphy of Lower Mt. Sharp: Relating Rover Observations to Orbital Predictions, in Lunar Planet. Sci. Conf. 47, abstract 1495.

Ming, D. W. et al. (2008), Geochemical properties of rocks and soils in Gusev Crater, Mars: Results of the Alpha Particle X-Ray Spectrometer from Cumberland Ridge to Home Plate, *J. Geophys. Res.*, *113*(E12S39), 28 PP., doi:200810.1029/2008JE003195.

Ming, D. W. et al. (2014), Volatile and Organic Compositions of Sedimentary Rocks in Yellowknife Bay, Gale Crater, Mars, *Science*, *343*(6169), 1245267, doi:10.1126/science.1245267.

Mittlefehldt, D. W. et al. (2016), Alumina + Silica ± Germanium Alteration in Smectite-Bearing Marathon Valley, Endeavour Crater Rim, Mars, in *Lunar Planet. Sci. Conf. 47*, Abstract 2086.

Morris, R. V. et al. (2015), Update on the Chemical Composition of Crystalline, Smectite, and Amorphous Components for Rocknest Soil and John Klein and

Cumberland Mudstone Drill Fines at Gale Crater, Mars, in *Lunar Planet. Sci. Conf. 46*, Abstract 2622.

Morris, R. V. et al. (2016), Silicic volcanism on Mars evidenced by tridymite in high-SiO2 sedimentary rock at Gale crater, *PNAS*, *113*(26), 7071–7076, doi:10.1073/pnas.1607098113.

Mortlock, R. A., and P. N. Froelich (1987), Continental weathering of germanium: Ge/Si in the global river discharge, *Geochim. Cosmochim. Acta*, *51*(8), 2075–2082, doi:10.1016/0016-7037(87)90257-2.

Mortlock, R. A., P. N. Froelich, R. A. Feely, G. J. Massoth, D. A. Butterfield, and J. E. Lupton (1993), Silica and germanium in Pacific Ocean hydrothermal vents and plumes, *Earth Planet. Sci. Lett.*, *119*(3), 365–378, doi:10.1016/0012-821X(93)90144-X.

Murnane, R. J., and R. F. Stallard (1990), Germanium and silicon in rivers of the Orinoco drainage basin, *Nature*, *344*(6268), 749–752, doi:10.1038/344749a0.

Nachon, M. et al. (2017), Chemistry of diagenetic features analyzed by ChemCam at Pahrump Hills, Gale crater, Mars, *Icarus*, *281*, 121–136, doi:10.1016/j.icarus.2016.08.026.

Nesbitt, H. W., and R. E. Wilson (1992), Recent chemical weathering of basalts, *Am J Sci*, *292*(10), 740–777, doi:10.2475/ajs.292.10.740.

Newsom, H. E. et al. (2014), Gale crater and impact processes –Curiosity's first 364 Sols on Mars, *Icarus*, doi:10.1016/j.icarus.2014.10.013.

O'Connell-Cooper, C. D., J. G. Spray, L. M. Thompson, R. Gellert, J. A. Berger, N. I. Boyd, E. D. Desouza, G. M. Perrett, M. Schmidt, and S. J. VanBommel (2017), APXS-derived chemistry of the Bagnold dune sands: Comparisons with Gale crater soils and the global martian average, *J. Geophys. Res. Planets*, 2017JE005268, doi:10.1002/2017JE005268.

Óskarsson, N. (1981), The chemistry of icelandic lava incrustations and the latest stages of degassing, *Journal of Volcanology and Geothermal Research*, *10*(1), 93–111, doi:10.1016/0377-0273(81)90057-3.

Paulson, A. J. (1997), The transport and fate of Fe, Mn, Cu, Zn, Cd, Pb and SO4 in a groundwater plume and in downstream surface waters in the Coeur d'Alene Mining District, Idaho, U.S.A., *Applied Geochemistry*, *12*(4), 447–464, doi:10.1016/S0883-2927(97)00013-9.

Pokrovski, G. S., and J. Schott (1998), Thermodynamic properties of aqueous Ge(IV) hydroxide complexes from 25 to 350°C: implications for the behavior of germanium and the Ge/Si ratio in hydrothermal fluids, *Geochim. Cosmochim. Acta*, *62*(9), 1631–1642, doi:10.1016/S0016-7037(98)00081-7.

Pokrovsky, O. S., G. S. Pokrovski, J. Schott, and A. Galy (2006), Experimental study of germanium adsorption on goethite and germanium coprecipitation with iron hydroxide: X-ray absorption fine structure and macroscopic characterization, *Geochim. Cosmochim. Acta*, *70*(13), 3325–3341, doi:10.1016/j.gca.2006.04.012.

Rampe, E. B. et al. (2017), Mineralogy of an ancient lacustrine mudstone succession from the Murray formation, Gale crater, Mars, *Earth and Planetary Science Letters*, doi:10.1016/j.epsl.2017.04.021.

Rieder, R., R. Gellert, J. Brückner, G. Klingelhöfer, G. Dreibus, A. Yen, and S. W. Squyres (2003), The new Athena alpha particle X-ray spectrometer for the Mars Exploration Rovers, *J. Geophys. Res.*, *108*(E12), 8066, doi:200310.1029/2003JE002150.

Rice, M. S. et al. (2017), Geologic overview of the Mars Science Laboratory rover mission at the Kimberley, Gale crater, Mars, *J. Geophys. Res. Planets*, *122*(1), 2016JE005200, doi:10.1002/2016JE005200.

Rieder, R. et al. (2004), Chemistry of Rocks and Soils at Meridiani Planum from the Alpha Particle X-ray Spectrometer, *Science*, *306*(5702), 1746–1749, doi:10.1126/science.1104358.

Sautter, V. et al. (2015), In situ evidence for continental crust on early Mars, *Nature Geosci.*, *8*(8), 605–609, doi:10.1038/ngeo2474.

Schmidt, M. E. et al. (2008), Hydrothermal origin of halogens at Home Plate, Gusev Crater, *J. Geophys. Res.*, *113*(E6), E06S12, doi:10.1029/2007JE003027.

Schmidt, M. E., J. A. Berger, D. Blaney, R. Gellert, J. P. Grotzinger, O. Forni, P. L. King, and N. Mangold (2014a), Geochemical Classification of Rocks in Gale Crater with APXS to Sol 360: Sediment Provenance, Mixing, and Diagenetic Processes, in *Lunar Planet. Sci., XLV*, Abstract 1504.

Schmidt, M. E. et al. (2014b), Geochemical diversity in first rocks examined by the Curiosity Rover in Gale Crater: Evidence for and significance of an alkali and volatile-rich igneous source, *J. Geophys. Res. Planets*, *119*(1), 64–81, doi:10.1002/2013JE004481.

Schmidt, M. E., J. A. Berger, R. Gellert, M. R. M. Izawa, D. W. Ming, L. Thompson, E. Desouza, M. Fisk, and G. Perrett (2016), APXS Classification of Lower Mount Sharp Bedrock: Silica Enrichment and Acid Alteration, in *Lunar Planet. Sci. Conf. 47*, Abstract 2043.

Schwenzer, S. P., and D. A. Kring (2013), Alteration minerals in impact-generated hydrothermal systems – Exploring host rock variability, *Icarus*, *226*(1), 487–496, doi:10.1016/j.icarus.2013.06.003.

Schwenzer, S. P. et al. (2012), Gale Crater: Formation and post-impact hydrous environments, *Planetary and Space Science*, *70*(1), 84–95.

Scribner, A. M., A. C. Kurtz, and O. A. Chadwick (2006), Germanium sequestration by soil: Targeting the roles of secondary clays and Fe-oxyhydroxides, *Earth Planet. Sci. Lett.*, *243*(3–4), 760–770, doi:10.1016/j.epsl.2006.01.051.

Squyres, S. W. et al. (2007), Pyroclastic Activity at Home Plate in Gusev Crater, Mars, *Science*, *316*(5825), 738–742, doi:10.1126/science.1139045.

Squyres, S. W. et al. (2012), Ancient Impact and Aqueous Processes at Endeavour Crater, Mars, *Science*, *336*(6081), 570–576, doi:10.1126/science.1220476.

Stolper, E. M. et al. (2013), The Petrochemistry of Jake_M: A Martian Mugearite, *Science*, *341*(6153), 1239463, doi:10.1126/science.1239463.

Symonds, R. B., W. I. Rose, M. H. Reed, F. E. Lichte, and D. L. Finnegan (1987), Volatilization, transport and sublimation of metallic and non-metallic elements in high temperature gases at Merapi Volcano, Indonesia, *Geochim. Cosmochim. Acta*, *51*(8), 2083–2101, doi:10.1016/0016-7037(87)90258-4.

Taylor, S. R. (1982), *Planetary Science: A Lunar Perspective*, Lunar and Planetary Institute, Houston, Tex.

Thomas, E., J. C. Varekamp, and P. R. Buseck (1982), Zinc enrichment in the phreatic ashes of Mt. St. Helens, April 1980, *Journal of Volcanology and Geothermal Research*, *12*(3–4), 339–350, doi:10.1016/0377-0273(82)90033-6.

Thompson, L. M. et al. (2015), Compositions of sedimentary strata, nodular features and veins at the base of Mount Sharp, Gale crater, Mars: an APXS perspective, *European Planetary Science Congress 2015,* Abstract EPSC2015–827.

Thompson, L. M. et al. (2016), Potassium-rich sandstones within the Gale impact crater, Mars: The APXS perspective, *J. Geophys. Res. Planets*, 2016JE005055, doi:10.1002/2016JE005055.

Thomson, B. J., N. T. Bridges, R. Milliken, A. Baldridge, S. J. Hook, J. K. Crowley, G. M. Marion, C. R. de Souza Filho, A. J. Brown, and C. M. Weitz (2011), Constraints on the origin and evolution of the layered mound in Gale Crater, Mars using Mars Reconnaissance Orbiter data, *Icarus*, *214*(2), 413–432, doi:10.1016/j.icarus.2011.05.002.

Tingzong, G., R. D. DeLaune, and W. H. Patrick Jr (1997), The influence of sediment redox chemistry on chemically active forms of arsenic, cadmium, chromium, and zinc in estuarine sediment, *Environment International*, *23*(3), 305–316, doi:10.1016/S0160-4120(97)00033-0.

Treiman, A. H., M. J. Drake, M.-J. Janssens, R. Wolf, and M. Ebihara (1986), Core formation in the Earth and Shergottite Parent Body (SPB): Chemical evidence from basalts, *Geochim. Cosmochim. Acta*, *50*(6), 1071–1091, doi:10.1016/0016-7037(86)90389-3.

Treiman, A. H. et al. (2016), Mineralogy, provenance, and diagenesis of a potassic basaltic sandstone on Mars: CheMin X-ray diffraction of the Windjana sample (Kimberley area, Gale Crater), *J. Geophys. Res. Planets*, *121*(1), 2015JE004932, doi:10.1002/2015JE004932.

VanBommel, S. J., R. Gellert, J. A. Berger, J. L. Campbell, L. M. Thompson, K. S. Edgett, M. J. McBride, M. E. Minitti, I. Pradler, and N. I. Boyd (2016), Deconvolution of distinct lithology chemistry through oversampling with the Mars Science Laboratory Alpha Particle X-Ray Spectrometer, *X-Ray Spectrom.*, doi:10.1002/xrs.2681.

VanBommel, S. J., R. Gellert, J. A. Berger, L. M. Thompson, K. S. Edgett, M. J. McBride, M. E. Minitti, N. I. Boyd, and J. L. Campbell (2017), Modeling and mitigation of sample relief effects applied to chemistry measurements by the Mars Science Laboratory Alpha Particle X-ray Spectrometer, *X-Ray Spectrom.*, doi:10.1002/xrs.2755.

Vaniman, D. T. et al. (2014), Mineralogy of a Mudstone at Yellowknife Bay, Gale Crater, Mars, *Science*, *343*(6169), 1243480, doi:10.1126/science.1243480.

Warren, P. H., G. W. Kallemeyn, and F. T. Kyte (1999), Origin of planetary cores: evidence from highly siderophile elements in martian meteorites, *Geochim. Cosmochim. Acta*, *63*(13–14), 2105–2122, doi:10.1016/S0016-7037(99)00156-8.

Williams, R. M. E. et al. (2013), Martian Fluvial Conglomerates at Gale Crater, *Science*, *340*(6136), 1068–1072, doi:10.1126/science.1237317.

Wood, S. A., and I. M. Samson (2006), The aqueous geochemistry of gallium, germanium, indium and scandium, *Ore Geology Reviews*, *28*(1), 57–102, doi:10.1016/j.oregeorev.2003.06.002.

Yang, S., M. Humayun, K. Righter, G. Jefferson, D. Fields, and A. J. Irving (2015), Siderophile and chalcophile element abundances in shergottites: Implications for Martian core formation, *Meteorit Planet Sci*, *50*(4), 691–714, doi:10.1111/maps.12384.

Yen, A. S. et al. (2005), An integrated view of the chemistry and mineralogy of martian soils, *Nature*, *436*(7047), 49–54, doi:10.1038/nature03637.

Yen, A. S. et al. (2006), Nickel on Mars: Constraints on meteoritic material at the surface, *J. Geophys. Res.*, *111*(E12), E12S11, doi:10.1029/2006JE002797.

Yen, A. S. et al. (2013), Evidence for a global martian soil composition extends to Gale crater, in *Lunar Planet. Sci., XLIV*, Abstract 2495.

Yen, A. S. et al. (2017), Multiple stages of aqueous alteration along fractures in mudstone and sandstone strata in Gale Crater, Mars, *Earth and Planetary Science Letters*, doi:10.1016/j.epsl.2017.04.033.

Zelenski, M., N. Malik, and Y. Taran (2014), Emissions of trace elements during the 2012–2013 effusive eruption of Tolbachik volcano, Kamchatka: enrichment factors, partition coefficients and aerosol contribution, *Journal of Volcanology and Geothermal Research*, *285*, 136–149, doi:10.1016/j.jvolgeores.2014.08.007.

Zolensky, M. E., M. K. Weisberg, P. C. Buchanan, and D. W. Mittlefehldt (1996), Mineralogy of carbonaceous chondrite clasts in HED achondrites and the Moon, *Meteoritics & Planetary Science*, *31*(4), 518–537, doi:10.1111/j.1945-5100.1996.tb02093.x.

5.10. Supplemental Materials

Supplementary information is presented in Figures 5-S1 through 5-S5 below. Please also refer to the following appendices for additional materials.

Appendix 5-1: APXS results for Zn, Ge, and selected oxides and elements in Gale Crater, sols 0-1360 is attached as the supplemental file named “Berger_Appendix-5-1.xlsx”.

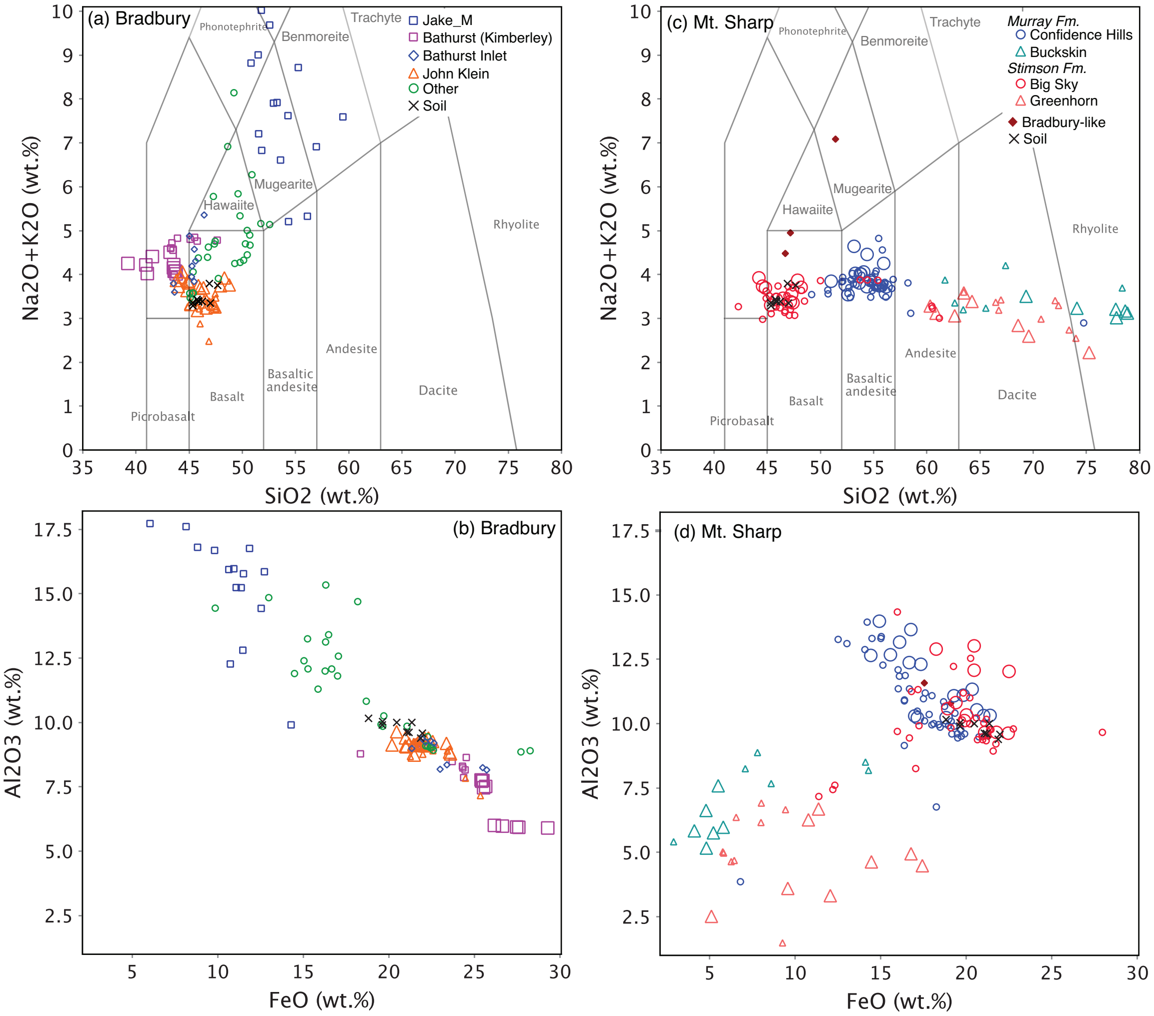

Figure 5-S1: Summary of APXS results for Gale Crater bedrock (without veins or concretions; S- and Cl-free basis) over the first 1360 sols of *Curiosity's* traverse. The symbols here and in the following supplemental figures signify APXS geochemical classifications defined by *Thompson et al.* [2016], and larger symbols denote APXS analyses of drill sites that have CheMin XRD analyses. (a) Total alkali versus silica classification (TAS) [*Le Maitre et al.*, 1989] of rocks in the Bradbury group indicate basaltic compositions at Yellowknife Bay (John Klein) and alkalic compositions in most

of the other classes. (b) Al_2O_3 versus FeO in the Bradbury group is consistent with a mafic/felsic trend, with the potassic basalt of Bathurst Inlet at the Kimberley [*Treiman et al.*, 2016] having low Al and high Fe, whereas the mugearitic Jake_M class has high Al and low Fe. (c) In the lower Mt. Sharp group, the TAS also indicates a basaltic composition for the Stimson formation bedrock (Big Sky) and silica enrichment in the fracture associated light-toned haloes (Greenhorn). The Murray formation bedrock (Confidence Hills) is consistently elevated in silica relative to the Stimson and average Mars (soil), and the Buckskin unit is highly enriched in silica. Units within the Mt. Sharp group have alkalic compositions (Bradbury-like) pointing to a genetic link or stratigraphic interbedding with the Bradbury group; these units are not currently well-understood. (d) The silica enrichment in the Stimson fracture haloes, as well as the Buckskin unit, have a corresponding decrease in Al_2O_3 and FeO. The legends in (a) and (c) define the symbols in (b) and (d), respectively.

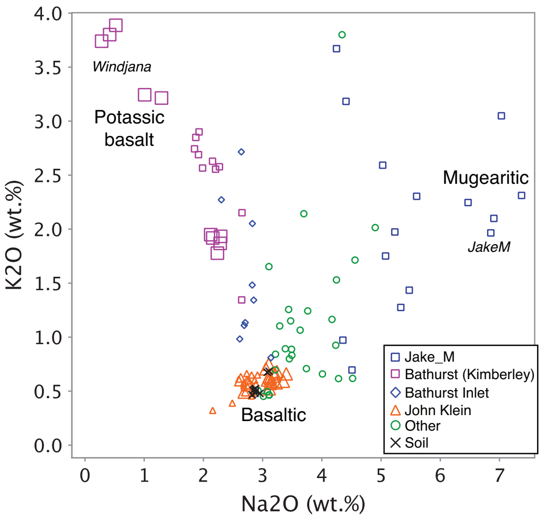

Figure 5-S2: Alkali element characteristics of the Bradbury group rocks (without veins or concretions; S- and Cl-free basis). Larger symbols denote APXS analyses of drill sites. The basaltic John Klein rocks have very little or no alkali depletion, which indicates very limited or no open system hydrolytic alteration [e.g., *Nesbitt and Wilson*, 1992], leading *McLennan et al.* [2013] to conclude that alteration was limited and largely isochemical at Yellowknife Bay. A similar conclusion was made by *Treiman et al.* [2016] for the sanidine-rich (21 wt%) basaltic drill target Windjana in the Kimberley formation. A plausible model for the Bradbury group sedimentary rock compositions involves the mixing of three igneous endmembers: basaltic, potassic basalt, and mugearitic [*Treiman et al.*, 2016]. That is, the source region for Gale Crater contains these three igneous lithologies, and they were physically mixed together during transport into the crater floor.

Intermediate compositions on the alkali element plot, for example, reflect simple mixtures of the three lithologies.

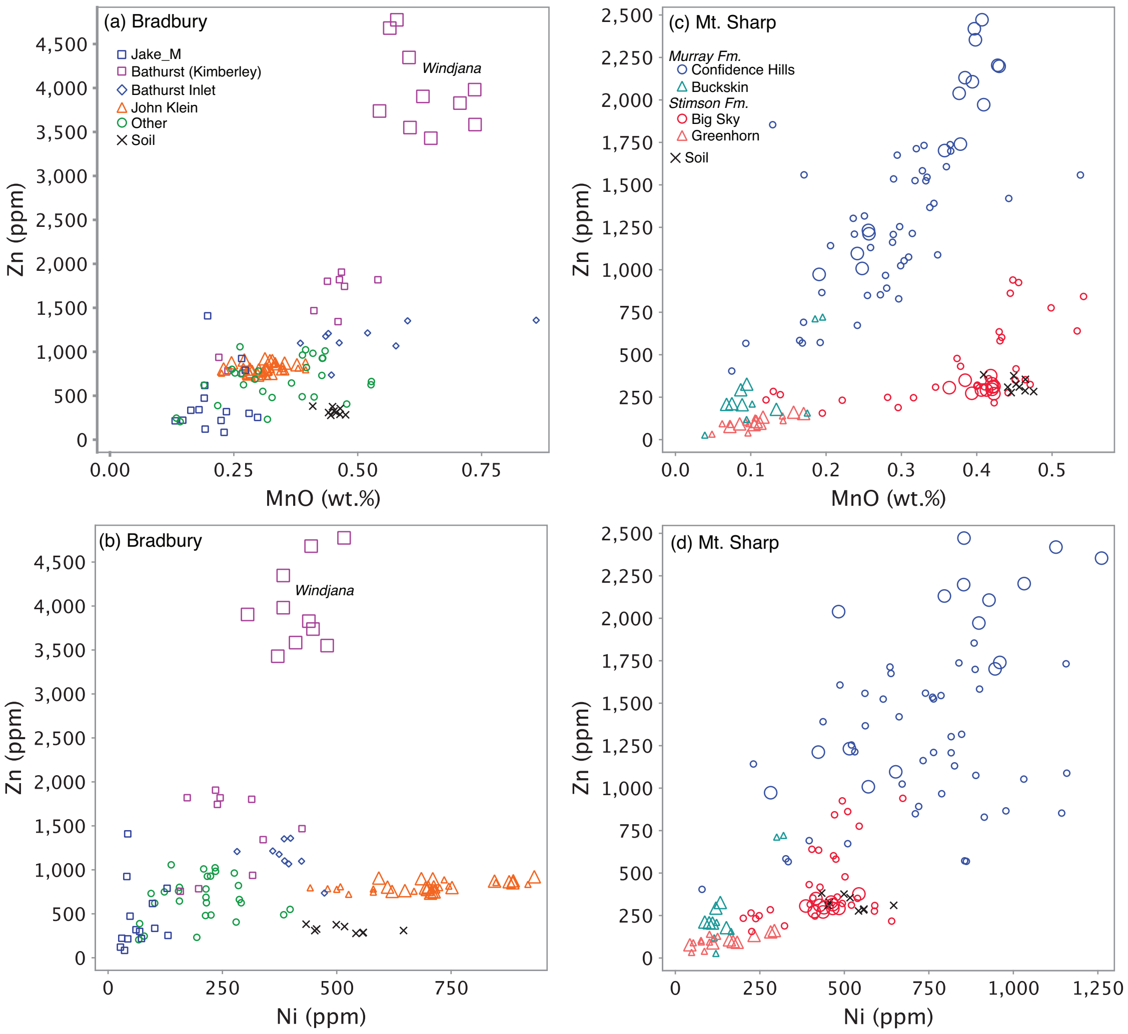

Figure 5-S3: APXS results for Mn, Ni, and Zn in Gale Crater bedrock (without veins or concretions; S- and Cl-free basis) over the first 1360 sols of *Curiosity's* traverse. Larger symbols denote APXS analyses of drill sites. (a, b) In the Bradbury group, Zn does not correlate with Mn or Ni. Low Zn and Ni in the Jake_M class likely reflect a minimally altered, or isochemically altered igneous mugearitic composition [*Stolper et al.*, 2013; *Schmidt et al.*, 2014]; elevated Ni in the John Klein mudstones at Yellowknife Bay can reasonably be accounted for by a mafic provenance and/or ~2% chondritic input [*McLennan et al.*, 2013]. An exception is the Dillinger member of the Kimberley formation where Zn and Mn are highly enriched (Stephen is not shown; Zn ~8100 ppm and Mn ~5 wt%). (c, d) The lower Mt. Sharp group contains evidence of the coincident mobilization of Mn, Ni, and Zn, particularly in the Stimson fracture haloes (Greenhorn),

where the three elements are depleted ~50 - 80% relative to the parent rock (Big Sky) [*Yen et al.*, 2017]. Zn correlates well with Mn (*r* = 0.85) and to a lesser degree with Ni (*r* = 0.72) in the Murray formation, and Mn and Ni correlate similarly (*r* = 0.71). In all Gale rocks, Ge does not correlate with Mn or Ni, neither within nor across units or compositional classes. Note that, for clarity, the Zn, Ni, and Mn axes are not set at the same scales.

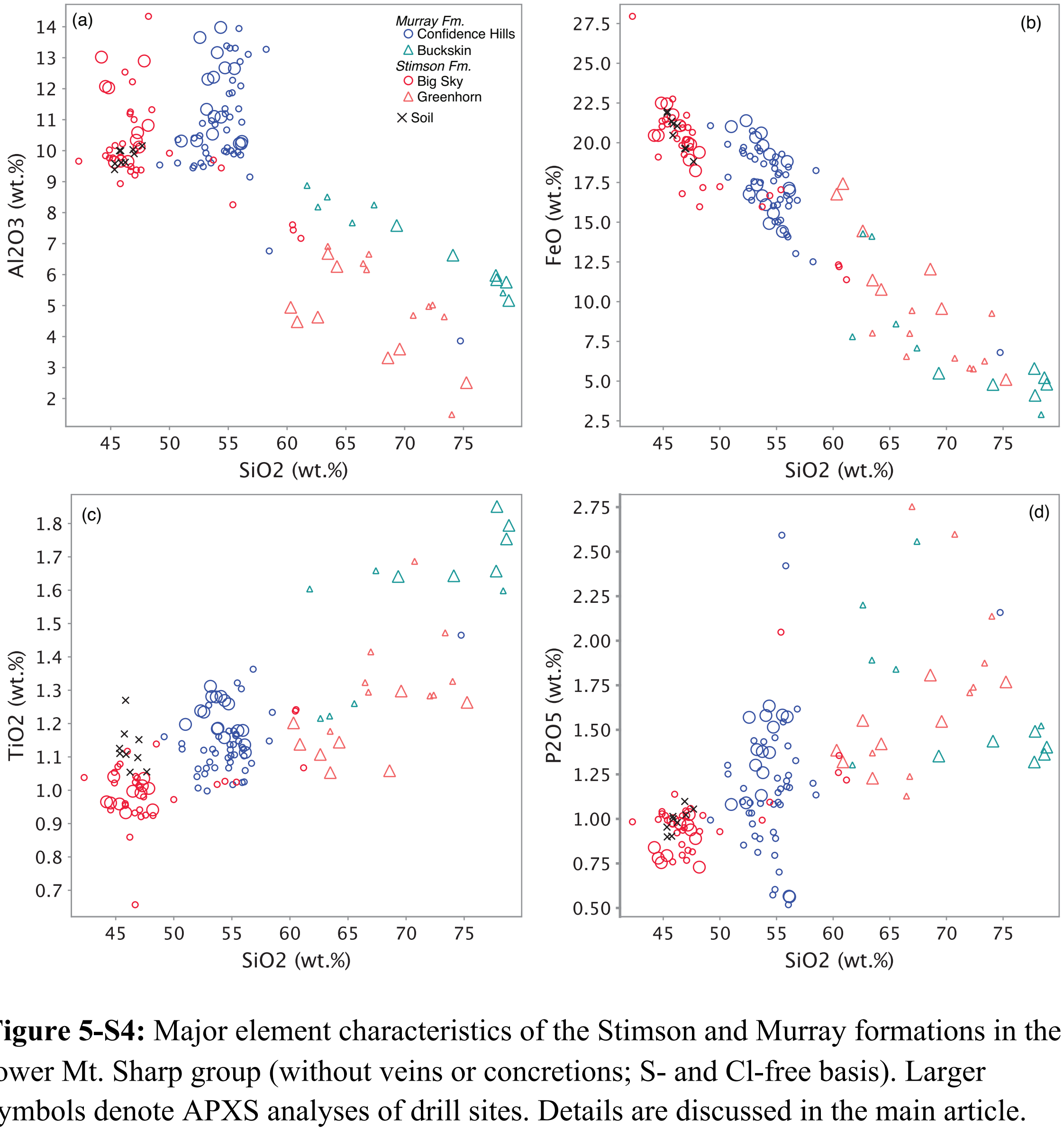

Figure 5-S4: Major element characteristics of the Stimson and Murray formations in the lower Mt. Sharp group (without veins or concretions; S- and Cl-free basis). Larger symbols denote APXS analyses of drill sites. Details are discussed in the main article.

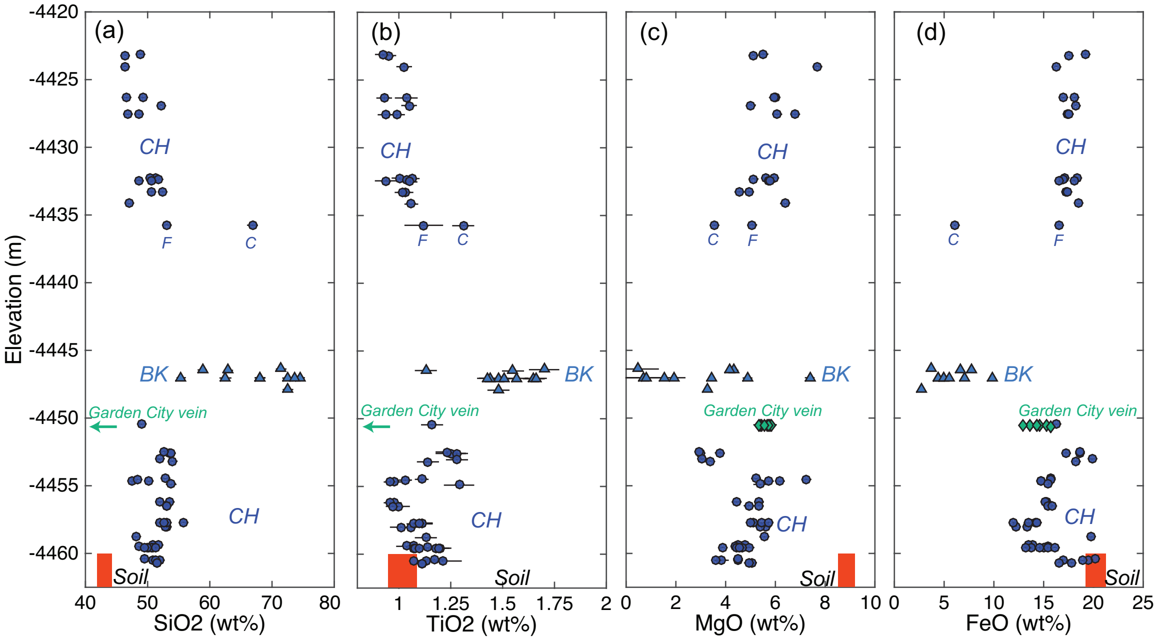

Figure 5-S5: Major element variation with elevation in the Murray formation bedrock. Compositional classes and the paired Ferdig (F) and Cody (C) targets (Table 5-3) are denoted and the symbols are as in Figure 5-5 in the main text. Gale soil concentrations are indicated by the red box. Larger symbols denote APXS analyses of drill sites.

Chapter 6

6. Concluding Remarks

A Ph.D. program that focuses on a Mars rover mission is alluring but precarious. That is, the potential for discovery is professionally and personally rewarding, but there is risk involved. Will the rover function properly? What is the rover going to find? Will I come up with novel ideas? Should I develop a 'plan B' project? In many ways, my graduate work has been a journey of exploration, with *Curiosity* as the vehicle and the MSL Engineering and Science Teams as my mentors and colleagues. It was driven by scientific hypotheses, but we had many uncertainties about what we would find.

Mars did not disappoint. When I started working on this dissertation in 2013, *Curiosity* had just finished its 260th Martian day in Gale Crater and was still in Yellowknife Bay only 230 m from the landing site. The alkalic Jake_M rock, found on the 46th day, had inspired a field project to re-examine the mugearites of Maunakea as a Mars analogue. The APXS had already discovered Zn and Ge enrichments in Yellowknife Bay that mirrored enrichments at other rover sites. The titanium observation tray was already established as a great dust collector. From that point on, continuing to the 1673rd Martian day that will be planned today, a rich and complex picture of Gale Crater was revealed. As such, I had access an extensive dataset from which I could derive novel ideas, propose useful interpretations, and write scientifically compelling manuscripts.

My journey of exploration has thus resulted in this dissertation, with chapters that seek to understand the discoveries of *Curiosity's* APXS in Gale Crater. Element mobility is the thread unifying the chapters, and together they constrain the aqueous history of Gale. The first component, Chapters 2 and 3, is an analogue field study of Maunakea and Kohala. We developed a framework for understanding the overlapping chemical trends attributed to igneous, alteration, and sedimentary processes occurring there. That framework was applied Gale Crater to demonstrate evidence of sedimentary mixing, igneous provenance, and acidic alteration. The Hawaiian samples were then analyzed with PIXE to establish a new APXS analogue for field studies. The second component of this dissertation, Chapters 4 and 5, is an examination of fluid-mobile elements in Gale Crater. Sulfur and chlorine are ubiquitous mobile elements on the surface of Mars, and much of it is associated with modern dust. We therefore devised a novel method for determining the composition of the dust. Chapter 5 is an investigation into the remarkable Zn and Ge enrichments in Gale, and presents evidence of early hydrothermalism and later diagenetic fluids based on the distribution and occurrence of the two elements.

I believe the analogue work presented here promises to be useful for future studies. My field study of Maunakea and Kohala is the first comprehensive Mars analogue investigation conducted primarily from the APXS perspective. Chapter 2 will be submitted to a peer-reviewed journal in 2017 and I believe it will provide a framework for interpreting APXS data, not only the discoveries at Gale Crater, but additionally at the MER sites. If, as R. V. Morris predicts, the hematite-bearing Rubin Ridge that *Curiosity* is currently approaching is indeed like the 'hematite ridge' he discovered at Maunakea, then we have a well-characterized set of relevant samples already evaluated for comparison and hypothesis-testing. In addition, we have established in Chapter 3 that PIXE is a reasonable APXS analogue. More investigation is needed to determine the accuracy of S analysis and the impact of olivine phenocrysts on Al attenuation assumptions, but the chapter should be suitable for publication in a journal pending that work. However, PIXE is arguably better than the flight equivalent testbed APXS because the regulatory concerns of the ^{244}Cm radioisotope source are eliminated, and spectral resolution is nearly the same as the MSL APXS on a cold night on Mars. The PIXE technique thus opens possibilities for other APXS-centric analogue experiments.

The chapters presenting Gale Crater results will also be useful for further investigations of Mars and Mars analogues. The dust composition we calculated will improve interpretations of sulfur and chlorine content in rocks, and it is available as a journal article that was published in Goephysical Research Letters in 2016. Deconvolutions of dust and the underlying rock substrate can now be done with greater certainty. In addition, an upper limit of S and Cl content in the dust is now established, which will also facilitate the unraveling of dust and rock in APXS data. The two elements are also an important concern for human exploration of Mars. Dust mitigation will be key for maintaining spacecraft components in part because the S and Cl in the dust will form salts and might affect the pH of moisture in pressure suits and habitats. Knowing the absolute concentrations of S and Cl in the dust will improve the efficiency of dust mitigation.

The use of Zn and Ge as a tracer pair also has promise for future work. Chapter 5 is now available as an accepted 2017 publication in the Journal of Geophysical Research. The two elements, when enriched together, are a likely signal of hydrothermal activity, which is a process linked to the genesis of life. They may thus be flags for sites with biosignature potential. The contrasting mobilities of Zn and Ge in low temperature fluids can further aid interpretations during future missions. If, as we suggest above, the acid sulfate alteration of the Murray formation is indicated by Zn and Ge fractionation in low pH fluids, then life genesis scenarios and biosignature potential will be affected. That is, widespread acidic fluids may be detrimental to the initial formation of microbial life at a particular site, and Zn and Ge may be a tool for understanding this. We therefore recommend future geochemical instruments consider Zn and Ge for their calibrations.

In the end, having a Ph.D. topic that rode along with a rover for 15 km has given me experience in field methods, laboratory analytical methods, geochemical modeling, geochemical data analysis, image analysis, presentations, scientific collaboration, manuscript writing, and more. Hopefully the preceding work will be a potent drop in humanity’s ocean of knowledge.

Appendices

Chapter 2

Appendix 2-1: A summary of XRF results is attached as an excel file 'Berger_Appendix-2-1.xlsx'.

Appendix 2-2: A summary of literature XRF results for Maunakea [*Morris et al.,* 2000; *Hamilton et al.*, 2008] is attached as an excel file 'Berger_Appendix-2-2.xlsx'.

Appendix 2-3: Summary of site and sample descriptions is attached as an excel file 'Berger_Appendix-2-3.xlsx'.

Appendix 2-4: Detailed maps of Maunakea sample sites are attached as a .pdf file 'Berger_Appendix-2-4.pdf'.

Appendix 2-5: Annotated thin section micrographs are attached as a .pdf file 'Berger_Appendix-2-5.pdf'.

Appendix 2-6: Summary of XRD results.

Sample	Rock Type	Powder XRD Results[1]	Micro-XRD Results[2]
MK-15-2a	Lava fresh	~90% plagioclase, ~5% hematite	
MK-15-3a	Lava fresh	~90% plagioclase	
MK-15-3b	Lava altered	~90% plagioclase	
MK-15-3c	Lava altered		Hand sample surface rind: some evidence of amorphous hump 20-35 2theta, high background at low 2theta, otherwise spotty pattern
MK-15-9b	Tuff		Thin section spots: plagioclase
MK-15-9c	Outwash	78% plagioclase, 18% diopside, 3% magnetite	
MK-15-10a	Sulfate float		Thin section XRD spots: Jarosite (yellow), alunite (white), more or less plagioclase, hematite, ilmenite
MK-15-15a	Lava fresh	56% Plagioclase, 26% diopside, magnetite, fluorapatite?	
MK-15-15b	Outwash	85% plagioclase, 10% diopside, 3% magnetite	
MK-15-22	Outwash	70% plagioclase, 25% diopside, 3% hematite	
MK-15-23a	Lava fresh	77% plagioclase, 18% diopside, ilmenite, magnetite	
MK-15-23b	Lava altered	75% plagioclase, 20% diopside, 5% hematite	
MK-15-24a	Lava fresh	70% Plagioclase, 20% diopside, magnetite, fluorapatite	
MK-15-24b	Lava altered	80% plagioclase, 13% diopside, 5% hematite	
MK-15-33b	Lava altered	Clinopyroxene, olivine, noisy Fe background	
MK-15-33c	Lava altered	50% olivine, 40% diopside, 10% hematite	
MK-15-34a	Lava fresh	75% plagioclase, 25% diopside	
MK-15-34b	Lava altered	65% plagioclase, 30% diopside, 5% hematite	
MK-15-35b	Lava altered		Thin section spots: plagioclase
MK-15-36a	Lava fresh	30% plagioclase, 60% diopside, 5% hematite, ferrosilite?	
MK-15-36b	Lava altered		Thin section spots: Mg-spinel, ferrosilite, ilmenite, pyroxene, goethite?, ferrihydrite?
MK-15-36c	Lava altered		Thin section spots: Rutile, spinel, gibbsite, hematite, some plagioclase and pyroxene
MK-15-37a	Lava fresh	45% Plagioclase, 40% diopside, 15% olivine	
MK-15-37b	Lava altered	15% Plagioclase, 50% diopside, 30% olivine, hematite, unidentified peak 56 2theta	
MK-15-37d	Lava altered		Thin section spots: Fe-spinel, ilmenite, hematite, plagioclase, olivine, goethite?, broad

			gibbsite peaks in fracture and vesicle fill
MK-15-37e	Lava altered	Maghemite, ilmenite, chromite, hematite, quartz	Powder: Maghemite, ilmenite, chromite, hematite, quartz
MK-15-38b	Lava altered		Hand sample surface rind: amorphous surface, possibly silica hump.
MK-15-38d	Lava altered		Thin section spots: Fe-spinel, ilmenite, hematite, plagioclase, olivine, goethite?, broad gibbsite peaks in fracture and vesicle fill
MK-15-41b	Lava altered		Thin section spots: Plagioclase, pyroxene, olivine, magnetite
MK-15-52a	Lava fresh	75% plagioclase, 25% diopside	
MK-15-52b	Lava altered	75% plagioclase, 20% diopside, 5% hematite	
MK-15-53	Diamict	65% Plagioclase, 30% diopside, hematite?, fluorapatite?	
MK-15-54b	Diamict	65% Plagioclase, 30% diopside, hematite?	
MK-15-61b	Coating		Hand sample surface rind: plagioclase, spinel, very spotty pattern

---

[1] Percentages are S-quant abundances with high uncertainty.

[2] Very high uncertainty due to commonly spotty patterns. The µXRD spot size was 300 µm.

Appendix 2-7: Summary of Petrographic Descriptions.

Sample	Rock Type	Observations (modal abundances are qualitative estimates)[1]
MK-15-2a	Lava fresh	Trachytic, 70% plag, 20% opaques, 5% olv
MK-15-3a	Lava fresh	Trachytic, 70% plag 15% opaques, 5% olivine contains apatite spicule inclusions.
MK-15-3c	Lava altered	Same as 3a with red staining and fine grained fracture fill, some isotropic plag
MK-15-4b	Tephra altered	Tephra, angular to subangular palagonitized glassy fragments, lithic fragments of hawaiite with plag in opaque matrix, red stained
MK-15-4a	Lava fresh	Trachytic, 70% euhedral plag, 15% opaques, 5% olv, very little alteration, plag contains apatite spicule inclusions. Large 100 µm euhedral opague phenocrysts. Diktytaxitic plag-bounded vesicles.
MK-15-7a	Lava fresh	Trachytic minimal to no alteration
MK-15-8	Lava fresh	Trachytic minimal to no alteration
MK-15-9a	Lava fresh	Trachytic, larger plag phenocrysts with melt inclusion trains? And diktytaxitic plag in vesicles
MK-15-9b	Tuff	Fragmented tephra, oxidative alteration, angular lithic fragments mostly
MK-15-10a	Sulfate float	breccia of fine-grained red, yellow, pale white matrix with angular clasts of hawaiitic fragments some plag phenocryst in the lithic fragments
MK-15-12	Tuff	palagonitized fragmented clasts with some plag phenocryst in the lithic fragments
MK-15-15a	Lava fresh	Highly vesicular trachytic Plag, 10% olv with some oxidative alteration but otherwise fresh
MK-15-16a	Lava altered	Opaque matrix, very fine grained trachytic plag phenocrysts
MK-15-16b	Coating	Opaque matrix, very fine grained trachytic plag phenocrysts
MK-15-19a	Lava fresh	Plag and olivine phyric basalt, some oxidative alteration
MK-15-20a	Lava fresh	olivine phyric basalt, plag, oxides, Minimally altered
MK-15-23a	Lava fresh	Trachytic, 70% plag, 20% opaques, 5% olv minimal alteration with scattered 1-2 mm oxides with K-spar clot
MK-15-23b	Lava altered	Trachytic, 23a with some red staining
MK-15-24a	Lava fresh	Trachytic, 70% plag, 20% opaques, 5% olv minimal alteration
MK-15-24b	Lava altered	Trachytic, 24a some red staining
MK-15-25a	Lava	Trachytic 70% plag, 20% opaques, 5% olv
MK-15-26a	Lava fresh	Trachytic 70% plag, 20% opaques, < 5% olv
MK-15-26b	Lava altered	Trachytic, 26a slight alteration- red staining
MK-15-27b	Slope deposit	Palagonitized tephra fragments angular glassy and lithic fragments, plag phenocryst in the lithic fragments
MK-15-27d	Slope deposit	Palagonitized tephra fragments angular glassy and lithic fragments, plag phenocryst in the lithic fragments
MK-15-29a	Lava fresh	Trachytic 70% plag, 20% opaques, < 5% olv minimal alteration
MK-15-29b	Lava altered	Trachitic, 29a with some palagonitization and or oxidative alteration
MK-15-29c	Tuff	Trachitic, 29a with some palagonitization and or oxidative alteration
MK-15-31	Lava fresh	Trachytic, 70% plag, 20% opaques, < 5% olv minimal alteration 1-2 mm plag phenocrysts
MK-15-33a	Lava fresh	Basalt, 50% plag, 20% olv, opaque matrix, abundant large olivine phenocrysts 1-3 mm, red staining (iddingsite) on olivine rims
MK-15-33b	Lava altered	33a moderately altered, more extensive iddingsite alteration of olicine, isotropic plag

MK-15-34a	Lava fresh	Plag phyric basalt, 50% plag, 20% olv, opaque matrix, less common olivine phenocrysts as 33a, fairly minimal weathering
MK-15-34b	Lava altered	34a with oxidative staining, some isotropic plag
MK-15-34c	Lava altered	34a with Extensive alteration, magnetite pseudomorphs after olivine?
MK-15-35a	Lava fresh	Trachytic, 65% plag, 25% opaques, < 5% olv fairly unaltered
MK-15-35b	Lava altered	Trachytic, 35a with isotropic plag and oxidative alteration
MK-15-36a	Lava fresh	Basalt, 50% plag some skeletal plag, isotropic plag cores, plag phyric
MK-15-36b	Lava altered	36a with Localized oxidative weathering, some isotropic plag
MK-15-36c	Lava altered	36a with Moderately highly altered, plag phenocrysts persist but disrupted habit, magnetite pseudomorphs?
MK-15-37a	Lava fresh	Olivine phyric basalt, 50% plag, 20% olv, 15% opaque, some iddingsite rims on olv 1-3 mm phenocrysts.
MK-15-37b	Lava altered	37a with More extensive iddingsite alteration of olivine
MK-15-37c	Lava altered	37a with Moderately altered, magnetite pseudomorps, isotropic plag
MK-15-37d	Lava altered	37a with Highly altered, filled vesicles, filled fractures, fine-graind secondary material
MK-15-38a	Lava fresh	Basalt, 50% plag, 25% opaques, 20% olv, Fairly unaltered
MK-15-38b	Lava altered	38a with Oxidative staining, isotropic plag
MK-15-38c	Lava altered	38a with more opaque matrix, plag less altered
MK-15-38d	Lava altered	38a like 38b, 38c, more extensively altered, vesicles filled with fine-grained clay-like
MK-15-39a	Lava fresh	Olivine phyric basalt, 1-3 mm phenocrysts very fine grained matrix, plag, olv, opaques, minimal alteration
MK-15-40a	Lava fresh	Olivine phyric basalt, 1-3 mm phenocrysts very fine grained matrix, plag, olv, opaques, minimal alteration
MK-15-40b	Lava altered	Like 40a but highly vesicular, olivine phyric basalt, some oxidative alteration
MK-15-41a	Lava fresh	Trachytic, 65% plag, 20% opaques, some olv, relatively unweathered, randomized plag, less of a flow texture than common
MK-15-41b	Lava altered	41a with trachytic, oxidative weathering and vesicle fill with fine-grained secondary material
MK-15-41c	Lava altered	41a but highly vesicular, some trachytic texture apparent, minimal alteration
MK-15-42a	Lava fresh	Trachitic, 65% plag, 15% opaques, some olv, plag phyric, some apparent fragments of different lithology with darker matrix
MK-15-43a	Tephra	Olivine phyric basalt, 1-3 mm olv phenocrysts, very fine grained matrix plag, some oxidative alteration
MK-15-45a	Lava fresh	Trachytic, 70% plag, 15% opaque, <5% olv, plag phyric, well defined flow texture
MK-15-48a	Lava fresh	Trachytic, 70% plag, 15% opaque, <5% olv, plag phyric, minimal alteration
MK-15-51a	Lava fresh	Olivine phyric basalt, highly vesicular, plag in opaque matrix, minimal alteration
MK-15-52a	Lava fresh	Trachytic, ~70% plag, 15% opaque, <5% olv, minimal alteration
MK-15-52b	Lava altered	Similar to 52a but with abundant vesicles and oxidative alteration
MK-15-53	Diamict	Breccia, fragments of different lithology, hawaiite < 60% plag, and mugeartite >60% plag
MK-15-54b	Diamict	Breccia, fragments of different lithology, hawaiite < 60% plag, and mugeartite >60% plag
MK-15-56a	Lava fresh	Fine-grained trachytic, >60% plag, minimal alteration
MK-15-59a	Lava fresh	Fine-grained trachytic, >60% plag, minimal alteration

MK-15-59b	Lava altered	Vesicle-rich same as 59a
MK-15-61a	Lava fresh	Trachytic, 60% plagm 15% opaque, 10% olv, olv phenocrysts 300 µm with acicular inclusions, nearly unaltered
MK-15-61b	Coating	Trachytic, 60% plagm 15% opaque, 10% olv, olv phenocrysts 300 µm with acicular inclusions, nearly unaltered
MK-15-62a	Lava fresh	Very Fine grained trachytic, >60% plag, opaques, nearly unaltered
MK-15-62b	Lava fresh	Very Fine grained trachytic, >60% plag, opaques, nearly unaltered
MK-15-66a	Lava fresh	Very Fine grained trachytic, >60% plag, nearly unaltered, large 1-3 mm euhedral opaques
MK-15-69	Lava fresh	Very Fine grained trachytic, >60% plag, opaques, nearly unaltered
MK-15-72a	Lava fresh	Very Fine grained trachytic, >60% plag, opaques, nearly unaltered
HWMK11	Tephra_Calcined	Highly vesicular, euhedral, apparently unaltered plag in opaque matrix, red oxidative alteration
HWMK12	Tephra_Fresh	Vesicular, plag phyric, euhedral, minimally altered opaque matrix
HWMK600	Tephra_Palagonitic	Vesicular, plag phyric euhedral and minimally altered, with opaque matrix showing some oxidative alteration
HWMK767	Tephra_Calcined	Highly vesicular, euhedral, apparently unaltered plag in opaque matrix, red oxidative alteration. Circular and sub-circular vesicles contain apparent diktytaxitic texture, clear prismatic 20 µm xl clusters protruding into vesicle- doesn't look like plag, could be secondary precipitate
HWMK768	Tephra_Calcined	Highly vesicular, euhedral, apparently unaltered plag in opaque matrix, red oxidative alteration
HWMK769	Tephra_Calcined	Breccia, angular to subangular lithick fragments with euhedral plag, apparent oxidative alteration with opaque (cementing?) matrix
HWMK774	Tephra_Sulfatetic	Similar to 951-2 Heterogeneous mix of highly altered, fine grained pale yellow, white, and red opaques
HWMK777	Tephra_Sulfatetic	Breccia, lithic fragments of hawaiitte, minimally altered, red oxidative alteration, cemented by pale yellow/white/red very fine grained oxides and sulfates which contain randomly arranged plag laths apparently suspended in the fine grained matrix
HWMK951-2	Tephra_Sulfatetic	Mostly mix of very fine grained pale white, pale yellow sulfates, and small reddish, nearly opaque grains dispersed in the fine-grained white and yellow sulfates. Plag lathes preserved as lighter laths, suspended in the sulfate. Some mixed lithic fragments with plag and opaque matrix cemented in the sulfates.
HWMK953	Tephra_Rind	Cross section of alteration rind ~1 cm thick. Less altered interior- plag laths in opaque matrix, altered rind pale yellow and white mixture with dispersed and clustered small red opaque grains.
HWMK958	Tephra_Sulfatetic	Similar to 951-2 Remnant vessicles, highly altered mostly mix of pale white, pale yellow, and small red opaque grains dispersed in the fine-grained white and yellow sulfates. Plag lathes preserved, suspended in the sulfate. Some mixed lithic fragments cemented in the sulfates.
HWMK959	Tephra_Sulfatetic	Similar to 951-2 Remnant vessicles, highly altered mostly mix of pale white, pale yellow, and small red opaque grains dispersed in the fine-grained white and yellow sulfates. Plag lathes preserved, suspended in the sulfate. Some mixed lithic fragments cemented in the sulfates.
HWMK976	Tephra_Sulfatetic	Similar to 951-2 Remnant vessicles, highly altered mostly mix of pale white, pale yellow, and small red opaque grains dispersed in the fine-grained white and yellow sulfates. Plag lathes preserved, suspended in the sulfate. Some mixed lithic fragments cemented in the sulfates.

---

[1] Abbreviations are as follows: plag = plagioclase; olv = olivine; xls = crystals.

Chapter 3

Appendix 3-1: A sample summary with PIXE results is attached as an excel file 'Berger_ Appendix-3-1.xlsx'. The oxides are corrected by the *ECF* and renormalized on a volatile-free basis.

Chapter 4

Appendix 4-1: The published manuscript "A Global Mars Dust Composition Refined by the Alpha Particle X-ray Spectrometer in Gale Crater" is attached as a .pdf file 'Berger_Appendix-4-1.pdf'.

Chapter 5

Appendix 5-1: APXS results for Zn, Ge, and selected oxides and elements in Gale Crater, sols 0-1360 is attached as a supplemental file named "Berger_Appendix-5-1.xlsx".

Cirriculum Vitae

Jeff A. Berger

Ph.D. Candidate, Department of Earth Sciences, University of Western Ontario

Education

Ph.D., Geology and Planetary Sciences, University of Western Ontario, *to be defended June 2017*
M.Sc., Earth and Planetary Science, University of New Mexico (2012)
B.Sc. with Honours, Geology, Portland State University (2009)

Research Experience

- Mars Science Laboratory Science Team Collaborator, UNM and UWO (2011 – present)
    - MSL APXS Strategic Planner – bridge strategic and science planning for the APXS instrument
    - MSL APXS Payload Uplink/Downlink Lead – support APXS instrument tactical operations
- New Mexico Infrared of Astromaterials Lab, UNM (2010 – 2012)
- Geomicrobiology and Electron Microscopy Lab, Portland State University (2008 –2009)

Teaching Experience

- Teaching Assistant, UNM, Geology 201, "History of the Earth" (2010 – 2011)
- Teaching Assistant, UWO, (2013 – 2015)
    - Earth Science 1022B, "Earth Rocks"
    - Earth Science 2212B, "Planetary Materials"
    - Earth Science 1083, "Life on Planet Earth"

Honours and Grants

- Ontario Graduate Scholarships (2015 – 2016 and 2016 – 2017)
- NASA Honour Award: Group Achievement Award for outstanding contributions to the NASA mission, MSL APXS Instrument Development and Science Team (2013 and 2015)
- Astromaterials Training and Research Opportunities (ASTRO) LPSC Travel Award, University of Western Ontario (2014)
- Natural Sciences and Engineering Research Council of Canada, CREATE Technologies and Techniques for Earth and Space Exploration Ph.D. Fellowship, University of Western Ontario (2013-2015)
- Astromaterials Training and Research Opportunities (ASTRO) Graduate Student Incentive Award, University of Western Ontario (2013)
- Outstanding First Year Teaching Assistant Award, University of New Mexico (2011)
- Graduated with departmental honours, B.S. in Geology, Portland State University (2009)
- NASA Oregon Space Grant, Portland State University (2009)
- Marvin Beeson Undergraduate Research Award, Portland State University (2009)

Professional Organizations

- Reviewer for Icarus (Solar System Studies)
- Geological Society of America (Planetary Geology Division)
- American Geophysical Union
- Mineralogical Association of Canada

First Authored Peer-Reviewed Articles

Berger, J. A., M. E. Schmidt, R. Gellert, N. I. Boyd, E. D. Desouza, R. L. Flemming, M. R. M. Izawa, D. W. Ming, G. M. Perrett, E. B. Rampe, L. M. Thompson, S. J. VanBommel, A. S. Yen (*2017*), Zinc and Germanium in the Sedimentary Rocks of Gale Crater on Mars Indicate Hydrothermal Enrichment Followed by Diagenetic Fractionation, *J. Geophys. Res. Planets*.

Berger, J. A., M. E. Schmidt, R. Gellert, J. L. Campbell, P. L. King, R. L. Flemming, D. W. Ming, B. C. Clark, I. Pradler, S. J. V. VanBommel, M. E. Minitti, A. G. Fairén, N. I. Boyd, L. M. Thompson, G. M. Perrett, B. E. Elliott, and E. Desouza (2016), A global Mars dust composition refined by the Alpha-Particle X-ray Spectrometer in Gale Crater, *Geophys. Res. Lett.*, doi: 2015GL066675.

Berger, J. A., P. L. King, A. Green, M. A. Craig, M. N. Spilde, S. P. Wright, T. S. Kunkel, and R. J. Lee (2015), Effect of halite coatings on thermal infrared spectra, *J. Geophys. Res. Solid Earth* doi: 2014JB011712.

Berger, J. A., P. L. King, R. Gellert, J. L. Campbell, N. I. Boyd, I. Pradler, G. M. Perrett, K. S. Edgett, S. J. VanBommel, M. E. Schmidt, R. E. H. Lee (2014), MSL-APXS titanium observation tray measurements: Laboratory experiments and results for the Rocknest fines at the Curiosity field site in Gale Crater, Mars, *J. Geophys. Res. Planets* doi:10.1002/2013JE004519.

Co-Authored Peer-Reviewed Articles

Rampe, E. B. and 24 authors including **J. A. Berger** (2017), Mineralogy of an ancient lacustrine mudstone succession from the Murray formation, Gale crater, Mars, *Earth and Planetary Science Letters*, doi:10.1016/j.epsl.2017.04.021.

O'Connell-Cooper, C. D., J. G. Spray, L. M. Thompson, R. Gellert, **J. A. Berger**, N. I. Boyd, E. D. Desouza, G. M. Perrett, M. Schmidt, and S. J. VanBommel (2017), APXS-derived chemistry of the Bagnold dune sands: Comparisons with Gale crater soils and the global martian average, *J. Geophys. Res. Planets*, 2017JE005268, doi:10.1002/2017JE005268.

VanBommel, S. J., R. Gellert, **J. A. Berger**, L. M. Thompson, K. S. Edgett, M. J. McBride, M. E. Minitti. N. I. Boyd. J. L. Campbell (2017), Modeling and mitigation of sample relief effects applied to chemistry measurements by the Mars Science Laboratory Alpha Particle X-ray Spectrometer. *Journal of X-ray Spectrometry*, doi: 10.1002/xrs.2755.

Yingst, R. A., **J. A. Berger**, B. A. Cohen, B. Hynek, and M. E. Schmidt (2017), Determining best practices in reconnoitering sites for habitability potential on Mars using a semi-autonomous rover: A GeoHeuristic Operational Strategies Test, *Acta Astronautica*, 132, 268–281, doi:10.1016/j.actaastro.2016.12.018.

Thompson, L.M., M. E. Schmidt, J. G. Spray, **J. A. Berger**, A. G. Fairén, J. L. Campbell, G. M. Perrett, N. I. Boyd, R. Gellert, I. Pradler, S. J. VanBommel (2016), Potassium-rich sandstones within the Gale impact crater, Mars: The APXS perspective. *J. Geophys. Res. Planets* 2016JE005055. doi:10.1002/2016JE005055

McCraig, M. A., G. R. Osinski, E. A. Cloutis, R. L. Flemming, M. R. M. Izawa, V.Reddy, S. K. Fieber-Beyer, L. Pompilio, F. van der Meer, **J. A. Berger**, M. S. Bramble, D. M Applin, (2016) Fitting the Curve in Excel®: Systematic Curve Fitting of Laboratory and Remotely Sensed Planetary Spectra. *Computers & Geosciences*. doi:10.1016/j.cageo.2016.11.018.

Lanza, N.L., Wiens, R.C., Arvidson, R.E., Clark, B.C., Fischer, W.W., Gellert, R., Grotzinger, J.P., Hurowitz, J.A., McLennan, S.M., Morris, R.V., Rice, M.S., Bell, J.F., **Berger, J.A.**, Blaney, D.L., Bridges, N.T., Calef, F., Campbell, J.L., Clegg, S.M., Cousin, A., Edgett, K.S., Fabre, C., Fisk, M.R., Forni, O., Frydenvang, J., Hardy, K.R., Hardgrove, C., Johnson, J.R., Lasue, J., Mouélic, S.L., Malin, M.C., Mangold, N., Martìn-Torres, J., Maurice, S., McBride, M.J., Ming, D.W., Newsom, H.E., Ollila, A.M., Sautter, V., Schröder, S., Thompson, L.M., Treiman, A.H., VanBommel, S., Vaniman, D.T., Zorzano, M.-P., (2016). Oxidation of manganese in an ancient aquifer, Kimberley formation, Gale crater, Mars. *Geophys. Res. Lett.* 2016GL069109. doi:10.1002/2016GL069109.

VanBommel, S. J., R. Gellert, **J. A. Berger**, J. L. Campbell, L. M. Thompson, K. S. Edgett, M. J. McBride, M. E. Minitti, I. Pradler, N. I. Boyd (2016), Deconvolution of distinct lithology chemistry through oversampling with the Mars Science Laboratory Alpha Particle X-ray Spectrometer. *Journal of X-ray Spectrometry,* doi:10.1002/xrs.2681.

Lasue, J., S. Clegg, O. Forni, A. Cousin, R. Wiens, N. Lanza, N. Mangold, L. Le Deit, O. Gasnault, S. Maurice, **J. A. Berger**, K. Stack, D. Blaney, F. Cécile, W. Goetz, J. Johnson, S. Le Mouelic, M. Nachon, V. Payré, W. Rapin, D Sumner (2016), Observation of > 5 wt % zinc at the Kimberley outcrop, Gale crater, Mars, *J. Geophys. Res. Planets*, 2015JE004946, doi:10.1002/2015JE004946.

Newsom, H.E., Mangold, N., Kah, L.C., Williams, J.M., Arvidson, R.E., Stein, N., Ollila, A.M., Bridges, J.C., Schwenzer, S.P., King, P.L., Grant, J.A., Pinet, P., Bridges, N.T., Calef, F., Wiens, R.C., Spray, J.G., Vaniman, D.T., Elston, W.E., **Berger, J. A.**, Garvin, J.B., Palucis, M.C., (2014), Gale crater and impact processes –Curiosity's first 364 Sols on Mars. *Icarus*. doi:10.1016/j.icarus.2014.10.013.

Campbell, J.L., King, P.L., Burkemper, L., **Berger, J. A.**, Gellert, R., Boyd, N.I., Perrett, G.M., Pradler, I., Thompson, L., Edgett, K.S., Yingst, R.A. (2014), The Mars Science Laboratory APXS calibration target: Comparison of Martian measurements with the terrestrial calibration, *Nucl. Instrum. Methods Phys. Res. B*, 323, 49–58. doi:10.1016/j.nimb.2014.01.011.

Cousin, A., Meslin, P.Y., Wiens, R.C., Rapin, W., Mangold, N., Fabre, C., Gasnault, O., Forni, O., Tokar, R., Ollila, A., Schröder, S., Lasue, J., Maurice, S., Sautter, V., Newsom, H., Vaniman, D., Le Mouélic, S., Dyar, D., Berger, G., Blaney, D., Nachon, M., Dromart, G., Lanza, N., Clark, B., Clegg, S., Goetz, W., **Berger, J. A.**, Barraclough, B., Delapp, D. (2014), Compositions of coarse and fine particles in martian soils at gale: A window into the production of soils, *Icarus,* doi:10.1016/j.icarus.2014.04.052.

Lanza, N.L., Fischer, W.W., Wiens, R.C., Grotzinger, J.P., Ollila, A.M., Cousin, A., Anderson, R.B., Clark, B., Gellert, R., Mangold, N., Maurice, S., LeMouelic, S., Nachon, M., Schmidt, M.E., **Berger, J.A.**, Clegg, S., Forni, O., Hardgrove, C., Melikechi, N., Newsom, H.E., Sautter, V. (2014), High manganese concentrations in rocks at Gale crater, Mars, *Geophys. Res. Lett.*, 10.1002/2014GL060329

Lanza, N.L., Ollila, A.M., Cousin, A., Wiens, R.C., Clegg, S., Mangold, N., Bridges, J.C., Cooper, D., Schmidt, M.E., **Berger, J. A.**, Arvidson, R.E., Melikechi, N., Newsom, H.E., Tokar, R., Hardgrove, C., Mezzacappa, A., Jackson, R.S., Clark, B., Forni, O., Maurice, S., Nachon, M., Anderson, R.B., Blank, J., Deans, M., Delapp, D., Léveillé, R., McInroy, R., Martinez, R., Meslin, P.-Y., Pinet, P. (2014), Understanding the signature of rock coatings in laser-induced breakdown spectroscopy data, *Icarus*, doi:10.1016/j.icarus.2014.05.038

Schmidt, M.E., Campbell, J.L., Gellert, R., Perrett, G.M., Treiman, A.H., Blaney, D.L., Olilla, A., Calef, F.J., Edgar, L., Elliott, B.E., Grotzinger, J., Hurowitz, J., King, P.L., Minitti, M.E., Sautter, V., Stack, K., **Berger, J. A.**, Bridges, J.C., Ehlmann, B.L., Forni, O., Leshin, L.A., Lewis, K.W., McLennan, S.M., Ming, D.W., Newsom, H., Pradler, I., Squyres, S.W., Stolper, E.M., Thompson, L., VanBommel, S., Wiens, R.C. (2014), Geochemical diversity in first rocks examined by the Curiosity Rover in Gale Crater: Evidence for and significance of an alkali and volatile-rich igneous source, *J. Geophys. Res. Planets*, 119, 64–81. doi:10.1002/2013JE004481.

Selected Conference Abstracts

Berger, J. A., M. E. Schmidt, R. L. Flemming, R. Gellert, D. W. Ming, R. V. Morris, (2017), Hawai'i and Gale Crater: A Mars Analogue Study of Igneous, Sedimentary, Weathering, and Alteration Trends in Geochemistry. Presented at 48th Lunar Planet. Sci. Abstract #2273.

Ming, D. W., A. S. Yen, R. Gellert, B. Sutter, **J. A. Berger**, L. M. Thompson, M. E. Schmidt, R. V. Morris, and A. H. Treiman (2016), Elemental Gains/Losses Associated with Alteration Fractures in an Eolian Sandstone, Gale Crater, Mars, in *AGU Fall Meeting*, vol. P11B-1860.

Berger, J. A., M. Schmidt, R. L. Flemming, and R. Gellert (2016), Element Mobility in Hawaiian Weathering Profiles: Constraints for Lower Mt. Sharp in Gale Crater, Mars (2016) Presented at Geological Society of America Annual Meeting doi: 10.1130/abs/2016AM-285459.

Gellert, R., M. Schmidt, **J. A. Berger**, N. Boyd, E. Desouza, C. O'Connell-Cooper, G. Perrett, L. M. Thompson, S. VanBommel, and A. S. Yen (2016), APXS Overview: Widespread, Open Hydraulic System and Multiple Fluid Conditions Indicated by Si Enrichment Trends in Gale Crater Sediments, Mars. Presented at Geological Society of America Annual Meeting doi: 10.1130/abs/2016AM-285724.

Berger, J. A., M. E. Schmidt, M. R. M. Izawa, R. Gellert, D. W. Ming, E. B. Rampe, S. J. VanBommel, A. C. McAdam, (2016), Phosphate Stability in Diagenetic Fluids Constrains the Acidic Alteration Model for Lower Mt. Sharp Sedimentary Rocks in Gale Crater, Mars, Presented at 47th Lunar Planet. Sci. Abstract 1652.

Gellert, R., **J. A. Berger**, N. Boyd, J. L. Campbell, E. Desouza, D, W, Ming, R. V. Morris, G. M. Perrett, M. E. Schmidt, L. M. Thompson, S. J. Vanbommel, A. S. Yen. (2016), Chemical Evidence for an Episode of Acidic Leaching at the Base of Mount Sharp, Gale Crater, Mars, as seen by the APXS, Presented at Lunar and Planetary Science Conference, vol. 47, p. 2368.

Berger, J. A., M. E. Schmidt, R. Gellert, N. I. Boyd, J. L. Campbell, E. Desouza, M. R. Fisk, G. M. Perrett, D. Tesselaar, L. M. Thompson, S. J. VanBommel, A. S. Yen, (2015) Chemical Composition of Diagenetic Features at Lower Aeolis Mons, Mars as Measured by Curiosity's APXS, Presented at AGU 2015 Fall Meeting, abstract #P43B-2121.

Gellert, R., **J. A. Berger**, N. Boyd, J. L. Campbell, E. Desouza, G. M. Perrett, L. M. Thompson, S. J. Vanbommel, A. S. Yen, (2015), Chemical Composition of lower Mount Sharp at Gale Crater, Mars, as measured by the APXS, Presented at AGU 2015 Fall Meeting, abstract #P43B-2120.

Berger, J. A., M. E. Schmidt, R. Gellert, J. L. Campbell, B. E. Elliott, P. L. King, D. W. Ming, G. M. Perrett, L. M. Thompson, S. J. VanBommel, (2015). Ge enrichments in sedimentary rocks in Gale Crater, Mars. Presented at Goldschmidt Conference 2015, abstract 23b 270.

Berger, J. A., M. E. Schmidt, R. Gellert, J. L. Campbell, N. I. Boyd, B. E. Elliott, M. R. Fisk, P. L. King, D. W. Ming, G. M. Perrett, L. M. Thompson, S. J. VanBommel, A. Yen, (2015). Germanium Enrichments in Sedimentary Rocks in Gale Crater, Mars: Constraining the Timing of Alteration and Character of the Protolith. Presented at Lunar Planet. Sci., XLVI. abstract 1564.

Gellert, R. **J. A. Berger**, N. Boyd, J. L. Campbell, E. Desouza, B. Elliott, M. Fisk, B. Pavri, G. M. Perrett, M. E. Schmidt, L. M. Thompson, S. J. Vanbommel, A. S. Yen, (2015), Chemical Evidence for an Aqueous History at Pahrump, Gale Crater, Mars, as Seen by the APXS, Presented at Lunar Planet. Sci., XLVI, vol. 46, p. 1855.

Yingst, R. A., **J. A. Berger,** B. A. Cohen, B. M. Hynek, M. E. Schmidt, (2015) A Test of Two Field Methods: Determining Best Practices in Reconnoitering Sites for Habitability Potential Using a Semi-Autonomous Rover, Presented at Lunar Planet. Sci., XLVI. Abstract 1640.

Berger, J. A., M. E. Schmidt, R. Gellert, M. R. Fisk, (2014). Zinc Enrichments in the Rocks of Gale Crater, Mars Measured by MSL-APXS Reflect Both High Zn in Jake_M Rocks and the Concentration of Zn in Sedimentary Cements, Presented at AGU 2014 Fall Meeting, Abstract P51E-3988.

Schmidt, M. E., M. Baker, **J. A. Berger**, M. R. Fisk, R. Gellert, S. M. McLennan, M. E. Newcombe, E. M. Stolper, and L. M. Thompson, (2014), Diverse, Alkali-Rich Igneous and Volcaniclastic Rocks Reflect a Metasomatised Mantle Beneath Gale Crater, Presented at AGU 2014 Fall Meeting, Abstract P33E–06.

King, P. L., **J. A. Berger**, M. R. Izawa, L. A. Loiselle, R. W. Henley, J. L. Wykes, R. Gellert, U. Troitzsch, C. L. Moore, R. A. Eggleton, B. C. Hyde, C. J. Renggli, and N. M. Semmler, (2014), Informing space science developments through simulating "volatile" materials and processes on planetary bodies. Presented at 14th Australian Space Research Conference.

Berger, J. A., M. E. Schmidt, R. Gellert, P. L. King, (2014), Comparing Gale Crater and Gusev Crater Enrichments of Fluid-Mobile Elements Measured by Alpha Particle X-ray Spectrometers on Mars. Presented at Lunar Planet. Sci., XLV, Abstract 2285.

Gellert, R., **Berger, J. A.**, Boyd, N.I., Campbell, J.L., Elliot, B., Farien, A., King, P.L., Leshin, L.A., Pavri, B., Perrett, G.M., Pradler, I., Schmidt, M.E., Squyres, S.W., Thompson, L., VanBommel, S., Yen, A.S., 2014. APXS Measurements Along the MSL Traverse at Gale crater, Mars. (2014) Presented at Lunar Planet. Sci., XLV. p. Abstract 1876.

Schmidt, M. E., **Berger, J. A.**, Blaney, D., Gellert, R., Grotzinger, J. P., Forni, O., King, P. L., Mangold, N., (2014). Geochemical Classification of Rocks in Gale Crater with APXS to Sol 360: Sediment Provenance, Mixing, and Diagenetic Processes. Presented at Lunar Planet. Sci., XLV. p. Abstract 1504.

Berger, J. A., Campbell, J. L., Edgett, K. S., Gellert, R., King, P. L., Perrett, G. M., Pradler, I., Schmidt, M. E., (2013). A Unique Measurement of Martian Dust by the Alpha Particle X-ray Spectrometer on Curiosity in Gale Crater, Mars. Presented at Geological Society of America Annual Meeting. Presented at Geological Society of America Annual Meeting, Denver, p. 138.

Berger, J. A., King, P. L., Gellert, R., Campbell, J. L., Boyd, N. I., Pradler, I., Perrett, G.M., (2013). MSL titanium observation tray measurements with APXS. Presented at Lunar and Planetary Science Conference 44, Abstract 1321.

Campbell, J.L., **Berger, J. A.**, Gellert, R., King, P. L., Perrett, G. M., Boyd, N. I., Edgett, K. S., Yingst, R. A., MSL Science Team, (2013). First Measurements of the MSL APXS Calibration Target on Mars. Presented at Lunar Planet. Sci., XLIV. p. Abstract 1506.

Gellert, R., **Berger, J. A.**, Boyd, N. I., Brunet, C., Campbell, J. L., Curry, M., Elliot, B., Fulford, P., Grotzinger, J. P., Hipkin, V., Hurowitz, J. A., King, P. L., Leshin, L. A., Limonadi, D., Pavri, B., Pradler, I., Marchand, G., Perrett, G. M., Scodary, A., Simmonds, J. J., Spray, J., Squyres, S. W., Thompson, L., VanBommel, S., Yen, A. S., MSL Science Team, (2013). Initial MSL APXS activities and observations at Gale crater, Mars. Presented at Lunar Planet. Sci., XLIV. Abstract 1432.

Schmidt, M. E., P. L. King, R. Gellert, B. Elliott, L. Thompson, **J. A. Berger**, J. Bridges, J. L. Campbell, B. Ehlmann, J. Grotzinger, J. Hurowitz, L. Leshin, K. W. Lewis, S. M. McLennan, D. W. Ming, G. Perrett, I. Pradler, E. M. Stolper, S. W. Squyres, A. H. Treiman and the MSL Science Team, (2013). APXS of First Rocks Encountered by Curiosity in Gale Crater: Geochemical Diversity and Volatile Element (K and Zn) Enrichment. Presented at 44th Lunar and Planetary Science Conference. Abstract #1278.

Berger, J. A., King, P. L., Spilde, M. N., Wright, S. P., Kunkel, T. S., Lee, R. J., (2012). Effect of Halite and Calcite Coatings on Thermal Infrared Spectra with Implications for Mars Exploration. Presented at AGU Fall 2012 Meeting. Abstract P13A–1898.

Berger, J. A., King, P. L., Kunkel, T. S., Spilde, M. N., Crisp, J. A., (2011). Thermal Infrared Spectroscopy of Halite-Coated Glasses — An Evaluation of Continuous Versus Discontinuous Coatings. Presented at Lunar and Planetary Institute Science Conference. Abstract 1574.

Hamilton, V. E., McDowell, M. L., **Berger, J. A.**, Cady, S. L., Knauth, L. P., (2011). Linking Spectral Features with Composition, Crystallinity, and Roughness Properties of Silica and Implications for Candidate Hydrothermal Systems on Mars. Presented at AGU Fall Meeting. Abstract 1763.

King, P. L., Izawa, M. R. M., Vernazza, P., McCutcheon, W. A., **Berger, J. A.**, Dunn, T., (2011). Salt- a critical material to consider when exploring the solar system. Presented at 42nd Lunar and Planetary Science Conference. Abstract 1985.

Berger, J. A., Cady, S. L., McDowell, M. L., Hamilton, V. E., (2009). Effect of surface roughness on the thermal infrared spectral characteristics of Mars-relevant silica-rich materials. Presented at Geological Society of America 41, 266.